

**PROGRESS TOWARD A NEGATIVE REFRACTIVE INDEX IN AN ATOMIC SYSTEM:  
SPECTROSCOPY AND SIMULATIONS OF A RARE-EARTH DOPED CRYSTAL**

by

Zachary J. Simmons

A dissertation submitted in partial fulfillment of  
the requirements for the degree of

Doctor of Philosophy

(Physics)

at the

UNIVERSITY OF WISCONSIN–MADISON

2015

Date of final oral examination: August 5, 2015

The dissertation is approved by the following members of the Final Oral Committee:

Deniz D. Yavuz, Professor, Physics

James E. Lawler, Professor, Physics

Mark Saffman, Professor, Physics

Thad G. Walker, Professor, Physics

Paul Campagnola, Professor, Biomedical Engineering

© Copyright by Zachary J. Simmons 2015

All Rights Reserved



## ACKNOWLEDGMENTS

We live in fantastic times that one has the opportunity to devote themselves to study, to learning as a job. For this I am deeply grateful.

There are many people that I would like to thank. First off, many thanks to Deniz. I cannot imagine a better mentor. He is possessed with enthusiasm about science, humility, and a great depth of understanding. I have learned a great deal from him and aspire to be as good a scientist and person.

A huge thanks to my lab group mates. One of the joys of being a graduate student is learning from your peers; I have learned much from mine.

A special thanks to Nick Brewer, much of the work in this document would not have been possible without his help. He has done a great job building up the experimental system, judiciously picking components like our user-friendly cryostat and integrating it all via computer into a powerful, flexible, experimental platform. He is going to be a great scientist. Thanks to Nick and Zach Buckholtz for all manner of help as I have been writing; I am so excited to see what they accomplish next with the experiment!

A big part of what made grad school a great experience for me was due to Josh Weber. Thanks for helping me with my quantum homework, bike scavenger hunts, and the unenviable task of proofreading this document. His help has made this thesis exponentially better.

It has been excellent learning about atomic localization from Jared Miles. It has been awesome seeing him develop and improve a very sophisticated experiment and I am grateful to him for including me in that work. Thanks also to Jared for commiserating during this thesis-writing process; it has been much more enjoyable because of it.

Thanks to Nick Proite for getting me started with Yavuzlab and thanks to Eli Mueller for some awesome laser improvements.

A huge thanks to Ann Austin, I so appreciate her helping us buy all the gear for our experiments. Thanks to Aimee and Renee Lefkow for so much help over the years; they always knew exactly how to help. Thanks to Joe Sylvester, Sara Yaeger, and Doug Dummer in the machine shop. I've always enjoyed the projects and thanks so much for teaching me.

Thanks to faculty that I have had the pleasure of working with including Mark Saffman and Michael Winokur. Thanks to Jim Reardon for many interesting conversations about teaching. Thanks to Susan Nossal for exposing me to the PLC and talking teaching. I am grateful for people in our department keeping the interests of the students a priority. Thanks to my students. I hope you've learned something from me; I've learned so much from you.

Thanks, of course, to my family, for all that you have given me. Thanks to Andrea for all your support, especially for putting up with me while I have been preparing this thesis.

# TABLE OF CONTENTS

	Page
<b>Table of Contents</b> . . . . .	iv
<b>Abstract</b> . . . . .	vii
<b>1 Introduction</b> . . . . .	1
1.1 Defining Negative Index . . . . .	1
1.2 An Aside: Metamaterials . . . . .	4
1.3 Chapter Summaries . . . . .	6
<b>2 Refractive Index Enhancement in Atomic Systems Using EIT</b> . . . . .	8
2.1 Resonances in Materials, Normal Refraction . . . . .	8
2.2 Index Modification via EIT, Theory . . . . .	10
2.2.1 EIT Math: Schrödinger approach . . . . .	10
2.2.2 EIT Math: Density matrix . . . . .	14
2.2.3 Relating Atomic Coherence to Refractive Index . . . . .	16
2.3 Index Modification Experiments . . . . .	22
<b>3 Atomic Negative Index Scheme</b> . . . . .	28
<b>4 Eu:YSO Spectroscopy and Structure</b> . . . . .	33
4.1 Eu:YSO Gross Structure/General information . . . . .	33
4.2 Our host crystal: YSO . . . . .	40
4.2.1 Crystal E-Field: Stark Splitting . . . . .	42
4.2.2 Crystal Electric Field: Inhomogeneous Broadening . . . . .	44
4.2.3 Crystal E-Field: Polarization Dependence . . . . .	45
4.3 Atomic Physics in Eu Relevant to Calculating Optical Transitions . . . . .	48
4.4 Studies Involving $\text{Eu}^{3+}$ Transitions in the Literature . . . . .	50

	Page
<b>5 Eu:YSO Decay, Broadenings and Crystal Effects</b> . . . . .	52
5.1 Non-Radiative Decay Mechanisms and Homogeneous Linewidth . . . . .	52
5.1.1 Ion-Ion Interactions and Ion-Host Interactions . . . . .	53
5.2 Experimentally Ascertaining Non-Radiative Decay Rates. . . . .	56
5.3 Estimating Phonon Decay Rates . . . . .	59
5.4 Modeling Pumping and Decay Routes/Conclusions: . . . . .	68
<b>6 Experimental Set-up</b> . . . . .	70
6.1 Laser System and Locking to Reference Cavity . . . . .	72
6.2 Getting Green: Second Harmonic Generation (SHG) . . . . .	79
6.3 Laser Switching and Frequency Shifting . . . . .	83
<b>7 Hole-Burning, Optical Pumping and Other Incoherent Effects</b> . . . . .	86
7.1 Fluorescence Spectroscopy . . . . .	86
7.2 Inhomogeneous Broadening . . . . .	90
7.3 Hyperfine Structure, Hole-Burning Theory, and Ion Class Distillation . . . . .	92
7.4 Hole Burning Experiment . . . . .	101
7.5 Hole-burning Width . . . . .	105
<b>8 Coherent Effects</b> . . . . .	108
8.1 6-level System Hamiltonian . . . . .	108
8.2 Rabi Flopping . . . . .	117
8.3 EIT . . . . .	119
<b>9 Going Forward</b> . . . . .	122
9.1 Experimental Improvements . . . . .	122
9.2 Left-Handed Waves . . . . .	124
9.3 Final Thoughts . . . . .	127

## APPENDICES

Appendix A: Assorted Math for EIT and the Density Matrix . . . . .	129
Appendix B: Index Enhancement Experiment . . . . .	143
Appendix C: Calculating Optical Transitions . . . . .	152
Appendix D: Kramers-Kronig Comments . . . . .	166
Appendix E: Lockboxes for Eu:YSO Experiment . . . . .	169

	Page
Appendix F: Broadening Suppression Idea . . . . .	179
<b>PUBLICATIONS</b> . . . . .	180
<b>REFERENCES</b> . . . . .	182

## Abstract

### **Progress toward a negative refractive index in an atomic system: spectroscopy and simulations of rare-earth doped crystal Eu:YSO**

*Zachary J Simmons*

*Under the supervision of Professor Deniz D. Yavuz*

*At the University of Wisconsin - Madison*

A material with a negative index of refraction would have interesting properties including: light refracting the ‘wrong’ way,  $\vec{E}$ ,  $\vec{B}$ , and  $\vec{k}$  forming a left-handed triad, and the prospect of lenses that could harness evanescent waves and beat the diffraction limit. Although there has been progress toward this in artificial materials, we seek an optical negative index in an atomic system.

A necessary ingredient of an atomic negative index is a strong magnetic response. This work describes our project to investigate an optical magnetic dipole transition in a rare-earth doped crystal. The document discusses relevant background material including the atomic structure of Eu:YSO and crystal-related issues, as well as construction of the experimental apparatus.

The response of the  ${}^7F_0 \rightarrow {}^5D_1$  transition in Eu:YSO is relatively strong and a great system for exploring optical magnetic dipole physics. Initial results from optical pumping experiments are described as well as simulation results for coherent effects including Rabi flopping and electromagnetically induced transparency (EIT). There is also discussion of current experimental issues and prospects. This system may be one of the most promising atomic systems in which to pursue experimental realization of left-handed wave phenomena.

# Chapter 1

## Introduction

The index of refraction describes the speed of light in a medium and is given by the ratio of the speed of light in vacuum to the speed in the medium:  $n = \frac{c}{v}$ . Hence,  $n = 1$  in outer space, while  $n = 1.5$  is a reasonable value for a piece of glass. Engineering the index of refraction in atomic systems to have interesting properties by harnessing coherent optical processes is a large theme/goal in the Yavuz group.

There are a some important implications/potential applications to engineering the refractive index. One significant consequence is that the wavelength of light in a medium goes like  $\lambda_n = \frac{\lambda}{n}$ . As a result, if one has a high-index media, the wavelength and possible focal spot size can be made smaller. This is clearly seen in Abbe's diffraction limit in microscopy, one of many ways to specify the resolution limit of an optical system, given by the wavelength divided by 2 times the numerical aperture:  $r_{Abbe} = \frac{\lambda}{2NA} = \frac{\lambda}{2n\sin(\theta)}$ . You can imagine submerging something being observed with a microscope in a higher-index medium thus boosting the NA and maximum resolution. Indeed, this is what is done with immersion microscope objectives. We will discuss refractive index enhancement to help us understand how we can modify the index through coherent atomic processes, but the lion's share of work discussed in this thesis is directed toward another refractive index modification goal: trying to make the index *negative*.

### 1.1 Defining Negative Index

A negative refractive index is harder to digest/interpret so let us spend some time now fleshing it out. Combining Maxwell's equations, one can derive the speed of an electromagnetic wave. In

vacuum, this gives us the origin of the familiar speed of light in terms of the electric permittivity and magnetic permeability in vacuum.

$$\nabla^2 \vec{E} = \mu_0 \epsilon_0 \frac{\delta \vec{E}}{\delta t} \quad (1.1)$$

$$c = \frac{1}{\sqrt{\epsilon_0 \mu_0}} \quad (1.2)$$

As we can see, the speed contains the square root of the product of these quantities. In a material that is able to be polarized and/or magnetized, the permittivity and permeability can differ from their values in vacuum giving a different wave speed:  $v = 1/\sqrt{\epsilon\mu}$ . The wave speed is given by:  $v = c/n$ , from which we can pull out the refractive index:

$$v = \frac{c}{n} \rightarrow n = \frac{\sqrt{\epsilon\mu}}{\sqrt{\epsilon_0\mu_0}} \quad (1.3)$$

According to Veselago, in order to get a negative index of refraction both the electric permittivity and magnetic permeability need to be negative [1]. At first glance, it would appear that this would not be enough necessarily as the product of two negative quantities is going to be positive. The index is given by the square root, so why choose the negative root? It turns out it is a little more complicated because these quantities are complex, there are real and imaginary components associated with any resonance. This will be discussed in the next chapter. We can get some insight if we look at the phase.

Writing the complex susceptibility and permeability as a relative magnitude with an explicit complex phase factor:

$$\frac{\epsilon}{\epsilon_0} = r_\epsilon e^{i\theta}, \quad \frac{\mu}{\mu_0} = r_\mu e^{i\phi} \quad (1.4)$$

If we dictate that these are negative real quantities, we know that:

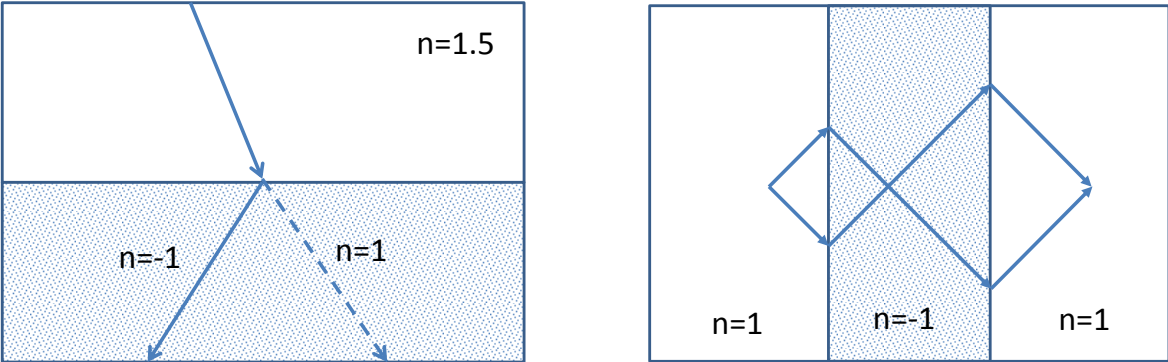
$$\pi/2 < \theta, \phi < 3\pi/2 \quad (1.5)$$

n becomes:

$$n = \sqrt{\epsilon\mu}e^{i(\theta+\phi)/2} \tag{1.6}$$

Now can n be real and positive? Well, if that were the case, then  $-\pi/2 < (\theta + \phi)/2 < \pi/2$ . This can't happen for any phase angle according to our argument in expression 1.5, so we know if the permittivity and permeability are real and negative, the index is as well. Using this same logic, we can also note that for waves to propagate ordinarily in negative index media, the imaginary part of the index needs to be positive as otherwise there would be gain. The absorption coefficient is proportional to the imaginary part of the index. As a result,  $0 < (\theta + \phi)/2 < \pi$ . Thus we can conclude that for negative index propagation:  $\pi/2 < 1/2(\theta + \phi) < \pi$ . Miloni discusses these kinds of arguments or see Ziolkowski and Heyman for a lot more depth[2, 3].

Media with a negative refractive index have some strange properties. One of the most frequently cited is that if n is negative, refraction happens in the opposite direction and the familiar Snell's law looks a little strange, as shown in the left panel of figure 1.1.



(a) Snell's Law

(b) 'Perfect Lens'

Figure 1.1: Negative Refraction entails some strange effects including: a) refraction in the 'wrong' direction and b) the possibility of a 'Perfect Lens' not limited by diffraction.

Although mentioned by Veselago as well, John Pendry in his publication, *Negative Refraction makes a Perfect Lens*[4], succinctly draws attention to one of the properties of negative index

materials that have generated so much interest, the prospect that one could create a lens that would not be limited by diffraction but that could harness evanescent waves and potentially image with unlimited resolution. The ray diagram is a little different from a normal lens; the rays cross in the middle of the slab, see the right panel of figure 1.1.

Another rather strange consequence mentioned by Veselago is that the  $k$ -vector for radiation in a negative index medium is directed toward, rather than away, the source. As a result, light in a negative-index medium reflecting off an object would impart momentum in the direction of the source. There would, as a result, be radiation *tension* rather than pressure. A laser beam in a negative index medium might function as a tractor beam, which is strange indeed.

We can use the publication of that paper by Pendry as a proxy for interest in this work as it is so often referred to in this field. As of June 2015, of the more than 500,000 articles published by the American Physical Society (which includes Physical Review and all related journals, stretching back to the late 1950s), Pendry's 2001 paper is about the 40th most popular, having been cited more than 4,000 times in the last 15 years.

## 1.2 An Aside: Metamaterials

Although negative index materials do not exist in nature, there has been significant progress in making negative index materials, albeit a particular kind, artificial engineered materials called metamaterials. Metamaterials are not the subject of this work, but we mention them to distinguish our approach and motivate why pursuing an alternative is worthwhile. Rather than relying on the microscopic properties of the material in aggregate to define the electromagnetic response, metamaterials contain engineered elements of the size scale of the excitation wavelength to influence and define the response. A clear example is the use of tiny metal rings to enhance magnetic response. Since metamaterials are engineered materials, they started out large (long wavelengths) and have moved to smaller wavelengths as the technology has improved. See figure 1.2 reproduced from a Nature Photonics publication by Soukoulis and Wegener[5]. There are now even negative-index metamaterials in the visible, as indicated by the solid triangles in the figure.

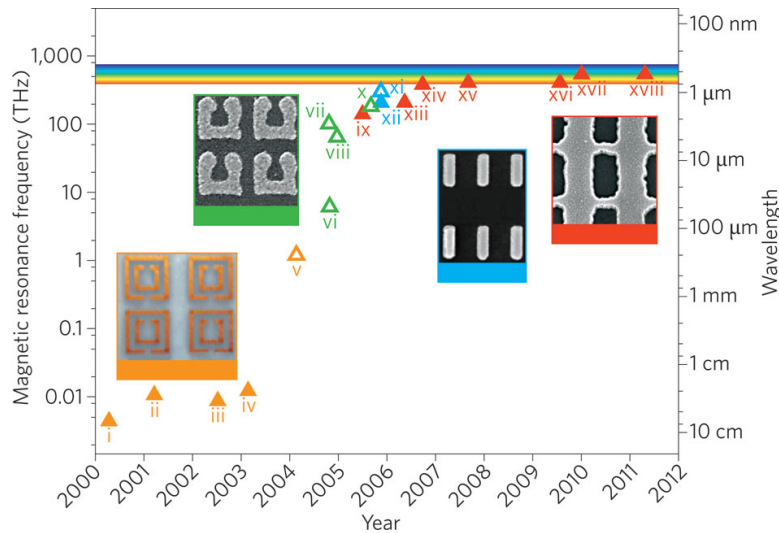


Figure 1.2: Progress in Metamaterials: advancement toward shorter wavelengths in negative-index metamaterials between 2002 and 2012, figure by Soukoulis and Wegener[5]. Although such approaches have marched toward smaller wavelengths as technology has improved, they still suffer from large absorption among other issues. Reprinted by permission from Macmillan Publishers Ltd: Nature [5], © 2015

Although they now reach into the visible, such engineered materials still suffer from lots of problems. An excellent source of information on these issues is a book chapter by Xiao and Shalaev titled *Tunable Active Optical Negative Index Metamaterials*[6]. There are significant limitations to the metamaterial approach. One is that there is generally large loss. For example, the structures often rely on using metal elements, and as we know, metal is not very transparent. Another issue is that their properties are set by their geometrical configuration and so are fixed once the engineered structure is created/assembled. As a result, they are not generally tunable. Towards both of these difficulties, Xiao cites progress. They overcome loss in some circumstances by adding a gain layer. They also propose a scheme toward making the materials adjustable by relating how liquid crystals can be incorporated and their properties adjusted by adjusting their temperature. Even so, the advancements are modest and as of yet are not at optical frequencies.

The limitations of these metamaterial approaches have led to interest in pursuing other routes and we pursue an atomic route toward a negative index. This approach also has limitations including a high atomic density requirement, the need for an optical magnetic response, and magnetic and electric transitions near the same frequency. But it also has some pretty significant advantages. One very interesting prospect of the atomic approach is that since it is a product of the interaction of lasers with an atomic system, the effects can be turned on and off or modified. This is quite a contrast to a metamaterial approach where it is largely fixed. The prospect of a modifiable atomic system is exciting from the perspective of imagining any of these materials integrated into an optical system. The potential of an atomic route is what motivates the work in this thesis. The layout of the chapters will be as follows:

### 1.3 Chapter Summaries

Chapter 2, [Refractive Index Enhancement in Atomic Systems Using EIT](#), discusses the theory and experiments that we have done to enhance the index of refraction in atomic systems. This introduces the theoretical framework in which the index of refraction can be manipulated via coherent atomic processes. This also introduces the reader to our past experiments that demonstrate these ideas. This material sets the stage for more sophisticated index-modification schemes like the negative index idea.

Chapter 3, [Atomic Negative Index Scheme](#), introduces the atomic negative index scheme specifically. This idea is built on the index modification ideas of the previous chapter and was explored and developed by Yavuz and a previous student, Dan Sikes[7, 8]. The testing, development, and simulation of this idea was the driving motivation behind pursuing experiments toward an atomic negative index. Looking for a suitable atomic system having relatively strong magnetic transitions and a high density led to rare-earth doped crystals.

Chapter 4, [Eu:YSO Spectroscopy and Structure](#), looks at the atomic structure of our Eu:YSO system. The atomic physics of rare-earth ions with their 4f structure is very interesting and complex. The crystal electric field causes a number of effects including broadenings and splitting of energy levels.

Chapter 5, [Eu:YSO Decay, Broadenings and Crystal Effects](#), is basically a background check on the rare-earth doped crystal system. It has been very interesting for us working in a solid instead of a vapor cell or optical trap, but as a solid brings a number of new challenges. Crystal-induced broadening mechanisms and decay mechanisms are explored. Phonons are discussed at length, a complicated and important issue for crystal-based experiments.

Chapter 6, [Experimental Set-up](#), lays out the experiment that we have built including: laser systems, laser locking, and cryostat.

Chapter 7, [Hole-Burning, Optical Pumping and Other Incoherent Effects](#), discusses results of incoherent experiments that we have done, including optical pumping, which in the context of our crystal system becomes spectral hole-burning. Time is spent discussing and explaining spectral hole-burning and ion class distillation as these issues become complicated and command of them is necessary for our future experiments. This chapter concludes with our latest experimental results and speculation as to current experimental limitations.

Chapter 8, [Coherent Effects](#), looks ahead to coherent optical phenomena we plan to pursue in the crystal. The Hamiltonian for our system is presented as well as simulation results incorporating our predictions and measurements so far. Simulations of Rabi flopping and EIT are presented as well as some notes about experimental considerations.

Chapter 9, [Going Forward](#), discusses proposed experimental improvements as well as a new route to negative index in atomic systems that has quickly jumped to the head of the pack as far as prospects for experimental observation of negative index/left-handed waves. This approach is not limited by density like previous atomic approaches. Future grad students no doubt will bring this to fruition.

Additionally, appendices will contain some more detailed supporting mathematics, related publications, details of using atomic structure calculation programs, discussion of experiment electronics, and other supplementary information.

## Chapter 2

### Refractive Index Enhancement in Atomic Systems Using EIT

Manipulating and engineering the index of refraction in atomic systems is a area of research we have been pursuing for a while in Yavuzlab. Our most recent work, theoretical work in negative index and left-handed waves, is built on a foundation of experience engineering the index to make it larger while at the same time canceling absorption. Before discussing the more recent negative-index work, let us provide some context by discussing these index-enhancement schemes, both theory and experiments.

#### 2.1 Resonances in Materials, Normal Refraction

It is useful to start with the anatomy of a ‘normal’ dispersion relationship, say in a piece of glass. The glass has resonances, different transitions in the material. The index of refraction is a complex quantity. At each resonance, there is increased absorption (corresponding to the imaginary part of the index) at that wavelength as well as a kink in the real part of the refractive index (corresponding to a change in the speed of light in the material with frequency). An example of a glass is in figure 2.1[9]. Notice there are resonances in the IR and UV parts of the spectrum, while the absorption in the visible (indicated by the grey band) changes little.

The index of refraction of the material can be related to the electric susceptibility through  $n = \sqrt{1 + \chi}$  *i. e.*, if we know the susceptibility, we know the index of refraction. The susceptibility is complex as well, the real part giving the index and the imaginary part relating to absorption. These resonances in the glass can be described by a widely employed classical expression for the susceptibility:

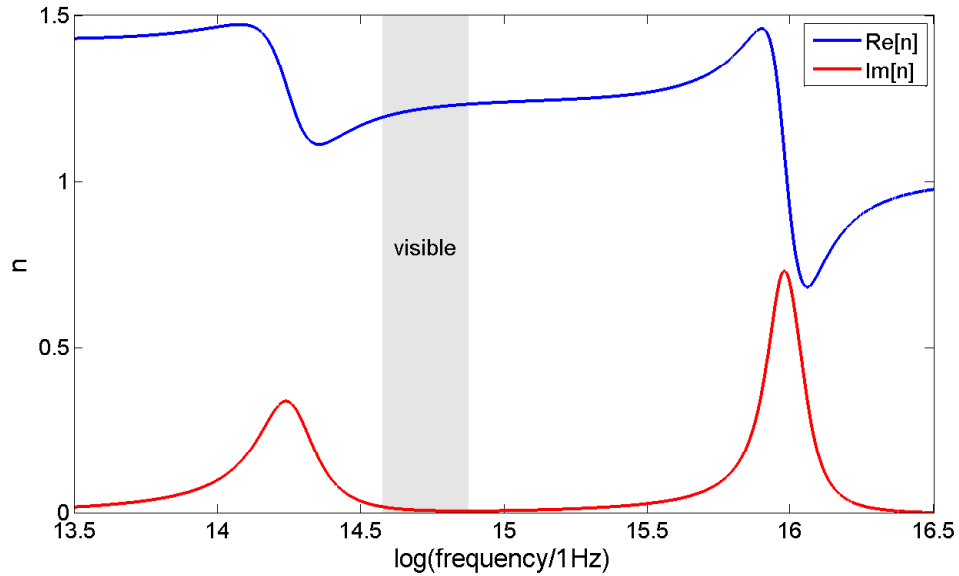


Figure 2.1: Example dispersion resonances in glass from [9]. Note that increases in the real part of the refractive index are all accompanied by increased absorption ( $\text{Im}[n]$ ) as well in the vicinity of a resonance.

$$\chi = \frac{Nq^2/m}{\omega_0^2 - \omega^2 + j\gamma\omega} \quad (2.1)$$

This comes from a classical picture, the Lorentz model, derived by treating the electron as a mass on a spring (electric restoring force) subject to a driving electric field and velocity-dependent damping. In a material, there would be a number of such resonances. In general, there is a gradual increase in the index with frequency between resonances and then a small region of anomalous dispersion, where the index decreases with increasing frequency. See figure 2.1; this picture is useful to convey the fact that in ‘normal’ materials like a piece of glass, whenever there is an increase in the index of refraction, it is associated with an increase in absorption.

## 2.2 Index Modification via EIT, Theory

With that picture in mind, let us next discuss how one can increase the refractive index without increasing absorption. To accomplish this we use a coherent optical process called Electromagnetically Induced Transparency (EIT). EIT is a fascinating and widely studied phenomenon. The core idea is that an atomic medium that would normally absorb a particular color can be rendered transparent to that color, provided an additional laser is appropriately applied to the system and that the system has the requisite atomic structure.

The lambda system shown in figure 2.2 is one such atomic system, although there are other level schemes that also exhibit EIT. The figure shows how in the lambda configuration, the two ground states are coupled to the excited state via probe and control lasers. This diagram is not comprehensive, but it exposes one to many of the pertinent features. Also note that there is minimal decay between the ground states and decay between ground states is not electric-dipole allowed. The probe is the beam that under appropriate conditions can pass through the system unabsorbed. In any case, the purpose of this figure is to familiarize ourselves with the general picture of the system we will be describing mathematically.

There are many excellent studies of this phenomenon, cited here are an excellent introduction by Harris as well as a quite comprehensive review by Fleischhauer[10, 11]. I was impressed by this undergrad thesis by Wes Erickson at Reed College, it has much of the same material as this section[12]. Scully and Zubairy's *Quantum Optics* is a great source of information on this topic as well[13].

### 2.2.1 EIT Math: Schrödinger approach

We describe the optical response of the atomic system with a frequency-dependent electric susceptibility, as mentioned above. It turns out this quantity is related, proportional, to the atomic coherence between levels that make up a resonant transition. For our probe laser, it is the coherence between levels 1 and 3 in the figure. We can calculate that coherence, among other things, by solving the Schrödinger equation or related Liouville-von Neumann equation(in the density matrix

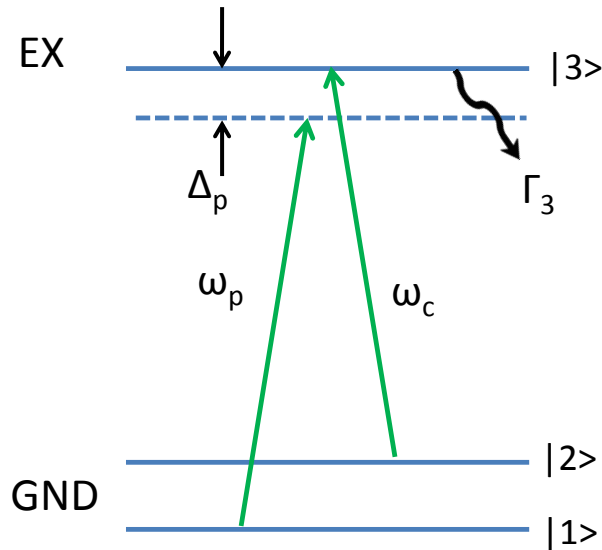


Figure 2.2: EIT level scheme:  $|1\rangle$  and  $|2\rangle$  are both coupled to  $|3\rangle$ . Decay from  $|3\rangle$  happens via  $\Gamma_3$ . Transitions between  $|1\rangle$  and  $|2\rangle$  are not dipole-allowed. Varying  $\Delta_p$  scans the probe through the resonance.

formalism). Let us spend some time looking at the math. Some of the details and a more fleshed out version of some of this material appears in appendix A, but we do want to present the main approach here. One way to look at the problem is to directly apply the Schrödinger equation.

$$i\hbar|\dot{\psi}\rangle = H|\psi\rangle \quad (2.2)$$

Where the Hamiltonian for our system is:

$$H = H_0 + H_1$$

$$H_0 = \hbar\omega_1 |1\rangle \langle 1| + \hbar\omega_2 |2\rangle \langle 2| + \hbar\omega_3 |3\rangle \langle 3|$$

$$H_1 = -\frac{\hbar}{2}(\Omega_p e^{-i\phi_p} e^{-i\omega_p t} |3\rangle \langle 1| + \Omega_c e^{-i\phi_c} e^{-i\omega_c t} |3\rangle \langle 2|) + H.c. \quad (2.3)$$

$$(2.4)$$

There are two pieces:  $H_0$  the energies of the levels, and  $H_1$ , the energy due to the interaction with the lasers. H.c. is the Hermitian conjugate. And writing down a wavefunction:

$$|\psi(t)\rangle = c_1(t)e^{-i\omega_1 t} |1\rangle + c_2(t)e^{-i\omega_2 t} |2\rangle + c_3(t)e^{-i\omega_3 t} |3\rangle \quad (2.5)$$

Note: we can apply a couple approximations/simplifications. One is the rotating wave approximation, where we discard terms that oscillate at the sum of the electric field frequency and level frequency. These terms will oscillate so quickly that the behavior will be averaged over on the time-scale we look at and so we do not need to resolve it. Another issue is the overall level energy. It constitutes an offset and we only care about the difference between energy levels when examining behavior, so we can subtract the energy of the lowest level and still see all the dynamics, *i.e.*, set:  $\omega_1 = 0$ ,  $\omega_2 = \omega_{12}$ ,  $\omega_3 = \omega_{13}$  This would recast the wavefunction:

$$|\psi(t)\rangle = c_1(t) |1\rangle + c_2(t)e^{-i\omega_{12} t} |2\rangle + c_3(t)e^{-i\omega_{13} t} |3\rangle \quad (2.6)$$

Plugging these wavefunctions in and doing some algebra, see appendix A.1 for details, one gets three coupled equations for the wavefunction coefficients:

$$\dot{c}_1 = \frac{i}{2}\Omega_p e^{i\phi_p} c_3 e^{-i\Delta_p t} \quad (2.7)$$

$$\dot{c}_2 = \frac{i}{2}\Omega_c e^{i\phi_c} c_3 e^{-i\Delta_c t} \quad (2.8)$$

$$\dot{c}_3 = \frac{i}{2}\Omega_p e^{-i\phi_p} c_1 e^{i\Delta_p t} + \frac{i}{2}\Omega_c e^{-i\phi_c} c_2 e^{i\Delta_c t} \quad (2.9)$$

These equations have been simplified by introducing detunings:  $\Delta_p = \omega_{13} - \omega_p$  and  $\Delta_c = \omega_{12} - \omega_{13} + \omega_c$  From these equations one can construct the coherences and populations, for example:

$$\begin{aligned} \rho_{11} &= c_1 c_1^* \\ \rho_{21} &= \rho_{12}^* = c_1^* c_2 \end{aligned} \quad (2.10)$$

This in turn allows for formulation of the population and coherence differential equations. Into these, we will incorporate one additional simplification, operating in a co-rotating frame, see

appendix A.2. This is done by subsuming the time-dependent exponential into the coherences, *i.e.*,

$$\begin{aligned}\tilde{\rho}_{31} &= \rho_{31} e^{i\phi_p} e^{-i\Delta_p t} \\ \tilde{\rho}_{32} &= \rho_{32} e^{i\phi_c} e^{-i\Delta_c t}\end{aligned}\quad (2.11)$$

The populations do not change under this transformation as they are real. We arrive at coupled equations for the various coherences and populations, for completeness, let us list them all:

$$\dot{\rho}_{11} = \frac{i}{2}\Omega_p(\tilde{\rho}_{31} - \tilde{\rho}_{13}) + \frac{\Gamma_{33}\rho_{33}}{2} - \Gamma_{11}\rho_{11}\quad (2.12)$$

$$\dot{\rho}_{22} = \frac{i}{2}\Omega_c(\tilde{\rho}_{32} - \tilde{\rho}_{23}) + \frac{\Gamma_{33}\rho_{33}}{2} - \Gamma_{22}\rho_{22}\quad (2.13)$$

$$\dot{\rho}_{33} = \frac{i}{2}(\Omega_p(\tilde{\rho}_{13} - \tilde{\rho}_{31}) + \Omega_c(\tilde{\rho}_{23} - \tilde{\rho}_{32})) - \Gamma_{33}\rho_{33}\quad (2.14)$$

$$\dot{\tilde{\rho}}_{12} = \frac{i}{2}(\Omega_p\tilde{\rho}_{32} - \Omega_c\tilde{\rho}_{13}) - i\tilde{\rho}_{12}(\Delta_c - \Delta_p) - \frac{(\Gamma_{22} + \Gamma_{11})}{2}\tilde{\rho}_{12}\quad (2.15)$$

$$\dot{\tilde{\rho}}_{13} = \frac{i}{2}(\Omega_p(\rho_{33} - \rho_{11}) - \Omega_c\tilde{\rho}_{12}) + i\tilde{\rho}_{13}\Delta_p - \frac{(\Gamma_{33} + \Gamma_{11})}{2}\tilde{\rho}_{13}\quad (2.16)$$

$$\dot{\tilde{\rho}}_{23} = \frac{i}{2}(\Omega_c(\rho_{33} - \rho_{22}) - \Omega_p\tilde{\rho}_{21}) + i\tilde{\rho}_{23}\Delta_c - \frac{(\Gamma_{33} + \Gamma_{22})}{2}\tilde{\rho}_{23}\quad (2.17)$$

$$\begin{aligned}\dot{\rho}_{21} &= (\dot{\rho}_{12})^* \\ \dot{\rho}_{23} &= (\dot{\rho}_{32})^* \\ \dot{\rho}_{31} &= (\dot{\rho}_{13})^*\end{aligned}\quad (2.18)$$

Note: To this we manually added the decays. We are assuming  $\rho_{33}$  decays via  $\Gamma_{33}$  to  $\rho_{11}$  and  $\rho_{22}$  equally. We are also assuming that there can be decay between the ground states, given by

$\Gamma_{11}$  and  $\Gamma_{22}$ . The electric susceptibility,  $\chi$  is a function of these coherences, as we will explain in section 2.2.3.

### 2.2.2 EIT Math: Density matrix

The density matrix, contains the quantum nature of the problem but also the statistics of different possible configurations, sort of a quantum phase-space for the system. Examining how the density matrix evolves in time leads to equations that describe the populations of states, coherences between different states, and how those evolve. Similar to how the Schrödinger equation describes the evolution of a wavefunction, the Liouville-von Neumann equation describes the time evolution of the density matrix, see appendix A.3. It also can naturally incorporate the decays.

$$\dot{\rho} = \frac{-i}{\hbar} [H, \rho] - \frac{1}{2} \{\Gamma, \rho\} \quad (2.19)$$

Now in order to use this machinery, we need to express the Hamiltonian as a matrix. For our problem the Hamiltonian is given by two pieces: the zero-field Hamiltonian, plus a part due to the dipole interaction of our applied lasers.

$$H = H_0 - \vec{\mu} \cdot \vec{E} \quad (2.20)$$

The zero-field Hamiltonian is just the energies associated with our 3 states:

$$H_0 = \begin{bmatrix} \hbar\omega_1 & 0 & 0 \\ 0 & \hbar\omega_2 & 0 \\ 0 & 0 & \hbar\omega_3 \end{bmatrix}$$

The dipole interaction has the following matrix elements:

$$\mu = \begin{bmatrix} 0 & 0 & \mu_{13} \\ 0 & 0 & \mu_{23} \\ \mu_{13} & \mu_{23} & 0 \end{bmatrix}$$

Notice, there are no matrix elements connecting states  $|1\rangle$  and  $|2\rangle$  because transitions between the ground states are not dipole-allowed. Our electric field has two components, the probe and control fields:

$$E = \frac{\hat{x}E_{0p}}{2} (e^{i\omega_p t} + e^{-i\omega_p t}) + \frac{\hat{x}E_{0c}}{2} (e^{i\omega_c t} + e^{-i\omega_c t})$$

We are going to assume the two transitions are far enough apart in frequency that probe only connects  $|1\rangle$  and  $|3\rangle$ , and control only connects  $|2\rangle$  and  $|3\rangle$ , *i.e.*, there is no cross-talk.

$$\mu \cdot E = \begin{bmatrix} 0 & 0 & \mu_{13} \frac{E_{0p}}{2} (e^{i\omega_p t} + e^{-i\omega_p t}) \\ 0 & 0 & \mu_{23} \frac{E_{0c}}{2} (e^{i\omega_c t} + e^{-i\omega_c t}) \\ \mu_{13} \frac{E_{0p}}{2} (e^{i\omega_p t} + e^{-i\omega_p t}) & \mu_{23} \frac{E_{0c}}{2} (e^{i\omega_c t} + e^{-i\omega_c t}) & 0 \end{bmatrix}$$

Also, since we know where this is going, we are going to employ the rotating-wave approximation as we did before. This amounts to dropping some of the electric field contributions that would otherwise contribute to rapidly oscillating terms in the problem. Apparently this approximation means that absorption will not be associated with de-excitation and emission will not be associated with excitation.

$$\mu \cdot E = \begin{bmatrix} 0 & 0 & \mu_{13} \frac{E_{0p}}{2} e^{i\omega_p t} \\ 0 & 0 & \mu_{23} \frac{E_{0c}}{2} e^{i\omega_c t} \\ \mu_{13} \frac{E_{0p}}{2} e^{-i\omega_p t} & \mu_{23} \frac{E_{0c}}{2} e^{-i\omega_c t} & 0 \end{bmatrix}$$

Which we can put in terms of Rabi frequencies:

$$H = \hbar \begin{bmatrix} \omega_1 & 0 & -\frac{\Omega_p}{2} e^{i\omega_p t} \\ 0 & \omega_2 & -\frac{\Omega_c}{2} e^{i\omega_c t} \\ -\frac{\Omega_p}{2} e^{-i\omega_p t} & -\frac{\Omega_c}{2} e^{-i\omega_c t} & \omega_3 \end{bmatrix} \quad (2.21)$$

This is not going to work very well for numerical integration purposes as the Hamiltonian contains terms that oscillate rapidly. However, we can change this via a unitary transformation,

essentially doing what we did before for the Schrödinger equation. See appendix A.4 This yields the following:

$$\tilde{H} = \hbar \begin{bmatrix} 0 & 0 & -\frac{\Omega_p}{2} \\ 0 & \Delta_p - \Delta_c & -\frac{\Omega_c}{2} \\ -\frac{\Omega_p}{2} & -\frac{\Omega_c}{2} & \Delta_p \end{bmatrix} \quad (2.22)$$

Now we can plug this into the Liouville-von Neumann equation and turn the crank to get density matrix equations. *i.e.*, 2.16 and related. This is a much more powerful way of going about this procedure than constructing things using the Schrödinger equation. As one incorporates more levels, the algebra of the Schrödinger approach is going to get unwieldy and the chance of mistakes is going to grow. It is also clearer to see some of the transformations/simplifications that we have made. Doing this via the density matrix will serve us well as we look at systems with more levels, so we introduce it now. We will come back to this for more complicated level schemes; see chapter 8 for application of this to our 6-level Eu system.

Now that we are confident in our differential equations for the coherences and populations, the question becomes how do we relate these to changing properties of the medium? The answer comes from looking at the susceptibility. From there, we can generate the familiar EIT curve of transmission vs. frequency detuning.

### 2.2.3 Relating Atomic Coherence to Refractive Index

#### Proportionality to Coherence

Let us restate our objective at this point. We need to relate the response of the atomic medium to the density matrix results we have derived above. The response of a media to the applied electric field is given by the polarization.

$$P = \epsilon_0 \chi E \quad (2.23)$$

We can relate the macroscopic polarization to our atomic density matrix description by recognizing that:

$$P = N \langle \hat{\mu} \rangle$$

The macroscopic polarization is the atomic number density times the expectation value of the dipole operator. Now the expectation value of the dipole operator (for our transition) is given by:

$$\langle \hat{\mu} \rangle = \rho_{31} \mu_{13} + \rho_{13} \mu_{31}$$

We calculated the coherences above by two different methods. Technically there is a contribution from each transition, but we are only concerned with the probe susceptibility at the probe transition. The control transition is far enough away that either the probe beam is very far detuned from it or the control response at the probe frequency is very small. Relating the two ways of looking at the polarization:

$$\epsilon_0 \chi E = N \langle \hat{\mu} \rangle$$

We can then solve for the susceptibility, recalling that we transformed our  $\rho$ 's via unitary transformation as in appendix A.4, and entering E explicitly:  $E = \frac{1}{2}(\mathcal{E} e^{i\omega_p t} + \mathcal{E}^* e^{-i\omega_p t})$

$$\epsilon_0 \chi \frac{1}{2} (\mathcal{E} e^{i\omega_p t} + \mathcal{E}^* e^{-i\omega_p t}) = N \left( (\tilde{\rho}_{31} e^{-i\omega_p t}) \mu_{13} + (\tilde{\rho}_{13} e^{i\omega_p t}) \mu_{31} \right)$$

Choosing terms with the same exponentials, gives:

$$\epsilon_0 \chi \frac{\mathcal{E}}{2} e^{i\omega_p t} = N \left( \tilde{\rho}_{13} e^{i\omega_p t} \mu_{31} \right)$$

$$\epsilon_0 \chi \frac{\mathcal{E}}{2} = N \tilde{\rho}_{13} \mu_{31}$$

Which gives us our susceptibility:

$$\chi = \frac{2N \tilde{\rho}_{13} \mu_{31}}{\epsilon_0 \mathcal{E}}$$

Which we can put in terms of a Rabi freq:  $\Omega_p = \frac{\mu_{31} \mathcal{E}}{\hbar}$

$$\chi = \frac{2N\mu_{31}^2}{\epsilon_0\hbar\Omega_p}\tilde{\rho}_{13} \quad (2.24)$$

This is a key connection, it shows the relationship between the electric susceptibility and the coherence. This fills out our picture: if we know the coherence (*i.e.*, from analysis of the density matrix in time by integrating the Liouville-von Neumann equation) then we can relate that to the electric susceptibility and index of refraction. The susceptibility is complex; this is linked to the fact that the coherence is also complex. This has to be the case in a dispersion relationship. In a Kramers-Kronig sense, a change in the real index entails a change in the imaginary index (absorption) as well. The size of the effect depends on the number density  $N$ , as well as the matrix element between the levels  $\mu_{31}$ . Larger density or stronger matrix elements means a stronger effect.

### Analytical Low-Power Probe Solution:

At this point our problem has become deriving the coherence between the states linked by the probe. This is a function of laser powers (Rabi frequencies), and detunings should give our desired EIT resonance shape, as well as a normal resonance shape when we turn off the control laser.

An analytical solution for the coherence can be found if we make some assumptions and consider that in steady state, all of our  $\dot{\rho}$  equations will be equal to zero. We'll assume that essentially all the population stays in the probe ground state; *i.e.*,  $\rho_{11} = 1$ . Starting from our equations for the coherences and employing these simplifications, we get the following coupled equations:

Our  $\dot{\tilde{\rho}}_{12}$ ,  $\dot{\tilde{\rho}}_{13}$ , and  $\dot{\tilde{\rho}}_{23}$  equations yield:

$$\begin{aligned} i\Omega_c\tilde{\rho}_{13} &= -(2i(\Delta_c - \Delta_p) + (\Gamma_{22} + \Gamma_{11}))\tilde{\rho}_{12} + i\Omega_p\tilde{\rho}_{32} \\ i\Omega_p + i\Omega_c\tilde{\rho}_{12} &= (2i\Delta_p - (\Gamma_{33} + \Gamma_{11}))\tilde{\rho}_{13} \\ \tilde{\rho}_{23} &= \frac{i\Omega_p\tilde{\rho}_{21}}{2i\Delta_c - (\Gamma_{33} + \Gamma_{22})} \end{aligned}$$

We can substitute these equations into each other and come up with an expression for  $\rho_{13}$  that only depends on Rabi frequencies, detunings, etc. See appendix [A.5](#).

$$\tilde{\rho}_{13} = \frac{i\Omega_p (2i(\Delta_c - \Delta_p) + (\Gamma_{22} + \Gamma_{11}))}{(2i(\Delta_c - \Delta_p) + (\Gamma_{22} + \Gamma_{11})) (2i\Delta_p - (\Gamma_{33} + \Gamma_{11})) - \Omega_c^2}$$

We can make some further simplifications. Let us assume the control beam is on resonance, *i.e.*,  $\Delta_c = 0$ . Let us also assume there is no decay between the ground states;  $\Gamma_{11} = \Gamma_{22} = 0$ .

$$\tilde{\rho}_{13} = \frac{2\Delta_p\Omega_p}{4\Delta_p^2 + 2i\Gamma_{33}\Delta_p - \Omega_c^2}$$

Put it all together to get the susceptibility:

$$\chi = \frac{N\mu_{31}^2}{\epsilon_0\hbar} \frac{2\Delta_p}{4\Delta_p^2 + 2i\Gamma_{33}\Delta_p - \Omega_c^2} \quad (2.25)$$

This is probably the simplest expression that contains all the behavior that we want to see. Let us plot it and see what it looks like. See figure 2.3.

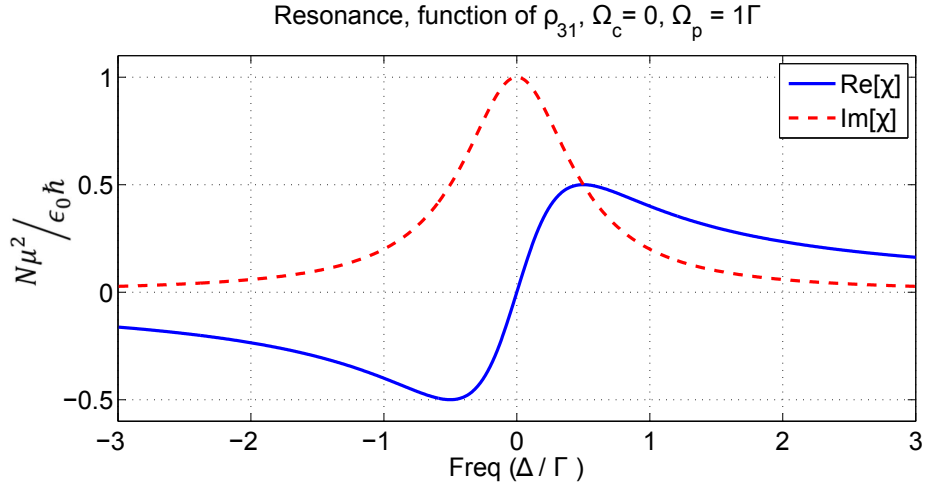


Figure 2.3: Real and Imaginary Electric Susceptibility of the probe with the control beam off. We recover a normal Lorentzian resonance.

As we can see there is a Lorentzian absorption shape and a dispersion, a resonance in the real part. It looks just like the resonances in glass that we discussed previously. Now let us turn on the control beam. See figure 2.4:

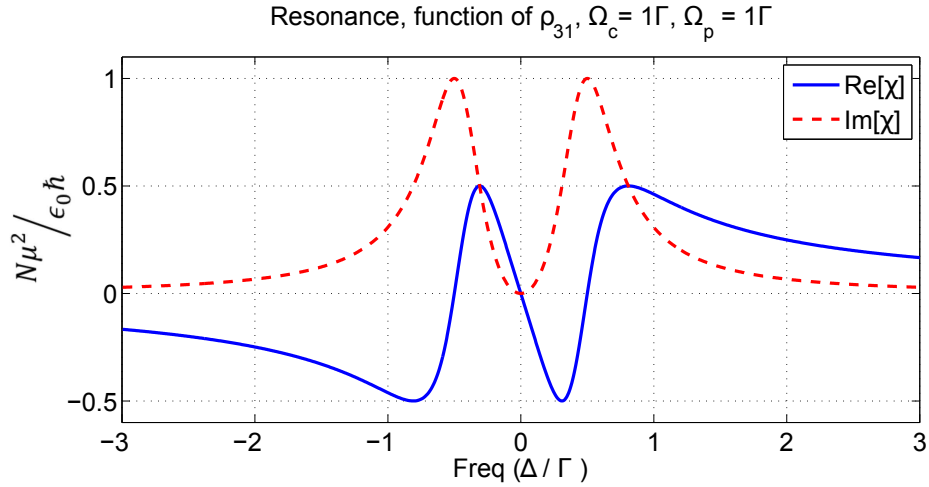


Figure 2.4: EIT: Real and Imaginary Electric Susceptibility, control beam on. In this situation, EIT causes there to be a transparency window in the middle of the absorption resonance. Notice also the steep dispersion.

This interesting shape is the Electromagnetically Induced Transparency (EIT) dispersion shape. In the center, where there was maximum absorption, there is now a transparency window in the imaginary part. The real part is more complicated as well. The large slope of the real part is what is responsible for ‘slow light’.

The context for the introduction of this EIT discussion was that we are interested in experiments where one can increase the index of refraction while canceling absorption. As you can see in figure 2.4, in the middle of the EIT resonance the absorption can be eliminated. This is of course a lot different than figure 2.3, a ‘normal’ resonance, in which when the index is deviating the most, there is also large absorption.

At first blush, however, this might not look like much of an improvement as the real part of the index is also zero in the center of the resonance. Also, despite the transparency window, there is still significant absorption when the index is large. This can be improved upon by adjusting the parameters. See figure 2.5; notice in this situation, increasing the control power splits the absorption window and leads to a larger frequency range with enhanced refractive index (real part of  $\chi$ ) and negligible absorption (imaginary part of  $\chi$ ).

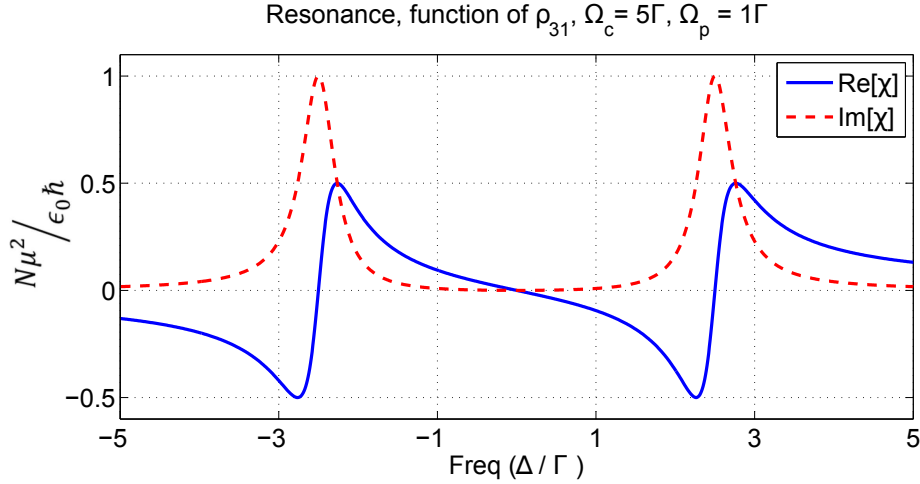


Figure 2.5: EIT: Real and Imaginary Electric Susceptibility, High Control Beam. Notice at high control intensity the EIT resonance splits and there is a wider region of negligible absorption.

The key idea is that by manipulating the coherence by applying lasers to the system, one can manipulate the index and absorption. This was the idea behind the first efforts in this direction [14, 15, 16]. They proposed something similar with a single laser detuned from both ground levels, *i.e.*, spaced equally between them. This gives a different shape, but the notion is the same, messing with the coherence causes there to be frequencies at which a probe laser would encounter an enhanced real refractive index while at the same time encountering negligible absorption.

### Relating the Susceptibility to Useful Quantities:

Now we have an expression for the susceptibility, it is proportional to the coherence and some factors. We would like to relate this to some measurable quantities in our system, namely the index of refraction and the absorption.

The index of refraction is given by (for small  $\chi$ ):

$$n = 1 + \frac{Re[\chi]}{2} \quad (2.26)$$

And the absorption is given by:

$$\alpha = \frac{\omega \text{Im}[\chi]}{c} \quad (2.27)$$

We introduce EIT not solely for its index-enhancement role; indeed there is a lot more interest in ‘slow light’ and applications that are related to the slope of the real part of the index. Part of the reason for introducing these ideas here is that concepts like atomic coherence and how to relate it to the electromagnetic response, etc. will be relevant to our later discussion. EIT is a prototypical experiment demonstrating coherent effects in an atomic system.

### Why Numerical Solution?

So the above is very useful to give us a feel for the problem but in practice we numerically integrate the density matrix equations. The results show us where the atomic populations are as well as the strengths of the coherences in time. The coherences we can then relate to the susceptibility, refractive index and absorption as described above. This is essential for two reasons:

1. Allows one to contend with the non-ideal circumstances, *i.e.*, high probe power, appreciable population of other levels, etc. It allows one more knobs to turn in efforts to emulate experimental conditions.
2. Allows for incorporation of time dynamics. Note: this is important if you are discussing population transfer, for example STIRAP: Stimulated Raman Adiabatic Passage.

### 2.3 Index Modification Experiments

After introducing the notion of enhancing/modifying the index via coherent processes like EIT, let me build on that by describing our experimental efforts including an experiment I did to increase the real part of the index while avoiding absorption.

The scheme is slightly different from what I have described so far but builds on some of the same ideas. It comes down to a couple main points. One is that in an actual experiment it can be difficult to measure the modification of the index, especially if there is any residual absorption. For example, one would need a long sample to see a time delay, but there would be significant

absorption with an optically thick sample. To put it another way it would be nice to totally eliminate the absorption rather than just suppress it compared to a ‘normal’ resonance. The other point is that we can also make negative absorption resonances, *i.e.*, gain resonances. We have explored this in multiple experiments[17, 18, 19].

The modification that lets us make gain resonances is that instead of using the on-resonance transitions for EIT, we can use the lambda scheme detuned from the excited state. We can operate as a Raman transition. The powerful thing about this is that it allows us to move the absolute frequency of the resonance. We actually create two resonances and can move them relative to each other by changing their single-photon detuning. As a result, it gives us tremendous flexibility to engineer the dispersion shape, much more freedom than an EIT resonance or the other single-resonance techniques discussed above. See fig 2.6 for a cartoon of the level scheme.

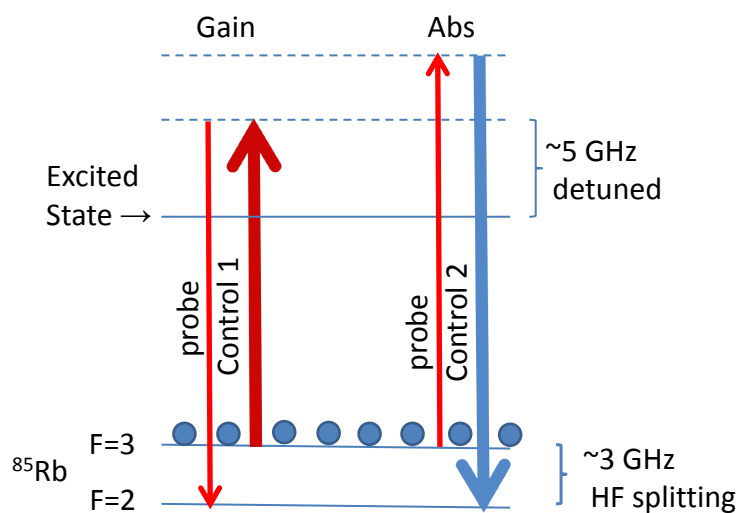


Figure 2.6: Refractive index engineering via Raman resonances. Population is first optically pumped to  $F=3$ . By having two control beams one spaced lower, one spaced higher by the ground state splitting, we can create gain and absorption resonances respectively.

The technique works as follows. Population is first pumped to  $F=3$ . Two Raman resonances are established using a common probe beam, where the two-photon resonance frequency corresponds to the hyperfine ground state spacing in  $^{85}\text{Rb}$ . The probe forms the higher energy beam in the

gain resonance, *i.e.*, a control beam is spaced 3 GHz below. The probe acts as the lower-energy beam in the absorption resonance, *i.e.*, a control beam is spaced 3 GHz above it. One way to think about it is that in order to equalize population between the ground states, the resonance with lower-energy control beam will need to emit probe photons, *i.e.*, experience gain. The resonance with the higher-energy control beam will need to absorb probe photons, *i.e.*, experience enhanced absorption.

The key is that the absolute location in frequency where these two resonances occur is controllable by changing the control beam frequencies. As a result the two resonances can be moved around relative to each other to get the desired dispersion shape. Refer to figure 2.7 for an experimental shot of gain and absorption resonances.

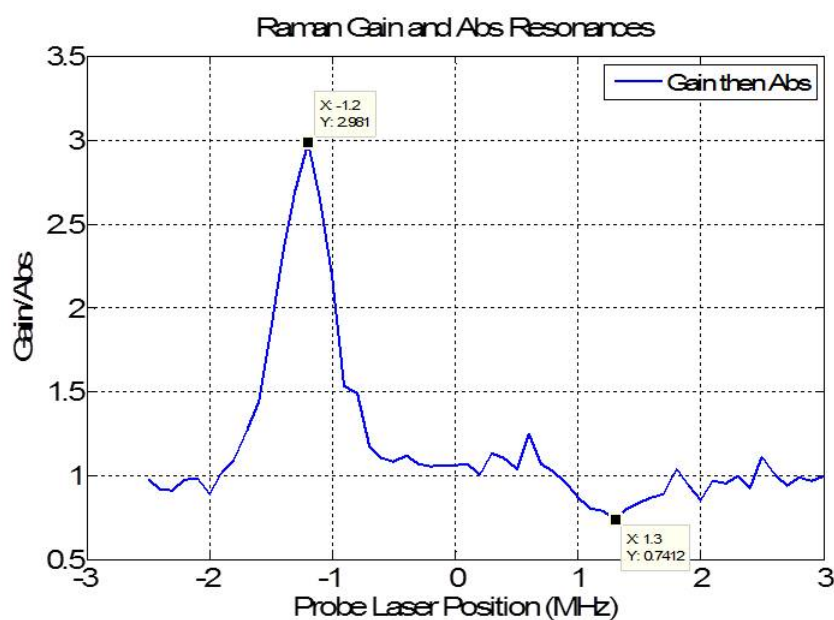


Figure 2.7: Experimental Raman resonances showing gain and absorption features adjacent to each other.

Moving the position of the resonances relative to each other corresponds to changing their single photon detuning. If the detunings for both resonances were exactly the same (accounting for the ground state frequency splitting), the gain and absorption features would lie exactly on top of each other. Instead, the detunings can be made very slightly different (*i.e.*, on the order

of the feature linewidth) and this allows the gain and absorption resonances to happen at slightly different positions in frequency. The key being that this can be fine tuned. Refer to figure 2.8 for a visualization of how by adjusting the the single photon resonances of each of the two Raman resonances, one can move the position of the gain and absorption in frequency. See fig 2.9 for an experimental example of this<sup>1</sup>.

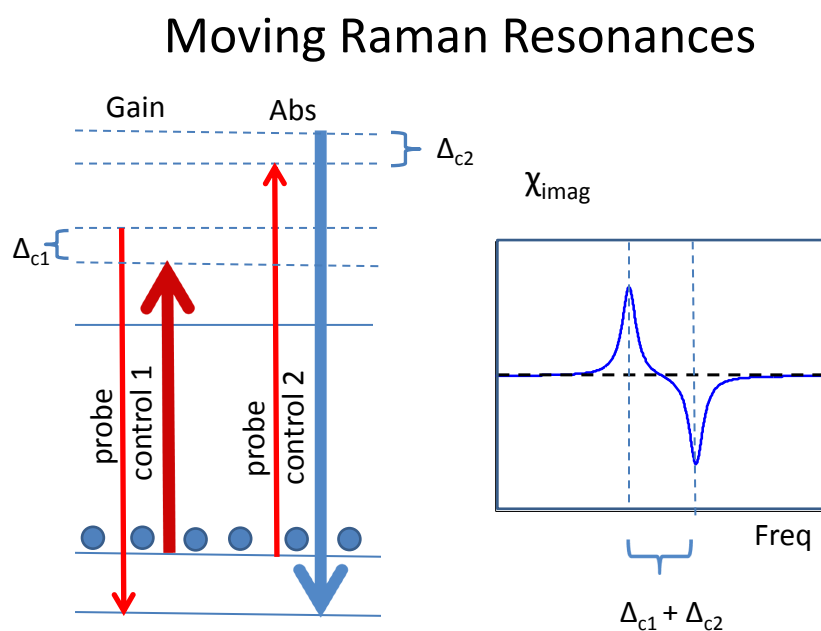


Figure 2.8: Modifying Refractive Index by Tuning Raman Resonances: Changing the single photon detuning for the absorption or gain resonances changes their relative frequency separation.

Now the important observation is that in the vicinity of zero absorption, the real part (and related refractive index) is enhanced. This helps to explain/justify the strategy of using two Raman resonances rather than a single EIT resonance to enhanced the index. Also, rather than measuring the index directly which is difficult, we will measure the gain and absorption in frequency and infer what the index looks like (the real part) based on causality through a Kramers-Kronig relationship. Indeed this is what we did in this experiment.

<sup>1</sup>Note: this figure as well as the figures in appendix B are reprinted with permission from [19] © 2015 by the American Physical Society.

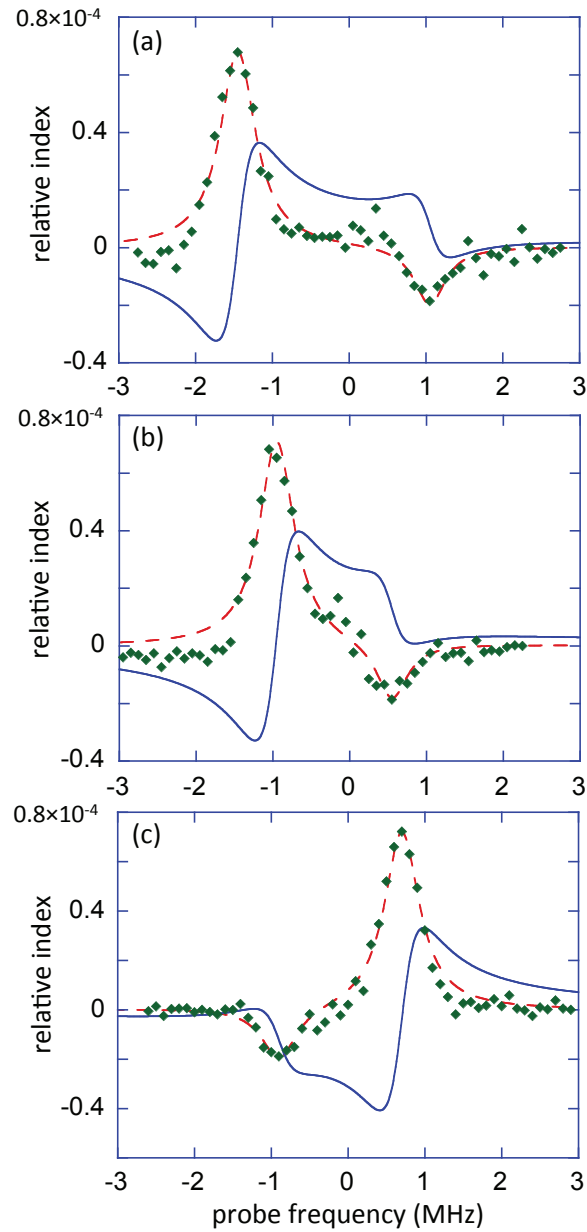


Figure 2.9: Refractive Index Engineering Experimental Data: The imaginary part of the refractive index (absorption or gain) is composed of two resonances and can be modified by changing their 2-photon detunings. Resonances can be made closer together, b), or even swapped, c). The inferred real part of the index is the solid blue line.

Interestingly, this is reminiscent of the ‘normal’ resonances that we discussed in regards to glass, except qualitatively the real and imaginary parts are swapped. There is a kink in the imaginary part as it goes between absorption and gain, while the real part is enhanced.

It is difficult to measure the real part of the index directly. Technically one can look for a time delay or look for focusing, as was done in a previous experiment in our lab[20]. However, we can measure the imaginary part as a function of frequency and then infer what the real part looks like via the Kramers-Kronig relationship. Qualitatively, this means that the imaginary and real parts of the susceptibility are related. If you know the imaginary (*i.e.*, absorption profile), then you have all the information that you need to find the real part. It comes about as a consequence of causality. I will relegate a derivation/further explanation to an appendix, but will state the result now:

$$\chi'(\omega) = \frac{2}{\pi} \int_0^{\infty} \frac{\omega' \chi''(\omega)}{\omega'^2 - \omega^2} d\omega' \quad (2.28)$$

What this expression means is that to find the real part of the index,  $\chi'(\omega)$ , for each frequency,  $\omega$ , one integrates the imaginary part,  $\chi''$ , weighted by  $\frac{\omega'}{\omega'^2 - \omega^2}$ . This is easy enough to do numerically. In figure 2.9, the experimental data are the green points. Applying the above Kramers-Kronig procedure to a smoothed version of the data (red dashed line) yields the blue trace, the inferred real part of the susceptibility.

The message from this chapter is that we have experimental experience modifying/manipulating the index of refraction in atomic vapor and theoretical experience with coherent atomic processes like EIT. From this, the next chapter will discuss a theoretical method to obtain a negative index in an atomic system.

This is only the broad strokes of the results of the experiment described in this chapter, for more information see Appendix B as well as the aforementioned publication[19].

## Chapter 3

### Atomic Negative Index Scheme

We discussed in the last chapter how we can engineer the index of refraction, enhance it a bit while canceling absorption, in an atomic system. This chapter will build upon that with a description of work done by Deniz and a former student Dan Sikes. See his thesis and publications for the details[7, 8, 21]. This work was built upon earlier work by others, especially Kastel and colleagues[22, 23]. I will not dwell on this because I did not work on it, but it is a crucial part of the story I am developing. Using ideas similar to what we already discussed, one can create a negative index.

As discussed in the introduction, the magnetic response of a material at optical frequencies is essentially zero. This is seen in the fact that we virtually always assume  $\mu = \mu_0$  when discussing electromagnetic problems. The idea that Dan and Deniz developed considers enhancing the magnetic response via an electric interaction (and technically the electric part via magnetic interaction). Mathematically, instead of the polarization just being proportional to the electric field and the magnetization only proportional to the magnetic field, there are cross-coupling terms, contributions denoted by  $\xi$  in the following equations.

$$\begin{aligned} P &= \epsilon_0 \chi_E E \\ M &= \frac{\chi_M}{\mu_0} B \end{aligned} \tag{3.1}$$

Becomes:

$$P = \epsilon_0 \chi_E E + \frac{\xi_{EB}}{c\mu_0} B \tag{3.2}$$

$$M = \frac{\chi_M}{\mu_0} B + \frac{\xi_{BE}}{c\mu_0} E \quad (3.3)$$

Now in this case, the important issue is that the magnetization depends on the electric field, can be enhanced by the electric field. Instead of the familiar  $n = \sqrt{\epsilon\mu}$  when these cross terms are incorporated,  $n$  becomes more complicated:

$$n = \sqrt{\epsilon\mu - \frac{(\xi_{EB} + \xi_{BE})^2}{4}} + \frac{i}{2}(\xi_{EB} - \xi_{BE}) \quad (3.4)$$

For a particular case where  $\xi$  s are engineered such that  $\xi_{EB} = -\xi_{BE} = i\xi$ . This reduces this refractive index expression to simply:

$$n = \sqrt{\epsilon\mu} - \xi \quad (3.5)$$

Now the goal is very clear: the cross-coupling coefficient needs to be larger than  $\sqrt{\epsilon\mu}$  in order for the index to be negative. This lifts the constraint that  $\epsilon$  and  $\mu$  be negative in order to get a negative index. If the cross-coupling is strong enough, the index can be negative despite  $\epsilon$  and  $\mu$ .

Figure 3.1 shows the level scheme. At first glance, it appears quite complicated. However, if we look at it from the perspective of the Raman index-enhancement scheme we talked about in the last chapter, we can recognize some familiar elements. First there are two Raman transitions to help cancel/offset the probe beam absorption. These are the two-photon transitions that contain  $E_{c1}$  and  $E_{c2}$  as well as levels  $|1\rangle$  and  $|2\rangle$ .

Building from the two Raman transitions, there is also the magnetic transition to level  $|m\rangle$ . The magnetic field driving this transition is the magnetic field associated with the probe laser beam that participates in the two Raman transitions.

Similar to the refractive index enhancement engineering we talked about in the previous chapter, this Raman route offers a tremendous advantage. Since the Raman transitions are not sensitive to absolute frequency, it allows for tuning the electric transition relative to the magnetic transition. This is very important compared to the other schemes discussed in the literature because it does not require the magnetic and electric levels to be essentially exactly the same absolute frequency.

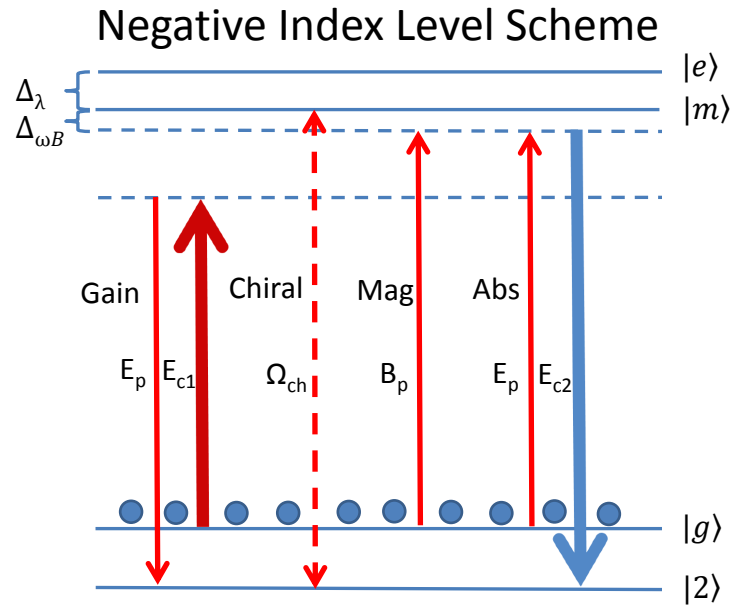


Figure 3.1: Raman Negative Index Level Scheme: Two Raman transitions,  $E_p/E_{c1}$  and  $E_p/E_{c2}$  through  $|e\rangle$ , address probe beam absorption. The magnetic transition is via the magnetic field of the probe beam,  $B_p$ , through level  $|m\rangle$ . The magnetic response is enhanced via the chiral coupling beam  $\Omega_{ch}$ . See [8] for a more comprehensive diagram.

The off-resonant Raman transition allows the electric part to be adjusted to compensate somewhat for its weaker magnetic counterpart.

The last piece of the anatomy to point out is the cross coupling,  $\Omega_{ch}$ . This links the electric and magnetic responses and provides the electric enhancement of the magnetization as in equation 3.3. Since this is between states of the same parity, this is either the magnetic field of a strong laser or a two-photon transition.

This scheme allows for a negative index via the chirality route. Dan and Deniz simulated this system for a variety of conditions, following the density matrix method I outlined in chapter 2,

albeit much more complicated than the simple three level system. I reproduce a figure from their work here to give a flavor. See figure 3.2<sup>1</sup>.

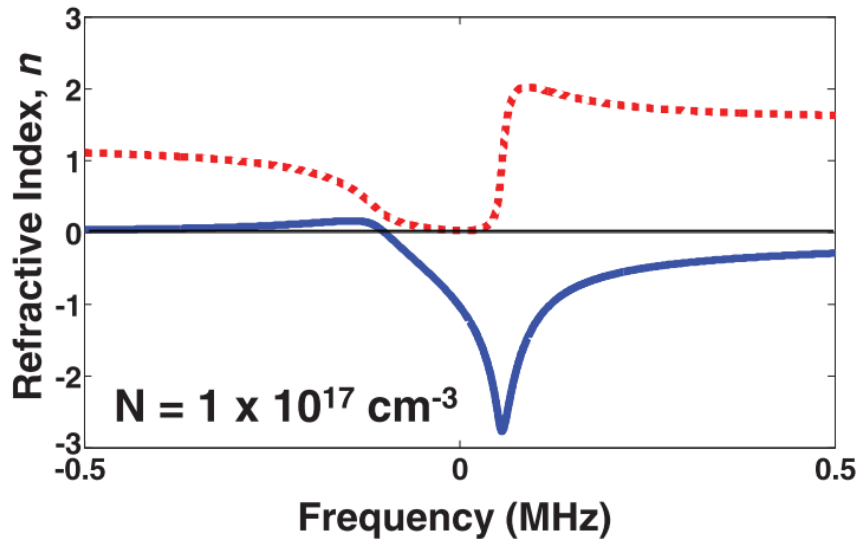


Figure 3.2: Raman Negative Index Simulation Results. Red dashed:  $\text{Im}[n]$ , Blue solid:  $\text{Re}[n]$ . Note that there is substantial negative real index where absorption goes to zero.

As you can see from this figure, where the imaginary part (red) goes to zero, there is a real part that is easily negative one. However, as you will also notice, this simulation curve is assuming a density of  $10^{17}/\text{cc}$ . Just as in the refractive index modification via EIT, the susceptibility is related to the density. Unfortunately, the density required by this scheme, although perhaps more realizable than other atomic schemes proposed so far, is still much too high for normal atom traps.

Part of the problem is that most optical magnetic dipole transition strengths are very weak compared to the electric dipole counter-parts. Comparing the interactions we find  $\frac{\mu_B \cdot B}{\mu_E \cdot E} \propto (\alpha Z)^2$ , where  $\alpha$  is the fine structure constant and  $Z$  is the atomic number. As a result, we turn to rare-earth elements as they have relatively strong magnetic transitions.

<sup>1</sup>Note: permission to use this figure granted by the authors of the publication in which it appears. Reprinted with permission from [8] © 2015 by the American Physical Society.

Although it is exciting to note that there has been tremendous progress trapping and cooling rare-earth atoms: Yb, Er, Dy, Tm have all been trapped and most recently Ho was trapped at UW, the densities are very low[24, 25, 26]. The highest quoted for erbium or dysprosium are about  $10^{11}/cc$ , many orders of magnitude below what would be required for a negative index scheme as I just described.

Note: these rare-earth trapping experiments are no small feat. Considering the complicated atomic structure of the rare-earths, it is often necessary to employ multiple lasers to repump from undesirable states where populations may get stuck, or to carefully pick a particular transition that has fortuitous pumping/decay dynamics. This represents substantial technical complexity.

These issues lead us to pursue a solid instead, a rare-earth doped crystal for our experimental system. This system offers two significant advantages: high density and relatively strong magnetic dipole transitions.

## Chapter 4

### Eu:YSO Spectroscopy and Structure

There are two reasons we have been drawn to working in a doped crystal. One is the potentially very high atomic density. The other is the availability of relatively strong magnetic dipole transitions. Rare-earth doped crystals present a promising system toward both of these goals. Surveying potential rare-earth ions, europium became a leading contender because of its strong visible magnetic dipole transition, the  ${}^5D_1 - {}^7F_0$  at about 527 nm. We chose the crystal yttrium orthosilicate (YSO) because it has been used extensively with Eu for quantum memory experiments[27].

Using atoms (really ions) embedded in a crystal represents a little bit of a departure/new direction for us as a lab. We have done experiments with Rb atoms in traps (see our localization work [28, 29]), Rb in vapor cells as I discussed in chapter 2, as well as worked with molecular gases for the modulation experiment, but not with atoms embedded in solids. This system presents some similar challenges as well as some opportunities to learn new physics. This chapter is meant to be a comprehensive survey on relevant background issues on the atomic structure of our transition and nearby relevant transitions in europium.

#### 4.1 Eu:YSO Gross Structure/General information

In our endeavor to realize an atomic negative index, one of the requisite ingredients is a relatively strong magnetic dipole transition. Rare-earth ions and rare-earth doped materials present an interesting opportunity toward this goal because of their structure. Because of their partially

filled f-shell, those electrons can have a lot of angular momentum, contributing to strong magnetic interactions. This, combined with the fact that there are many configurations, leads to a rich spectroscopic structure and good hunting ground for strong magnetic transitions.

An interesting related fact regarding the rare-earths is that their partially filled 4f shell sits inside the filled 5s and 5p shells, shielding it from perturbation by the crystal. Figure 4.1 shows the radial charge density for a rare-earth ion and how the 4f sits inside the 5s, 5p, (and 6s) shells.

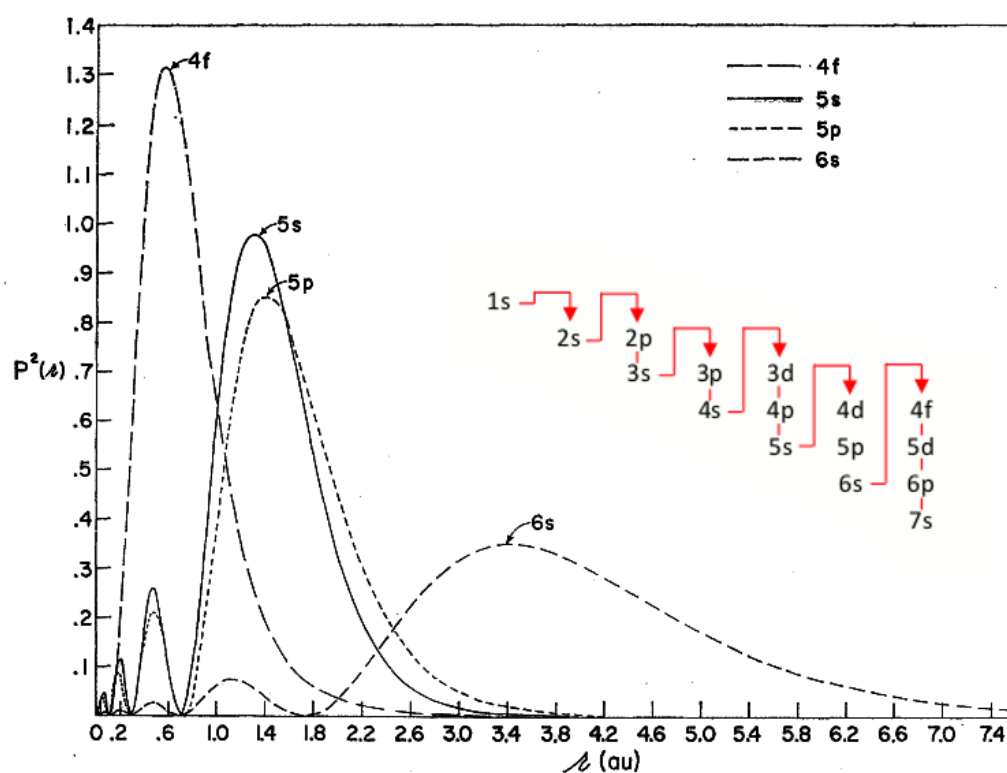


Figure 4.1: Radial charge density plot for Rare-Earth ion  $Gd^{3+}$  from [30];  $Eu^{3+}$  would be very similar. 5s and 5p lie largely outside the 4f, shielding it from the crystal environment. Overlay shows shell filling order and how 5p and 5s shells fill before the 4f. Reprinted figure with permission from [30] © 2015 by the American Physical Society

This leads to the intra-configurational transitions (like our magnetic dipole transition for example) being very narrow. In an interesting UW-Madison connection, these narrow transitions were

commented on by John Van Vleck way back during the development of the foundations of atomic physics[31].

I should mention, as crystal dopants, most rare-earths ionize by losing 3 electrons, the two from the 6s level and one from the 4f, leaving the 5p and 5s full. For europium, this means that in the crystal the  $\text{Eu}^{3+}$  ion 4f level has  $7-1=6$  electrons. As in simple configurations, we can find the ground state in  $\text{Eu}^{3+}$  in the LS coupling scheme using Hund's rules. It will be the state that maximizes spin, so  $S = 6 \times 1/2 = 3$ . Also, it will be the state that has the largest value of orbital angular momentum, so for 6 electrons with possible values of L being integers from -3 to 3, the largest possible total value is 3,  $L=3+2+1+0-1-2=3$ . Finally, it will be the term that has lowest total angular momentum, so  $J = S + L = 0$ . This means that the ground term for  $\text{Eu}^{3+}$  is  ${}^7F_0$

For excited states, we can no longer use Hund's rules to ascertain the order of energies or what the terms are although that structure can be calculated or measured. For  $\text{Eu}^{3+}$  the lowest energy excited term (not in the  ${}^7F$  manifold) is the  ${}^5D_0$  followed by the  ${}^5D_1$ . Our transition of interest is the  ${}^7F_0 - {}^5D_1$  at approximately 527 nm.

Figure 4.2 shows calculated energy levels for Eu:YSO up to about  $50,000 \text{ cm}^{-1}$ . (Labels above about  $30,000 \text{ cm}^{-1}$  are omitted for clarity.) As you can see, the structure gets quite complicated, although thankfully we are only interested in the first 10 or so levels. Our magnetic dipole transition is indicated by the green arrow. There are some other optical transitions that are stronger and that we need to understand, the dominant ones being the red  ${}^5D_0 \rightarrow {}^7F_1$  and yellow  ${}^5D_1 \rightarrow {}^7F_2$ . These will be discussed in subsequent sections and an appendix about calculating transitions, see appendix C. I will note that we have seen some of this structure, including these strong lines via fluorescence spectroscopy. See figure 7.2.

Let us zoom in on the energy structure of our transition of interest (See figure 4.3.) and identify the different effects and their energy scales. There are a number of issues that arise because of the influence of the crystal on the Eu ions. For one, the crystal electric field splits the  $m_j$  levels, so there are three instead of one  ${}^7F_0 - {}^5D_1$  lines, separated by a fraction of a nm ( $\sim 10$ s of  $\text{cm}^{-1}$ ). The next smallest scale feature to note is the fact that there are 2 unique crystal sites, *i.e.*, two places where Eu can replace Y in the crystal, with slightly different environments for the dopant ion. As

a result, each of the three Stark-split lines becomes two, separated by a few  $\text{cm}^{-1}$ , giving 6 lines total. Additionally there is inhomogeneous broadening due to the crystal electric field; every ion in the crystal sees a slightly different static electric-field crystal environment. This means that each of the 6 lines is a few GHz wide at liquid He temps. We will discuss the influence of the crystal in more detail in the next section.

Next, independent of the crystal environment, there is hyperfine structure due to the fact that Eu has nuclear spin  $I=5/2$ . This energy scale is much smaller, exhibiting structure at the  $\sim 10$ -100 MHz scale. There are two ions ( $^{151}\text{Eu}$  and  $^{153}\text{Eu}$ ) so there is also a parallel set of lines from the other ion that differ on the 10s of MHz scale. These lines are all overlapping and buried beneath the inhomogeneously broadened structure of the line. This hyperfine structure is the energy level structure that we will make use of in our experiments. Since it is so important to our experiment, it is worth taking a moment to discuss it.

What we are calling hyperfine structure in Eu is not exactly the *hyperfine* structure that we talk about say in rubidium; it is not an energy shift that depends on  $m_f$ , where  $\mathbf{F}$  is the result of coupling nuclear spin and angular momentum ( $\mathbf{F} = \mathbf{I} + \mathbf{J}$ ). In Eu, the energy scales between effects that depend on  $m_j$  and effects that depend on  $m_i$  are vastly different. To put it another way, although we make use of energy level structure resulting from states having different  $m_i$ , everything we do is within a spectral line of particular  $m_j$ . Denoting this effect as hyperfine structure is appropriate as it has the same energy scale and depends on the nuclear spin.

Specifically, the effect in Eu is identified as an electric quadrupole and magnetic pseudo-quadrupole interaction of the form  $\mathbf{I} \cdot \mathbf{Q} \cdot \mathbf{I}$ . Equation 4.1 shows its contribution to the spin Hamiltonian. Note, the interaction we are discussing is only the last term, but I will include all the terms as we may find this of interest later. This Hamiltonian is discussed by Longdell and Macfarlane [32, 33].

$$H = \mathbf{B} \cdot g_J^2 \mu_B^2 \Lambda \cdot \mathbf{B} + \mathbf{B} \cdot \mathbf{M} \cdot \mathbf{I} + \mathbf{I} \cdot \mathbf{Q} \cdot \mathbf{I} \quad (4.1)$$

Leaving aside the magnetic terms for now, the quadrupole term depends on nuclear spin  $\mathbf{I}$  as well as an interaction matrix  $\mathbf{Q}$ . Longdell discuss in detail parameterizing this interaction for  $^{151}\text{Eu}$ ;

the same analysis and description could be performed for  $^{153}\text{Eu}$ . We will discuss the hyperfine energy levels more later in the context of optical pumping, spectral hole-burning and EIT. (See figure 7.6.) For now, it is interesting to note that just like the hyperfine structure depends on the magnitude of possible total angular momentum  $\mathbf{F}$ , the hyperfine structure in Eu depends on the magnitude of the possible projections of  $\mathbf{I}$ . As a result, Eu's nuclear spin of  $5/2$  leads to 3 states corresponding to:  $|m_I| = 5/2, 3/2, 1/2$ .

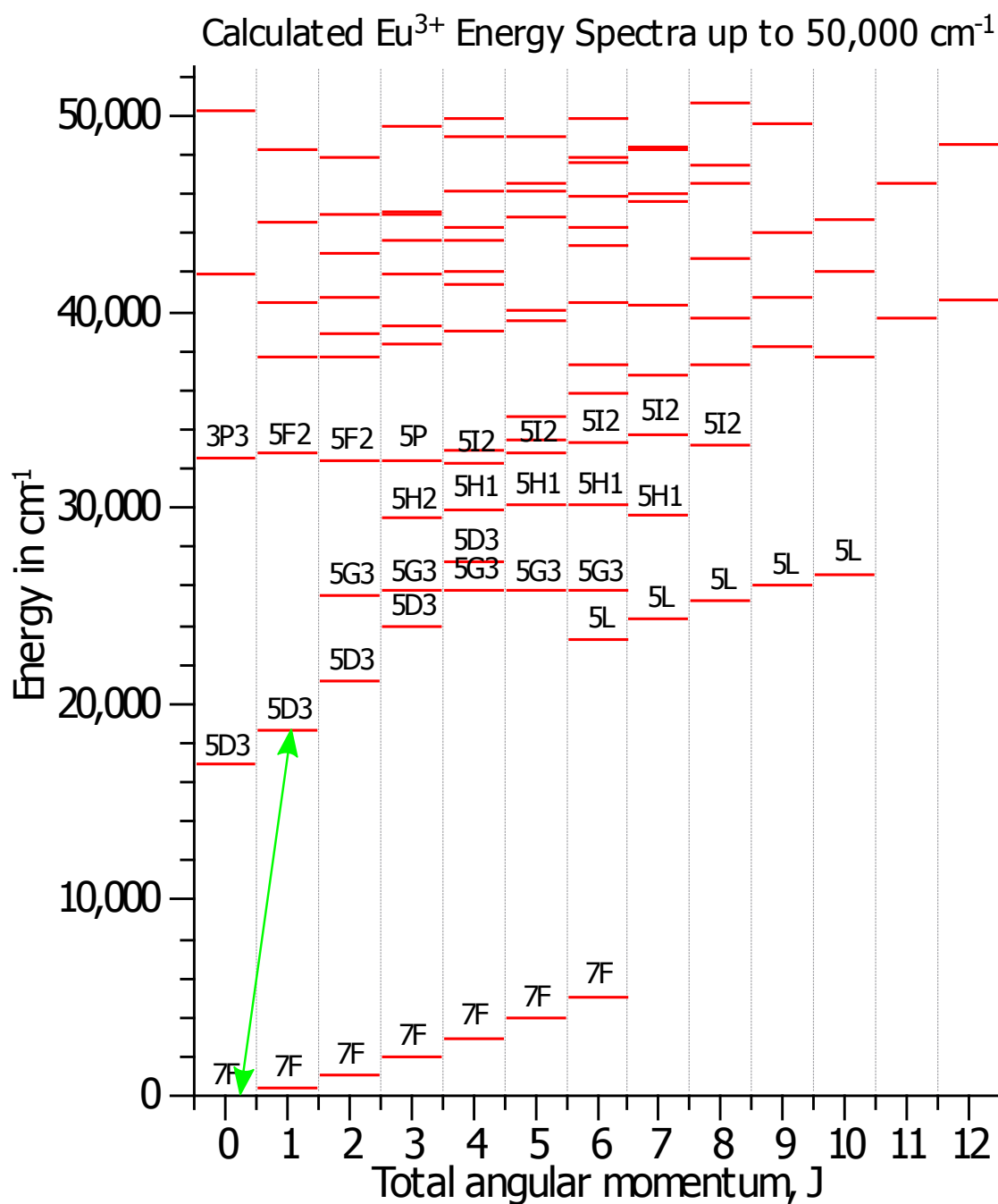


Figure 4.2:  $\text{Eu}:\text{YSO}$  energy levels up to  $50,000 \text{ cm}^{-1}$ .  $\text{Eu}^{3+}$  has some of the most complex structure as there are many (3003) possible ways to arrange its 6 electrons in the 4f shell. Regarding the level labels, the first number is the spin degeneracy ( $2S+1$ ), the letter gives the orbital angular momentum quantum number (L), and the last number (if there is one) is the seniority number.

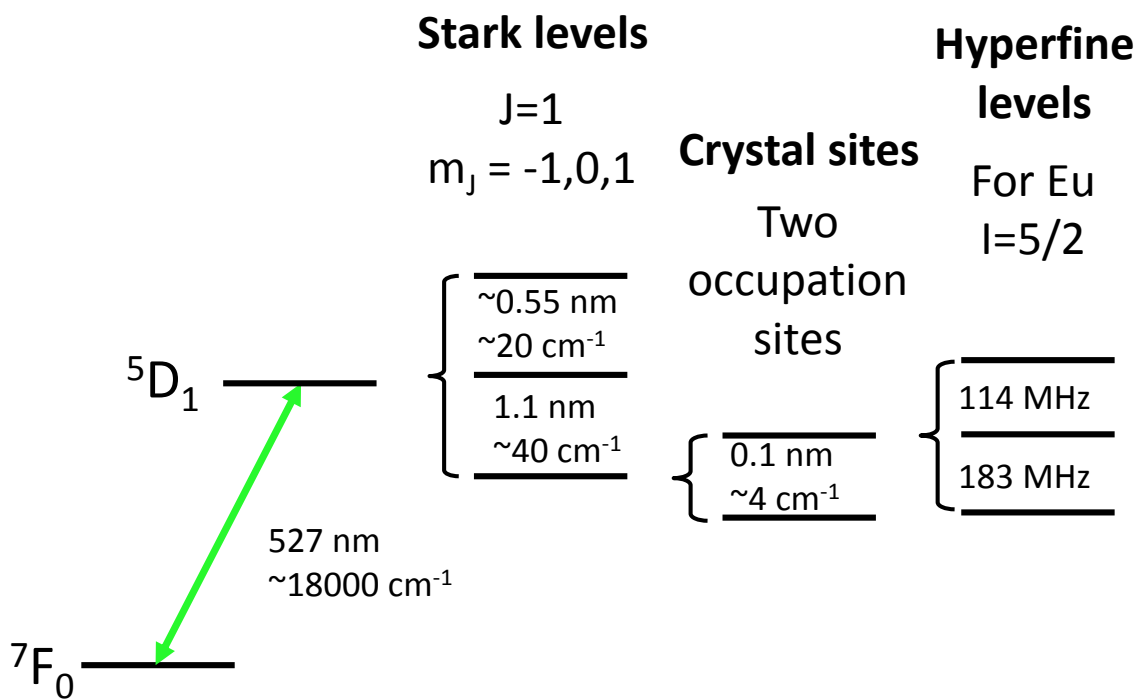


Figure 4.3: Eu:YSO transition of interest at about 527 nm. Note: there are different effects that split the spectral line. Three  $m_j$  are split by the crystal electric field and two unique sites in the crystal lead to twice as many spectral lines,  $3 \times 2 = 6$  total. We select one of these six lines and operate on the hyperfine structure of that line.

## 4.2 Our host crystal: YSO

Our host crystal is yttrium orthosilicate,  $\text{Y}_2\text{SiO}_5$ , or YSO for short. This crystal was chosen as it has been used for many quantum memory experiments utilizing the yellow  $^5D_0 - ^7F_0$  line in  $\text{Eu}^{3+}$  at 580 nm[27]. It turns out that Eu ions are a very good replacement for yttrium so when a Eu displaces a Y, the crystal is little disturbed. This also results in little abuse to our Eu ions which is part of why they are able to exhibit relatively small broadening while being incorporated into a solid.

Information about the structure of YSO comes primarily from x-ray diffraction (XRD) studies as early as the 1960s[34, 35]. There is some disagreement/confusion about the crystal parameters cited in the early literature. Part of this is due to the interesting fact that there are actually two different crystal configurations, polymorphs, for YSO, denoted in the literature by: X1- $\text{Y}_2\text{SiO}_5$  and X2- $\text{Y}_2\text{SiO}_5$ ; evidently we are interested in the X2 polymorph. Becerro and Escudero do a good job of summarizing and clarifying this issue as well as reviewing the early literature and data on YSO and also supplementing older XRD data with other data such as NMR[36]. See Cannas for another more modern paper regarding YSO structure[37].

A great paper by Li and colleagues relates some of the crystallographic properties and straightens out the orientation of the crystal[38]. Yttrium orthosilicate  $\text{Y}_2\text{SiO}_5$  (YSO) is a monoclinic biaxial crystal of the  $C_{2h}^6(C2/C)$  space group. The unit cell of a monoclinic crystal looks like a rectangular solid with a parallelogram as a base, the dimensions specified by 3 unit cell lengths and an angle, according to Li, for YSO  $a=12.5 \text{ \AA}$ ,  $b=6.72 \text{ \AA}$ ,  $c=10.42 \text{ \AA}$  and  $\beta = 102.68^\circ$ , where  $\beta$  is the obtuse angle in the parallelogram. Figure 4.4 gives the orientation of the crystallographic axes relative to the lab coordinates. Our crystal is cut along D1, D2 and b. See figure 4.5 a) for an image of the unit cell of the YSO crystal showing its constituent ions <sup>1</sup>.

Biaxial crystals have two optical axes, *i.e.*, two orientations that exhibit no birefringence. The specific symmetry properties of the crystal itself are less important to us, refer to the above citations

---

<sup>1</sup>Note: this image is generated from a crystal information file (CIF) that incorporates the data from the Maksimov paper (see: ICSD-28021). The image is generated using a program called Mercury. The CIF file can be found in the Inorganic Crystal Structure Database (ICSD) database:[http://www2.fiz-karlsruhe.de/icsd\\_web.html](http://www2.fiz-karlsruhe.de/icsd_web.html)

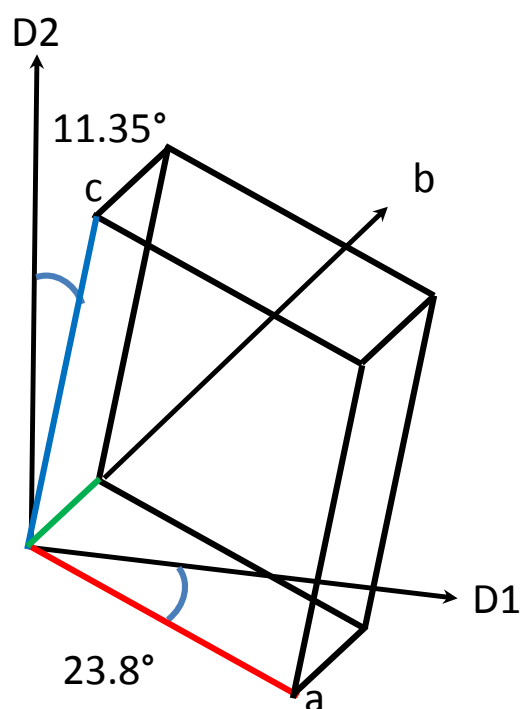


Figure 4.4: Orientation of crystallographic axes relative to lab axes. Monoclinic crystal unit cell looks like a rectangular solid with parallelogram for a face. Our crystal is prepared such that the face is orthogonal to  $b$ , *i.e.*, our laser is parallel to  $b$ .

for more information. However, we are concerned with the symmetry at the Eu dopant sites. The symmetry at Eu sites is the lowest kind: not symmetrical, technically point group  $C_1$ . In general the symmetry of an ion site can have implications on allowed transitions and Stark splittings. Broadly speaking, if the ion site possessed a high degree of symmetry, different orientations could appear identical and as a result degenerate in energy. As a result, highly symmetrical crystal sites can possess fewer spectral lines, whereas ions in more disordered circumstances will present more/all possible lines. In any case, since Eu sits at sites of  $C_1$  symmetry, there are no site symmetry-imposed limits on possible spectral lines.

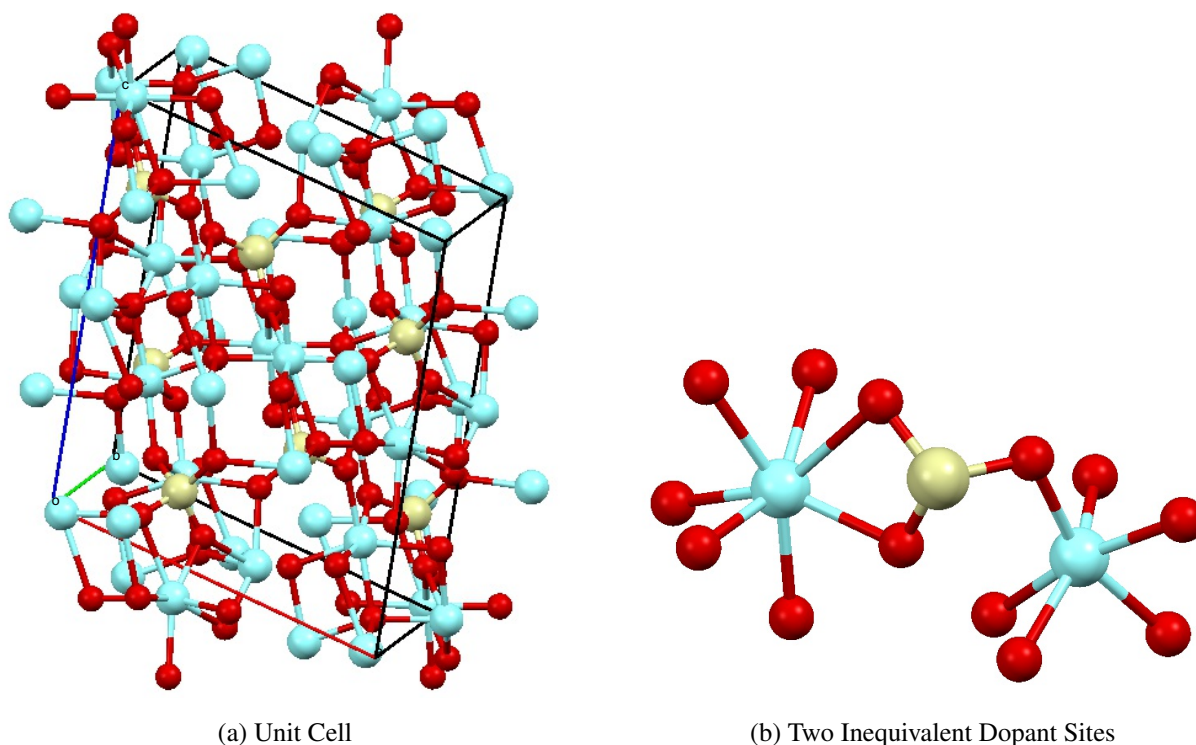


Figure 4.5: YSO crystal. Oxygen ions are red, silicon yellow, and yttrium (or europium) teal. Monoclinic unit cell a), looks like a rectangular solid with a parallelogram for a base. Europium can replace yttrium in two inequivalent crystal sites. ‘Site 1’ has 6 nearby ions (coordination number) whereas ‘site 2’ has 7. This is depicted in b) with outer surrounding ions removed. ‘Site 2’ is the teal ion on the right while ‘site 1’ is the teal ion on the left in b).

### 4.2.1 Crystal E-Field: Stark Splitting

As mentioned above, one consequence of our  $\text{Eu}^{3+}$  ions being embedded in a crystal rather than being free ions, is that they experience Stark shifts due to the electric field of the crystal; this splits the  $m_j$  of the  ${}^5D_1$  level. This results in there being three levels split by about  $50 \text{ cm}^{-1}$ , instead of one line. We choose to operate on the lowest level of ‘site 2’ as it is the strongest one present in the fluorescence spectroscopy, see figure 4.6 or figure 7.3. This is because for the higher-lying lines there is more phonon decay which causes broadening and thus the lines are weaker. The energy splittings due to the Stark shift in the crystal ( $\sim 50 \text{ cm}^{-1}$ ) are very susceptible to phonon

decay which will be discussed in chapter 5. Shen has a nice figure of the 3 split spectral lines in Eu:YSO[39] which I reproduce in figure 4.6. Note, we have observed some of this same structure as shown in figure 7.3.

Note figure 4.6 also exhibits the  $3 \times 2$  spectral lines due to the fact there are two unique Eu dopant sites as mentioned above. The sites are slightly different and as a result the  $m_j$  spectral lines become pairs split by a few  $\text{cm}^{-1}$ . The difference between sites in terms of the crystal can be in part explained in terms of coordination number, *i.e.*, how many nearest neighbor crystal ions a site has. The site we operate on, quoted as ‘site 2’ in the literature, has a coordination number of 7; there are that many crystal ions within 3 angstroms of the Eu ion. The other site, ‘site 1’ has a coordination number of 6. See figure 4.5 b) for a detail with the other crystal ions removed.

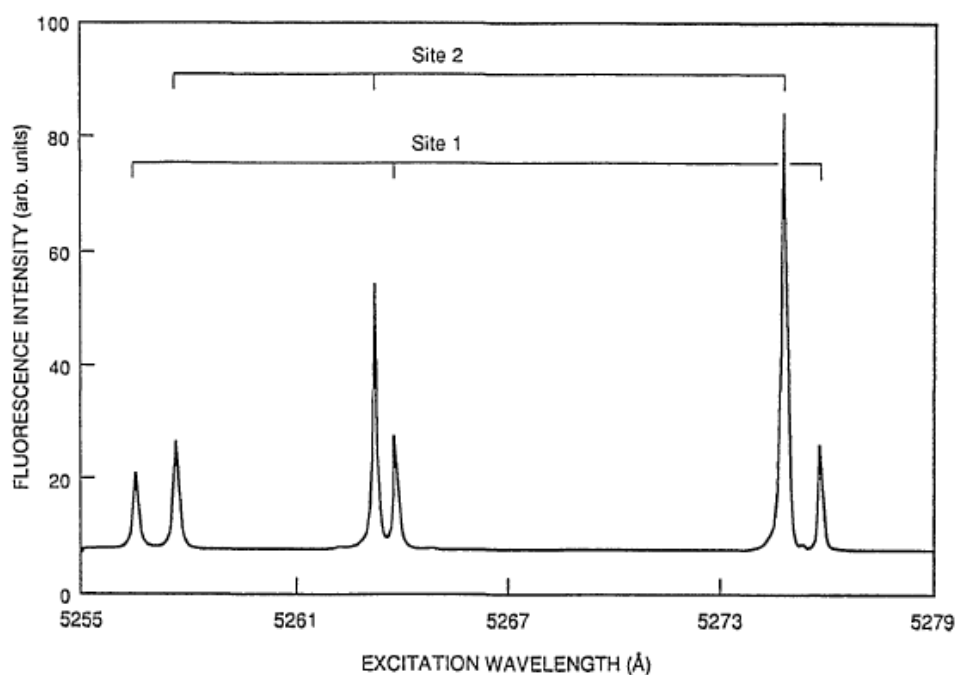


Figure 4.6:  ${}^5D_1$  Stark Splitting, borrowed from Shen[39]. Each pair of line corresponds to an  $m_j = +1, 0, -1$ . There are pairs of lines because of the two crystal dopant sites in YSO. Reproduced with permission © 2015 Optical Society of America.

Although it would be difficult to calculate the Stark shift for the 4f explicitly, let us try and estimate and see if the observed Stark-splitting is reasonable based on what we estimate the electric field to be inside the crystal. Using the idea of summing up the E-field contributions of surrounding ions in the crystal (see figure 4.8) we find the electric field to be approximately  $10^{12}$  V/m at Eu dopant ‘site 2’. We can imagine our europium ion as a cloud of charge surrounding its nucleus, polarized by the influence of the crystal electric field. The polarized charge distribution will experience an energy shift[40]. This is quadratic in E as it is the interaction of an induced dipole with the electric field.  $\Delta E = -1/2 \times 4\pi\epsilon_0 E_0^2 a_0^3$  Evaluating this, one finds that an electric field on the order of  $10^{10}$  V/m would cause the observed amount of Stark splitting. This is much weaker than the estimated electric field inside the crystal and so points to the role of the filled 5s and 5p in shielding the 4f level.

### 4.2.2 Crystal Electric Field: Inhomogeneous Broadening

The Stark shift in the crystal also induces line broadening. The overall inhomogeneously-broadened linewidth of our level, the  $^5D_1$ , is about 3 GHz. We have measured this as well as shown in figure 7.4. This is a similar issue to the Doppler shift in an atomic vapor but instead of each atom or ion having a slightly different velocity, each ion has a slightly different position in the crystal and slightly different resulting Stark shift. Although the shift is large, it is manageable compared to the Doppler shift because unlike it, our crystal-induced inhomogeneous broadening is frozen-in. Atoms can’t thermalize Stark-induced energy differences and so we can select a sub-population of ions in the crystal to work with and that sub-population can be isolated for a long period of time. This selection can be accomplished via spectral hole-burning, which will be discussed in chapter 7.

Figure 4.7 shows a cartoon explaining the origin of the inhomogeneous broadening. The crystal lattice is not perfect due to strains and imperfections, and dopant ions occupy slightly different locations in the crystal. This leads to each dopant ion experiencing a slightly different Stark shift. Each ion’s homogeneous linewidth is quite narrow, indicated by  $\Gamma_h$  in the figure. However, the combination of all the differently Stark-shifted homogeneous lineshapes creates a much larger

overall inhomogeneous lineshape, its width indicated by  $\Gamma_i$ . In quantum memory experiments, this difference in linewidths  $\Gamma_i/\Gamma_h$  is a sort of storage capacity metric and figure of merit for a system.

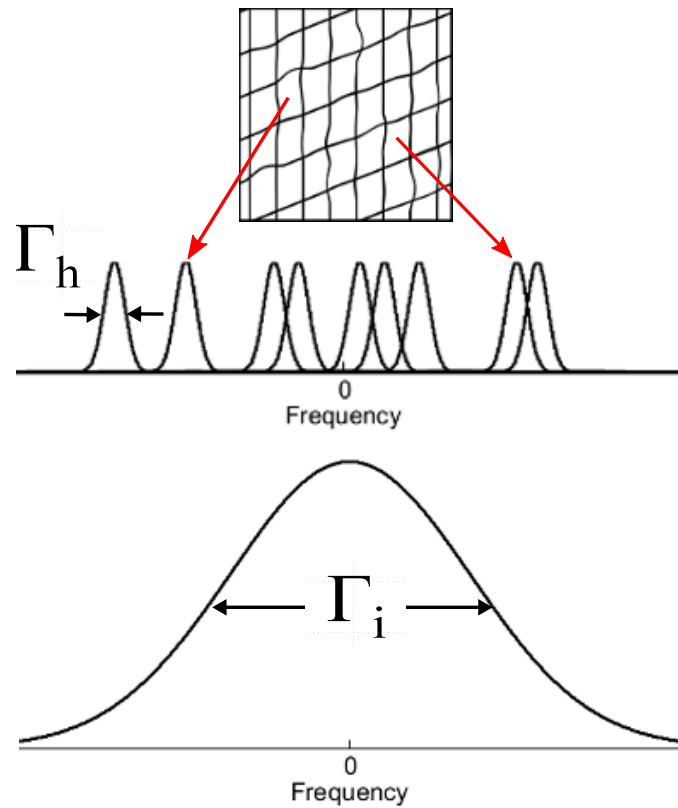


Figure 4.7: Inhomogeneous Broadening: the crystal has imperfections and all the ions are at slightly different locations in the crystal. This leads to each ion having a slightly different Stark shift. When the resonances from each ion are combined, their distribution determines the overall inhomogeneous broadening shape. For our system the homogeneous linewidth is about 30 kHz, while the inhomogeneous linewidth is about 3 GHz.

### 4.2.3 Crystal E-Field: Polarization Dependence

One intriguing side-note regarding the two unique crystal sites is that they have very different input laser polarization dependence. ‘Site 1’ has little appreciable polarization dependence, while the response of ‘site 2’ depends very sensitively on the input laser’s linear polarization. It is

possible to basically turn the response of ‘site 2’ on and off by rotating the laser polarization. Also, ‘site 2’ has a much stronger response, perhaps from being more polarized. Why is this the case? Can we explain this by considering the crystal structure? Note: if the size of the hyperfine structure should serve as a proxy for the strength of the electric field at the dopant site, in addition to stronger polarization dependence, it also makes sense that ‘site 2’s hyperfine structure is larger than ‘site 1’s.

A crude approach would be to add up the electric field contributions in the vicinity of the Eu ions due to the surrounding ions in the crystal, *i.e.*,  $E_{tot} = \sum_i \frac{q_i}{4\pi\epsilon_0 r_i^2} \hat{r}_i$ . Perhaps we can see a difference between the two sites. We can explore this by taking advantage of crystal information file analysis programs. In this case I used a program called Crystal Maker and had it spit out the locations of all the ions immediately surrounding the dopant site. Adding up the contributions from the ions within about 30 angstroms of the Eu ion seemed sufficient to get nice stable Electric field values; more contributions did not change the values much. Since the ions are on the order of a couple angstroms in diameter, I decided to look at a cube 2 angstroms across and see what the electric field looked like in that cube. Figure 4.8 shows the cube for the two sites overlaid on top of each other. This is oriented so we are looking down the axis of the crystal our laser points down. The blue is ‘site 1’, and red is ‘site 2’.

As you can see the electric field is larger for site 2, about  $3\times$  larger on average in the  $r=1$  Åsphere volume of the Eu dopant sites. This seems to agree with our hypothesis, that the site with larger coordination number will experience a larger electric field and be more polarized. More polarized should mean its excitation depends more strongly on the incident laser polarization. If we take the electric field vectors within a  $r=1$  Åsphere and compare their directions we find that ‘site 2’ is more uniform as well. The vectors in the vicinity of ‘site 2’ deviate on average by a couple degrees, whereas for ‘site 1’, the average deviation is more like 8 degrees. Perhaps ‘site 1’ experiencing a less homogeneous electric field environment relates to its not responding as strongly to laser polarization.

This issue of sensitive dependence to input laser polarization has been noticed before in Eu:YSO. Shen mentions it specifically with regards to the  ${}^7F_0 \rightarrow {}^5D_1$  transition and that the ‘site 2’ response

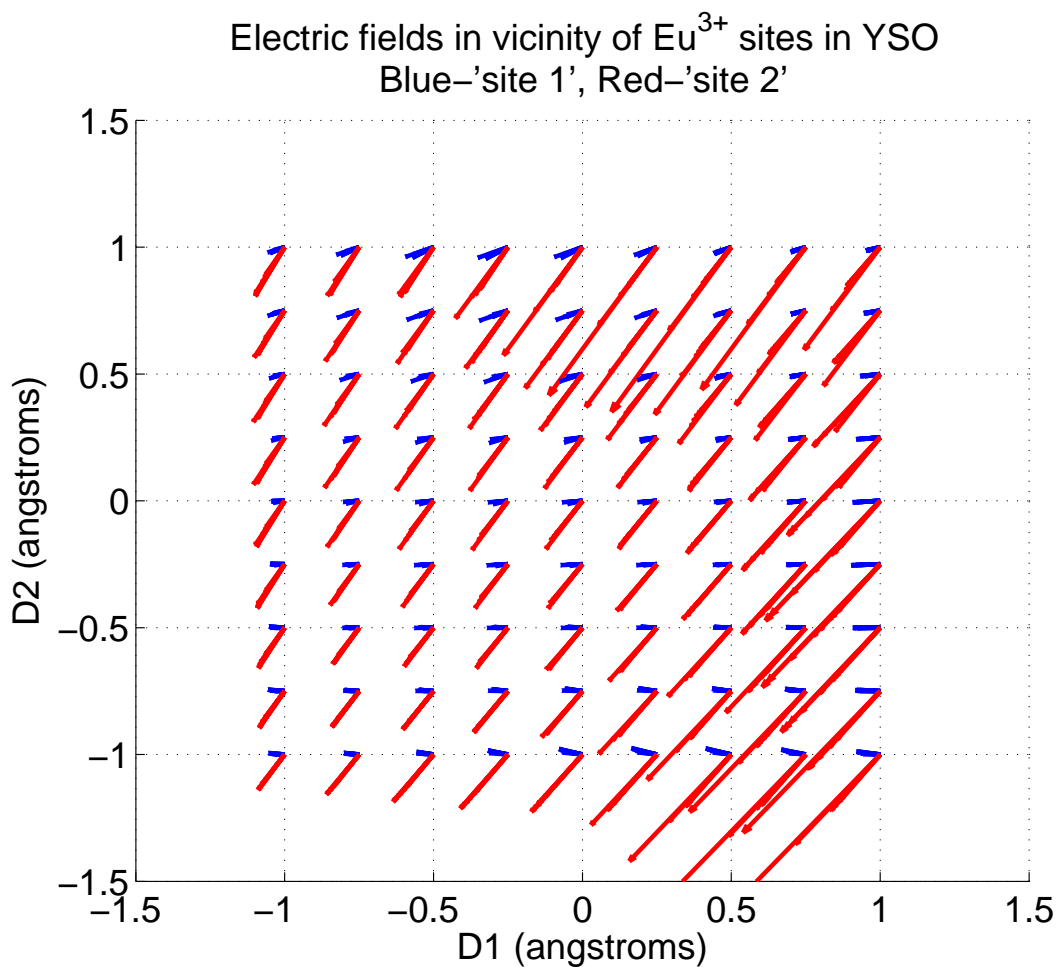


Figure 4.8: Electric field distributions in the vicinity of Eu ions. Looking down the experiment-axis of our crystal at a 3D volume with electric field vectors from both sites plotted on top of each other, blue being 'site 1', red 'site 2'. The longer red arrows illustrate the stronger electric field present at 'site 2', the site we use in our experiments. Not obvious from the figure is that the directions of the electric field vectors for 'site 2' are more uniform as well.

could be nearly extinguished by rotating polarization while 'site 1' was much less sensitive[39]. Unfortunately, they were unsure of their crystal orientation compared to their laser polarization. Könz also mentions this effect and links it to the crystallographic axes and compares the strength

along all lab directions[41]. Similar to Shen, they observe a stronger extinction on site 2, specifically a strong effect when aligned along the D1 axis and a weak effect along D2. Unfortunately though for comparison purposes, they were investigating the quantum memory transition  ${}^7F_0 - {}^5D_0$ . This is a higher-order transition and it is unclear whether it would have different laser polarization dependence than our magnetic dipole transition.

In the lab, we have noticed the strongest response with horizontal laser polarization. Our crystal is cut along the D1 and D2 axes; we are not sure which is the horizontal axis, but we know it is one or the other. That being said, there does not seem to be an obvious relationship (*i.e.*, parallel or perpendicular) between the electric field direction of about -124 degrees (the direction of the red arrows in figure 4.8) when looking down the b-axis in the crystal and the preferred laser polarization. Considering the complex structure of 4f terms, perhaps this is not unexpected. This remains a puzzle.

### 4.3 Atomic Physics in Eu Relevant to Calculating Optical Transitions

Although it is a complicated task, we can calculate the energy levels and transition strengths in our  $\text{Eu}^{3+}$  ion using existing codes. I looked at two codes, the Cowan code for calculations for the free ion and a package called RELIC (Rare Earth Level and Intensity Calculation) for calculating transitions in the crystal [42, 43]. For more information about these codes and how they work see appendix C.

I will briefly mention some of the issues that we need to be cognizant of when performing such calculations. One main consideration is that a heavy complicated ion like Eu is in the intermediate coupling regime. What this means is that neither LS or JJ coupling is a particularly good basis. There is competition between the spin-orbit interaction and the Coulomb interaction between electrons. To get a feel for the size of this effect, consider that it splits the J levels in a given manifold, and as we know from working in our system, that splitting is significant:  $\sim 1700 \text{ cm}^{-1}$  between the  ${}^5D_1$  and  ${}^5D_0$  and  $\sim 500\text{-}1000 \text{ cm}^{-1}$  in the ground  ${}^7F$  manifold. Let me emphasize that this is not a crystal-related issue, but purely due to Eu being a complex atom.

Another very interesting atomic physics issue that is purely a consequence of the complexity of Eu is that different configurations can have the same term symbol representation in LS coupling. In other words, since there are so many different ways to arrange  $\text{Eu}^{3+}$ 's 6 electrons, some of those arrangements have the same quantum numbers. This necessitates another quantum number (a label) to distinguish the terms called the seniority number, see Cowan or Tanner [42, 44]. This number is often indicated in parenthesis following the term. One way to think about it is from the perspective of parent terms. Imagine coupling one electron less than how many you are trying to couple (this would be 5 of 6 electrons in  $\text{Eu}^{3+}$ ). This initial coupling forms a parent term. Coupling the last electron to different parent terms may yield the same resultant LS term. The seniority number differentiates between parent terms. The value of the seniority number is usually unimportant, but it appears that they are normally assigned by energy from highest to lowest. In our case, we are working with the  ${}^5D(3)_1$  level but there are also  ${}^5D(2)_1$  and  ${}^5D(1)_1$  terms at higher energy. You can see these numbers indicated in figure 4.2. Note, as we are going to be talking about the  ${}^5D(3)$  levels a lot, we will just assume the seniority number but for clarity not write it all the time.

A related very interesting detail that is often glossed over is that in the LS basis our wavefunctions are not pure. Tanner talks about this[44] and gives the  $\text{Eu}^{3+} {}^7F_0$  term as an example:  ${}^7F_0 = -0.966 {}^7F_0 + 0.188 {}^5D(1)_0 - 0.168 {}^5D(3)_0 + \dots$ . In other words, the  ${}^7F_0$  ground state is only about 93%  ${}^7F_0$  and has contributions from other terms. Although this ground term is quite pure, in general they need not be. Additionally, to emphasize, this is not a crystal effect, but a feature of the atomic structure. You can see the LS wavefunction composition in the Cowan code output. These effects are dealt with in both the Cowan code and RELIC.

As far as crystal effects, one consequence of being in the crystal is that transitions that are not allowed in the free ion become allowed (a little) and in fact may be stronger than the allowed magnetic dipole transitions[44]. These transitions are called 'forced electric dipole' transitions. There can be magnetic dipole transitions and forced electric dipole transitions between the same levels. This is exciting from the perspective of trying to achieve a negative refractive index as

it represents a system with electric and magnetic transitions at exactly the same frequency. This could be very interesting if a workable set of levels could be found.

Additionally, the perturbing influence of the crystal environment can affect the magnetic dipole (M1) transitions, although the M1 transitions are much more weakly influenced by the crystal environment than forced electric dipole transitions.

There is a large and established body of theoretical work that investigates intra-F-level transitions in rare-earth doped crystals and glasses. The theory is known as Judd-Ofelt theory, after the architects of the original theory[45, 46]. I am fond of this paper[43] on the subject by Hehlen, Brik and Kramer. Walsh also has a nice chapter on the subject[47]. This theory is what is implemented by RELIC; see appendix C for more information. I relate the most important results here.

${}^7F_0 - {}^5D_1$ matrix element	Value ( $\mu_B$ )
Cowan code	0.15
RELIC	0.52

Table 4.1: Magnetic dipole matrix elements calculated with the Cowan code for the free ion and RELIC for the ion in a crystal.

#### 4.4 Studies Involving $\text{Eu}^{3+}$ Transitions in the Literature

It is interesting that a lot of useful and intriguing spectroscopic information about these rare-earth doped crystals was investigated experimentally as long as 50 years ago. For example, see Weber[48]; he looked at Eu and even calculated some decay rates for the transitions we are interested in, albeit in a different crystal host,  $\text{Y}_2\text{O}_3$ :

This is a different crystal than YSO but we can pull out some intriguing information. First, Weber's calculated decay rates from  ${}^5D_0$  and  ${}^5D_1$  lie between what the Cowan code tells us for the free ion and what RELIC tells us for Eu:YSO. This seems at least reasonable.

Something else that is interesting is that Weber calculates the forced electric decay rate contributions to be about  $10\times$  larger than RELIC does for YSO. It would be possible that this is due

Excited State	$A_{ed}(\text{Hz})$	$A_{md}(\text{Hz})$	Radiative LT ( $\mu\text{s}$ )	Observed LT ( $\mu\text{s}$ )
${}^5D_0$	930	109	963	$860 \pm 20$
${}^5D_1$	878	105	1020	$160 \pm 5$ (77K)

Table 4.2:  $\text{Eu} : \text{Y}_2\text{O}_3$   ${}^5D$  Transition Rates calculated by Weber[48].  $A_{ed}$  and  $A_{md}$  are the electric dipole and magnetic dipole transition rates. LTs are lifetimes.

Excited State	RELIC $A_{ed}(\text{Hz})$	RELIC $A_{md}(\text{Hz})$	COWAN $A_{md}(\text{Hz})$
${}^5D_0$	83	153	16
${}^5D_1$	82	257	45

Table 4.3: RELIC and Cowan predictions for  $\text{Eu}:\text{YSO}$   ${}^5D$  Transition Rates

to the difference in crystal host, but if we apply Judd-Ofelt parameters for  $\text{Y}_2\text{O}_3$  and calculate the forced electric dipole rates, although they are larger:  $\sim 130\text{Hz}$  for each, they are still much smaller than Weber's numbers. There seems to be some other source for the discrepancy.

## Chapter 5

### Eu:YSO Decay, Broadenings and Crystal Effects

#### 5.1 Non-Radiative Decay Mechanisms and Homogeneous Linewidth

There are a number of reasons why it is important to determine all the optical and nonradiative decay rates in our system:

1. It sets the minimum homogeneous linewidth. This relates to experimental laser powers and what we can expect to see in terms of interaction strength and minimum spectral feature widths.
2. We need to understand all the decay paths to know if population is accumulating somewhere we do not want it to be.
3. It is interesting, encompassing issues that have been recognized for a long time (although new to our lab) as well as processes that largely unexplored as they are not a priority for quantum memory experiments in the same material. Also, there is limited information in the literature on our crystal host.

Perhaps the most significant issue that distinguishes our system from much of the existing work on Eu:YSO and related materials (primarily experiments directed at quantum memories) is that unlike those, our system is not the doubly forbidden  ${}^5D_0 - {}^7F_0$  580 nm yellow line in  $\text{Eu}^{3+}$ . Instead we are working on the  ${}^5D_1 - {}^7F_0$  which is about 1700-1800  $\text{cm}^{-1}$  higher in energy than the yellow line and is magnetic-dipole allowed. It turns out that the largest decay route is nonradiative decay from  ${}^5D_1 \rightarrow {}^5D_0$ . Once population reaches  ${}^5D_0$ , the story is basically the same as for the yellow line, having the same optical decay channels. There are a variety of nonradiative decay

and dephasing mechanisms. Many are pretty unimportant to us, either because our choice of crystal host fortuitously largely suppresses them, or because they are still a lot smaller than the nonradiative decay to the  ${}^5D_0$  level. However, we do need to discuss them and quantify their influence. A useful source for information on these nonradiative decay mechanisms is a thesis by Lutz Petersen at Zurich on Praseodymium in YSO[49]. Much of the information is applicable since we are using the same host, and it is presented at an approachable level. Also, very useful papers for our ion and host are by Yano and Graf[50, 51, 52]. They focus on the quantum memory transition, but these papers do a good job discussing a number of decay and dephasing mechanisms. Let me list them, using terminology similar to Yano and Graf:

$$\Gamma_h = \Gamma_{lifetime} + \Gamma_{Eu-Eu} + \Gamma_{Eu-host} + \Gamma_{phonon} \quad (5.1)$$

$\Gamma_{lifetime}$  is the linewidth contribution due to the underlying radiative lifetime; for us this is a few hundred Hz according to RELIC calculated optical decay rates.  $\Gamma_{Eu-Eu}$  is the influence of dopant ion-ion interactions, *i.e.*, excited dopant ions disturbing/broadening the linewidths of the other dopant ions.  $\Gamma_{Eu-host}$  is the interaction between the Eu ions and the host crystal. Finally, the last term  $\Gamma_{phonon}$  is due to phonon interactions. Graf distinguishes between two different mechanisms: equilibrium (thermal) phonons and non-equilibrium phonons, *i.e.*, phonons that result from other nonradiative relaxations in the system and then interact and cause broadening of other transitions. Graf also includes another term he calls  $\Gamma_{TLS}$ , evidently corresponding to effects from “two level systems”. Apparently this is an issue for glassy systems and probably not relevant for us, so I left it out of my list. Thankfully for our understanding, our system will be very similar to the  ${}^5D_0$  level for the purposes of a lot of these effects investigated by Yano and Graf.

### 5.1.1 Ion-Ion Interactions and Ion-Host Interactions

One source of decay in the crystal is dopant ions interacting with each other. Thankfully for us, we are working with a non-Kramers ion, that is an ion with an even number of electrons in the 4f. There are no unpaired electrons susceptible to spin flips. The dipole moment of the excited Eu is sufficiently different from the ground state that it interacts with Eu in the ground state,

changing their energy slightly. This ion-ion interaction depends on the ion concentration as well as the fraction of ions that are in the excited state, *i.e.*, if one takes doping concentration or laser intensity to zero, the ion-ion piece goes away. Yano investigates this and discusses its intensity dependence[51]. As we would expect, if one drives the system harder, there is more population in the excited state and as a result, more ion-ion interaction, and thus more broadening. Note: his sample was 0.1% doped, as is ours, so this comparison to our experiment should be very relevant. By taking linewidth measurements at different intensities, he comes up with a linear relationship between laser intensity and broadening:

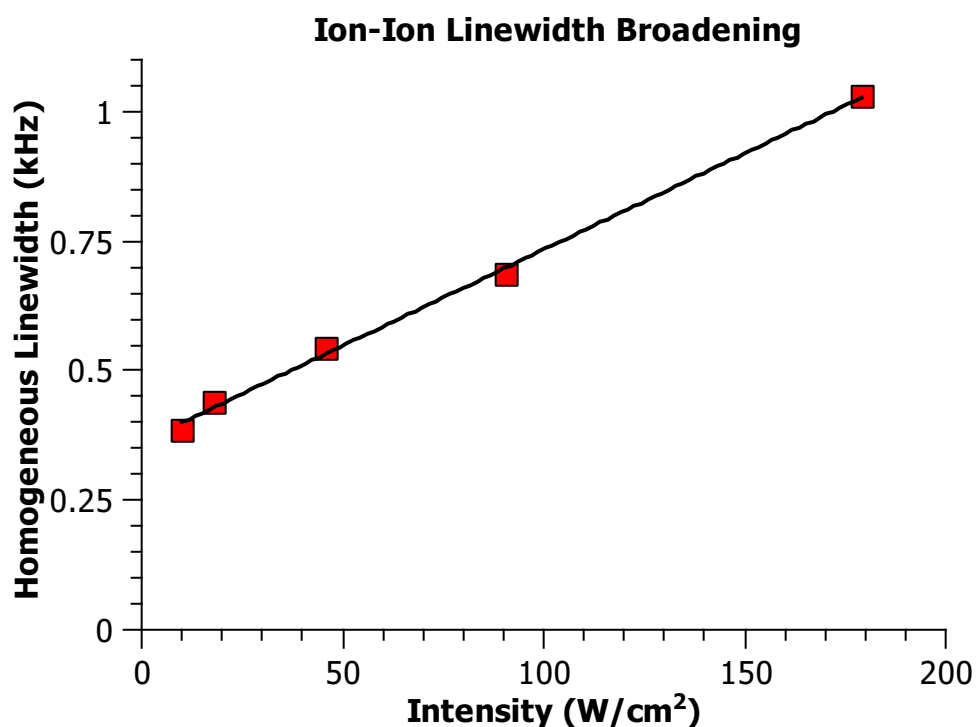


Figure 5.1: Ion-ion linewidth broadening mechanism, data from Yano [51]. Note the linear dependence on driving intensity. For reasonable intensities, this effect would add less than 1 kHz to homogeneous linewidth.

This is for our ion in the same host at comparable temperature (6K) as well as the same site, ‘site 2’. This reveals a couple interesting pieces of information. For one, the ion-ion interaction is approx  $3.4 \text{ Hz/W/cm}^2$ . Additionally, extrapolating back to zero laser intensity gives the residual broadening, presumably due to ion-host interactions. In this case, it is approximately 280Hz. Although this was for the  ${}^5D_0$  level, this effect is probably similar for the  ${}^5D_1$  level. I would not expect it to vary significantly between the two unless population in the  ${}^5D_1$  level is for some reason much more effective at disrupting neighboring Eu ions than population in the  ${}^5D_0$  level. Besides, as we will see when we discuss phonons,  ${}^5D_1$  population quickly relaxes to  ${}^5D_0$ . In any case, although these rates are quite small, they are comparable to our underlying lifetime-based decay rate of perhaps a couple hundred Hz.

Graf and co-authors have an excellent more recent paper that goes into more detail about this effect[52]. They make the additional point that the fraction of ions that are excited also depends on where in frequency in the overall inhomogeneous feature one is operating. This is because the location (frequency) in the inhomogeneous broadening changes the effective density and number of ions that can be excited. Even so, taking this into account they still observe a maximum broadening of perhaps a few kHz due to this mechanism. Also, consistent with Yano, they observe a minimum homogeneous linewidth at zero intensity of about 330Hz.

As for the ion-host interaction, this is a situation where the crystal choice makes a big difference. This effect is discussed in detail with regards to quantum memory experiments as they seek as narrow a homogeneous linewidth as possible. Since the constituents of YSO, principally Si and O, have small magnetic moments, they interact little with the Eu and cause little broadening. Y has a larger moment, but since it is never as close to a Eu ion in the crystal, it does not contribute much either. This effect may be largely irrelevant for us as most of these processes will be much smaller than any phonon mechanisms. Konz has good discussion of this and related issues as well[41].

A point of clarification regarding the term ‘excitation-induced fluorescence’ about which there is a lot of discussion in the literature that I found rather confusing. As far as I can tell, this is the same as what I have labeled as ion-ion interactions. I will stick with ion-ion interactions as I think it is a clearer term. Graf goes into a lot of detail about this effect and different causes for it. If this

were to be an effect that was limiting the experiment, this mechanism would probably be the first place to look. This ion-ion interaction is not to be confused with another effect called ‘spectral diffusion’ as mentioned by Yano[51] for example. To try to distinguish between the two, it is helpful to think about the time scales. The ion-ion interaction (excitation-induced fluorescence) is basically instantaneous and occurs as a result of neighboring excited Eu ions disturbing other Eu ions. Spectral diffusion, on the other hand, is caused by fluctuating host spins causing comparatively slow variations in the potential at Eu ion sites. This effect would be related to host-ion interactions but add a comparatively slow time-varying aspect. It would also depend on the dopant ions. Yano discusses how they do not see this spectral diffusion effect for YSO probably for the same reason there is little host-ion-based broadening. The fact that the YSO crystal atoms generally have small nuclear magnetic moments and  $\text{Eu}^{3+}$  is a non-Kramers ions largely suppresses it. In any case, ‘spectral diffusion’ should not be an issue for our system.

The natural lifetime is self explanatory and the above discussion covers ion-ion interactions as well as ion-host interactions so we understand the first three items in our list of decay mechanisms in eq. 5.1. In the next section we will look into the remaining mechanism: phonon decays.

## 5.2 Experimentally Ascertaining Non-Radiative Decay Rates.

Phonon decay is going to be the main nonradiative decay mechanism that we need to consider. There are a few different instances where we need to account for it, in particular decay from  ${}^5D_1$  to  ${}^5D_0$ , decay between the ground states, and decay between hyperfine states.

One important issue with our investigations is to ascertain the decay rate between the  ${}^5D_1$  and  ${}^5D_0$  level as this is the dominant decay for our level, and understanding that informs our other investigations. This is also a significant difference between our system and many other investigations with Eu:YSO.

One way to ascertain the decay rate is to look at the time dynamics of the fluorescence as suggested by Weber and Schaefele[53]. They talk specifically about the  ${}^5D_1 \rightarrow {}^5D_0$  nonradiative transition followed by radiative decay out of the  ${}^5D_0$  level and describe it with a function of two exponentials:

$$I = C \left( \exp\left(\frac{-t}{\tau_{5D_1 \rightarrow 5D_0}}\right) - \exp\left(\frac{-t}{\tau_{5D_0 \rightarrow 7F}}\right) \right) \quad (5.2)$$

What this amounts to is a pulse in fluorescence, where  $I$  stands for intensity and  $C$  is a scaling parameter. The front of the pulse, the turn-on behavior, gives the nonradiative decay from  ${}^5D_1$  to  ${}^5D_0$  and is governed by  $\tau_{5D_1 \rightarrow 5D_0}$  in the expression. The tail of the pulse gives the optical decay time from  ${}^5D_0$ , and depends on  $\tau_{5D_0 \rightarrow 7F}$  in the expression.

We performed this measurement by flashing a brief ( $\sim 5 \mu\text{s}$ ), bright ( $\sim 50 \text{ mW}$ ), pulse of green light on the crystal and then observing the fluorescence. See inset of figure 5.2 for a cartoon of the levels involved in the experiment. The duration of the green pulse is chosen to be substantially shorter than the fastest process we hope to observe. We expect that the nonradiative part is much faster than the radiative part. This is what we observe; see figure 5.2 for the experimental data. Note: initially this measurement did not make sense as the  ${}^5D_1$  decay time seemed too fast, but adding a filter to block fast green light contamination fixed the problem.

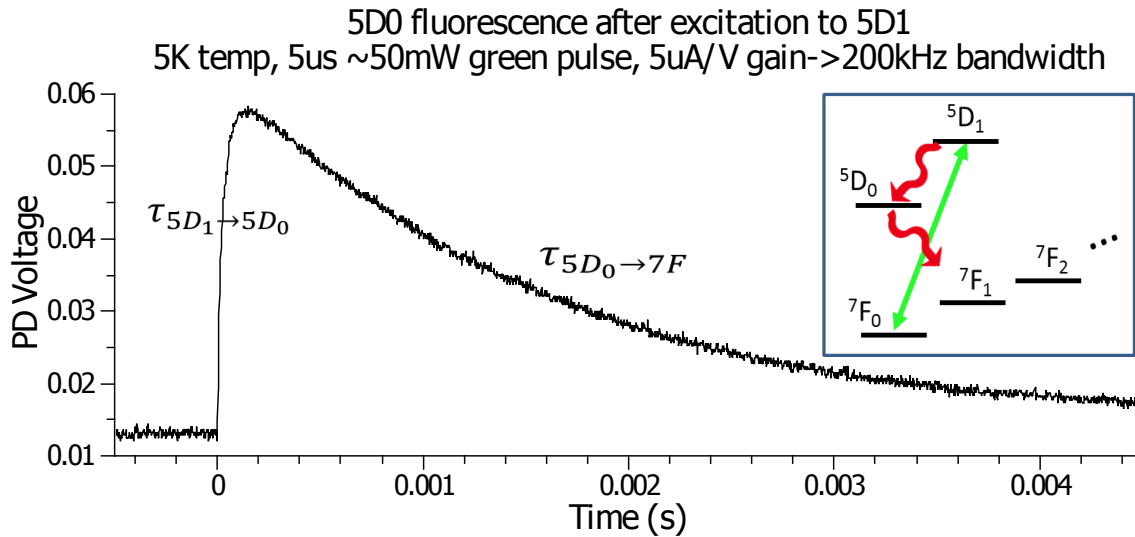


Figure 5.2: Eu:YSO fluorescence in time. Fluorescence out of the crystal after excitation by an intense  $5 \mu\text{s}$  duration pulse. The front part of the pulse gives the fast nonradiative decay  ${}^5D_1 \rightarrow {}^5D_0$ . The slow tail gives the optical decay from  ${}^5D_0$

The front part of the pulse gives the the  ${}^5D_1$  nonradiative decay time,  $\tau_{5D_1 \rightarrow 5D_0}$ , and it is measured here at  $33 \mu s$  (decay rate of 30 kHz). Looking at Weber's paper (different crystal and at LN temps) they observe a decay time from  ${}^5D_1 \rightarrow {}^5D_0$  of about  $100 \mu s$ . Additionally, Weber has a measurement for this multiphonon rate in a different publication for the  ${}^5D_1 \rightarrow {}^5D_0$  in a different crystal host at LN temps as 15kHz (lifetime of  $65 \mu s$ )[54]. Also, Shen measured this same  ${}^5D_1 \rightarrow {}^5D_0$  transition and found a nonradiative decay rate of about 20kHz (lifetime  $50 \mu s$  for Eu:YSO at comparable temps to us. In any case, our measurement is similar to the above quoted measurements. It does not make sense to me that Weber would measure longer decay times at higher temperatures, but the discrepancy is also not huge, within a factor of 2 or so.

The back end of the pulse gives the optical decay from the  ${}^5D_0$  level. This curve is so slow we can get a nice shape and I measure it at 1.61 ms. This is right in line with what Yano observes for the optical lifetime of the  ${}^5D_0$  level[50]. That long lifetime (and narrow linewidth) points to all the interest in the  ${}^5D_1 - {}^7F_0$  transition in Eu:YSO for use in quantum memories. Explicitly the linewidth is related to the decay time by :

$$\Gamma_h = \frac{1}{2\pi T_1} \simeq 99 Hz$$

A couple notes about this  ${}^5D_0$  lifetime measurement. First off, this is very similar to what is expected for this transition. I did however observe a spread in T from perhaps 1.5 to 1.8ms; these differences are probably influenced pretty heavily by the fit and 'how much' of exponential decay curve is included, as well as how noisy the curve is for a given gain setting and other technical issues. I did not see a clear trend with temperature. The lowest temperatures were not necessarily the longest lifetimes. This is expected as the optical decay rate should not really depend on temperature.

This was done at 5K with a  $5 \mu s$  long pulse as well as sufficient photodiode gain in order to get a nice shape. We do need to be mindful of the gain, as large gain will not let us resolve the sharp turn-on. For this gain setting, the photodiode bandwidth is better than 200kHz. The ability to see fast behavior was checked by flashing some of the excitation green directly into the photodiode. This pulse was square, ensuring that both the PD response was fast and the laser turn-on was fast

as well. (It is controlled via a delay generator controlling an RF switch to an AOM, so should be  $<100$  ns turn-on time.) Also, the pulses are built up from 64 averages, as individual shots are quite noisy for this low power/high bandwidth configuration.

This was done at high excitation power  $\sim 50$  mW so that there was sufficient fluorescence to see on the photodiode for a short pulse and as little gain as possible. The beam was focused with a 400mm lens, so the intensity is perhaps  $150$  W/cm<sup>2</sup>. It is possible that there is a laser-intensity phonon-decay mechanism that is driving up the decay rate, but the broadening mechanism I am familiar with: ion-ion interactions (excitation-induced frequency shifts), even for this intensity are only supposed to be on the order of perhaps a few kHz. Also, as it is a dephasing mechanism rather than decay mechanism, it should not be reflected in this decay measurement.

We can also investigate the duration of the pulse and other population issues by looking at a simple pumping/rate-problem model. Although the experimental fluorescence curve basically tells us the population in  ${}^5D_0$  with time, it does not tell us what is in all the other levels in the problem. The model duplicates the same kind of behavior we observe from this flashing experiment, but also allows us to infer the populations in levels we do not see fluorescence from.

### 5.3 Estimating Phonon Decay Rates

Now that we have been able to confirm that the  ${}^5D_1$  decay time is reasonable, let us see if we can calculate/estimate the nonradiative decay rates for the  ${}^5D_1 \rightarrow {}^5D_0$  and other transitions, as these will be very important to any sort of rate-problem analysis. It is useful to organize these by energy scale, as at different scales, we need to consider different processes.

$${}^5D_1 \rightarrow {}^7F_{1,2,..} \sim 18000 \text{ cm}^{-1} :$$

Phonon decay directly from the excited manifold to the ground manifold is very unlikely, as the energy difference is quite large compared to the maximum possible phonon energy and so would require many, many phonons. This means that for this energy scale, the decay is almost totally radiative. It is part of the allure of these rare-earth doped crystals that these optical lines (the lines from lowest level in a manifold to lowest level in the ground manifold) can be quite narrow despite

being in a solid. This is also confirmed by the fact that the decay from the  ${}^5D_0$  is basically equal to the radiative lifetime, *i.e.*, there are essentially no phonon contributions.

$${}^5D_1 \rightarrow {}^5D_0 \sim \mathbf{1700\text{ cm}^{-1}} :$$

This decay is the most important for understanding our system. Since it is the dominant decay from our excited state it will set the homogeneous linewidth for our experiments. At this energy scale, direct (single phonon) or Raman or Orbach (2-photon) processes will not have sufficient energy for such a decay. As a result, the main nonradiative decay mechanism that we need to consider is multiphonon decays. In general this is very challenging thing to calculate as one needs information like electron-phonon matrix elements which are going to depend on the particular crystal. Meltzer mentions this in a book chapter: *Line Broadening Mechanisms and Their Measurement*[55]. As an aside, this book is one of the most topical and comprehensive on topics of interest in our optical system.

Fortunately there has been some progress using a simple empirical ‘law’ to describe this process; see van Dijk[56] and Ray [57]. The basic idea is that as far as multiphonon processes are concerned, an n-order process is much more likely than n+1 order process. As a result, the process is essentially completely moderated by the highest energy phonons (of which the fewest would be required for a given transition). It also means that for decay between two levels with a smaller energy gap, fewer phonons are required and the process is much more likely to occur. This can be written as an exponential relationship:  $k_{nr} = \beta \exp(-\alpha \Delta E)$  where  $\alpha$  and  $\beta$  are fitting parameters that depend on the material and  $\Delta E$  is the energy of the transition, the gap the phonons need to bridge.

At this point, it would be useful to clarify what we mean by ‘highest energy phonons’. This is determined by the crystal, and one route for explaining this is to look at the Debye temperature for the material, Petersen[49] discusses this and points to a publication on YSO[58] that identifies its Debye temperature,  $\theta_D = 580K$ . The Debye temperature can be thought of as the temperature associated with the highest-energy phonon mode the crystal can support. It is proportional to the speed of sound in the material, and so one way to think about it is that harder (faster) materials

can support higher-energy vibrations. We can relate this temperature to the phonon energy via Boltzman's constant, *i.e.*,  $\theta_D k_B = E_{max} \rightarrow 400 \text{ cm}^{-1}$  for YSO. This number is the maximum phonon energy, and lets us identify a little more precisely the required order of a multiphonon process when discussing different energy differences. As we can see, the  ${}^5D_1 \rightarrow {}^5D_0$  process is going to require something  $> 4$  phonons (of the highest possible energy) in order to happen.

Now we can discuss this energy gap law in a little more detail. I will follow van Dijk most closely[56]. I like that their paper includes a table of information about different crystals and seems to be the the most comprehensive treatment of the subject. Although there are not fitting parameters for YSO, even if we do not have precise numbers we can estimate and come up with some general conclusions regarding nonradiative decay in our system. As I mentioned before, the nonradiative decay rate depends exponentially on the energy. Jan Dijk and Shuurmans write it this way, with a modification where they subtract off two factors of the maximum phonon energy:

$$k_{NR} = \beta_{el} \exp[-\alpha(\Delta E - 2\hbar\omega)] \quad (5.3)$$

There is a big incentive to use this because of its simplicity, only depending on two parameters:  $\alpha$  which is related to the electron-phonon coupling, and  $\beta_{el}$  which encompasses the electronic coupling. Additionally, van Dijk and Shuurmans' formulation is better than the original as it reduces the variability in the fitting parameter  $\beta_{el}$  from orders of magnitude to within about a factor of 10. The fitting procedure is better behaved. From above, we know that the maximum energy of phonons in YSO is about  $400 \text{ cm}^{-1}$ . We also know the gap in this case is  $\sim 1715 \text{ cm}^{-1}$ ; however we do not know  $\alpha$  and  $\beta_{el}$  for our material. Let us examine values for similar crystals they have in their paper (we can compare their maximum phonon energies for insight) and see what sort of range of rates we predict for the  ${}^5D_1 \rightarrow {}^5D_0$  rate. A value of  $\alpha$  of perhaps  $\sim 4 - 5 \times 10^{-3} \text{ cm}$  seems reasonable;  $\beta_{el}$  is less clear but somewhere between  $0.5 - 4 \times 10^7 / \text{s}$  should cover the entire range. Trying different values of these parameters in this range yields a nonradiative rate,  $k_{nr}$ , of about 100 kHz to 1 MHz for the  ${}^5D_1 \rightarrow {}^5D_0$  transition.

But this decay rate estimate is much too fast! Let us consider this as an opportunity to discuss an additional complication that unfortunately really limits the power of this simple exponential

energy-gap scheme in our system. It turns out that there are selection rules at play with regards to phonon transitions as well. Weber goes into some detail on this issue[54]. Apparently, since the phonon transitions are between same-parity electronic states, for low J there arises a selection rule very much like that for the forced electric dipole transitions; *i.e.*,  $J=1$  to  $J=0$  is not allowed. In figures C.4 and C.5, notice that there is no forced electric dipole transition between  ${}^5D_1$  and  ${}^5D_0$ . The low-lying  ${}^7F$  levels have the same restriction. There is also suppression based on the order of the process when the number of phonons required is larger than  $|(J - J') - (J + J')|$ . This is why the ‘Selection Rule Limited’ case of the  ${}^7F_6 \rightarrow {}^7F_3$  transition is suppressed in figure 5.3. Weber (and others) discuss these issues and note that the measured  ${}^5D_1$  multiphonon rate is conspicuously smaller because of this selection rule issue than all the other transitions they looked at, as well as much smaller than would be predicted by this exponential energy-gap method.

If we apply this phonon transition selection rule consideration to our previous estimate of the rate for the  ${}^5D_1 \rightarrow {}^5D_0$  transition, we can expect the measured rate to be perhaps  $100\times$  smaller than the estimate. We measure a rate of about 30 kHz. A naive prediction using the exponential energy gap method with our best estimates for crystal parameters and not incorporating any selection rule considerations estimates a rate perhaps  $3\text{-}30\times$  larger than what we measure. In light of this selection rule issue, our predicted number is not so unreasonable compared to what we observe.

Considering the number of assumptions being made here, I think this is quite good. Although we can’t really ascertain anything more quantitative about the  ${}^5D_1 \rightarrow {}^5D_0$  issue, the exponential energy-gap law can still give us some insight about transitions between  ${}^7F$  levels. We will discuss this in the next section.

**${}^7F_2 \rightarrow {}^7F_1 \rightarrow {}^7F_0$ , etc.  $\sim 500 \text{ cm}^{-1}\text{-}1000 \text{ cm}^{-1}$**

The energy scale of transitions between levels in the  ${}^7F$  manifold is slightly smaller than the  ${}^5D_1 \rightarrow {}^5D_0$  transition, and the exponential energy gap scheme should apply here as well. If we have an understanding of the nonradiative rate for the  ${}^5D_1 \rightarrow {}^5D_0$  transition, we can see what similar parameters give for the  ${}^7F$  rates. Qualitatively we can predict a few things: First, the energy gaps are smaller, so the rate should be larger. Additionally, at least for the higher-lying  ${}^7F$

levels, there will not be the selection rule restriction, although that restriction will come into play for levels with small  $J$ , *i.e.*, transitions between  ${}^7F_2$ ,  ${}^7F_1$  and  ${}^7F_0$ . Finally, unlike the forced electric dipole transitions between  ${}^7F$  levels, the dependence on energy gap is going to heavily suppress transitions that hop levels in the cascade; *e.g.*, there will be essentially no  ${}^7F_6 \rightarrow {}^7F_4$ . When applying this exponential energy gap estimate scheme, figure 5.3 shows what we see comparing the  ${}^5D_1$  and  ${}^7F_6$  transitions.

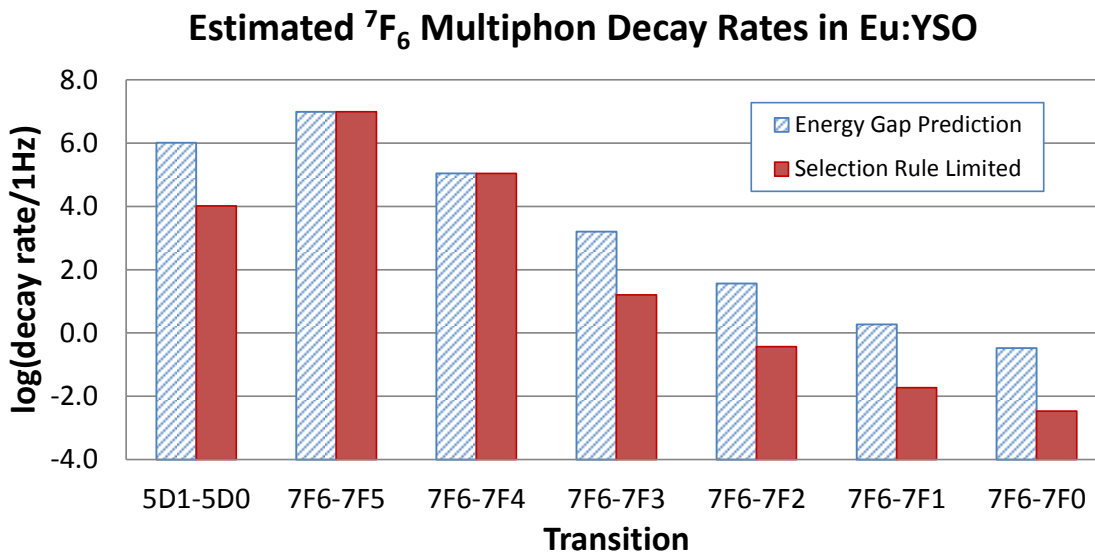


Figure 5.3:  ${}^7F_6$  nonradiative decay rates estimate: Decays to levels other than the closest are suppressed, as the energy gap is larger. Also, decays to levels with small  $J$  or that require many phonons are suppressed by selection rules.

Note: for this I picked parameters to give us a  ${}^5D_1 \rightarrow {}^5D_0$  transition rate of about 1 MHz, before incorporating a crude estimated suppression factor of 100 because of the selection rule issue, giving an adjusted rate of 10kHz, on the scale of what we observe. The important conclusion is that for this conservative estimate, the decay from  ${}^7F_6$  is much faster than the decay from  ${}^5D_1$ . Among possible transitions out of  ${}^7F_6$ , as we expect, the  ${}^7F_6 \rightarrow {}^7F_5$  dominates. The second largest is at least a  $100\times$  smaller. Figure 5.4 looks at estimates for only the comparatively strong transitions.

The important conclusion from this discussion is that even if we do not know the actual numerical values of the decay rates, we do know that the  ${}^7F$  transitions should be significantly faster

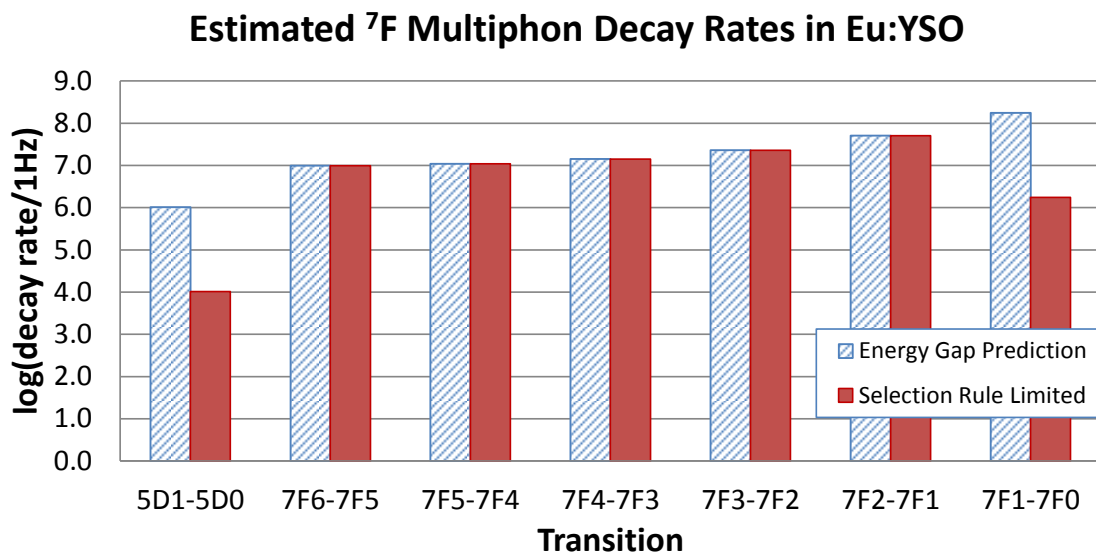


Figure 5.4:  ${}^7F$  nonradiative decay rates estimate. This gives us confidence that relaxation between states in the  ${}^7F$  manifold will happen much faster than decay from  ${}^5D_1$ . In other words population will not accumulate in some undesirable ground state.

than the  ${}^5D_1$ , probably on the order of MHz. This is good because it means that there should not be any population accruing in any  ${}^7F$  state (besides  ${}^7F_0$ ). The relaxation to the ground state should be quite fast, probably faster than a Rabi frequency that we would apply. If population were to accumulate anywhere, it would be in the  ${}^5D_0$  state, as radiative decay from there appears to be the slowest process in the problem. There is some discussion in van Dijk about if the exponential energy gap idea breaks down for smaller energy gaps, say a few  $100\text{ cm}^{-1}$ , but if anything the rate is probably faster, so for our purposes this is not a problem. For very small energy differences like the hyperfine energy scale, this idea is no longer applicable; this is discussed in the *Hyperfine Splitting* section below.

One question that arises both with  ${}^5D_1 \rightarrow {}^5D_0$  and  ${}^7F$  phonon decays is what happens with temperature? I think the answer is not much. This question gets at the distinction between thermal and acoustic phonons. We can think of thermal phonons as the ambient motional excitations rattling around in the crystal, while acoustic phonons are the modes the crystal will support. Different crystals would of course support different phonon energies and would have different phonon

spectral structure. At 5K, this distribution would be peaked at about  $3.5 \text{ cm}^{-1}$ , so small that it would not have any bearing on the multiphonon decay channels we have discussed so far. The high-energy phonon modes that are responsible for the multiphonon decays in our system are not going to be thermally populated until comparatively high temperature. As a result, over a range of temperature from very low to relatively warm there is not much of a change for these processes. Weber[53] shows temperature making little difference up to 300K or so for the  ${}^5D_0$  lifetime, and 200K or thereabouts for the (closer-in-energy decay destination)  ${}^5D_1$ .

### **Stark-level splitting, $\sim 50 \text{ cm}^{-1}$**

This energy scale is small enough that potentially a single phonon could directly cause decay, and this decay would be comparatively likely. However, thankfully we are operating on the lowest level in the  ${}^5D_1$  manifold and so should be immune to this as an experimental problem. See figure 4.6.

### **Hyperfine Splitting (Spectral Hole Lifetimes), $\sim 100 \text{ MHz}$**

The hyperfine splitting is very small compared to the other energy scales we have discussed. This brings up a number of questions:

1. Why is this hyperfine lifetime so long?
2. Is there a selection-rule or momentum conservation issue that prevents phonons from mixing the hyperfine ground states?
3. What is the temperature dependence of this phonon process?

This issue is addressed explicitly by Könz[41]. Könz lays out the different processes that determine the spectral hole (*i.e.*, hyperfine ) lifetime. It turns out that there are two main contributing processes: Raman processes and Orbach processes. Both are two-phonon processes, the Orbach via an on-resonant upper level, the Raman through a virtual level. At first glance, one would expect from the exponential energy gap arguments discussed above that the hyperfine decay rate would be very fast, as the energy separation is very small. However, direct single phonon processes are

suppressed because of a lack of phonons at such low energy. Orbach discusses this in his original paper[59]. It comes about because the single-phonon rate depends on the number of phonons at a given energy, and if the phonon energy is a lot smaller than  $k_B T$ , there are not many phonons at that energy available. Orbach (page 475) describes how the number of phonons in the vicinity  $d\omega$  of some frequency is[59]:

$$n(\omega + d\omega) = \frac{3V\omega^2 d\omega}{8\pi^3 v^3 \left[ \exp\left(\frac{\hbar\omega}{k_B T}\right) - 1 \right]} \quad (5.4)$$

$V$  is the volume and  $v$  is the propagation speed in the crystal. The maximum of this phonon distribution is for phonons at  $k_B T$ . If the required phonon energy for a direct process is much smaller than  $k_B T$ , there are not many available, and the rate is slow. Because of this, higher-order (2-phonon) processes like the Raman and Orbach processes can become the more likely decay route. Könz fits these effects for our system, with the following simple function, where A is the Orbach contribution, and B is the Raman piece:

$$\tau_{hole} = \left[ \frac{A}{\exp\left(\frac{\delta E}{k_B T}\right) - 1} + BT^7 \right]^{-1} \quad (5.5)$$

The Raman contribution has  $T^7$  temperature dependence, noted other places in the literature, for example[60]. For very low temperatures, the Raman part dominates, but for slightly higher temps,  $>12\text{K}$ , the Orbach process takes over. Könz and colleagues notice a huge difference in spectral hole lifetime between 5 and 17K, which have lifetimes of 2 days and less than 1 second, respectively. This is shown in figure 5.5:

A final general comment on temperature dependence regarding these processes compared to the multiphonon processes discussed above: it makes sense that for these processes, since the energy change is so much smaller (MHz), they would exhibit much lower turn-on temperature. Raman and Orbach processes are dependent on the thermal distribution of available phonons to participate in the mechanism, whereas the multiphonon decay is not.

We have looked at phonon decays at a variety of energy scales, filling in the last term of expression 5.1. One note of clarification, all the phonon processes we have discussed have been

## Hyperfine/Spectral Hole Decay Rate

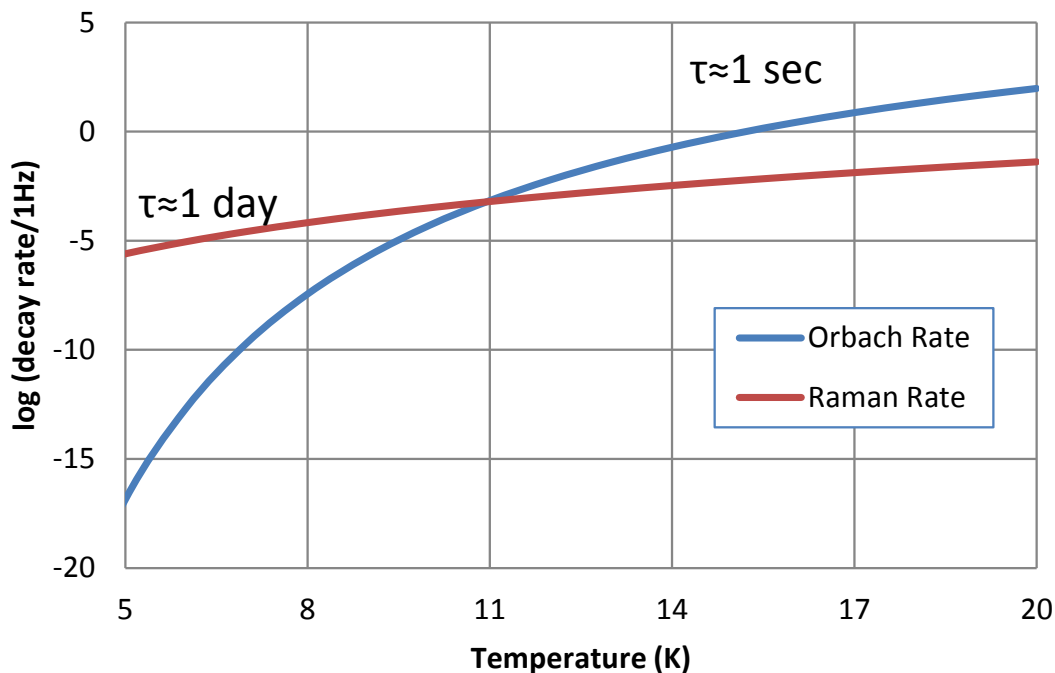


Figure 5.5: Decay at hyperfine energy scales is mediated by two different 2-phonon processes. Raman processes dominate below about 11K, whereas Orbach processes take over above. The extreme sensitivity to temperature means a 15 degree temperature change results in 6 orders of magnitude increase in decay rate.

equilibrium processes; they do not depend on phonons that have been introduced into the system from other decays. Graf discusses non-equilibrium phonon processes at length[52]. Such a process is potentially similar to ion-ion interactions in that if you turn up the laser power the effect would increase. You would in principle be introducing more phonons into the crystal via nonradiative decay paths, and this excess would be available to participate in other decays. Also, much like many of the other broadening mechanisms that are investigated in Eu:YSO with very narrow transitions quantum memory transitions in mind, this effect is most likely quite small, perhaps 100's of Hz. Graf and colleagues describe how it is also less likely in Eu than Pr because of the  $m_j$  energy

splitting being larger for Eu. For our purposes, the effect would probably be both negligible and indistinguishable from any ion-ion interaction. However, if we should later observe at higher power laser-power dependent enhanced decay, this effect would be a good one to investigate further.

I should also clarify here that the lifetime and multiphonon decay processes are decay (T1) processes. The ion-ion and ion-host processes are dephasing (T2) processes. This is relevant when doing, say, density matrix simulations, as there could be dephasing that degrades coherences but does not affect populations. Also, our decay measurement (See figure 5.2.) does not reflect the additional dephasing, but a spin-echo measurement, for example, would.

Weighing the different contributions to the homogeneous linewidth in our list in expression 5.1, we can sum up by saying that the dominant contribution is the multiphonon decay from  ${}^5D_1$  to  ${}^5D_0$ . The optical decay routes from  ${}^5D_1$  are very similar in strength to those from  ${}^5D_0$ , and so we can estimate that the lifetime contributes perhaps a couple 100 Hz. Ion-host interactions in Eu:YSO may contribute to this a few 100 Hz of dephasing; ion-ion and non-equilibrium phonon interactions perhaps a couple kHz at high intensity. (We could characterize/investigate this if we observe a problem). All of these effects are much smaller than the multiphonon decay rate.

#### 5.4 Modeling Pumping and Decay Routes/Conclusions:

Let us summarize our best estimates of decay rates and matrix elements here that we have discussed in the last two chapters.

Now that we have decent estimates for our decay rates, we can plug them into a rate model and plot the populations in different states, see figure 5.6.

This plot mirrors our experimental curve in figure 5.2; it is generated with a  $5 \mu\text{s}$  long driving pulse, same as the experiment. Populations is pumped from the  ${}^7F_0$  (red) to  ${}^5D_1$  (green) where it relaxes quickly to  ${}^5D_0$  (blue). Population ultimately all ends up in  ${}^7F_0$  (red) via fast nonradiative relaxation from the other  ${}^7F$  levels populated by the slow optical decay from  ${}^5D_0$ . Since the decays between the ground state levels are so fast, no appreciable population ever accumulates in any of the other  ${}^7F$  levels (purple).

Quantity	Value
${}^5D_1 - {}^7F_0$ matrix element (from Cowan)	$0.15\mu_B$
${}^5D_1 - {}^7F_0$ matrix element (from RELIC)	$0.52\mu_B$
${}^5D_0$ decay time	1.6ms
${}^5D_0$ decay rate $\left(\frac{1}{2\pi\tau}\right)$	99Hz
${}^5D_1$ decay time	$33\mu s$
${}^5D_1$ decay rate $\left(\frac{1}{2\pi\tau}\right)$	4.8kHz

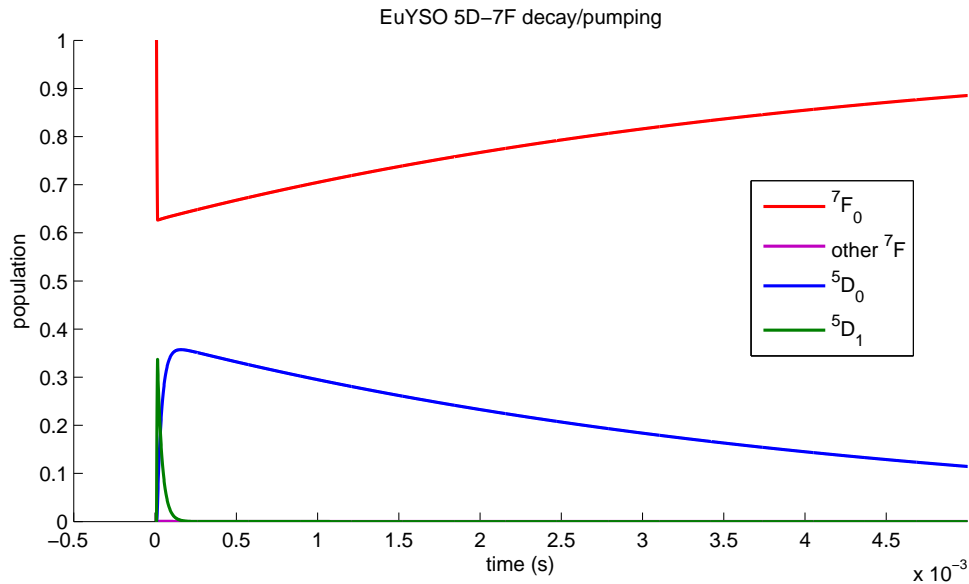
Table 5.1: Eu:YSO  ${}^7F_0 \rightarrow {}^5D_1$  transition and related parameters

Figure 5.6: Incoherent pumping/decay analysis. Combining what we have learned about the different decay rates we can emulate what we saw experimentally while keeping track of where the population is. Driving with a  $5\ \mu s$  long laser pulse, population is excited to  ${}^5D_1$  (green) where it quickly decays to  ${}^5D_0$  (blue). Ultimately, after slow optical decay from  ${}^5D_0$  and fast decay between the  ${}^7F$  levels, all the population accumulates back in  ${}^7F_0$ .

## Chapter 6

### Experimental Set-up

Let us start with a diagram of the system, and then we can go into detail about the sub-systems.

Figure 6.1 shows the entire experimental setup.

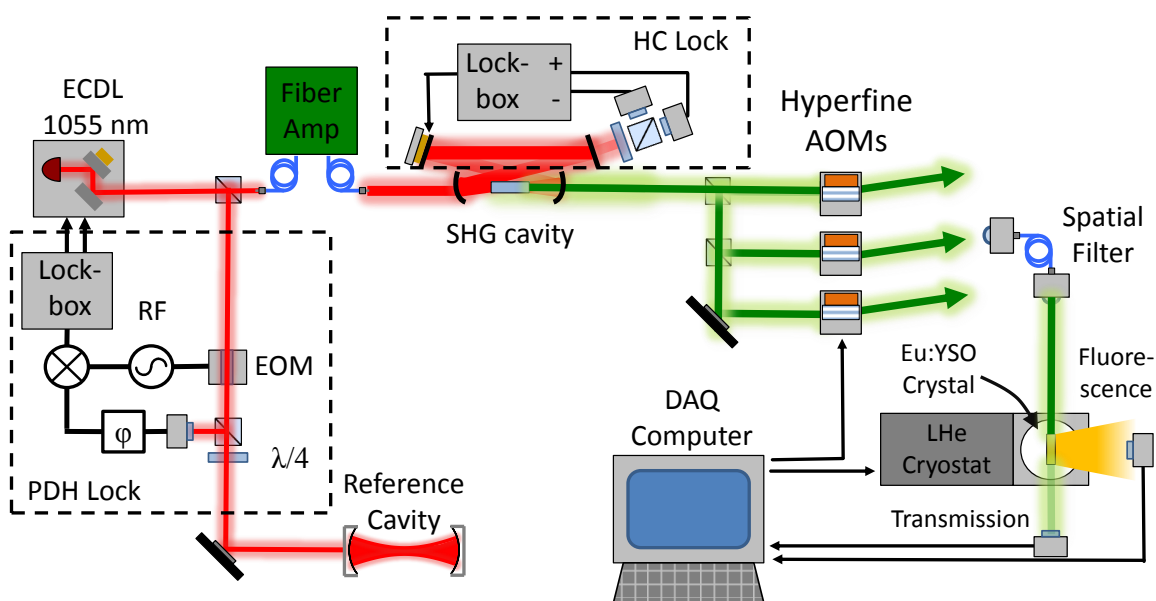


Figure 6.1: High-level diagram of the experiment. ECDL is the extended-cavity diode laser at 1055 nm that seeds the system. PDH is the Pound-Drever-Hall subsystem that locks the diode laser to a reference cavity. The amplified IR is frequency doubled in the SHG bowtie cavity locked via Hänsch-Couillaud locking. The (now green) light is shifted by AOMs to match the desired hyperfine splittings. Experiment beams are then sent to the Eu:YSO crystal housed in a liquid helium cryostat.

The experiment fits on a single optical table.

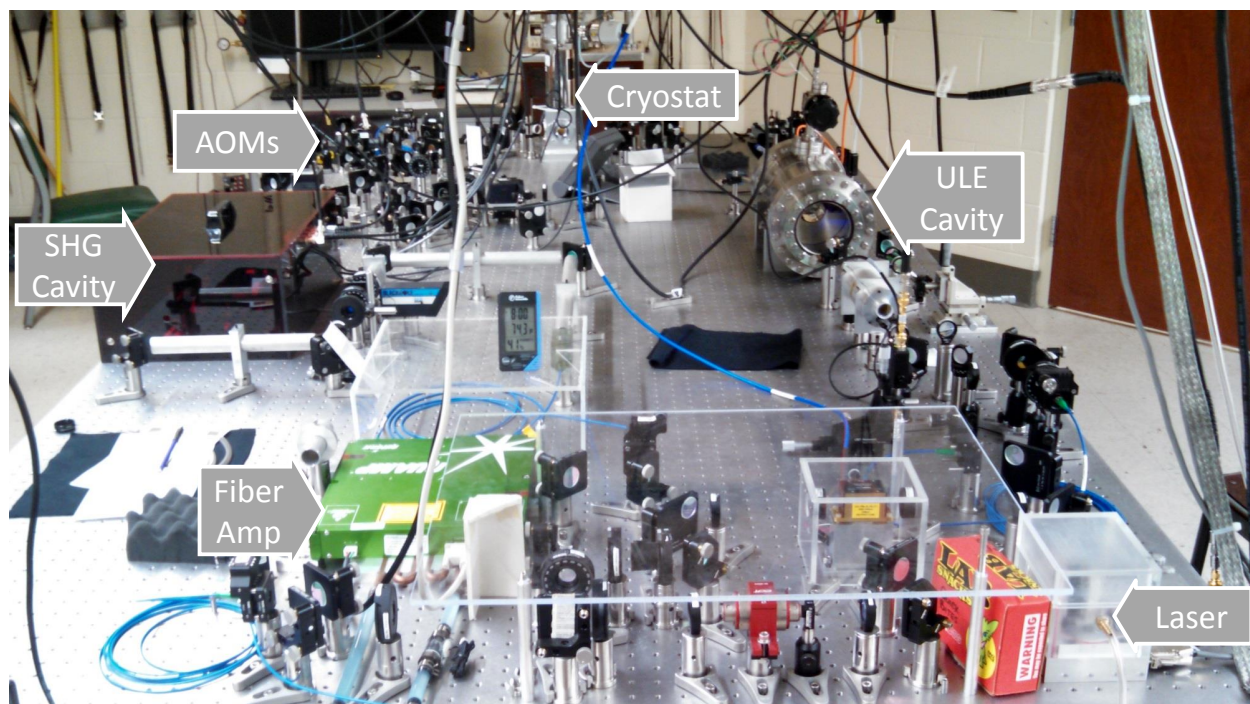


Figure 6.2: Picture of our optical table.

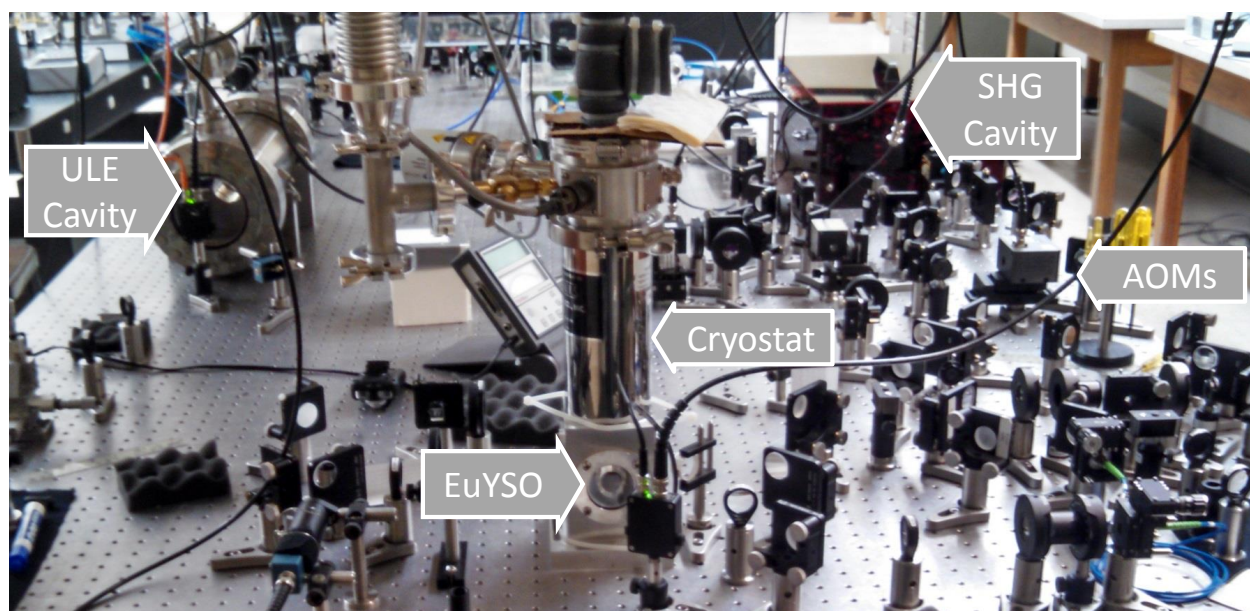


Figure 6.3: View of the cryostat

## 6.1 Laser System and Locking to Reference Cavity

In order to interrogate this green transition in Eu:YSO, we need a narrow-frequency, stable laser at that color. How narrow? Less than the linewidth of the transition, which is on the order of 10s of kHz as discussed in the last chapter. How stable? Well, we do not want the laser to move more than a fraction of the linewidth while we are performing an experiment that might take several minutes. We also require on the order of a watt of power to provide for loss due to downstream optical elements such as AOMs and fibers, and for combining beams. The short story is that we get this power by frequency-doubling an infrared laser at 1055 nm.

The root of the laser system for the experiment is a diode laser with optical feedback, an extended-cavity diode laser. This design takes the very short low-finesse diode laser and embeds it in a longer cavity where one of the mirrors is a wavelength-selective element, a diffraction grating. The laser is labeled as ECDL in figure 6.1. We use such lasers in most of our work in YavuzLab and despite their sometimes temperamental behavior, they are capable of remarkably narrow linewidths; we have observed 10s of kHz.

Our extended-cavity diode laser design is based on the common design by Arnold and improved by Hawthorn [62, 61]. We have attempted better thermal performance by replacing the back of the mirror mount with a single-piece mount, but have not noticed apprecieable improvement in stability or performance. The laser diode is from Q-photonics (part number: QLD-1060-50S-AR) and is wavelength selected for 1055 nm. Q-photonics provide this service for an addtional fee. The grating in the set-up is from Thorlabs as are the collimating optics.<sup>1</sup>

To encourage the laser to be as stable as we require and to narrow its linewidth, we need some additional tricks. We do not have the luxury of locking the laser to an atomic frequency reference, as can be done when working with rubidium via saturated absorption locking[63], so instead we lock the laser to a high-stability Fabry-Perot cavity made from ultra-low-expansion (ULE) glass. This is a good method for us as we have experience working with optical cavities, although there are other potential laser-stabilization schemes like locking the laser to a spectral hole burned in the

---

<sup>1</sup>Note to Yavuz Lab: See the wiki for a white-paper discussing some of our efforts to understand and improve diode laser performance.

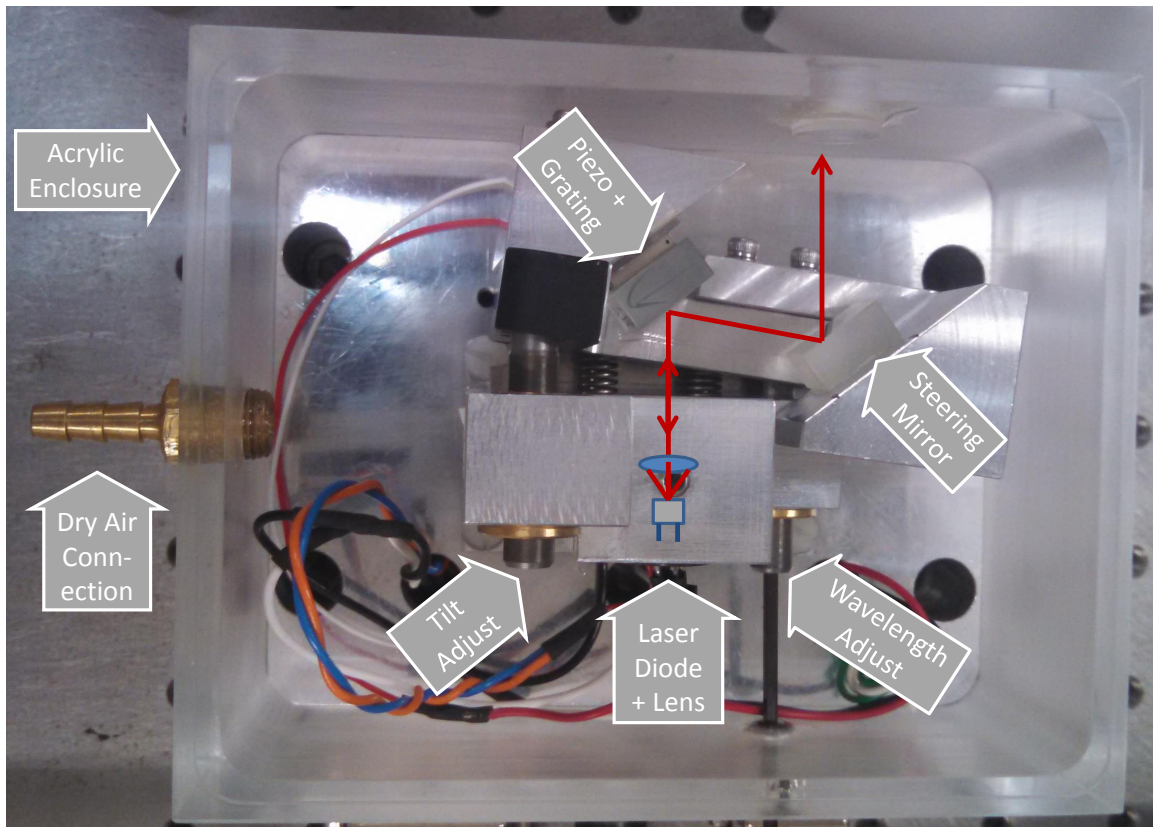


Figure 6.4: Extended Cavity Diode Laser (Top View). Design based on[61]. Built around a modified mirror mount, the set-up incorporates an extended cavity which provides sharper laser modes as well as optical feedback via a diffraction grating that directs a chosen wavelength back into the laser diode. The diode is not visible but is housed in a collimation tube with an aspheric collimating lens. An additional mirror keeps the output direction relatively constant with mechanical adjustment/tune-up. Overlay shows approximate beam bath and location of diode and lens.

crystal; see Chen for example [64]. This cavity was made by Research Electro-Optics, is 10cm long and has a finesse of 2500. This is identified as ‘Reference Cavity’ in figure 6.1. The cavity is housed in a vacuum can to isolate it from thermal variations.

## Locking to Reference Cavity

We lock to the cavity using Pound-Drever-Hall locking. I will not discuss this in detail as this is a widely-used technique and many others have discussed the technical details at length, see for example previous theses from our group as well as the informative and comprehensive paper by Black [65, 66, 67]. However, since laser-locking is a big part of our experiment and we employ two different types of locks, let me explain the basic ideas qualitatively as well as compare the different techniques and put them in the general context of laser locking.

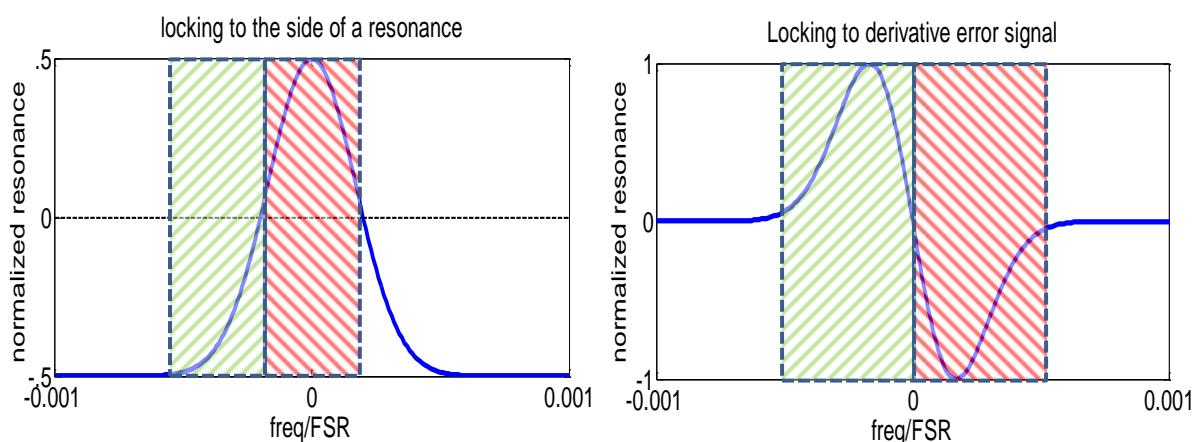


Figure 6.5: Basic laser locking ideas. Locking to the side of a resonance is depicted in the left panel. Locking to the derivative of a resonance is shown on the right. The shaded regions represent the locking capture bandwidth. Green indicates that the feedback circuit should increase the laser frequency, red indicates that the feedback circuit should decrease the laser frequency.

In general, in order to implement feedback to lock a laser to a cavity or absorption feature, etc., one needs to create an error signal. Crudely, the error signal would tell you if the laser frequency is too high: decrease the frequency, if it is too low: increase the frequency. Consider, for example, some Gaussian resonance shape, perhaps due to transmission through a cavity. You can imagine generating an electrical signal proportional to that optical feature via a sensor. Since that feature is symmetrical in frequency you can't tell which direction you need to adjust the laser to maintain resonance; this is insufficient as an error signal.

An idea that was used in the early days of laser-locking is to lock to the side of such a resonance. Consider the left panel of figure 6.5. (Note: this cartoon resonance has similar characteristics to our reference cavity.) In this instance, we have set the laser power output set-point at half the max value of the resonance. Looking at the figure, the green shaded region indicates where if the frequency were too low, there is a signal of one polarity; too high, there is a signal of the opposite sign in the red shaded region. This is sufficient to lock a laser, but suffers from some serious limitations. For one, if the system hop over the top of the resonance, to the right of the red region, one loses the ability to lock. Additionally, if the amplitude of the laser changes, it changes relative to the effective set-point and so couples amplitude noise into frequency noise. Finally, if one makes the cavity better, with sharper resonances, the resonance gets narrower and, as a result, harder to lock to; *i.e.*, the locking capture bandwidth decreases with increasing cavity finesse.

A better method is to use an error signal that is a derivative of the resonance signal. See the right side of figure 6.5. In this case, the polarity and amplitude variation problems are fixed, but we still suffer from a capture bandwidth problem. Bring in Pound-Drever-Hall (PDH) locking, named after its originators [68]. In this case, we add side-bands to the laser (provided our modulation frequency is sufficiently large to allow the cavity to discriminate between carrier and sidebands; Refer to Black section IVB[65]). These sidebands add additional structure to the error signal as in the left side of figure 6.6. As a result, you can see how the error signal now has the correct polarity and appreciable magnitude over a much larger capture bandwidth and as a result, is not solely tied to the sharpness of the cavity resonance, but also to the applied modulation frequency. The capture bandwidth benefit is significant. To drive this point home, the right side of figure 6.6 re-plots the resonance from figure 6.5 on the same frequency scale as the left side; it is perhaps  $25\times$  the capture bandwidth and shows the huge advantage of the PDH approach. Employing the expression in Black [65], this PDH resonance shape is approximately what we see based on our cavity finesse as well as modulation frequency. Note: this is not the only way to improve the error signal capture bandwidth for a laser lock; I will talk about another method shortly with regards to laser frequency-doubling.

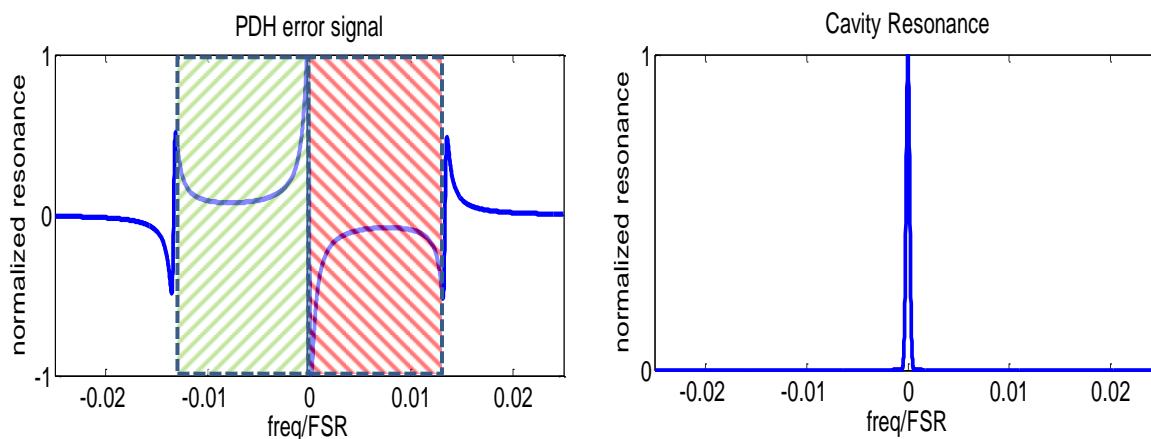


Figure 6.6: PDH locking has the advantage of a large capture bandwidth, set by the modulation frequency. The PDH error signal in the left panel is much wider compared to the width of the cavity resonance by itself, which is shown in the right panel.

We can compare our estimated error signal and resonance peak with what we observe in the lab, shown in 6.7. The experimental signals look pretty similar. You can also see the sidebands in the transmitted signal. Note: our experimental signal does not always look this clean. Normally, we operate with less gain in effort to decrease the locked laser linewidth. This makes the error signal look smaller relative to noise, although it still gives acceptable locking performance.

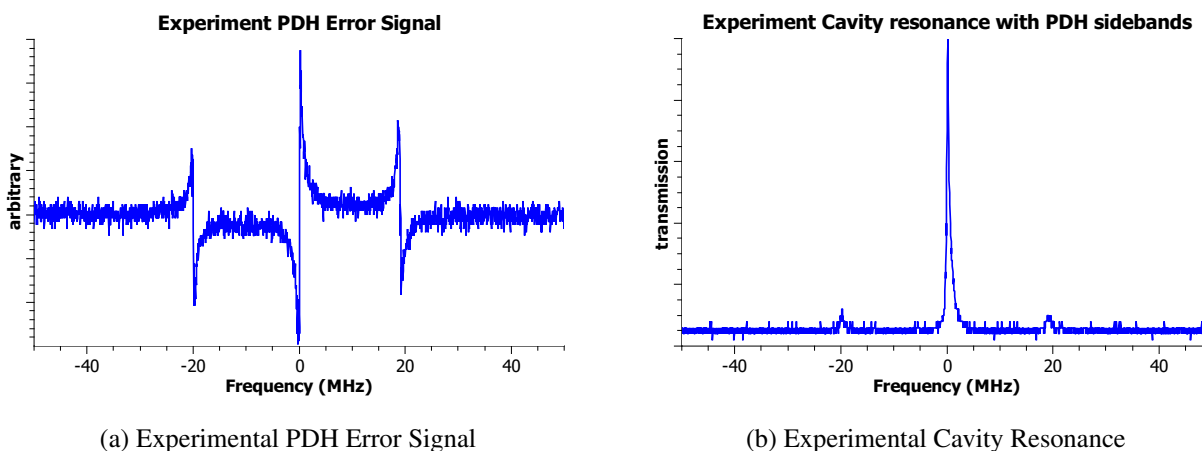


Figure 6.7: Experimental PDH signals

The relevant experimental components of this locking system are indicated in figure 6.1 in the box labeled PDH. The laser is split and a branch is sent to the reference cavity. Before it reaches the cavity, it is modulated with an electro-optic modulator (EOM) driven by an RF source at 20 MHz. Light that bounces off/is ejected from the cavity passes back through the  $\lambda/4$  plate and is rejected by the beam-cube to the photodiode. That photodiode signal is mixed with the same RF that is used to drive the EOM. This produces the error signal as shown in the left panel of figure 6.6. That error signal is used to lock the cavity, *i.e.*, it is fed back to the laser so that it stays locked to a cavity transmission peak. There are actually 2 branches to the feedback, a ‘slow’ (low frequency) branch that goes to a piezo-electric transducer that controls the ECDL cavity length, and a ‘fast’ (high frequency) branch that injects a tiny amount of current directly to the diode. This is indicated by two arrows in figure 6.1. The lockbox electronics are not anything new or revolutionary, but I did try to incorporate good practices and ideas seen in other lockboxes. See appendix E for circuit diagrams and further information on that subject. There is also a more detailed diagram of the PDH electronics in this appendix that includes the components used; see section E.7.

In any case, as a consequence of locking to the ULE cavity, the laser is very stable. We have not quantified or optimized for temperature yet, but estimating based on spectral hole-burning performance, there is no appreciable movement, less than say 100kHz over many minutes. Based on ULE expansion parameters, we can estimate the frequency stability of the cavity. The glass expands at worst 30 ppb/°C [69]. This corresponds to something like 8.5 MHz/ °C for our reference cavity. We should be able to keep the temperature stable to 0.01 °C fairly easily in the vacuum can, giving us a worst-case stability estimate of 85 kHz already, with the prospect of doing much better considering that when the cavity is at optimal temperature, its expansion will be much smaller. In contrast, before we had the ULE cavity (we had to return it for repair and the repair took many months), we locked to an invar cavity instead. Despite being a low thermal expansion material, it would fluctuate on the order of MHz/min. If the lab temperature was increasing, you could see spectral holes trend in one direction for example. In retrospect, had we know the ULE cavity repair would take so long, we would have put that invar cavity in our vacuum can during that period.

Additionally, locking to the ULE cavity narrows the linewidth of the laser considerably. The linewidth of the free-running ECDL is on the order of 500 kHz. The ULE cavity is 10 cm long and so has a free spectral range of 1.5 GHz and its mirrors give a finesse of 2500. This means that the Fabry-Perot cavity peaks have a FWHM of about 600 kHz. When the locking procedure is working well, we can expect to lock to close to the transmission peak, achieving perhaps an additional factor of 10-100 in narrowing. This means we would expect the laser to have a linewidth of perhaps 10s of kHz. Indeed this is what we observe. See figure 6.8 for a representative measurement. We have observed better than than this, perhaps 25kHz, but that is also about the limit of the resolution of our linewidth measurement instrument. In any case, we are confident that the laser linewidth is comparable or narrower than the transition linewidth.

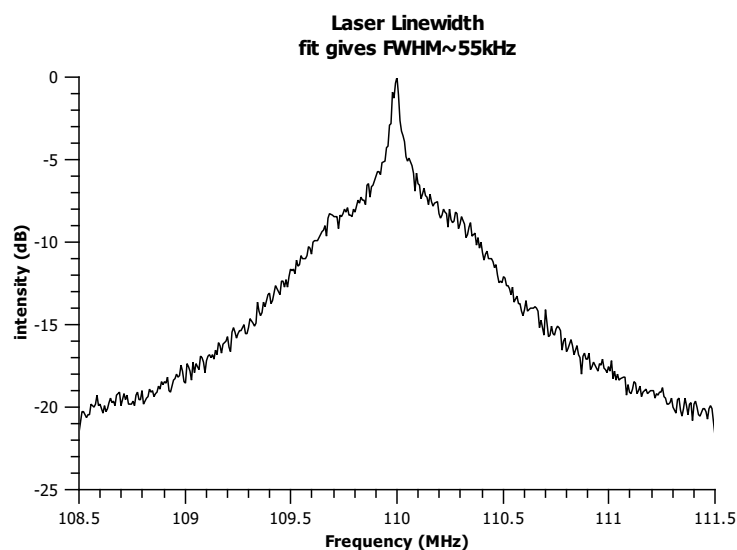


Figure 6.8: Representative measurement of our laser linewidth. We have observed better, perhaps half this width, but are unable to measure linewidths narrower than that because of instrument limitations.

I would add that there is a caveat, the laser performance is quite variable, frustratingly variable, depending sensitively on laser current, temperature, humidity, grating position and movement, as

well as other (unknown) factors. This is an open area of work in Yavuzlab. Obtaining better diode laser performance and reliability would benefit all our experiments. <sup>1</sup>

Referring back to the main diagram of the experiment, figure 6.1, a portion of the stabilized diode laser output is sent to the fiber amplifier. 527 nm is tantalizingly close to the 532 nm of a doubled YAG: a workhorse green laser but not close enough to let us use a YAG for our IR laser/amplifier. As a result we employ a ytterbium-doped fiber amplifier which has a larger range of potential operating colors and can be tailored to operate at 1055 nm. Our amplifier is from Nufern (Part no. SUB-1301). It is capable of a maximum output power of 10 W from an input power of a few mW (1-15 mW). The fiber amplifier is fiber-coupled and easy to work with and has a nice spatial mode compared to tapered amplifiers which we have also worked with at this wavelength. The output is linearly polarized and preserves the linewidth of the seed laser to less than 10kHz.

## 6.2 Getting Green: Second Harmonic Generation (SHG)

The fiber-amplifier infrared output is frequency-doubled to get green light. Yavuzlab member Nick Brewer built the doubling set-up, and so I will not describe it in detail here, but let me give a general description.

Second Harmonic Generation (SHG) is a nonlinear optical process that takes two photons at one frequency and converts them to one photon at double the frequency. This technique provides a way to build light sources at colors otherwise not available directly as laser sources. This occurs by means of a crystal or material that has appreciable nonlinear susceptibility,  $\chi^{(2)}$ . As a result, in addition to the linear polarization,  $\vec{P} = \epsilon_0\chi^{(1)}\vec{E}$ , there will also be nonlinear polarization  $\vec{P}_{NL} = \epsilon_0\chi^{(2)}\vec{E}^2$ . Explicitly inserting  $\vec{E} = E_0e^{-j\omega t}$ :

$$P_{NL} = \epsilon_0\chi^{(2)}(E_0^2e^{-j2\omega t} + E_0^2e^{j2\omega t} + 2E_0^2) \quad (6.1)$$

---

<sup>1</sup>Note to Yavuz Lab: See Yavuzlab wiki for a white-paper discussing and attempting to catalog some of these issues and various misadventures in trying to fix them/improve laser performance.

We can see that there are components at  $2\omega$ . Thus the polarized media driven with an IR laser at frequency  $\omega$  will radiate at  $2\omega$ . This process is the simplest version of a variety of nonlinear optical processes that can also harness higher-order nonlinearities or mix different frequencies. It is a very powerful technique. There are some technical complications, for example  $\omega$  and  $2\omega$  are not going to propagate in phase automatically on account of dispersion, so care must be taken to phase-match the two colors. Our crystal (KTP from Raicol) is periodically poled to address this issue. It is placed on a TEC to control its temperature and so allow for tuning it for different operating wavelengths.

Additionally, although the process is quite weak, the  $\vec{E}^2$  dependence means that increasing the intensity greatly increases the amount of second harmonic light produced. A common route to boost the intensity in the nonlinear medium is to place the crystal in an optical cavity. The finesse of such a cavity need not be exceptionally high, on the order of 10-100, but this higher circulating power significantly increases the output. We place our crystal in a ring cavity with a bowtie configuration rather than a linear Fabry-Perot. This has some advantages including avoiding standing-wave effects in the crystal and the fact that such a ring cavity is directional, so the  $2\omega$  light is emitted from the cavity more or less in one direction. You can see the bowtie shape of the cavity in the block diagram of our system, figure 6.1. The SHG cavity length in our system is about 0.5 m and the beam waist at the crystal about  $35 \mu\text{m}$ . The beam is focused as this is another way to boost intensity, and as a result, SHG conversion efficiency.

This cavity introduces a technical issue, however, in that one needs feedback to keep the cavity in resonance in order to have high circulating intensity; it is a problem very similar to controlling the ECDL cavity length. Tying back to the discussion in the last section, this problem requires a laser lock. In this case, however, rather than lock the laser to a cavity, we will lock the cavity to our (stabilized) laser. We are going to use a different scheme for this application called Hänsch-Couillaud locking. Hänsch-Couillaud locking relies on an imbalance in the amount of light of perpendicular polarizations reflected (or transmitted) from the cavity to produce an error signal. The following discussion is informed by a couple very useful papers: the original paper by Hänsch

and Couillaud and a paper about a transmission-version of the technique by Vainio, Bernard, and Marmet[70, 71].

How it works: Polarized light from the laser is incident on the cavity. The cavity requires an internal polarizer, but in our application the nonlinear crystal serendipitously provides the polarization selection. The transmission axis of the polarizing element is rotated relative to the incident laser polarization. The incident laser light can be thought of as components where the component with the same polarization as the incident light will see the cavity as transmissive when on resonance, while the perpendicular component will see the cavity as very lossy. The component that is transmitted will pick up a phase shift relative to the component that is promptly rejected. That phase shift between the polarization components can be used to create a net elliptically polarized monitoring beam that provides the basis of the error signal. If the cavity is on resonance, the phase shift would disappear. Depending on which side of the resonance you are on, the phase shift will be opposite and the error signal will indicate that. The elliptically polarized monitoring light is sent to a polarization analyzer which looks at the two components. Differential comparison of the photodiodes looking at the two components gives the error signal. The polarization analyzer and box to represent the feedback electronics are depicted in figure 6.1, in the section labeled HC lock.

It is also worth noting that Vainio and colleagues go into a lot of detail for basically our exact application[71]. In their set-up, they utilize the transmitted light from the cavity to form their error signal, which has the advantage of the cavity acting as a filter. This is very useful as there is the potential for other cavity modes to oscillate because of the birefringence of the SHG crystal as well as the possibility of higher-order spatial cavity modes. See their paper for details[71]. We do observe some of this behavior, modes other than what we want for optimal SHG, in our set-up.

In the general context of laser locking, the Hänsch-Couillaud technique also features a robust capture bandwidth; *i.e.*, the error signal is appreciable in more than just the immediate vicinity of the cavity resonance. This thesis by Sieghart has some nice figures of this[72]. This is portrayed in the left panel of figure 6.9. These figures are representative of our SHG cavity, which has a finesse on the order of 50 and a length of about 0.5 m. As a result, this span depicted in the figure is something like -75 to 75 MHz. As you can see, there is appreciable error signal through that

whole frequency range. Another advantage to this technique is that the method also requires no external laser modulation as in Pound-Drever-Hall.

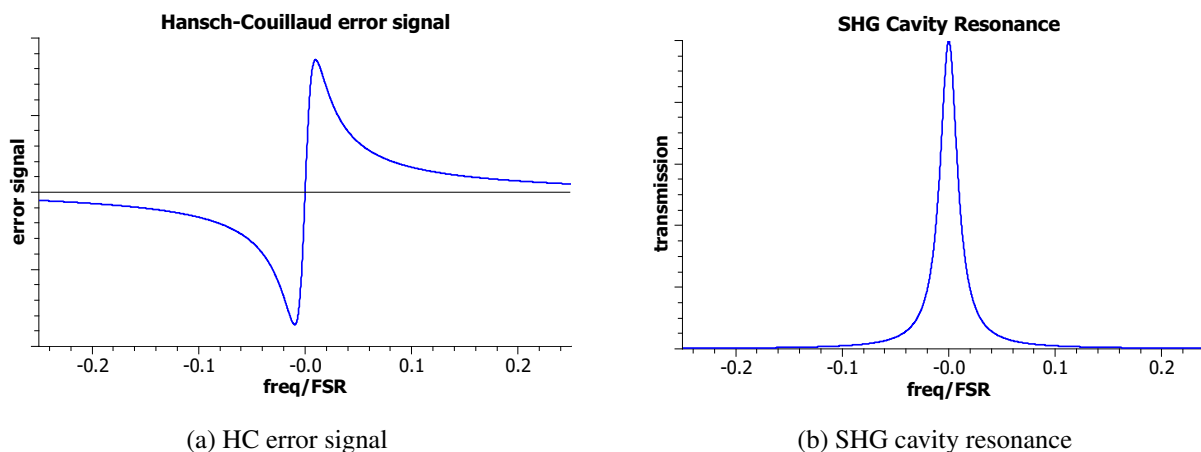


Figure 6.9: Hänsch-Couillaud Locking error signal. Notice the error signal has appreciable magnitude over a capture range much wider than the cavity resonance. In our experimental set-up, the span in this figure is about 150 MHz.

There are a couple mechanical issues concerning the set-up relevant to the electronics and locking for this application. One issue is the mechanical resonance frequency of the piezoelectric transducer-mount-mirror system that is used to control the cavity length. This resonance frequency can be found by scanning the laser frequency and ramping the piezo frequency. At the piezo frequency where there is a sudden increase in range over which the laser is transmitted, one knows the piezo-mirror system is oscillating, and you have found the resonance frequency, which is approximately 420 Hz for our system. This is relevant to the electronics design in that we need to make sure that we are not feeding back to the piezo near its resonance frequency. In circuit terms, we want the gain to roll off much lower than 420 Hz in order to avoid making the cavity resonate. We also want a healthy phase margin at the resonance frequency. We had problems with this initially. We used too much piezo gain and saw the piezo resonate when trying to lock the cavity. We had to add more low-pass filtering as a result. See appendix E for more information about the electronics design.

Another mechanical issue is that the SHG cavity is large and prone to being disturbed by air-currents, temperature fluctuations, etc. As a result, the whole thing is placed inside a plastic box to isolate it a bit from the room; this makes a huge difference. This is the dark red box in figure 6.2.

A final mechanical or at least temperature-related issue we need to consider in the crystal is related to tightly focusing the IR laser. Thus far we have been able to achieve perhaps 500 mW of green power reliably with about 5 W incident IR light. We have seen hints of higher output power and better efficiency, but it is not stable. We think the reason is that the tightly-focused beam changes the optical path length inside the doubling crystal in a dynamic way because the crystal heats up. This becomes more of an issue at higher intensity. This effect is mentioned by Ricciardi[73]. Changing the cavity configuration to a larger beam waist would decrease intensity, but would probably ameliorate the thermal lensing issues and give us better stability, allowing us to operate at higher input power.

### 6.3 Laser Switching and Frequency Shifting

After the SHG cavity we have green light for our experiment but we need to be able to switch it on and off and shift it to get the appropriate hyperfine separations between different beams. This is left indefinite in figure 6.1 as it is liable to be reconfigured. Figure 6.10 shows the current experiment configuration.

The excited state hyperfine ordering is unknown for our system. We have it set up currently so that the repumper operates through the far excited state as the sum of the excited hyperfine splittings will be constant. To put it another way, we can't operate through the adjacent excited state because we are not sure what the hyperfine splitting is, we do not know which it is. We also do not know what transitions are going to be strongest. Hopefully, Rabi flopping measurements would let us ascertain which transitions are strongest and we can then configure our set-up to operate on those. Alternatively, we may be able to model the hole-burning and optical pumping and fit it, shedding light on the hyperfine excited state ordering and transition strengths. Nilsson has a great paper on a technique they used to resolve the excited hyperfine structure in PrYSO [74]. The transition in praseodymium they investigated has very similar qualitative hyperfine structure

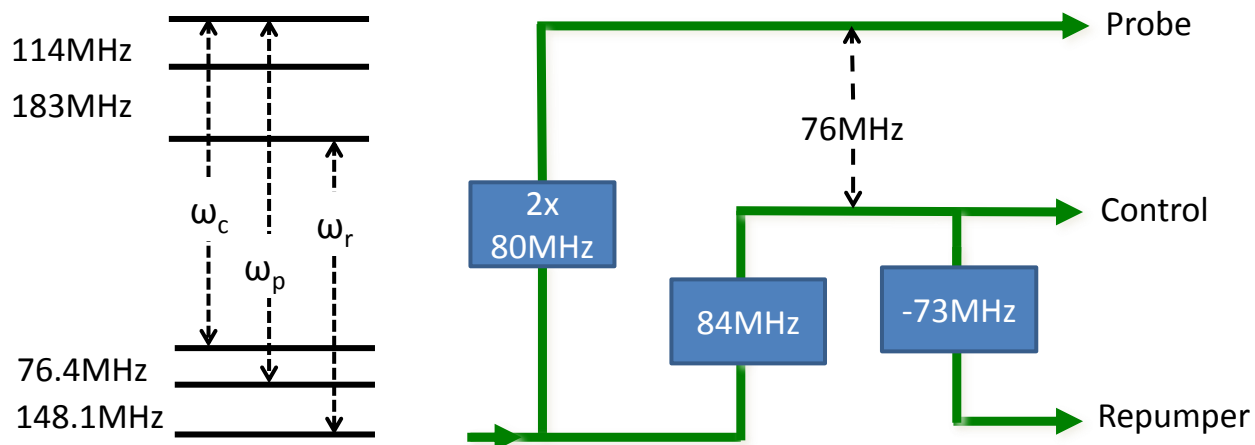


Figure 6.10: AOM set-up to generate experiment beams. The three lasers for the experiment shown on the left:  $\omega_c$ ,  $\omega_p$ , and  $\omega_r$  are generated by the combination of AOMs shown on the right. Note: the excited state hyperfine ordering is unknown. This configuration guarantees that we are resonant with all three ground states, but is not necessarily optimal. Ideally, we would set up to operate our probe and control beams through whatever excited state has the largest matrix element/response, but we do not know which that is yet.

to europium:  $I=5/2$  and so three hyperfine states, although the spacings are smaller. They noticed a factor of 100 difference in oscillator strengths between the strongest and weakest transitions. If Eu were to be similar, that would be a big incentive to determine which transitions is best to operate on.

A technical design point: usually we are shifting one of the beams, the probe, over a frequency range, so we have it set up double-passed so as to prevent changes in pointing with frequency. The AOMs are made of fused silica so can take high visible optical intensity, although they require higher RF drive power ( $\sim 5$  W) compared to the more RF-efficient but optically fragile  $\text{TeO}_2$  AOMs<sup>1</sup>. Currently we are doing everything with 80 MHz AOMs, but we also have a 210 MHz AOM as well that may be useful if we choose to change the repumper configuration.

<sup>1</sup>An interesting side-note regarding AOMs: surplus AOMs (I think originally intended for old argon-ion lasers) have so far served us pretty well for our laser set-up. They are branded as Newport (part no. N35085), which I think was absorbed by NEOS and since by Gooch and Housego. It appears you can get basically the same part new, but these old ones appear to have very large crystals for some reason,  $\sim 1$  cm aperture.

These shifted beams are combined and launched into a fiber to assure that they are well-overlapped and have nice spatial modes. The beams are then sent through our crystal. The crystal is housed in a Janis ST-100 continuous flow cryostat which allows us to get to below 5K. We have a hole in the side of the crystal holder so we can observe fluorescence out the side of the crystal in addition to transmission when investigating hole-burning, etc. The crystal is from Scientific Materials in Montana, 0.1% natural abundance Eu-doped YSO. We have investigated upgrading to single-isotope doping, but it is very expensive and we plan to avoid this modification unless absolutely necessary. The AOMs are run with a delay box driving their switches for precision timing. Having precise temporal control is important when investigating coherent processes. The whole set-up is computer controlled, allowing for control of the AOM protocol from the computer as well as reading the photodiode outputs and even changing the cryostat temperature. In the event one wants to erase any spectral holes, this is a very convenient feature. We will explore experiments we have done so far with this set-up in the next chapter.

## Chapter 7

# Hole-Burning, Optical Pumping and Other Incoherent Effects

### 7.1 Fluorescence Spectroscopy

The first experiment we performed with Eu:YSO was fluorescence spectroscopy. A special thanks to Mike Wood and the Lawler lab for helping us by letting us use their large grating spectrometer. At that point we did not have the cryostat or the rest of our current experimental apparatus, so we chilled the crystal with liquid nitrogen. We also did not have the laser system built so we excited the crystal with a UV LED. See the left panel of figure 7.1 for a cartoon of the experimental set-up.

A high-power LED centered at 365 nm (Mightex LCS-0365-02-38) was used to excite  $\text{Eu}^{3+}$  ions in the crystal. 365 nm ( $\sim 27,400 \text{ cm}^{-1}$ ) is resonant with many excited states. See the right panel of figure 7.1. The crystal was housed in the side of a can filled with LN with a mirror behind it. Fluorescence is collected by a large lens in front of the crystal and focused onto the input slit of the spectrometer. Spectra are produced as multiple overlapping diffraction orders on a two-dimensional CCD image (separated in one dimension by the grating, in the other by a prism). The spectral lines are extracted and stitched together via computer. Mike Wood discusses the instrument here [75].

There are many closely-spaced excited states, see figure 4.2. Since decay between the excited states is much more likely than optical decay out of the excited states, most of the population first relaxes nonradiatively to  ${}^5D_0$ . Almost all the fluorescence is actually from the  ${}^5D_0$  state. The energy gap between the lowest  ${}^5D$  and highest  ${}^7F$  level is quite large, on the order of  $12,000 \text{ cm}^{-1}$ ,

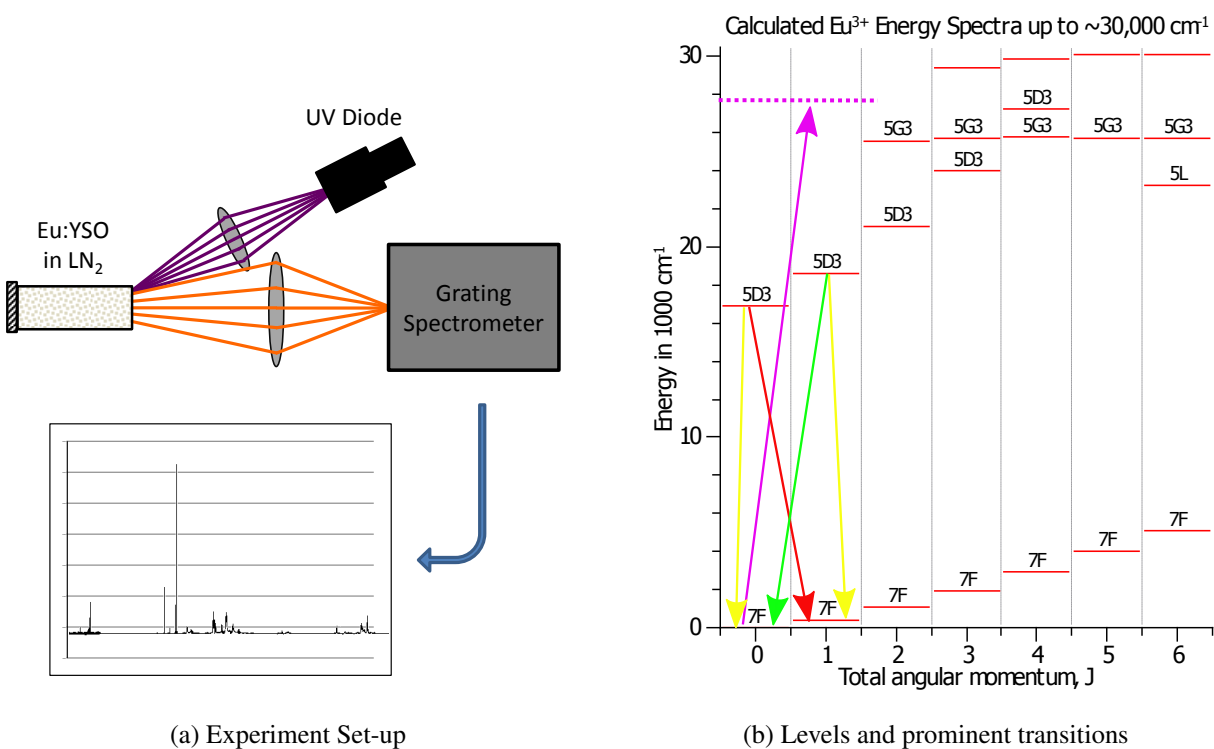


Figure 7.1: Fluorescence Experiment: a) Eu excited by 365 nm UV LED, fluorescence analyzed with grating spectrometer, see experimental spectrum in next figure. b) LED light populates higher-lying states which decays nonradiatively to  $^5D$ . The fluorescence is orange, mostly composed of red and yellow transitions from  $^5D_0$ .

so decay is very unlikely by other than optical means. Even at higher temperatures, decay from  $^5D_0$  is more or less entirely optical.

This was sufficient to see some of the gross structure, and our experimental spectra bears this out. There is also sufficient optical decay from  $^5D_1$  to at least recognize/identify our transition of interest; see figure 7.2. Ideally we would do a fluorescence spectroscopy experiment again but at LHe temperature and with green excitation. This would eliminate any possibility of higher-lying optical lines and should sharpen the features. Also, if we could more precisely measure the spectrum, integrating over all the peaks would let us ascertain the relative strengths of the different

transitions. If we could ascertain the oscillator strengths, we would be able to try fitting for Judd-Ofelt parameters as well, see appendix C. This would be a consequential experimental result, as there is little in the way of published Judd-Ofelt fits for Eu:YSO.

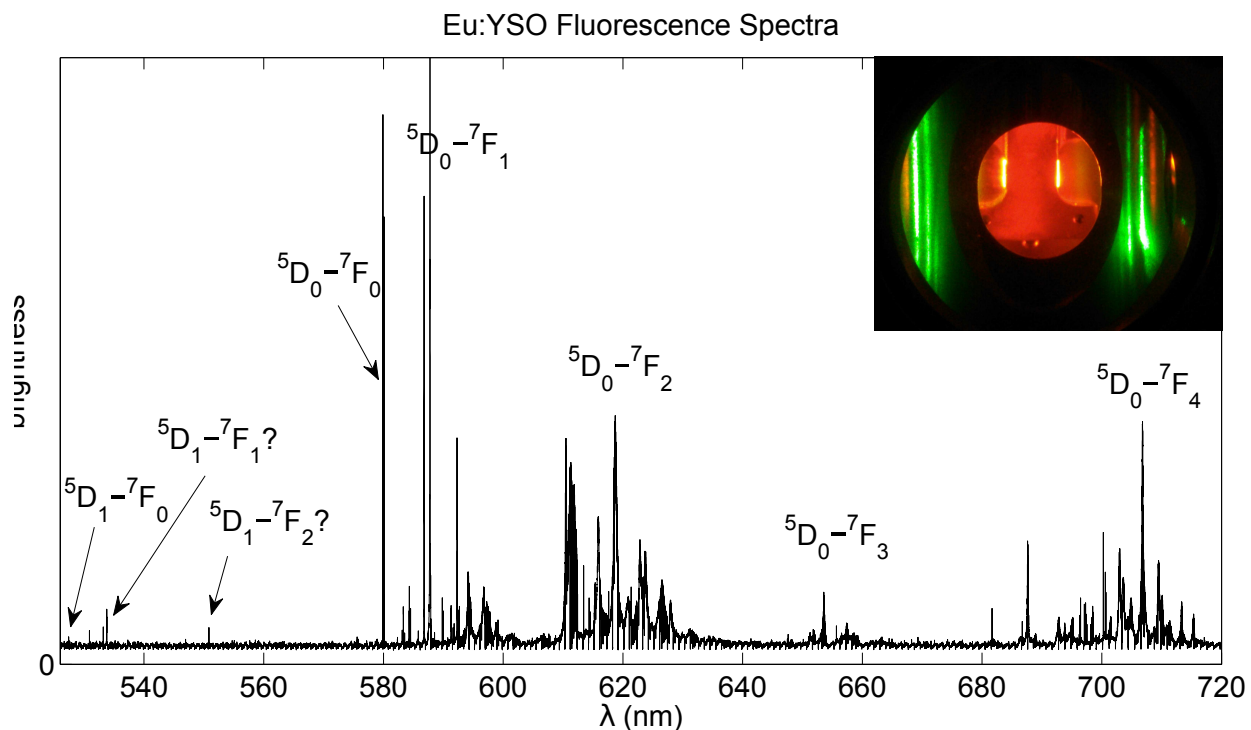


Figure 7.2: Eu:YSO Fluorescence Spectrum: Spectra from Eu:YSO excited by LED at 365 nm, temperature 77K. Prominent groups of lines are noted.  ${}^5D_1$  lines are much weaker than  ${}^5D_0$ , as nonradiative decay from  ${}^5D_1$  is much faster than optical decay out of  ${}^5D_1$ .  ${}^7F$  levels of larger  $J$  have more individual lines ( $2J+1$ ) and are broadened by additional phonon decay to lower-lying  ${}^7F$  levels. The inset shows fluorescence from our later green laser-based experiment in the cryostat. The fluorescence is orange because it is mostly composed of  ${}^5D_0 \rightarrow {}^7F_1$  at about 590 nm,  ${}^5D_0 \rightarrow {}^7F_2$  at about 620 nm, and  ${}^5D_0 \rightarrow {}^7F_0$  at 580 nm.

After working a lot with rubidium at near-IR, the fluorescence from the crystal is very interesting; it appears bright orange. The inset includes an image of the crystal fluorescing in a later cryostat experiment. The green is scatter from our driving laser, the orange is fluorescence from

the crystal. It appears orange as there are significant contributions from the red  ${}^5D_0 \rightarrow {}^7F_2$  transition group, yellow  ${}^5D_0 \rightarrow {}^7F_1$  transition group as well as some yellow from the quantum memory transition:  ${}^5D_0 \rightarrow {}^7F_0$ . Interestingly, the yellow transition is brighter than we would expect based purely on selection rules and Judd-Ofelt theory, implying it is enhanced by some other mechanism.

Additional  ${}^5D_1$  spectral lines are obscured by the stronger  ${}^5D_0$  line groups. Another observation is that the lines to higher lying  ${}^7F$  levels are more complicated because they have more possible  $m_j$ . These lines are also much broader than the lower-lying ones, because they experience more phonon decay. Although it is not an allowed transition ( see figure C.3), there is appreciable fluorescence from the  ${}^5D_0 \rightarrow {}^7F_3$  group. This means that there is some mechanism that is enhancing this transitions, perhaps a higher-order crystal effect.

Next, let us zoom in on our transitions of interest, in the far left corner of the figure 7.2. See figure 7.3. In principle there are 6 spectral lines, one for each  $m_j$  projection and twice that because of the two crystal sites. We are only able to see a few of those lines, but thankfully our line of interest is the brightest (which is why we chose it). It is shown at 527.4 nm. The blue lines on the figure are where we expected the 6 lines to be. There are slight discrepancies  $\sim 0.1$  nm between where we observed the line and where we expected it; that is probably an issue of calibrating the spectrometer; we were using it for visible lines when they normally use it for UV for that configuration. Also, I should mention, the discontinuities in the spectra are artifacts. When diffraction orders overlap, one can be brighter than the other, causing a discontinuity.

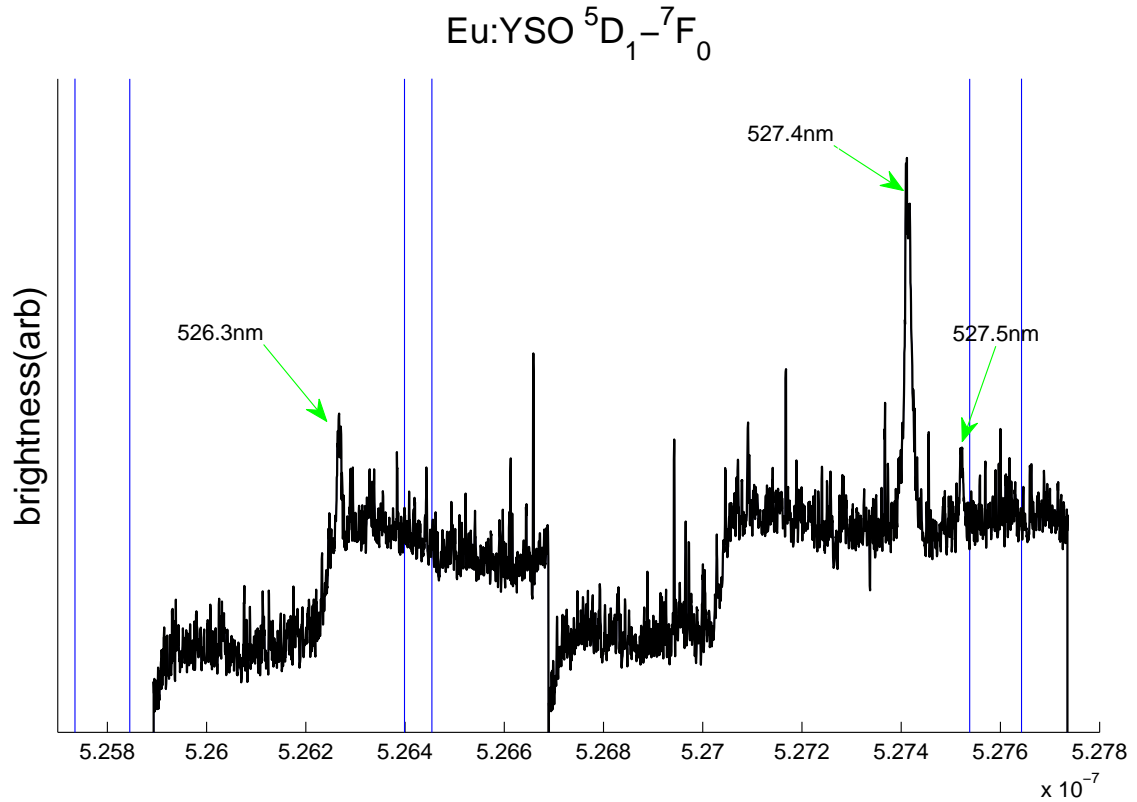


Figure 7.3:  ${}^5D_1 \rightarrow {}^7F_0$  Transition detail. Our line is resolved, with hints of another crystal site and  $m_j$  line. Identifiable spectral features are indicated with arrows. The 6 blue lines indicate where we expect the  ${}^5D_1 - {}^7F_0$  spectral lines.

## 7.2 Inhomogeneous Broadening

This relatively simple experiment was followed by a period where we built the laser system, and acquired a cryostat. The next subject that we wanted to look at was more detailed spectroscopy of our particular resonance. In other words, zooming in on our peak in figure 7.3. We did this by manually scanning our IR laser, keeping the doubling cavity locked to it and recording the transmission through the crystal (now at 5K). This suffers from the problem that the laser can mode-hop while scanning, disrupting the scan. Also, the measurement can be saturated if done with too little power. If the laser is very weak, it will get completely absorbed at the peak of the inhomogeneous broadening where the optical depth is largest, but also completely absorbed in the

vicinity of the peak. This results in a flat region of no transmission and so does not preserve the inhomogeneous broadening shape. Examining our experimental scan, we find it is about 5 GHz wide[76]; it should be a little narrower than that but our measurement exhibits some saturation.

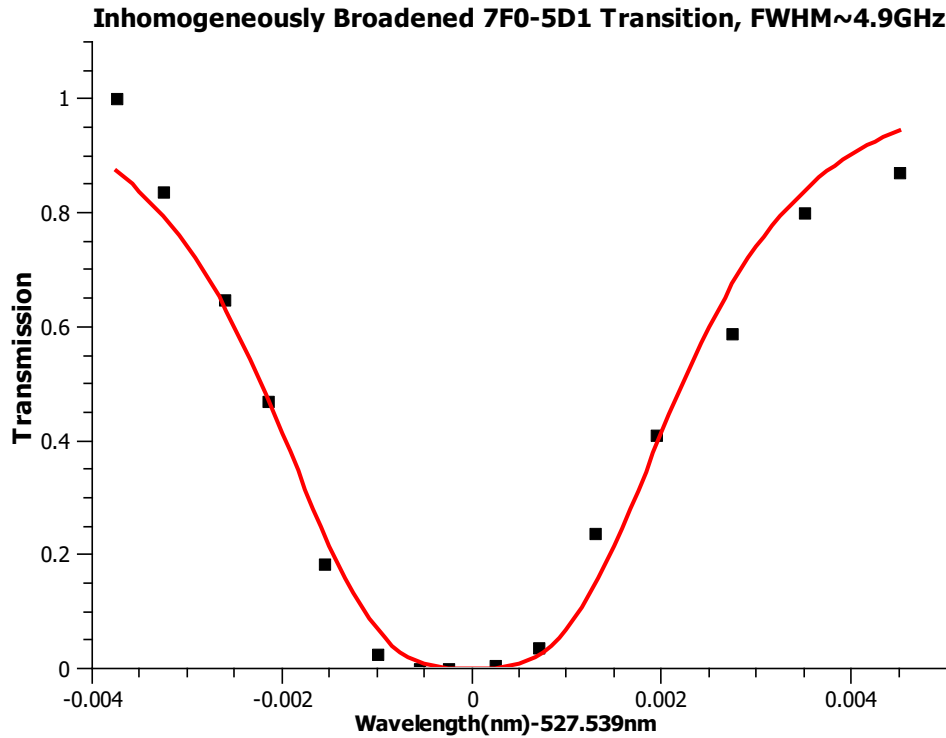


Figure 7.4: Experimental absorption scan of the  ${}^7F_0 - {}^5D_1$  transition. FWHM 5 GHz. Scan has some saturation, actual linewidth should be a little less.

The large inhomogeneous linewidth is an asset for quantum memory experiments, as the ratio of inhomogeneous and homogeneous linewidths  $\Gamma_i/\Gamma_h$  is a figure of merit and gives a sense of how many holes (bits) can be stored in the inhomogeneous broadening. For us, this inhomogeneous broadening is a negative factor, as it decreases our effective density, which goes like  $\Gamma_h/\Gamma_i$ .

Since the inhomogeneous broadening is at about a factor of 10 larger energy scale than the hyperfine structure that we want to make use of in our experiments, the inhomogeneous broadening is the root cause of the need to do ion class distillation, as described in the next section. However, before we do that, I want to mention one potential other method of dealing with the inhomogeneous broadening. Instead of selecting a sub-population from the broadened distribution, it may be

possible to suppress the broadening. The basic idea is that one could use two equal and opposite Stark shifts provided by an additional laser such that if an ion is off-resonance, the Stark shifts tend to push the ion back into resonance. Thinking in terms of a distribution of atoms, this amounts to spectral narrowing. See appendix F for more information; the idea is discussed in this publication [77].

### 7.3 Hyperfine Structure, Hole-Burning Theory, and Ion Class Distillation

So far I have described how we have seen fluorescence and have seen some of the gross fluorescence structure as well as the Stark-splitting of our transition and inhomogeneous broadening (Stark) of that transition as well. Many of these crystal level-shifting issues can be ignored simply because we choose which peak we are going to operate on, *i.e.*, we choose one of the 6 ( $3 m_j \times 2$  crystal sites) lines. We pick the strongest one, the lowest energy  $m_j$  projection in ‘site 2’. We have also measured the nonradiative decay rate for the  ${}^5D_1$  level and the optical decay rate for  ${}^5D_0$ ; this is described in section 5.2.

The hyperfine energy structure lies obscured within the inhomogeneous broadening. This, unfortunately for us, is the atomic structure we want to take advantage of in order to investigate coherent phenomena like: Rabi flopping, EIT, and ultimately index modification schemes that rely on coherent effects. We can operate within this inhomogeneous line by employing spectral hole-burning, specifically a judicious application of hole-burning I will call ion class distillation. This procedure lets us distinguish the hyperfine structure and select from the many simultaneously resonant classes of ions, one class with which to do our experiments. In terms of optical pumping, we will burn a spectral trough and then pump only the class of ions that we choose back into the trough. Figure 7.5 shows a cartoon representation of the result of ion class distillation. A spectral trough is burned all the way through the crystal and is repopulated with only one class of ions; they are responsible for the small feature in the center of the trough. Understanding this procedure motivates much of the material investigated in this chapter.

First, let us look at a figure of the hyperfine structure for  ${}^{153}\text{Eu}$ . See figure 7.6. What we know about this can be found in, for example [39, 51]. As we can see, the hyperfine structure is similar

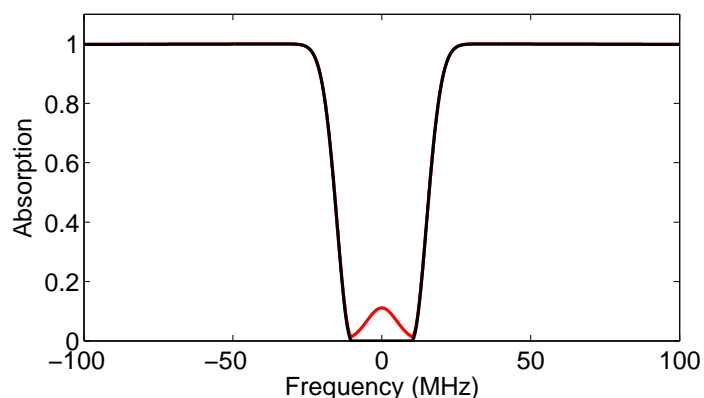


Figure 7.5: Ion Class Distillation Cartoon. A spectral trough is burned through the inhomogeneous broadening (black line) and repopulated with one class of ions (red bump).

in scale to what we might see in other more common AMO systems like Rb. The spacings are on the order of hundreds of MHz, accessible via AOMs. We will note that the states are actually the projection of I, not F as we are accustomed when looking at hyperfine structure. This is because the energy scales of J and I are so disparate in the crystal: ions of different  $m_j$  differ by 10s of  $\text{cm}^{-1}$  while different  $m_i$  differ by only 100s of MHz ( $0.003 \text{ cm}^{-1}$ ). We will also note that there is a parallel structure for the other isotope in our crystal,  $^{151}\text{Eu}$ , where the spacings are significantly different (about half as large). We will discuss the implications of this further below.

The main challenge regarding the hyperfine structure is that the inhomogeneously-broadened line is really composed of many homogeneous lines with different Stark shifts. As a result, at a particular frequency in the overall inhomogeneous distribution, there are actually different transitions (between hyperfine states) that are on-resonance, different classes of ions Stark-shifted by different amounts. This is a significant problem for us as we want to operate on a single class of ions at a time, otherwise we may be driving different channels with different matrix elements at the same time. Not to mention that there would be, for example, problems like absorption attributed to other classes of ions that would also make things more difficult to understand. This would make it more challenging to understand the behavior of the system if we have an average response of multiple classes instead of the response of a single class.

## EIT Scheme

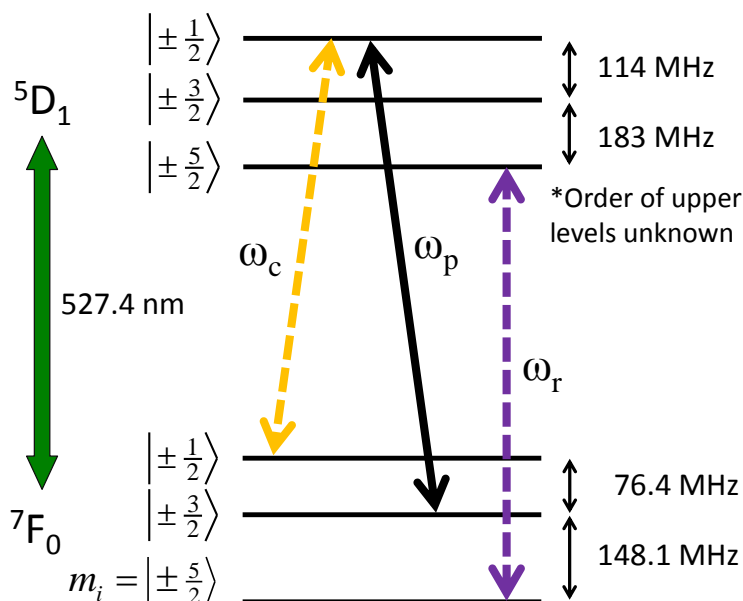


Figure 7.6:  ${}^7F_0 - {}^5D_1$  transition hyperfine structure (strongest  $m_j$ , strongest site: ‘site 2’).  $\omega_p$  is the probe laser,  $\omega_c$  the control laser, and  $\omega_r$  the repumper laser. Note: excited level ordering is unknown.

In order to operate on a single class at a time, we need to employ optical pumping/hole-burning in such a way as to only select one class. An additional complication is that we do not know the order of the hyperfine excited states.

Figure 7.7 is an attempt to clarify this. I will explain first from the perspective of optical pumping and then discuss hole-burning. The top shows the inhomogeneous line. If we were to park the laser in the middle of that lineshape, we would find that there are nine different classes of Eu ions that are resonant, depicted by the green arrows connecting the nine different combinations. If we look at one particular transition and see how that changes for each class, we see that they span about 500 MHz; this is drawn on top of the inhomogeneous distribution. Since this is smaller than the inhomogeneous broadening, we are confident that different classes are similarly populated at the middle of the inhomogeneous feature.

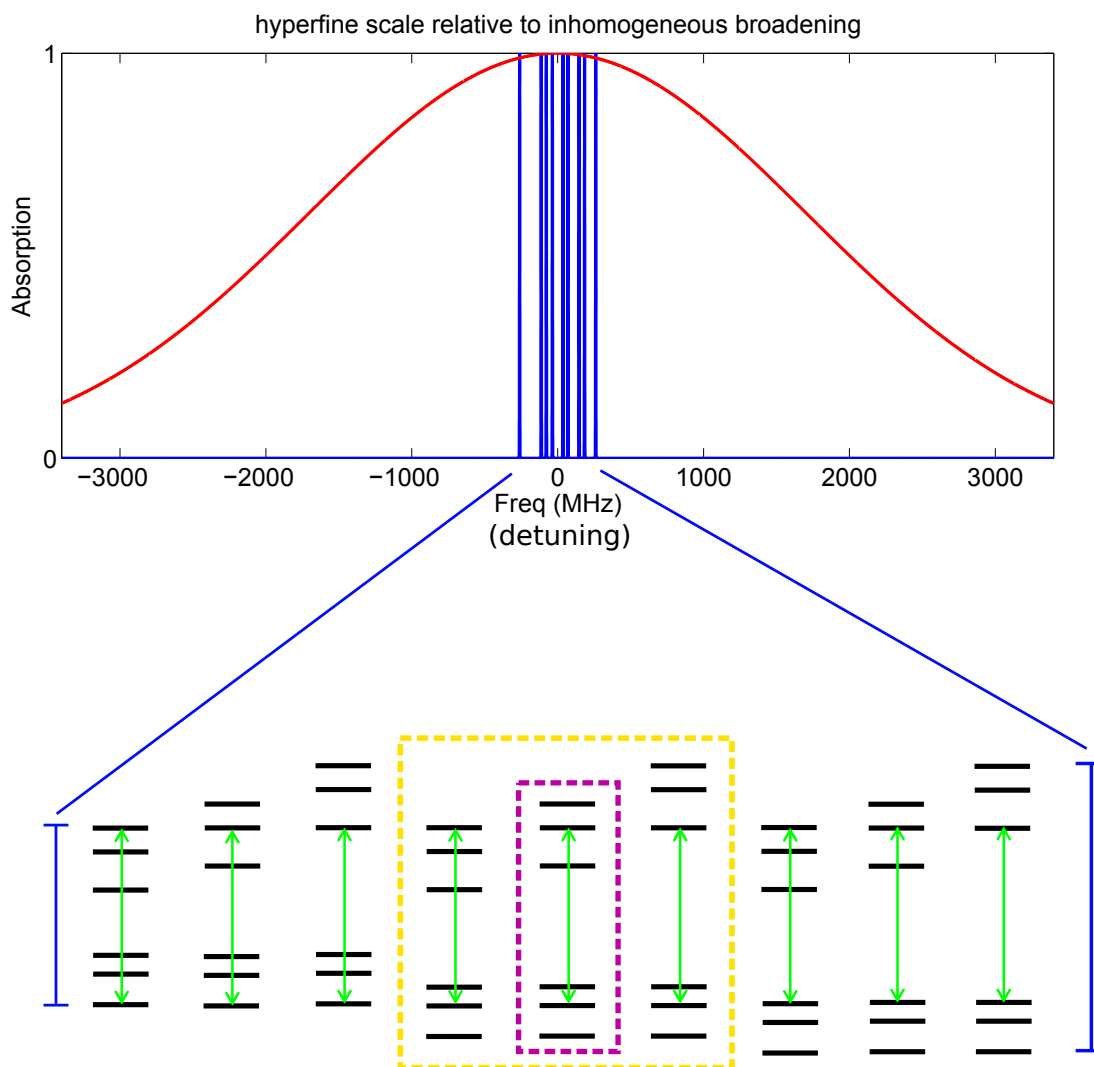


Figure 7.7: Spectral Class Distillation: Since the hyperfine spacing is less than inhomogeneous linewidth, multiple transitions are resonant with the probe simultaneously. The control beam connects to a different ground state, but still can connect through all 3 excited levels; in other words it is resonant with the three classes in the orange box. The repumper connects through a different ground state *and* different excited state so is only resonant with one class of the 9 the probe is resonant with. This is indicated by the purple box.

From the perspective of optical pumping, the control beam, given by the orange dashed arrow in 7.6 will be resonant with classes of ions that have the correct hyperfine ground state structure. These are shown by the orange box in figure 7.7. However, that still leaves three different possible excited states, three classes. The repumper, depicted by the purple dashed line in figure 7.6, connects to the other hyperfine ground state. This is necessary as we do not want population to be lost to that state. It also connects to a different excited state than our EIT beams, this is because we do not want it to interfere with any coherent processes, should we want to have it on at the same time. We also choose it to go through the excited state furthest from the probe and control excited state. This is because, since we do not know the ordering of the excited states, we want to be sure that it connects, *i.e.*, the sum of the excited state splittings is independent of order. Now this may not be an ideal configuration because we may be operating on a channel that has a weaker matrix element. However, until we are able to discern the order, at least we know that this channel exists. We may want to change this in the future. The repumper beam is only resonant for one particular class of ions, indicated by the purple dashed box in figure 7.7. Thinking in terms of optical pumping, were we to leave these three beams on, eventually the only class that would be interacting with our lasers would be the class in the purple box. All the other classes would be pumped to a hyperfine state that connects to no laser to pump it back. By controlling the relative power or timing on the three beams we can pump to a particular hyperfine ground state for that one particular class, select that class. This is what I mean by ion class distillation.

Another way to think about this is from the perspective of spectral hole-burning. When we talk about hole-burning we are interested in where the population is removed from the inhomogeneous broadening and where it goes in the inhomogeneous broadening as a result of the application of our laser. We are interested in the resulting shape as a function of frequency of the overall absorption (or transmission) and the changes in that structure due to our applying a laser. Thinking in terms of hole-burning allows us to investigate whether we can put the class that we want, and only that one, back into a wide spectral trough burned into the crystal. This is a little more difficult to digest as when we start accounting for all the spectral holes and anti-holes, the spectra get very complicated. But now that we have discussed the optical pumping perspective, let us talk about hole-burning.

So what happens when we park the laser in the inhomogeneous linewidth, *i.e.*, burn a hole? Let us examine a cartoon system with two ground and two excited states first in order to understand the concepts before presenting results for our system with 3 excited and 3 ground states. This discussion will follow a diagram by Nilsson [74].

As shown in figure 7.8, two excited states and two ground states entails four simultaneous resonant levels, provided the inhomogeneous broadening is substantially larger than the ground level structure and excited level structure. The central hole at zero frequency (1) is deepest because this corresponds to all four classes. Adjacent to the central hole are two side-holes (2) separated from the central hole by the excited state splitting. These two side-holes each correspond to two classes: a) and c) for one side-hole, b) and d) for the other. Since they do not correspond to all classes they are shallower. Hole burning pumps the population to the other ground state. This is reflected as an excess, enhanced absorption. These excesses or anti-holes are located a factor of the ground state splitting away from the central hole, e.g. (3). These features also only correspond to two classes each, a) and b) for the one, c) and d) for the other. Finally there are also side anti-holes. These correspond to one class each, for example (4) would correspond to a), so they are the smallest features.

Hopefully this clarifies how hole-burning spectra are manifested and gives the reader an idea how we can extend this picture to our more complicated system. In our case there are side-holes at the sum of the excited state splittings, as well as anti-holes at the sum of the ground state splittings, not to mention additional side anti-holes at all the combinations. Our spectra is also complicated by the fact that we have two overlapping spectra due to the two isotopes present. If we plot what this will look like for our system, taking into account the homogeneous linewidth we have observed so far on the order of 1 MHz, we see the following as shown in figure 7.9. The solid blue is the hole-burning spectrum from  $^{153}\text{Eu}$  and the dashed red is the spectrum from the  $^{151}\text{Eu}$ . As you can see, the structure is rich.

Now this hole-burning discussion gets at an issue not captured by the optical pumping discussion. When you pump population back, it is possible that in addition to the population that you want (and depending on the width of the holes or laser) there may be additional anti-holes from

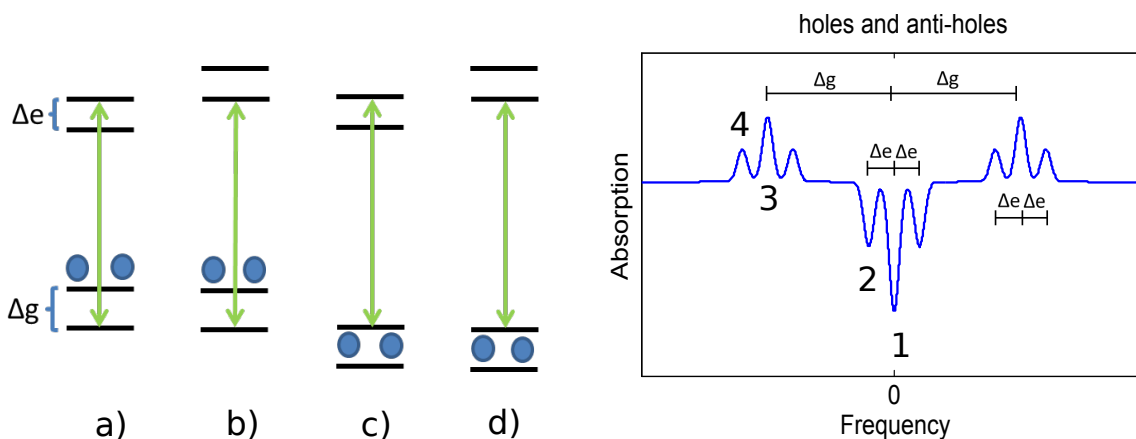


Figure 7.8: Hole-burning Cartoon: Main hole corresponds to all 4 classes of ions. Side holes  $\Delta e$  away are half the depth because they only correspond to 2 classes. Antiholes are  $\Delta g$  away and correspond to 2 classes each. There are also side anti-holes that correspond to a single class and as a result are smaller than anti-holes. Similar figure in[74].

unfortunate combinations that happen to be at about the same place in frequency (some places may be inadvertently pumped to). This is doubly likely as we have a whole other isotope to consider.

Figure 7.9 shows an approximation of the hole-burning spectrum that results from one laser interacting with the inhomogeneous distribution for our system. Note: all matrix elements are assumed to be of the same strength.

This gross hole-burning spectrum is interesting and gives you a sense of the complexity, but let us zoom in on a few parts to examine some of the consequences. One consequence is that there are anti-holes much closer to zero frequency detuning than we might initially suspect. As a result, this sets the maximum width of a spectral trough that you are able to burn by sweeping the hole-burning laser before you encounter an anti-hole and start pumping some population back into the other side of the pit. Figure 7.10 shows the hole-burning spectrum around zero detuning. As you can see, there are some small anti-holes within 15 MHz of zero. As a result, if one were to burn a trough 15 MHz wide, you start putting some population *back* once it exceeds that width.

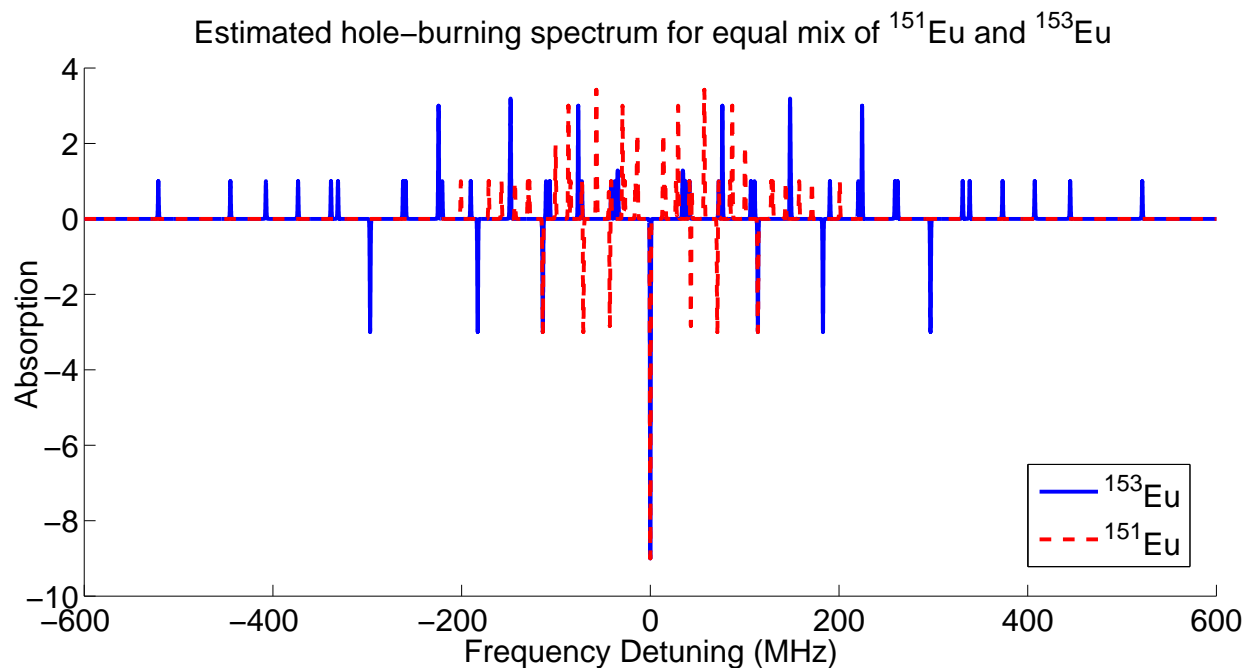


Figure 7.9: Simulated holeburning spectrum for combination of  $^{151}\text{Eu}$  and  $^{153}\text{Eu}$ . Feature linewidths set at 1 MHz. Combination of spectra from both ions causes rich structure/complications.

Another interesting hole-burning issue is not reflected in this gross spectrum but happens when we apply the control and repump lasers for spectral distillation. It so happens that the frequency of the repumper laser as related to the probe is:  $\omega_r = \omega_p - \Delta_{Ex1} - \Delta_{Ex2} + \Delta_{Gnd1} = \omega_p - 114 - 183 + 148.1 = \omega_p - 148.9$  MHz. Unfortunately one of the ground state splittings is 148.1 MHz. As a result, when we turn on the repumper we can put population back into the center of our trough, but we are liable to also put population (potentially more) at the location of the anti-hole less than 1 MHz away from the center, see figure 7.11.

This figure is generated assuming 500 kHz spectral hole widths; this is narrower than we have observed thus far but makes it easier to identify the different contributions. There is the red curve: this is the control beam pumping back into the hole, a control beam anti-hole. There is the short blue feature directly beneath it: this is the repumper pumping back into the hole as well. It is weaker as this is a side-antihole rather than one of the main antiholes for the repumper. Right

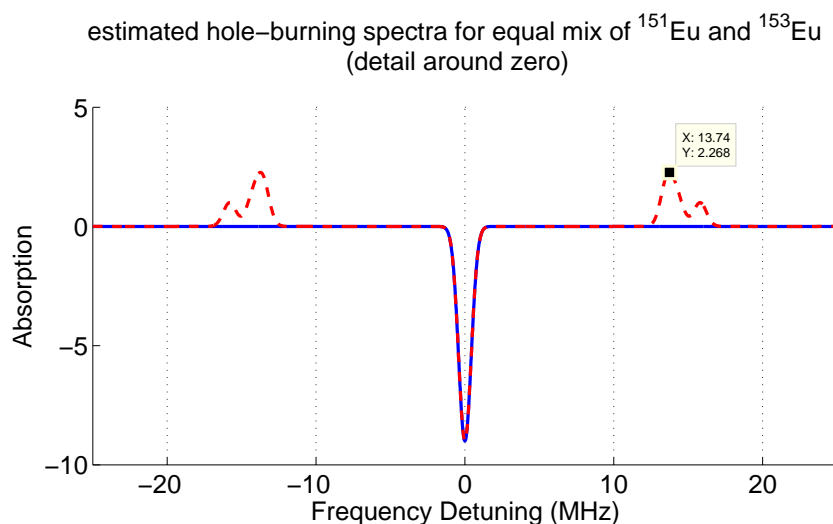


Figure 7.10: Hole-burning spectrum detail around zero frequency detuning. Anti-holes within 15 MHz means that when sweeping a spectral trough, if the sweep is larger than that, some population will be pumped back to the other side of the trough.

next to it is the large blue feature: this is the repumper anti-hole at 148.1 MHz mentioned above. Notice that fortuitously there are no  $^{151}\text{Eu}$  peaks right on top of our desired features that we have burned back into the center of the trough. The closest appears to be about 4 MHz away. This additional anti-hole structure complicates the outlook for class distillation as a strong laser may lead to populating other anti-holes that happen to be at similar frequencies. These issues may be responsible for some interesting experimental behavior we have seen thus far that will be relayed in the next section.

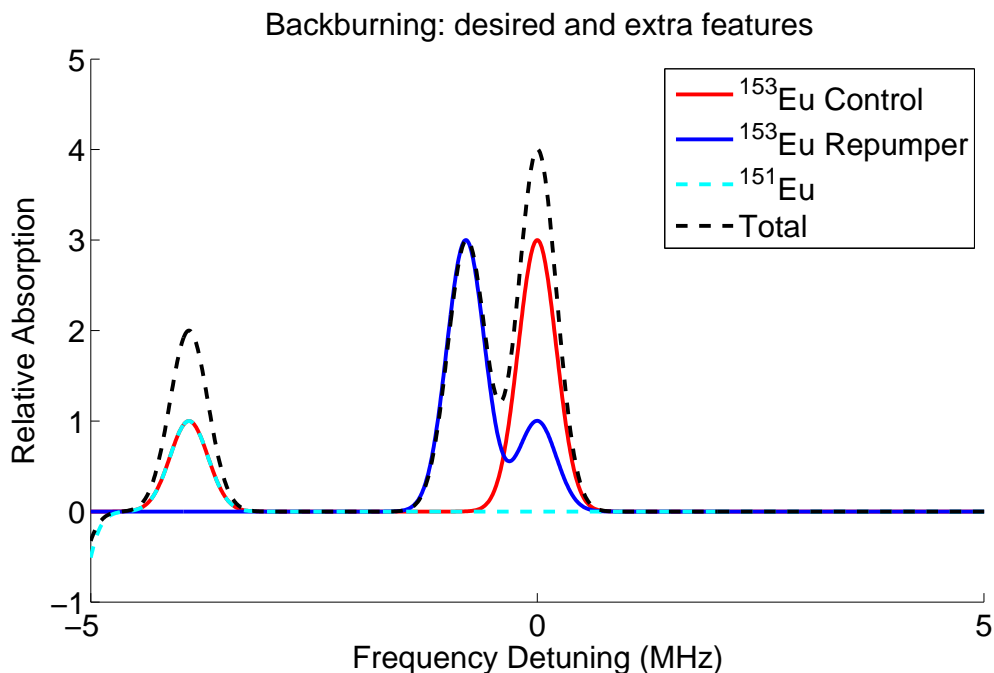


Figure 7.11: Features from control and repumper: If we apply our control and repumper lasers, we will pump  $^{153}\text{Eu}$  population back to the center of the spectral trough, but also to an additional feature about 1 MHz from the center. Thankfully, there are no predicted  $^{151}\text{Eu}$  features in the center.

#### 7.4 Hole Burning Experiment

Thus far we have been unable to resolve hole-burning spectra on top of the inhomogeneous linewidth at the same time. This is a technical issue in that we need to smoothly tune the laser and keep the doubling set-up locked over the whole inhomogeneous line ( $\sim$ few GHz), which has proven elusive. We are working on a laser upgrade to address this issue.

As a result, the hole-burning features that we have seen are only for a single hole/small frequency sweeps, (1) in figure 7.8. We have not been able to see any anti-holes, for example. Figure 7.12 shows a single spectral hole. We have seen narrower spectral holes, less than 1 MHz wide, but not significantly narrower. We are puzzled why the hole is not much narrower; naively we would

expect the hole to be at best twice the experimental laser linewidth or twice the homogeneous linewidth, whichever is wider.

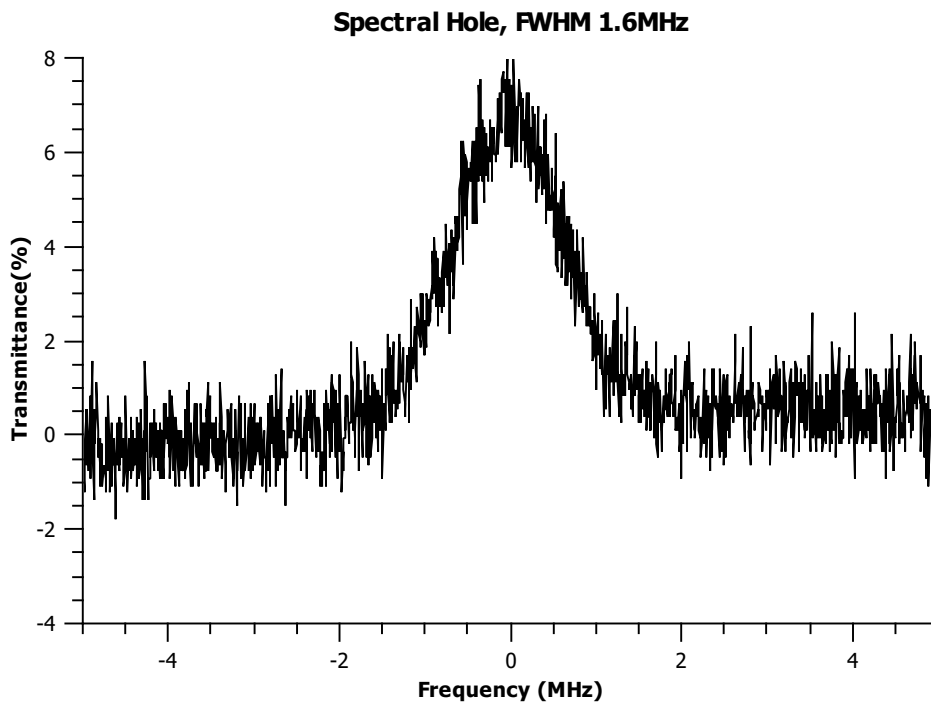


Figure 7.12: A single narrow spectral hole burned in the  ${}^7F_0 - {}^5D_1$  inhomogeneous feature.

Note: this and subsequent scans are centered about the middle of the inhomogeneous broadening, which we set as zero to more easily appreciate the widths of spectral features. This and the following figures have been normalized to have the same transmittance. If the traces look suspiciously the same depth, this is because they have been scaled this way rather than having an arbitrary vertical axis. This is not intended to be misleading but more to be representative, *i.e.*, for the first scans in this set of data, about 8% of the laser made it through the crystal. The others are assumed to be similar and are normalized similarly. This was burned at relatively low power, about  $1 \mu W$ . These experimental conditions are not close to burning all the way through the crystal, there is still significant absorption if only 8% of the laser makes it through.

That is not to say we can't burn all the way through the crystal. Turning up the power to a couple mW, we can burn a hole such that we get negligible absorption in the center of the spectral

hole. This is reassuring as there is not some sub-class of ions that relax more quickly and refuse to be optically pumped or something to that effect. If that were the case, that would present a problem for future experiments.

Figure 7.13 shows a spectral trough, that is, we can intentionally burn a feature wider than a single hole by sweeping the frequency of the laser used to burn the feature. This is interesting/useful, as we plan to burn a trough and then pump population corresponding to the class we want to use for our experiments back into the center of it. Note: there are limitations on the possible width; see the discussion around figure 7.10.

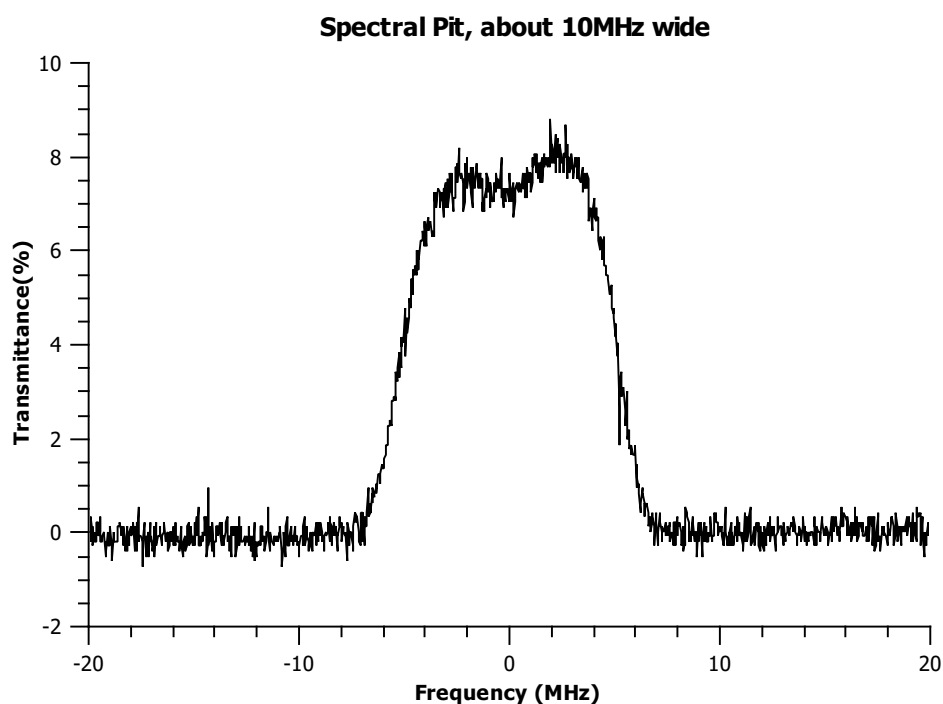


Figure 7.13: Spectral trough/pit created by sweeping hole-burning laser. Class distillation requires burning a trough all the way through the crystal and refilling with only the class of ions we want to do our experiments with.

We can also create more than one spectral feature at a time. This hints at the quantum memory application; imagine storing information in series of spectral holes burned in the crystal. Figure 7.14 shows a scan with three spectral holes.

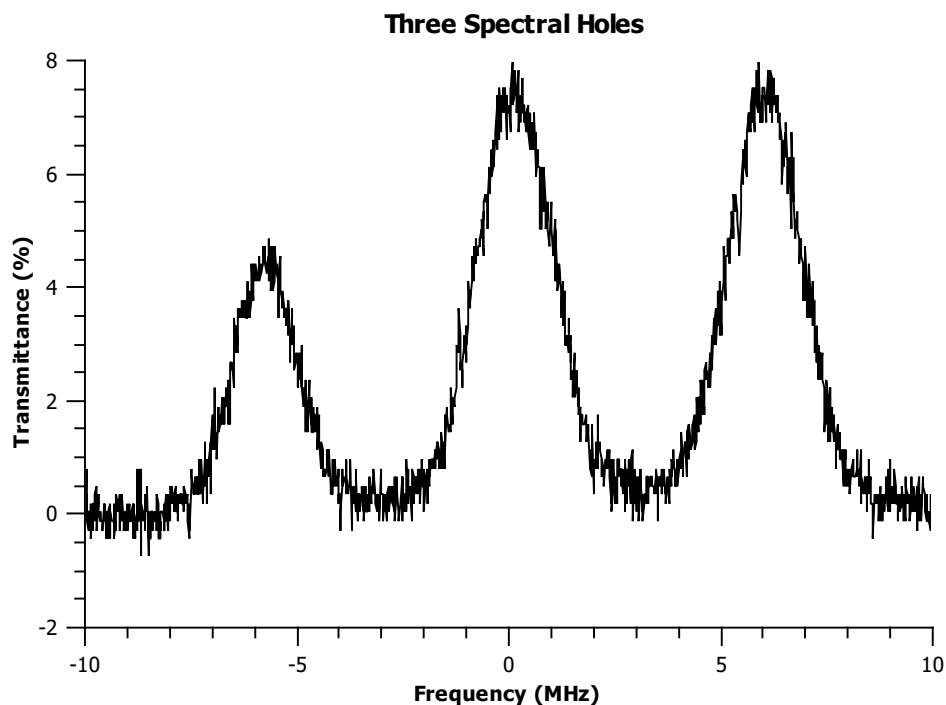


Figure 7.14: Three spectral holes burned in the inhomogeneous line.

We are also starting to be able to put population back into a trough. This gets at why we are doing this, to select a class of Eu ions to work with. This is sort of the first step to this spectral distillation process, burn everything away and put back what you want to work with. Figure 7.15 shows some pumping back on a shallow hole.

In figure 7.15 we take a spectral trough, and by turning on two lasers spaced by the appropriate hyperfine splitting, we can put population back into the hole. This is what we see when turning on the control and repumper lasers. Both lasers have an effect. The black trace is the spectral trough and the red trace is the pit with some population put back into the hole. The large dip on the left of center may be due to additional pumping by the repumper laser as discussed above; see figure 7.11. The feature locations do not match up exactly on center as the AOM frequencies were not chosen exactly on center. Additionally, the excited state hyperfine splittings are not known to high precision, so there may be some discrepancy there. As far as depth, we according to predictions, we would assume the center feature would be deepest, but this is not the case and we do not know

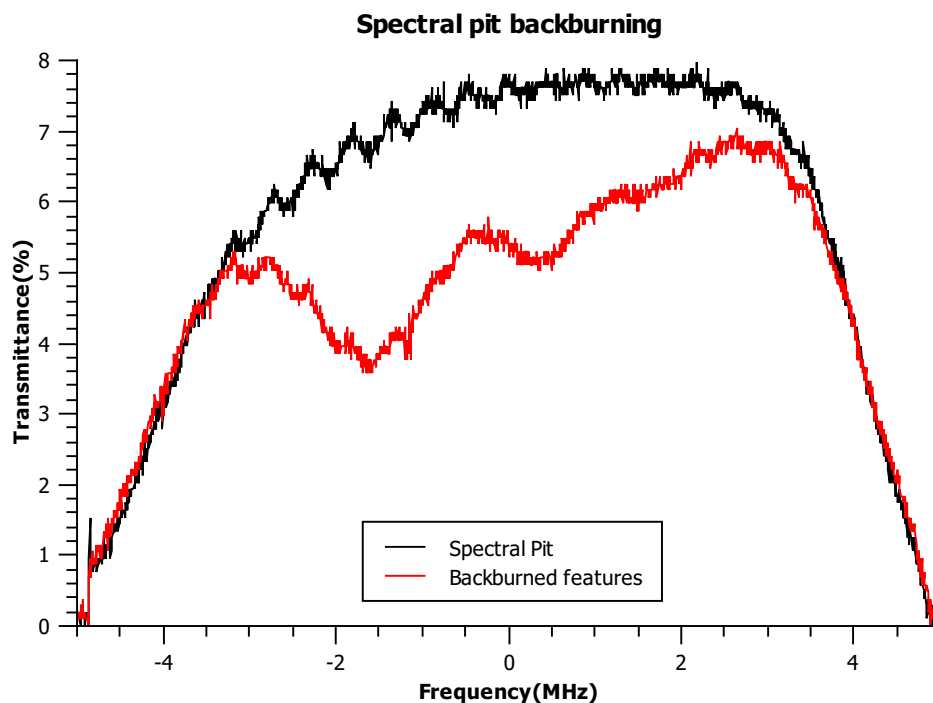


Figure 7.15: We can also pump population back into a spectral trough. This is an important operations for our future experiments. The black trace is a spectral trough. The red trace is the spectral trough after turning on the control and repumper lasers. Some population is pumped back into the spectral trough. The large off-center feature may be due to an additional anti-hole as discussed in figure 7.11.

why. Hopefully as we improve our hole-burning procedure, we will be able to generate narrower features and more accurately identify which features in the hole-burning spectrum correspond to which hyperfine energy splittings.

## 7.5 Hole-burning Width

One issue we need to understand before it is likely that we will see success with coherent processes is the width of spectral features that we can burn in the crystal. We have been unable to see very narrow features. Minimum feature size we would expect to see is holes at twice the homogeneous linewidth[78]; we have not seen anything near that small yet.

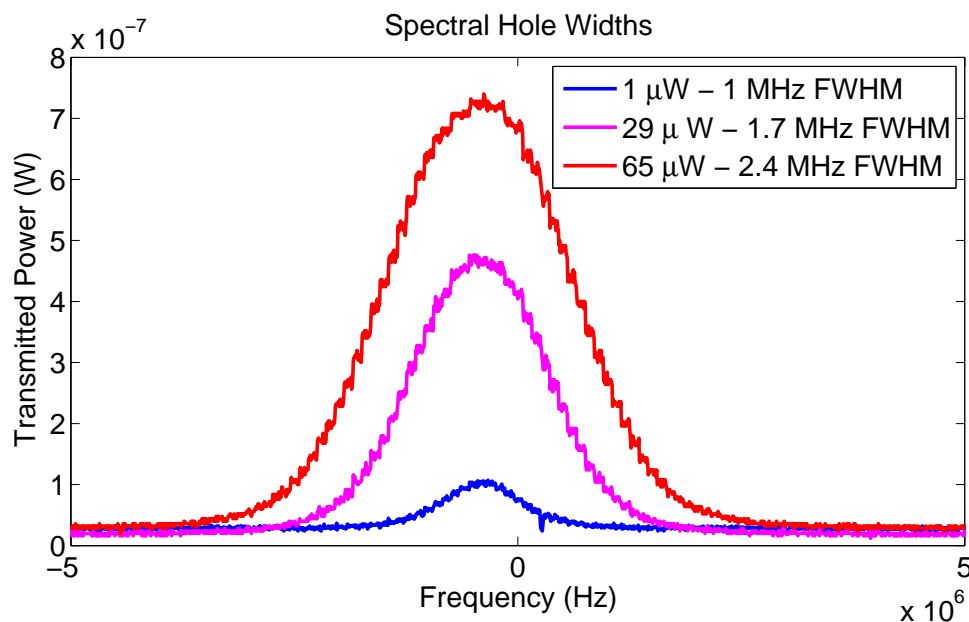


Figure 7.16: Experimental hole-burning widths as a function of burning intensity. Holes get deeper and wider with increasing intensity.

Part of this appears to be due to saturation. If we are saturating, we expect features to get broader with increasing intensity. This is what we observe in figure 7.16. Notice the hole depths change with intensity as well, which is another issue we need to consider. If we plot the spectral hole widths as a function of hole-burning intensity we see an increase, as shown in figure 7.17. This is reasonable as we expect a square root functional dependence with intensity, see Seigman Ch 30 [78].

It is possible we will be able to improve this somewhat with a thinner crystal, but I think a model of the optical pumping process that incorporates the volume of the crystal would be very useful to help understand these effects. Better understanding the hole-burning processes will no doubt help when we transition to looking for coherent processes, as discussed (theoretically) in the next chapter.

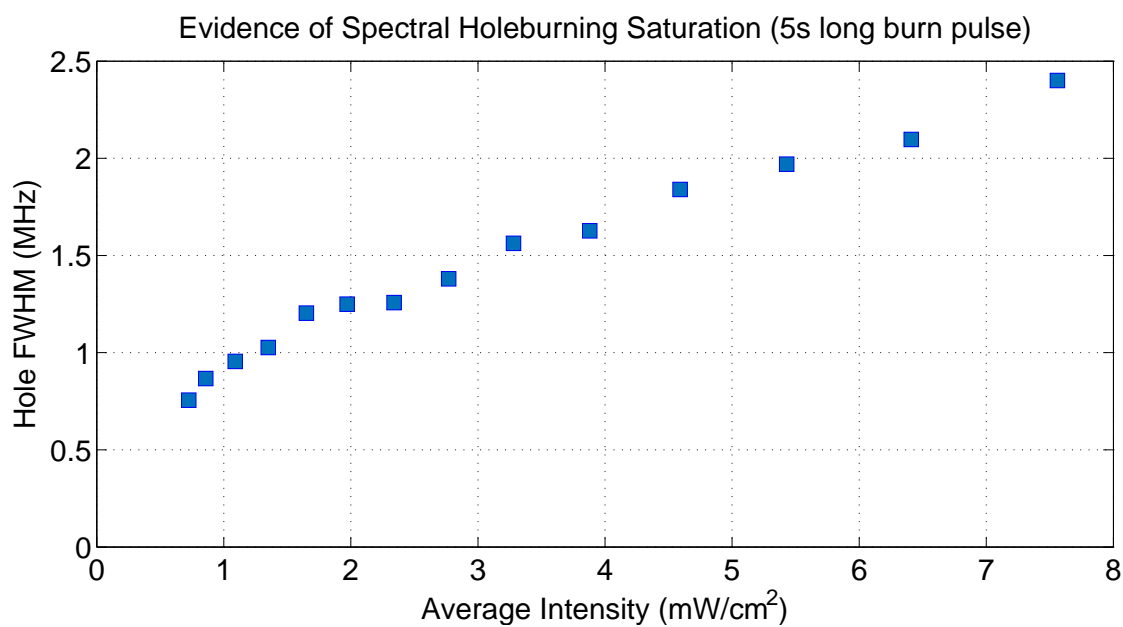


Figure 7.17: Hole-burning widths with intensity: Holes get wider with increasing intensity in the intensity range where we would like to operate, indicating we are saturating features burned in the crystal.

## Chapter 8

### Coherent Effects

This chapter delves into more complicated, coherent atomic effects that we hope to see in our rare-earth doped crystal system. There are a couple obstacles to this so far. Probably the main issue that has thwarted us is that our spectral holes are a lot broader than we would like. Until we get that issue figured out, it seems unlikely we will see strong coherent effects, as it is like we are working with a lot less laser power than we think we are. We also are not certain of matrix element strengths, or what the hyperfine excited state structure looks like exactly. Hopefully, more sophisticated modeling of the hole-burning and Rabi-flopping experiments will allow us to nail down the excited state hyperfine structure and accurately measure the matrix elements.

#### 8.1 6-level System Hamiltonian

Before jumping into results, I want to discuss the Hamiltonian for the system. This material is a direct extension of section 2.2, except instead of the 3-level electric dipole system, we are looking at a 6-level system with magnetic dipole interactions. There are a lot of similarities and a few important differences. To start, let me re-present our level scheme in figure 8.1.

As discussed earlier, we are operating on the magnetic dipole transition  ${}^7F_0 - {}^5D_1$  at approximately 527 nm. The beams that we use to form our lambda scheme for EIT, are the probe and control,  $\omega_p$  and  $\omega_c$ , respectively, that connect ground states  $|2\rangle$  and  $|3\rangle$  to the excited state  $|6\rangle$ . There is also a re-pumper beam that connects the remaining ground state,  $|3\rangle$ , through a different excited state,  $|5\rangle$ . This beam is essential to the class distillation process as discussed in the last chapter. Additionally, there is an excited state that is not connected to the system by a laser. Initially the

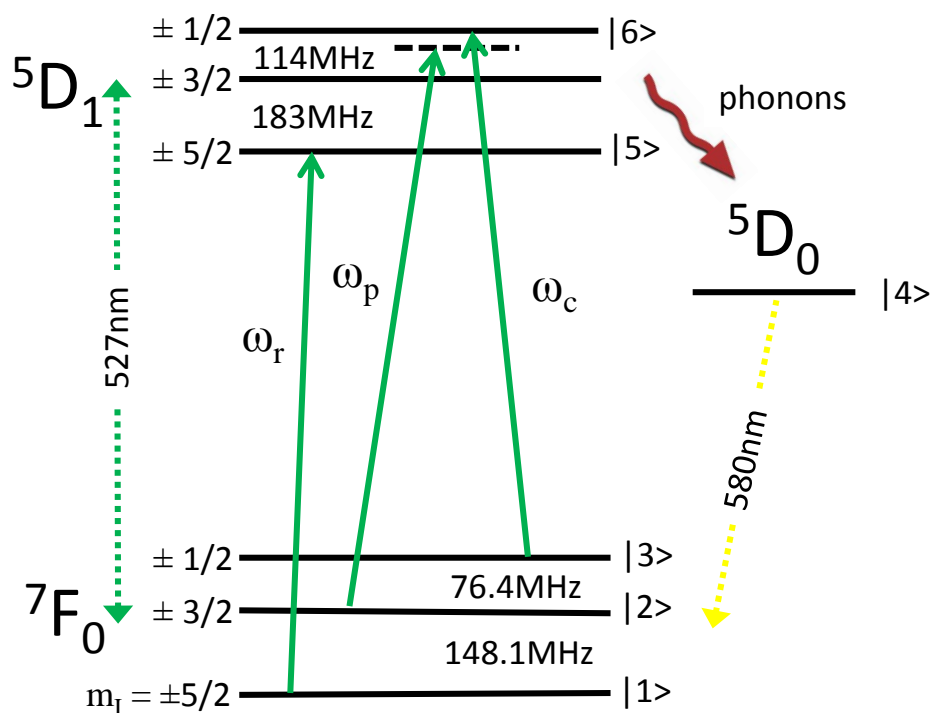


Figure 8.1:  $^{153}\text{Eu}:\text{YSO}$  hyperfine structure (site 2) with EIT scheme and decays.

simulation incorporated that level but was later modified to include the  $^5D_0$  level instead, as it is much more important to the behavior of the system. Population reaches  $^5D_0$  via multiphonon decay from  $^5D_1$  as discussed in chapter 5, from there it decays optically to the ground manifold and ultimately  $^7F_0$ .

One of the differences with these Eu:YSO experiments compared to our previous work is that we are working with an optical magnetic dipole transition rather than an electric dipole transition. This is challenging as these transitions are quite weak, but also pretty interesting because there has not been a lot of experiments with them. In fact, only earlier this year has there been experimental confirmation of an optical magnetic dipole transition due *solely* to the magnetic field of the driving laser[79]. The experiment was done on our transition in Eu incidentally, although they used a different host system.

In terms of the math, the electric dipole and magnetic dipole interactions are of the same form.

$$H_{E1} = -\hat{d} \cdot \vec{E} = -e\vec{r} \cdot \vec{E} \quad (8.1)$$

vs.

$$H_{M1} = -\hat{\mu} \cdot \vec{B} \quad (8.2)$$

However, the electric dipole operator is odd, so only matrix elements between states of different parity will be non-zero; this is the electric dipole selection rule. The magnetic dipole interaction on the other hand is even, and so will connect states of the same parity. This is the magnetic dipole selection rule. Normally when we think of this, we think in the LS coupling scheme where parity is  $(-1)^L$ . For both E1 and M1 transitions, spin should not change. We know our transition is magnetic because it is within the  $4F^6$ ; it is not a transition to a shell of different parity. Notice, however, that if one examines the terms involved in our transition  ${}^7F_0 \rightarrow {}^5D_1$ , both L and S are changing by one so this seems like it should not be allowed on account of parity and spin. It turns out this is another example of the consequences of working with a heavy atom that is in the intermediate coupling regime. In intermediate coupling these selection rules are relaxed. In any case, it is convenient to parameterize the strength of these interactions using the Rabi frequency. For electric dipole interactions:

$$\Omega_{E1} = \frac{\mu_{E1}E}{\hbar} \quad (8.3)$$

Where  $\mu_{E1}$  are the matrix elements of the electric dipole operator between ground and excited states. The situation is very similar for magnetic interactions:

$$\Omega_{M1} = \frac{\mu_{M1}B}{\hbar} \quad (8.4)$$

Considering  $B = E/c$ , we can put the magnetic dipole matrix elements in terms of an effective electric dipole matrix element to compare their strengths, *i.e.*,  $\mu_{E1_{eff}} = \mu_{M1}/c$ . This is useful as it allows us to compare the strengths of electric and magnetic interactions in terms of say the same laser intensity (electric field).

We can get a feeling for the relative strengths of these interactions by comparing them in atomic units. The atomic unit for magnetic dipole moment is the Bohr magneton:  $\frac{e\hbar}{2m_e}$ . The atomic electric dipole moment is  $ea_0$ . Comparing and minding the factor of  $c$ :

$$\frac{\mu_{M1}}{\mu_{E1}} = \frac{\mu_b/c}{ea_0} = \frac{1}{2} \frac{e^2}{4\pi\epsilon_0\hbar^2} = \frac{\alpha}{2} \simeq \frac{1}{275} \quad (8.5)$$

As we saw in chapter 4, examining the matrix element for our system, we estimated  $\mu \simeq 0.5\mu_B$  or  $\mu_{E_{eff}} \simeq 2 \times 10^{-3}ea_0$ . In other words we found the matrix elements to be about  $500\times$  weaker than say the Rb electric dipole transition  $5^2S_{1/2} - 5^2P_{3/2}$ . This is reasonable given our expectation for the difference between magnetic and electric transitions.

Another thing that is convenient about this complementarity between the M1 and E1 transitions is that we can use our same simulations machinery that we used for electric dipole EIT for magnetic dipole interactions, provided we put it in terms of an effective electric dipole matrix element. Thus,  $\mu_{E1_{eff}}$  lets us use our same programs. We cannot have the program *calculate* matrix elements or determine whether they were allowed, but because we explicitly state which transitions are allowed and the matrix elements are an input parameter, this approach is ok. In any case now that we have introduced the magnetic dipole interaction, Rabi frequencies, and other relevant parameters, let us introduce the Hamiltonian.

$$\tilde{H} = \frac{\hbar}{2} \begin{bmatrix} 0 & 0 & 0 & 0 & -\Omega_r & 0 \\ 0 & 0 & 0 & 0 & 0 & -\Omega_p \\ 0 & 0 & 2(\Delta_p - \Delta_c) & 0 & 0 & -\Omega_c \\ 0 & 0 & 0 & 0 & 0 & 0 \\ -\Omega_r & 0 & 0 & 0 & 2\Delta_r & 0 \\ 0 & -\Omega_p & -\Omega_c & 0 & 0 & 2\Delta_p \end{bmatrix} \quad (8.6)$$

This is the Hamiltonian after applying a unitary transformation to eliminate oscillatory pieces and facilitate simulation (numerical integration of the density matrix equations). See appendix A.6 for details about the transformation for the 6-level system. Notice the Rabi frequencies from the probe, control and repumper lasers. Detunings for each appear in the diagonal terms. Notice also that the Hamiltonian does not have any terms resonant with  $\rho_{44}$ . This is the  ${}^5D_0$  state. Although it is not connected via laser, the other excited levels will decay there, populating it.

Let us not neglect the detuning definitions here, where  $\omega_n$  correspond to the frequencies associated with each level:

$$\begin{aligned} \Delta_p &= \omega_6 - \omega_2 - \omega_p = \omega_{26} - \omega_p \\ \Delta_r &= \omega_5 - \omega_r - \omega_1 = \omega_{15} - \omega_r \\ \Delta_c &= \omega_6 - \omega_3 - \omega_c = \omega_{36} - \omega_c \end{aligned} \quad (8.7)$$

We also need the decays to incorporate in the Liouville-von Neumann equation:

$$\Gamma' = \gamma + \Gamma = \begin{bmatrix} \gamma_1 & 0 & 0 & 0 & 0 & 0 \\ 0 & \gamma_2 & 0 & 0 & 0 & 0 \\ 0 & 0 & \gamma_3 & 0 & 0 & 0 \\ 0 & 0 & 0 & \gamma_4 & 0 & 0 \\ 0 & 0 & 0 & 0 & \gamma_5 & 0 \\ 0 & 0 & 0 & 0 & 0 & \gamma_6 \end{bmatrix} + \begin{bmatrix} 0 & 0 & 0 & 0 & 0 & 0 \\ 0 & 0 & 0 & 0 & 0 & 0 \\ 0 & 0 & 0 & 0 & 0 & 0 \\ 0 & 0 & 0 & \Gamma_4 & 0 & 0 \\ 0 & 0 & 0 & 0 & \Gamma_5 & 0 \\ 0 & 0 & 0 & 0 & 0 & \Gamma_6 \end{bmatrix} \quad (8.8)$$

The  $\gamma$  matrix on the left is the decays between the hyperfine levels. This decay is exceedingly slow. The  $\Gamma$  matrix on the right contains the excited state decays.  $\Gamma_5$  and  $\Gamma_6$  are set as the same and contain the optical decay to the ground state directly, as well as the much larger decay to  ${}^5D_0$ , *i.e.*,  $\Gamma_5 = \Gamma_6 = \Gamma_{optical \rightarrow {}^7F} + \Gamma_{phonon \rightarrow {}^5D_0}$ . Let us denote the phonon decay route from  ${}^5D_1$  to  ${}^5D_0$  as  $\Gamma_p$ . In other words, the decays from the two hyperfine excited hyperfine levels that we are working with almost all go through  $\rho_{44}$ , the  ${}^5D_0$ . Decay from that level is governed by  $\Gamma_4$ , which is the optical decay rate from  ${}^5D_0$ .

We need one more ingredient. The last thing that we have not captured is where things decay *to*. This is not part of the Liouville-von Neumann equation as I have formulated the problem, but I can add it in easily enough and set it up as an additional matrix. For ease of integration and compactness, Let us call it matrix  $\Gamma_{cons}$  for decay conservation matrix, and I have denoted the contributions it makes to the  $\dot{\rho}$  vector as  $\dot{\rho}'$ .

$$\dot{\rho}' = \Gamma_{cons}\rho = \begin{bmatrix} 0 & \frac{\gamma}{2} & \frac{\gamma}{2} & \frac{\Gamma}{3} & \frac{\Gamma}{3} & \frac{\Gamma}{3} \\ \frac{\gamma}{2} & 0 & \frac{\gamma}{2} & \frac{\Gamma}{3} & \frac{\Gamma}{3} & \frac{\Gamma}{3} \\ \frac{\gamma}{2} & \frac{\gamma}{2} & 0 & \frac{\Gamma}{3} & \frac{\Gamma}{3} & \frac{\Gamma}{3} \\ 0 & 0 & 0 & 0 & \frac{\gamma}{2} + \frac{\Gamma_p}{2} & \frac{\gamma}{2} + \frac{\Gamma_p}{2} \\ 0 & 0 & 0 & \frac{\gamma}{2} & 0 & \frac{\gamma}{2} \\ 0 & 0 & 0 & \frac{\gamma}{2} & \frac{\gamma}{2} & 0 \end{bmatrix} \begin{bmatrix} \rho_{11} \\ \rho_{22} \\ \rho_{33} \\ \rho_{44} \\ \rho_{55} \\ \rho_{66} \end{bmatrix} \quad (8.9)$$

Examining this, there is hyperfine decay ( $\gamma$ ) from ground states to other ground states and excited states to other excited states. There is optical decay, given by  $\Gamma$  from all three excited states to all the ground states. Note: the optical decay rates from  ${}^5D_0$  and  ${}^5D_1$  might initially seem like they would be significantly different as the  ${}^5D_0 \rightarrow {}^7F_0$  transition is forbidden, but if we talk about the rate from  ${}^5D_0$  or  ${}^5D_1$  to all the  ${}^7F$  levels, there are allowed transitions for both, and they are pretty comparable. In any case, they are both pretty small, a few hundred Hz. The last piece to note is the phonon decay piece,  $\Gamma_p$ . This is the additional larger decay from  ${}^5D_1$  to  ${}^5D_0$ .

One additional note about decays: There is one place where population can leak out as I have the problem set up for integration. There are three hyperfine excited states, but we only have two

in our simulation as the other is not driven with a laser. As a result, decay from the other excited states that would have gone there is lost. This is not a problem as the decay rate is exceedingly slow. Ignoring this small population leak was preferable to having another level in the simulation.

Now that we have all the ingredients, we can put them together. Employing the Liouville-von Neumann equation:

$$\dot{\rho} = \frac{-i}{\hbar} [H, \rho] - \frac{1}{2} \{\Gamma, \rho\}$$

With our population conserving piece, this becomes:

$$\dot{\rho} = \frac{-i}{\hbar} [H, \rho] - \frac{1}{2} \{\Gamma, \rho\} + \Gamma_{cons}\rho \quad (8.10)$$

A few notes about simulating the system: The above framework introduces all the pieces, driving Rabi frequencies, detunings from different levels and how/where all the decays fit in. As for numerical values, there are a few relevant parameters that we need to incorporate, which are summarized in table 5.1. The Rabi frequencies are derived from our applied laser intensities and calculated/estimated matrix elements from chapter 4. We measured the decay rate from  $^5D_0$  in chapter 5; see figure 5.2. We restate our parameters here: our matrix element is about  $0.5\mu_B$ , decay rate  $\Gamma_p$  is about 30kHz, the optical decay rates:  $\Gamma_4, \Gamma_5, \Gamma_6$  are on the order of a couple hundred Hz. The hyperfine decay rate  $\gamma$  is very slow; I have seen it quoted as 24/hour[41, 80].

The atomic coherence due to a magnetic dipole transition affects the index of refraction in the same manner as that due to an electric dipole transition. Similar to equation 2.24 and following, we can related the coherence to the *magnetic* susceptibility and refractive index.

For a magnetizable material instead of a polarizable one, we have a magnetic susceptibility:

$$n = \frac{\sqrt{\epsilon_0\mu}}{\sqrt{\epsilon_0\mu_0}}$$

$$\mu = \mu_0(1 + \chi_m) \quad (8.11)$$

For small susceptibilities:

$$n \simeq 1 + \frac{1}{2}\chi_m$$

To find that susceptibility we look to the magnetization:

$$M = \chi_m H = \frac{\chi_m}{\mu_0} B$$

Magnetization is also related to the microscopic magnetic dipoles:

$$M = N \mu_m \rho_m$$

Where  $\mu_m$  represents magnetic dipole matrix elements, and  $\rho_m$  represents the atomic coherences due to the magnetic dipole interaction. We can then solve for  $\chi$ . Note: writing B explicitly and matching exponential terms introduces a factor of 1/2 to B.

$$\chi_m = \frac{2\mu_0 N \mu_m \rho_m}{B} \quad (8.12)$$

Note the similarity to the electric version:

$$\chi_{E_{eff}} = \frac{2\mu_0 N \mu_{E_{eff}} \rho_m}{\epsilon_0 E} \quad (8.13)$$

The calculation procedure consists of numerically integrating the coupled  $\dot{\rho}$  equations that result from applying the Liouville-von Neumann equation. We can incorporate time dependence, the laser beams turning on and off for example, by making Rabi frequencies into time-dependent quantities. It turns out that when the quantities are varying in time, it is actually easier to just compute the Liouville-von Neumann equation numerically at each integration step rather than employing a function. Thanks to Nick Brewer for pointing this out. The integration is done in Matlab, as Matlab does well with the numerical matrix operations.

There is one other number that we will need for simulations that we have not discussed thus far, the effective density. We became interested in rare-earth doped crystals in part because of the possibility that they would offer very high densities compared to atomic vapors or traps. However, the density that we get to utilize in the crystal is not as high as we might have originally thought, as we can't use all the transitions. Let us look at the numbers: YSO ( $Y_2SiO_5$ ) has a density of  $4.44g/cm^3$  according to Scientific Materials, where we got the crystal[81]. Given its atomic

weight of 285.9 g/mol and our doping concentration of 0.1%; this corresponds to a  $\text{Eu}^{3+}$  number density of  $1.87 \times 10^{19}/\text{cc}$  which is very high. However there are a few factors that make the effective density much lower:

$$\rho_{Eu_{eff}} = \rho_{Eu} \times \frac{1}{2} \times \frac{1}{2} \times \frac{\Gamma_{homo}}{\Gamma_{inhomo}} \simeq 5 \times 10^{13}/\text{cc} \quad (8.14)$$

There is a factor of 1/2 since we only use one of the two more or less equally abundant isotopes,  $^{151}\text{Eu}$  and  $^{153}\text{Eu}$ . There is also a factor of 1/2 because we only utilize Eu ions in one of the two possible more or less equally occupied crystal sites. The largest factor comes from the inhomogeneous broadening. We do not make use of the whole inhomogeneously broadened line, but a sub-population whose width is set by the homogeneous linewidth. For us this is on the order of 30 kHz/3 GHz, a factor of  $10^{-5}$ . All this results in an effective density much lower than the actual Eu ion density, but still significant by atomic cell or trap standards. We could increase the doping concentration or get a single-isotope-doped crystal to increase the density. Additionally, it may be possible to increase the effective density by suppressing some of the inhomogeneous broadening as discussed in appendix F.

Let us summarize our simulation parameters in a table:

Parameter	Value	Source
Matrix Element $\mu$	$0.5\mu_B$	RELIC code
phonon decay rate $\Gamma_p$	30 kHz	measured
optical decay rate $\Gamma$	250 Hz	RELIC/for example[51]
hyperfine decay rate $\gamma$	24/hr	for example [80, 41]
effective Eu density	$5 \times 10^{13}/\text{cc}$	estimated

Table 8.1: Eu:YSO simulation parameters

## 8.2 Rabi Flopping

Now that we have a handle on the simulation procedure and have either measurements or estimates for the numbers that go into the simulation, let us take a look at some simulated coherent effects. The first effect we would like to examine is Rabi flopping. Observing this in the experiment would really give us some confidence in our parameters, in particular matrix elements, as we could extract them from the Rabi frequency:  $\Omega_B = \frac{\mu B}{\hbar}$ . Rabi flopping should be simpler to see than other coherent effects as we only need the one laser. Ideally, once we get this working, we would look at all the different possible transitions to ascertain their respective matrix elements. This is important, as we could choose our level scheme to use the strongest transitions. Also, if we knew the matrix elements, we would be able to perhaps simulate the spectral hole-burning spectrum more accurately and resolve the excited level ordering.

One challenge with Rabi flopping is that one needs to consider the spatial extent/intensity variation across the beam as different intensities correspond to different Rabi frequencies. One way to mitigate this is to use a large driving beam with a small probing beam or to use a pinhole to only look at the center of the excitation where the excitation is more uniform. Additionally, focusing and the higher intensity along the beam could be an issue, so we want to make sure to not focus too tightly. Figure 8.2 illustrates this. If we were to probe the entire beam profile, we would see a weighted average of Rabi frequencies, from zero at the wings to the maximum in the center. The weighting factor would come from the fraction of the ionic population exposed to a particular laser intensity. The left panel a) is a topographical map of cross-sectional beam intensity. The height of a particular slice indicates its intensity, whereas its area indicates its weighting factor. Averaging Rabi frequencies from the whole beam profile would totally wash out the effect. The right panel, b) shows what we need to do: in this case it is sample the center 50  $\mu\text{m}$  worth of the beam, where the intensity is relatively constant. This is what is used in the simulation.

The curve in figure 8.3 gives the density matrix simulation of Rabi-flopping on the ground state. The red dotted trace is if we observe across the whole beam, as in figure 8.2 a). The blue solid trace is if we were to look only at the center, as in figure 8.2 b).

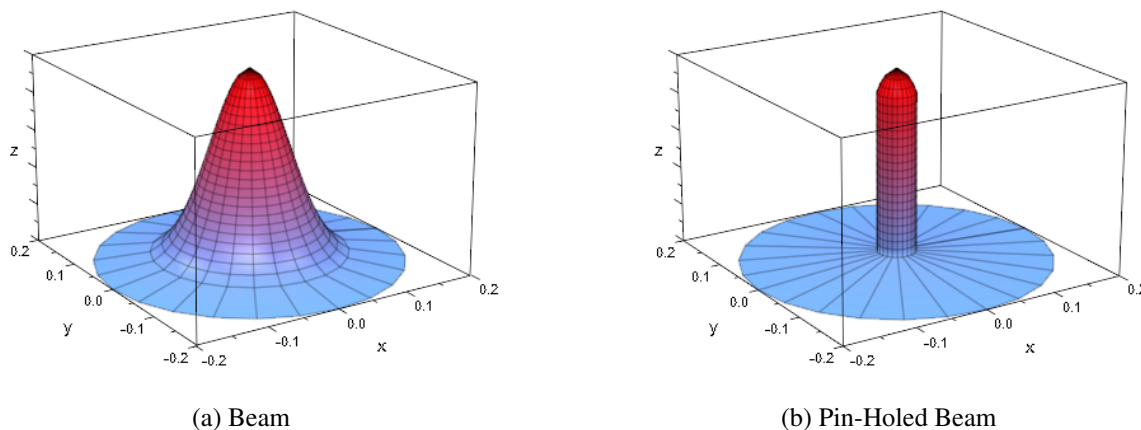


Figure 8.2: The need to sample only part of the Rabi beam. (Note: z axis is intensity.) Rather than sample the whole beam a), we need to sample only the center b) if we hope to get a measurable Rabi frequency. Doing otherwise, the combination of different Rabi frequencies due to varying intensity across the beam would wash out the signal.

We could potentially probe this experimentally by looking at absorption with a separate probe beam while the driving Rabi-flopping beam is on to see if we can see variations in absorption with time as the population flopped in and out of the probed state. Alternatively, we could look at fluorescence correlated with a certain time after the application of the Rabi-beam; changing the delay time would hopefully change the amount of fluorescence and allow us to map out the excited population as a function of time.

According to the simulation, we should be able to see evidence of Rabi flopping with very modest experimental parameters. Ideally as a result of this experiment we would have an indirect measurement of the matrix element for particular hyperfine transitions based on their Rabi flopping frequencies. This would inform the EIT experiments described in the next section.

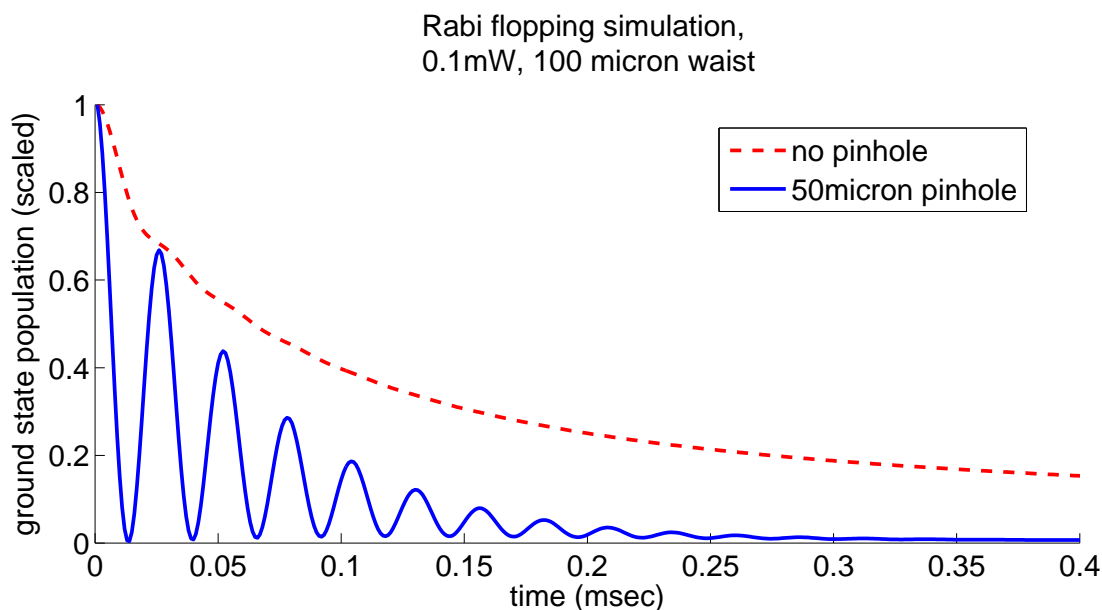


Figure 8.3: Rabi flopping simulation, ground state population

### 8.3 EIT

Eventually we would like to see electromagnetically induced transparency (EIT). This would be an exciting result as EIT on a magnetic dipole transition has not to our knowledge been accomplished. This would give us confidence in our ability to drive coherent processes in our rare-earth doped crystal system, a necessary ingredient for a negative-index scheme as discussed in chapter 3. Let us put our density matrix simulation to work on the EIT problem.

Figure 8.5 is generated with a  $300 \mu\text{s}$  long probe pulse and a  $400 \mu\text{s}$  long control pulse. The control pulse turns on  $100 \mu\text{s}$  earlier than the probe, and both beams turn off simultaneously, as shown in figure 8.4. The beam waist is  $100 \mu\text{m}$ , the probe power is  $1 \mu\text{W}$ , and the control power is  $1\text{mW}$ . The matrix element, decays, and other parameters are given in table 8.1.

One thing we still need to set is timing parameters. We have the control and repumper on initially, pumping population to the probe ground state. Then the control and repumper turn off. This is followed by the EIT sequence where the control turns back on and the probe (much weaker) turns on shortly after. A time slice near the end of the pulse is what forms a point in the dispersion

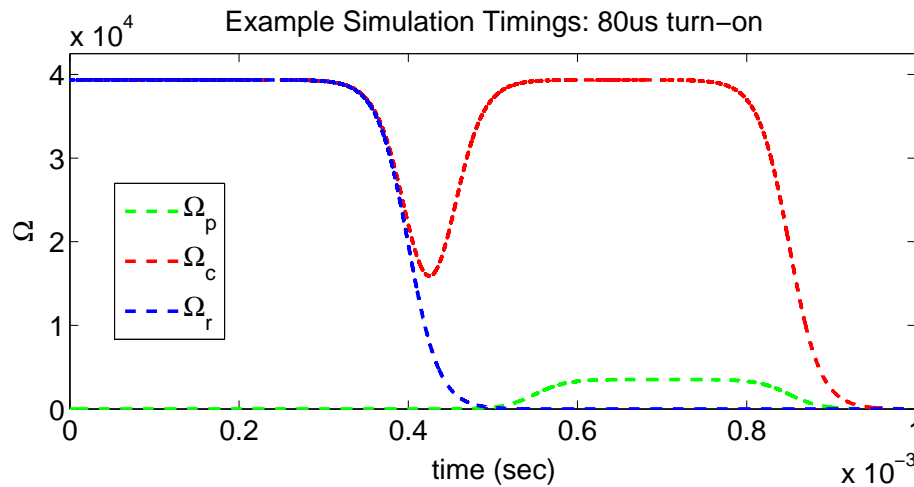


Figure 8.4: Example Simulation Timings.  $\Omega$ 's denote the Rabi frequencies for the different experiment beams. The control beam turns on before probe in the EIT sequence. The turn-on time needs to be on a similar time scale to the decay rate.

curve in figure 8.5. Repeating the simulation with different detunings generates additional points that together create the full EIT dispersion curve.

Although the features are small in magnitude, the sharpness of the dispersion (the large derivative of the index) means very 'slow' light, according to  $v_g = c/n_g$ , where  $n_g = n(\nu) + \nu \frac{dn(\nu)}{d\nu}$ . Remarkably, this would correspond to a group velocity on the order of 200m/s!

There are a variety of things we could explore with this simulation, for example investigating the effect of different strength matrix elements or the effect of modifying the timings. For example, figure 8.6 shows an example of a simulations where the lasers turn on at AOM switching times compared to turning on gradually as in the previous figure. As you can see, there is some additional structure on the EIT scan from the non-adiabatic nature of the laser turn-on. Looking at the populations and coherence in time gives a sense of the extent of the adiabaticity. Such an exploration is interesting and very accessible with this simulation procedure.

There is a whole host of effects that can be explored via density matrix simulations. This should prove useful to compare to experiments when we start getting experimental coherent results.

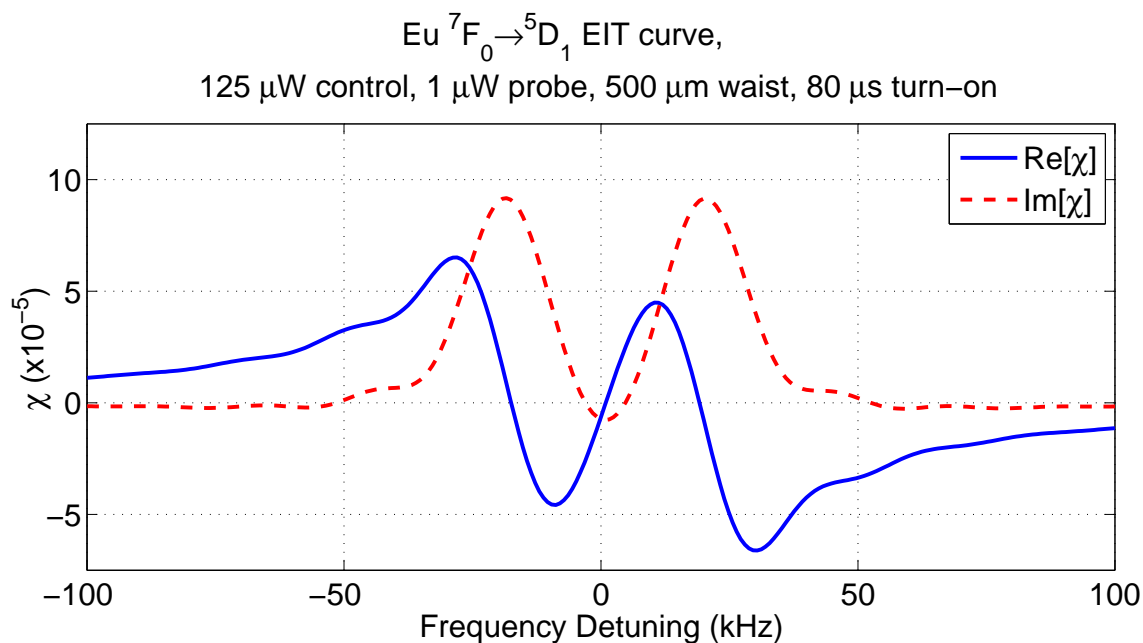


Figure 8.5: Eu:YSO  ${}^7F_0 - {}^5D_1$  EIT simulation. Note the very narrow resonance.

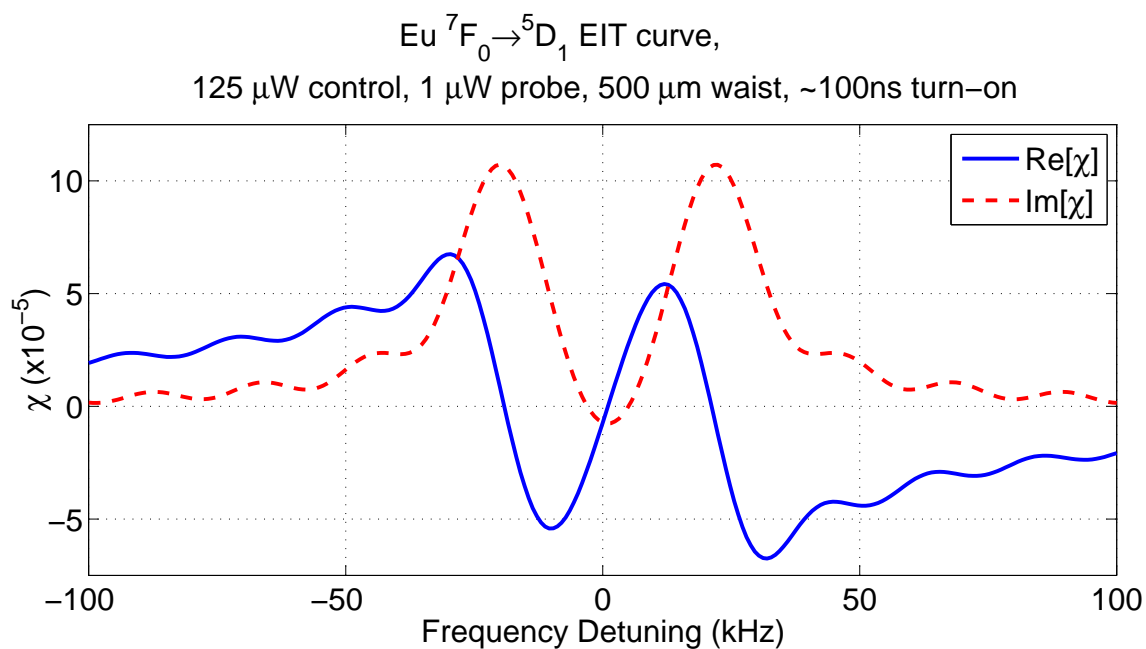


Figure 8.6: Eu:YSO  ${}^7F_0 - {}^5D_1$  EIT simulation with fast ( $\sim 100$  ns) beam turn-on. Notice how changing the time-dynamics of the beam switching adds structure to the dispersion shape.

## Chapter 9

### Going Forward

#### 9.1 Experimental Improvements

As of yet, we have not seen any coherent effects: Rabi flopping or EIT, nor have we seen spectral holes as narrow as we would hope to see. There are a number of experimental improvements we are planning to implement, including:

**External Magnetic Field:** Currently the most pressing limitation to the experiment is that the spectral holes do not appear to be as narrow as we would like. This could be an indication that our laser is misbehaving, but the measured linewidth appears correct. Some of the effect is saturation as discussed in section 7.5, but this may not entirely explain the issue.

It appears that applying a magnetic field (by just placing permanent magnets in the cryostat adjacent to the crystal) may allow for potentially much narrower spectral holes. Chen seems to suggest this could have a dramatic effect [64], although we do not exactly understand the mechanism. He notes that applying a 1000 G magnetic field to their Eu:YSO system allowed them to improve their hole-burning width (on  ${}^5D_0$ ) from  $\sim 1$  MHz to 10s of kHz.

This improvement does not appear to be attributable to a decrease in the ion-host interaction, an excited-state broadening mechanism. The constituent ions of YSO have small nuclear moments, and given the fact that Eu is a non-Kramers ion, we would expect this effect to be small, as discussed in section 5.1.1. Equall shows an applied magnetic field reducing the homogeneous linewidth by 100 Hz or so[82]; it does not appear that a magnetic field will appreciably reduce the excited state linewidth.

However, perhaps there is an effect that causes the spectral holes to broaden but not disappear. As it is now, the Zeeman levels should be degenerate, as we are not applying a magnetic field. However, perhaps in the crystal environment, crystal host nuclear spin flips at slow time scales are sufficient to mix the (almost) degenerate Zeeman ground states and cause problems/broadening. If that were the case, applying a magnetic field would suppress host spin-flips, in turn limiting mixing between hyperfine ground states and lessen the hole broadening. Mathematically, in terms of the quadrupole Hamiltonian, equation 4.1, there is a term that depends on the interaction of  $B$  with  $I$ . Perhaps biasing with a larger magnetic field would suppress any magnetic field fluctuations around zero due to host nuclear spins. Estimating the size of a magnetic field (via  $\mu/r^3$ ) at an Eu ion site due to host nuclear moments and the ion separations in the crystal would suggest very small fields, 10s of Gauss, which does not seem sufficient to cause such Zeeman shifts.

Zeeman fluctuations seem to be the mechanism suggested by Ahlefeldt, although they investigate it for a different crystal system  $EuCl_3 \cdot 6H_2O$  [83]. They notice a decrease in sensitivity to magnetic field fluctuations and increase in coherence time upon application of a magnetic field. We are just starting to investigate this, but plan to try placing our crystal in a magnetic field from a couple permanent magnets placed around the crystal in the cryostat. We also plan to model the effect.

**Different Doping.** There are a couple things we could try with the crystal that would help us get stronger interactions. We could get a single isotope crystal, which do exist, although they are very expensive. Another thing we could do is to try higher Eu ion doping. This would help our Eu density. This would most likely increase the linewidth of our transition, due to ion-ion interactions. However, we do not care about our linewidth as much as those interested in quantum memory experiments, who want very narrow spectral holes. As a result, we might be able to get away with higher doping. Also, it is not clear at this point, but we are going to try a thinner crystal as it may help with saturation.

## 9.2 Left-Handed Waves

As discussed in chapter 1, the traditional route to a negative index is to manipulate the system so both the electric permittivity  $\epsilon$  and magnetic permeability  $\mu$  are negative. This is challenging as one needs strong electric and magnetic resonances in a material at about the same wavelength, and there are not really strong magnetic resonances in materials at optical frequencies. The scheme presented in chapter 3 is an atomic route using Raman transitions and chiral (cross-coupling) response. Metamaterials are another entirely different route.

This last section will mention another route that is being pursued in Yavuzlab. I will not go into detail as I have not worked on this subject, but it does provide a really nice book-end to this body of work and offer a very promising experimental direction as well. The following is based on a paper by Deniz Yavuz and Nick Brewer[84]. The argument is as follows:

Starting from Maxwell's (curl) equations in a material:

$$\begin{aligned}\nabla \times \vec{E} &= -\frac{\delta \vec{B}}{\delta t} \\ \nabla \times \vec{H} &= \frac{\delta \vec{D}}{\delta t}\end{aligned}\tag{9.1}$$

Assuming a plane wave solution, Maxwell's equations can be written:

$$\begin{aligned}\vec{k} \times \vec{E} &= \mu\omega\vec{H} \\ \vec{k} \times \vec{H} &= -\epsilon\omega\vec{E}\end{aligned}\tag{9.2}$$

Now a traditional negative index material, in the sense first proposed by Veselago[1], would make  $\mu$  and  $\epsilon$  negative, these wave equations would pick up a negative sign:

$$\begin{aligned}\vec{k} \times \vec{E} &= -\mu\omega\vec{H} \\ \vec{k} \times \vec{H} &= \epsilon\omega\vec{E}\end{aligned}\tag{9.3}$$

We can recognize how these equations are left-handed compared to the normal right-handed originals, equations 9.2. This is in contrast to the idea proposed by Deniz and Nick, where the equations are rendered left-handed not by changing the sign of  $\mu$  and  $\epsilon$ , but by means of adding an external polarization and magnetization that is large and opposite.

$$\begin{aligned}\vec{k} \times \vec{E} &= \mu\omega(\vec{H} + \vec{M}) \\ \vec{k} \times \vec{H} &= -\omega(\epsilon\vec{E} + \vec{P})\end{aligned}\tag{9.4}$$

Now the magnitude of the relationship between the propagating fields and externally applied magnetization and polarization needs to be carefully chosen, *i.e.*, if:  $\vec{H} = -\vec{M}_{ext}/2$  and  $\vec{E} = -\vec{P}_{ext}/2\epsilon_0$ . Note there is also a condition on the relative strengths of the magnetization and polarization that  $\frac{|M_{Ext}|}{|P_{Ext}|} = c$ , *i.e.*, the magnetization has to be relatively very strong as the magnetic response is relatively weak. The phase relationship is set by using one common laser for both the magnetization and polarization. Notice that when these relationships are obeyed and inserted into equations 9.4, the result will have the same left-handed character as equations 9.3. In other words, this external polarization and magnetization technique gives left-handed wave behavior by a means other than switching the sign of  $\mu$  and  $\epsilon$ . In terms of our experimental set-up, the idea is to magnetize and polarize the crystal via another laser, the IR laser that we already have. The magnetization is accomplished via a two-photon transition  ${}^7F_0 \rightarrow {}^5D_1$ , while the polarization is achieved by a two-photon transition via the nonlinear susceptibility of the crystal  $\chi^{(2)}$ , *i.e.*, on another transition in the crystal. Figure 9.1 shows the proposed energy level scheme.

An experiment might look something like figure 9.2. The external polarization and magnetization is accomplished via the IR laser. The laser is tuned such that the polarization and magnetization have the right magnitude and phase relative to each other. We can imagine the IR laser creating a channel or tunnel through the crystal with appropriate magnetization and polarization. This magnetized and polarized channel can support ‘normal’ right-handed green waves as well as left-handed green waves. With no initial seed pulse, there would be some of both. Should there be any other green light, generated via SHG for example, it will be distinguishable from left-handed

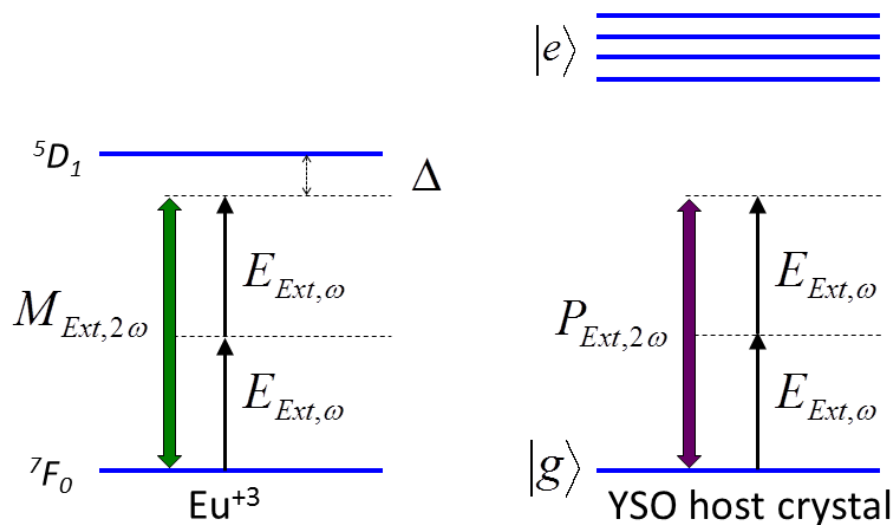


Figure 9.1: Externally Polarized and Magnetized (EPM) Medium Energy Level Scheme: A two-photon transition on  ${}^7F_0 \rightarrow {}^5D_1$  magnetizes the crystal, while polarization happens via  $\chi^{(2)}$  response on the crystal energy levels themselves.

waves because they will refract oppositely at the interface. Interestingly this refraction would happen on the IR input side.

In the context of this thesis, I just want to present enough of this to relate a potential experiment. This is a very active area of research in the group. There is still much work to be done to untangle/distinguish exactly between traditional negative index materials and these externally polarized and magnetized (EPM) left-handed materials. One difference, for example, is that in such an EPM material, the group velocity and phase velocity are parallel, whereas they are anti-parallel in regular negative-index materials. Deniz and Nick have done numerical simulations of Maxwell's equations on this, see their paper for more information and their simulations[84].

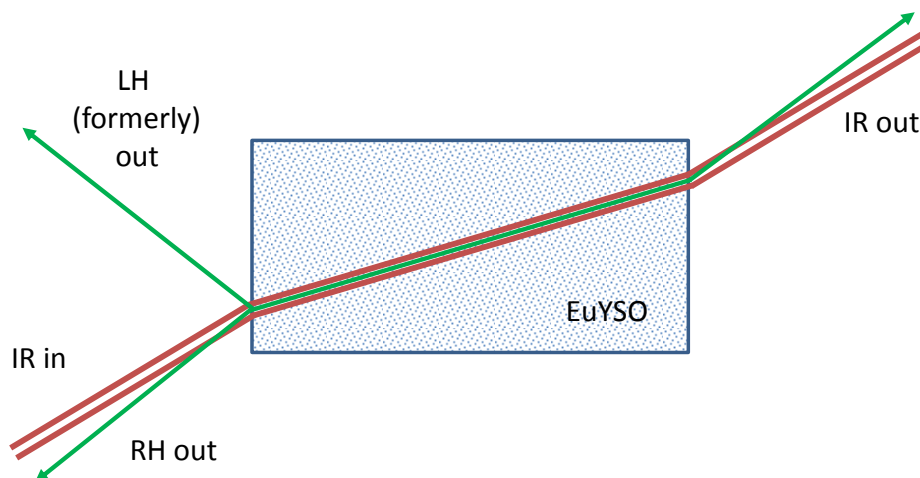


Figure 9.2: Idea for experiment to demonstrate left-handed waves. External polarization and magnetization is accomplished via an IR laser, forming a tunnel that can support left-handed waves, portrayed by the double maroon line. Left-handed waves refract opposite ‘normal’ right handed waves, making them distinguishable.

### 9.3 Final Thoughts

This external polarization and magnetization (EPM) approach offers a very tantalizing prospect in that it does not require some minimum density in order to work, as opposed to the atomic approach discussed in chapter 3. As a result, experimentally generating detectable left-handed waves is probably much more likely to be successful with this approach. Not to mention, this new approach is much simpler. Rather than having Raman laser systems for an electric and magnetic transition as well as a cross-coupling laser, this scheme requires a single IR laser for the external source of polarization and magnetization, and this is a laser we already have since we get green by doubling IR. This EPM approach is also desirable because it is not so wedded to the atomic structure- *i.e.*, the electric and magnetic transitions need not be at the same frequency.

Although we started out building this experimental system to investigate an aspect of an atomic negative-index proposal as described in chapter 3, this new external magnetization and polarization route seems much more promising. Even so, the near-term experimental goal to see magnetic EIT

in of itself is still very exciting. This work contributes to this effort by examining many aspects of our new Eu:YSO experimental system including the atomic structure of relevant Eu levels and some of the consequences of using a doped crystal as an atomic system. This thesis puts these current experiments in the context of experimental index modification, which we have experience with, while also offering simulations to point the way forward toward coherent effects.



## Appendix A: Assorted Math for EIT and the Density Matrix

### A.1 Algebra of applying Schrödinger equation to derive wavefunction coefficients:

Apply the Schrödinger Equation to the three-level wavefunction, equation 2.5, with applied coupling and probe lasers:

$$i\hbar|\dot{\psi}\rangle = H|\psi\rangle \quad (\text{A.1})$$

$$\begin{aligned} i\hbar|\dot{\psi}\rangle &= \\ i\hbar\left((\dot{c}_1 + c_1(-i\omega_1))e^{-i\omega_1 t}|1\rangle + (\dot{c}_2 + c_2(-i\omega_2))e^{-i\omega_2 t}|2\rangle + (\dot{c}_3 + c_3(-i\omega_3))e^{-i\omega_3 t}|3\rangle\right) \\ H|\psi\rangle &= \\ \hbar\omega_1 c_1 e^{-i\omega_1 t}|1\rangle + \hbar\omega_2 c_2 e^{-i\omega_2 t}|2\rangle + \hbar\omega_3 c_3 e^{-i\omega_3 t}|3\rangle \\ -\frac{\hbar}{2}\Omega_p e^{-i\phi_p} e^{-i\omega_p t} c_1 e^{-i\omega_1 t}|3\rangle - \frac{\hbar}{2}\Omega_c e^{-i\phi_c} e^{-i\omega_c t} c_2 e^{-i\omega_2 t}|3\rangle \\ -\frac{\hbar}{2}\Omega_p e^{i\phi_p} e^{i\omega_p t} c_3 e^{-i\omega_3 t}|1\rangle - \frac{\hbar}{2}\Omega_c e^{i\phi_c} e^{i\omega_c t} c_3 e^{-i\omega_3 t}|2\rangle \end{aligned}$$

Combining and simplifying:

$$\begin{aligned} (i\dot{c}_1 + c_1\omega_1)e^{-i\omega_1 t}|1\rangle + (i\dot{c}_2 + c_2\omega_2)e^{-i\omega_2 t}|2\rangle + (i\dot{c}_3 + c_3\omega_3)e^{-i\omega_3 t}|3\rangle = \\ \omega_1 c_1 e^{-i\omega_1 t}|1\rangle + \omega_2 c_2 e^{-i\omega_2 t}|2\rangle + \omega_3 c_3 e^{-i\omega_3 t}|3\rangle - \frac{1}{2}\Omega_p e^{-i\phi_p} e^{-i\omega_p t} c_1 e^{-i\omega_1 t}|3\rangle \\ -\frac{1}{2}\Omega_c e^{-i\phi_c} e^{-i\omega_c t} c_2 e^{-i\omega_2 t}|3\rangle - \frac{1}{2}\Omega_p e^{i\phi_p} e^{i\omega_p t} c_3 e^{-i\omega_3 t}|1\rangle - \frac{1}{2}\Omega_c e^{i\phi_c} e^{i\omega_c t} c_3 e^{-i\omega_3 t}|2\rangle \end{aligned}$$

Multiply by each bra, one at a time, to get equations in terms of the coefficients  $c_1, c_2, c_3$ :

$$\begin{aligned}
(i\dot{c}_1 + c_1\omega_1) e^{-i\omega_1 t} &= \omega_1 c_1 e^{-i\omega_1 t} - \frac{1}{2} \Omega_p e^{i\phi_p} e^{i\omega_p t} c_3 e^{-i\omega_3 t} \\
(i\dot{c}_2 + c_2\omega_2) e^{-i\omega_2 t} &= \omega_2 c_2 e^{-i\omega_2 t} - \frac{1}{2} \Omega_c e^{i\phi_c} e^{i\omega_c t} c_3 e^{-i\omega_3 t} \\
(i\dot{c}_3 + c_3\omega_3) e^{-i\omega_3 t} &= \omega_3 c_3 e^{-i\omega_3 t} - \frac{1}{2} \Omega_p e^{-i\phi_p} e^{-i\omega_p t} c_1 e^{-i\omega_1 t} - \frac{1}{2} \Omega_c e^{-i\phi_c} e^{-i\omega_c t} c_2 e^{-i\omega_2 t}
\end{aligned}$$

Simplify:

$$\begin{aligned}
\dot{c}_1 e^{-i\omega_1 t} &= \frac{i}{2} \Omega_p e^{i\phi_p} e^{i\omega_p t} c_3 e^{-i\omega_3 t} \\
\dot{c}_2 e^{-i\omega_2 t} &= \frac{i}{2} \Omega_c e^{i\phi_c} e^{i\omega_c t} c_3 e^{-i\omega_3 t} \\
\dot{c}_3 e^{-i\omega_3 t} &= \frac{i}{2} \Omega_p e^{-i\phi_p} e^{-i\omega_p t} c_1 e^{-i\omega_1 t} - \frac{i}{2} \Omega_c e^{-i\phi_c} e^{-i\omega_c t} c_2 e^{-i\omega_2 t}
\end{aligned}$$

Solving for the time derivatives:

$$\begin{aligned}
\dot{c}_1 &= \frac{i}{2} \Omega_p e^{i\phi_p} c_3 e^{-i(\omega_3 - \omega_1 - \omega_p)t} \\
\dot{c}_2 &= \frac{i}{2} \Omega_c e^{i\phi_c} c_3 e^{-i(\omega_3 - \omega_2 - \omega_c)t} \\
\dot{c}_3 &= \frac{i}{2} \Omega_p e^{-i\phi_p} c_1 e^{-i(\omega_1 - \omega_3 + \omega_p)t} + \frac{i}{2} \Omega_c e^{-i\phi_c} c_2 e^{-i(\omega_2 - \omega_3 + \omega_c)t}
\end{aligned}$$

Functionally the same in terms of relative energies:

$$\begin{aligned}
\dot{c}_1 &= \frac{i}{2} \Omega_p e^{i\phi_p} c_3 e^{-i(\omega_{13} - \omega_p)t} \\
\dot{c}_2 &= \frac{i}{2} \Omega_c e^{i\phi_c} c_3 e^{-i(\omega_{13} - \omega_{12} - \omega_c)t} \\
\dot{c}_3 &= \frac{i}{2} \Omega_p e^{-i\phi_p} c_1 e^{-i(-\omega_{13} + \omega_p)t} + \frac{i}{2} \Omega_c e^{-i\phi_c} c_2 e^{-i(\omega_{12} - \omega_{13} + \omega_c)t}
\end{aligned}$$

We can further clean up our equations by introducing detunings..

$$\dot{c}_1 = \frac{i}{2}\Omega_p e^{i\phi_p} c_3 e^{-i\Delta_p t} \quad (\text{A.2})$$

$$\dot{c}_2 = \frac{i}{2}\Omega_c e^{i\phi_c} c_3 e^{-i\Delta_c t} \quad (\text{A.3})$$

$$\dot{c}_3 = \frac{i}{2}\Omega_p e^{-i\phi_p} c_1 e^{i\Delta_p t} + \frac{i}{2}\Omega_c e^{-i\phi_c} c_2 e^{i\Delta_c t} \quad (\text{A.4})$$

These kinds of expressions are found in Scully (pg 224) for example[13].

## A.2 Constructing Density Matrix Terms and the Co-rotating Frame

This next section is the algebra for constructing density matrix terms,  $\rho_S$ , from the coefficient equations. We can derive our density matrix terms by taking appropriate combinations and keeping in mind the definitions of the populations and coherences:

$$\begin{aligned} c_1 c_1^* &= \rho_{11} \\ c_1 c_2^* &= \rho_{12} \\ \rho_{21} &= \rho_{12}^* = c_1^* c_2 \text{ etc.} \end{aligned} \quad (\text{A.5})$$

For example, to get the  $\rho_{11}$  derivative, take:

$$\begin{aligned} \dot{\rho}_{11} &= c_1^* \frac{d}{dt} c_1 + c_1 \frac{d}{dt} c_1^* = c_1^* \frac{i}{2} \Omega_p e^{i\phi_p} c_3 e^{-i\Delta_p t} + c_1 \frac{-i}{2} \Omega_p e^{-i\phi_p} c_3^* e^{i\Delta_p t} \\ \dot{\rho}_{11} &= \frac{i}{2} \Omega_p (\rho_{31} e^{i\phi_p} e^{-i\Delta_p t} - \rho_{13} e^{-i\phi_p} e^{i\Delta_p t}) \end{aligned} \quad (\text{A.6})$$

Similarly, for the derivatives of the populations:

$$\begin{aligned}\dot{\rho}_{22} &= c_2^* \frac{d}{dt} c_2 + c_2 \frac{d}{dt} c_2^* = c_2^* \left( \frac{i}{2} \Omega_c e^{i\phi_c} c_3 e^{-i\Delta_c t} \right) + c_2 \left( \frac{-i}{2} \Omega_c e^{-i\phi_c} c_3^* e^{i\Delta_c t} \right) \\ \dot{\rho}_{22} &= \frac{i}{2} \Omega_c \left( \rho_{32} e^{i\phi_c} e^{-i\Delta_c t} - \rho_{23} e^{-i\phi_c} e^{i\Delta_c t} \right)\end{aligned}\quad (\text{A.7})$$

$$\begin{aligned}\dot{\rho}_{33} &= c_3^* \frac{d}{dt} c_3 + c_3 \frac{d}{dt} c_3^* = c_3^* \left( \frac{i}{2} \Omega_p e^{-i\phi_p} c_1 e^{i\Delta_p t} + \frac{i}{2} \Omega_c e^{-i\phi_c} c_2 e^{i\Delta_c t} \right) \\ &\quad + c_3 \left( \frac{-i}{2} \Omega_p e^{i\phi_p} c_1^* e^{-i\Delta_p t} + \frac{-i}{2} \Omega_c e^{i\phi_c} c_2^* e^{-i\Delta_c t} \right) \\ \dot{\rho}_{33} &= \frac{i}{2} \left( (\Omega_p e^{-i\phi_p} e^{i\Delta_p t} \rho_{13} + \Omega_c e^{-i\phi_c} e^{i\Delta_c t} \rho_{23}) - \Omega_p e^{i\phi_p} e^{-i\Delta_p t} \rho_{31} - \Omega_c e^{i\phi_c} e^{-i\Delta_c t} \rho_{32} \right)\end{aligned}\quad (\text{A.8})$$

Similarly, now looking at the off-diagonal terms:

$$\begin{aligned}\dot{\rho}_{12} &= c_2^* \frac{d}{dt} c_1 + c_1 \frac{d}{dt} c_2^* = c_2^* \left( \frac{i}{2} \Omega_p e^{i\phi_p} c_3 e^{-i\Delta_p t} \right) + c_1 \left( \frac{-i}{2} \Omega_c e^{-i\phi_c} c_3^* e^{i\Delta_c t} \right) \\ \dot{\rho}_{12} &= \frac{i}{2} \left( \Omega_p e^{i\phi_p} e^{-i\Delta_p t} \rho_{32} - \Omega_c e^{-i\phi_c} e^{i\Delta_c t} \rho_{13} \right)\end{aligned}\quad (\text{A.9})$$

$$\begin{aligned}\dot{\rho}_{13} &= c_3^* \frac{d}{dt} c_1 + c_1 \frac{d}{dt} c_3^* = c_3^* \left( \frac{i}{2} \Omega_p e^{i\phi_p} c_3 e^{-i\Delta_p t} \right) + c_1 \left( \frac{-i}{2} \Omega_p e^{i\phi_p} c_1^* e^{-i\Delta_p t} + \frac{-i}{2} \Omega_c e^{i\phi_c} c_2^* e^{-i\Delta_c t} \right) \\ \dot{\rho}_{13} &= \frac{i}{2} \left( \Omega_p e^{i\phi_p} e^{-i\Delta_p t} \rho_{33} - \Omega_p e^{i\phi_p} e^{-i\Delta_p t} \rho_{11} - \Omega_c e^{i\phi_c} e^{-i\Delta_c t} \rho_{12} \right) \\ \dot{\rho}_{13} &= \frac{i}{2} \left( \Omega_p e^{i\phi_p} e^{-i\Delta_p t} (\rho_{33} - \rho_{11}) - \Omega_c e^{i\phi_c} e^{-i\Delta_c t} \rho_{12} \right)\end{aligned}\quad (\text{A.10})$$

$$\begin{aligned}\dot{\rho}_{23} &= c_3^* \frac{d}{dt} c_2 + c_2 \frac{d}{dt} c_3^* = c_3^* \left( \frac{i}{2} \Omega_c e^{i\phi_c} c_3 e^{-i\Delta_c t} \right) + c_2 \left( \frac{-i}{2} \Omega_p e^{i\phi_p} c_1^* e^{-i\Delta_p t} + \frac{-i}{2} \Omega_c e^{i\phi_c} c_2^* e^{-i\Delta_c t} \right) \\ \dot{\rho}_{23} &= \frac{i}{2} \left( \Omega_c e^{i\phi_c} e^{-i\Delta_c t} (\rho_{33} - \rho_{22}) - \Omega_p e^{i\phi_p} e^{-i\Delta_p t} \rho_{21} \right)\end{aligned}\quad (\text{A.11})$$

$$\begin{aligned}\dot{\rho}_{21} &= c_1^* \frac{d}{dt} c_2 + c_2 \frac{d}{dt} c_1^* = c_1^* \left( \frac{i}{2} \Omega_c e^{i\phi_c} c_3 e^{-i\Delta_c t} \right) + c_2 \left( \frac{-i}{2} \Omega_p e^{-i\phi_p} c_3^* e^{i\Delta_p t} \right) \\ \dot{\rho}_{21} &= \frac{i}{2} \left( -\Omega_p e^{-i\phi_p} e^{i\Delta_p t} \rho_{23} + \Omega_c e^{i\phi_c} e^{-i\Delta_c t} \rho_{31} \right) = (\dot{\rho}_{12})^*\end{aligned}\quad (\text{A.12})$$

$$\dot{\rho}_{23} = (\dot{\rho}_{32})^* \quad (\text{A.13})$$

$$\dot{\rho}_{31} = (\dot{\rho}_{13})^* \quad (\text{A.14})$$

So this is good, but it would be better to get rid of all the time-dependent exponentials. We can do this by a sort of change of variables, where we subsume the phase and detunings into the definitions of the coherences; this is known as going to a co-rotating frame. For example, if we define  $\tilde{\rho}$  as such:

$$\tilde{\rho}_{31} = \rho_{31} e^{i\phi_p} e^{-i\Delta_p t} \quad (\text{A.15})$$

We can simplify things further:

$$\dot{\rho}_{11} = \frac{i}{2} \Omega_p (\tilde{\rho}_{31} - \tilde{\rho}_{13}) \quad (\text{A.16})$$

$$\tilde{\rho}_{32} = \rho_{32} e^{i\phi_c} e^{-i\Delta_c t} \quad (\text{A.17})$$

$$\dot{\rho}_{22} = \frac{i}{2} \Omega_c (\tilde{\rho}_{32} - \tilde{\rho}_{23}) \quad (\text{A.18})$$

$$\dot{\rho}_{33} = \frac{i}{2} ((\Omega_p \tilde{\rho}_{13} + \Omega_c \tilde{\rho}_{23}) - \Omega_p \tilde{\rho}_{31} - \Omega_c \tilde{\rho}_{32}) \quad (\text{A.19})$$

Note: the populations are real, so  $\rho_{11} = \tilde{\rho}_{11}$ , etc. Also we can come up with  $\tilde{\rho}_{12}$  with this procedure as well:

$$\tilde{\rho}_{12} = \frac{\tilde{\rho}_{13} \tilde{\rho}_{32}}{\rho_{33}} = \rho_{12} e^{-i(\phi_p - \phi_c)} e^{-i(\Delta_c - \Delta_p)t} \quad (\text{A.20})$$

However, with the cross terms we have to think more carefully about the time derivative: So what is time derivative in terms of our substitutions?

$$\begin{aligned} \dot{\tilde{\rho}}_{12} &= e^{-i(\phi_p - \phi_c)} e^{-i(\Delta_c - \Delta_p)t} (\dot{\rho}_{12} + \rho_{12}(-i(\Delta_c - \Delta_p))) \\ &= e^{-i(\phi_p - \phi_c)} e^{-i(\Delta_c - \Delta_p)t} \dot{\rho}_{12} + \tilde{\rho}_{12}(-i(\Delta_c - \Delta_p)) \rightarrow \\ \dot{\rho}_{12} &= (\dot{\tilde{\rho}}_{12} - \tilde{\rho}_{12}(-i(\Delta_c - \Delta_p))) e^{i(\phi_p - \phi_c)} e^{i(\Delta_c - \Delta_p)t} \end{aligned} \quad (\text{A.21})$$

Plugging it in:

$$\begin{aligned} \dot{\rho}_{12} &= \frac{i}{2} (\Omega_p e^{i\phi_p} e^{-i\Delta_p t} \tilde{\rho}_{32} e^{-i\phi_c} e^{i\Delta_c t} - \Omega_c e^{-i\phi_c} e^{i\Delta_c t} \tilde{\rho}_{13} e^{i\phi_p} e^{-i\Delta_p t}) = \\ &= (\dot{\tilde{\rho}}_{12} - \tilde{\rho}_{12}(-i(\Delta_c - \Delta_p))) e^{i(\phi_p - \phi_c)} e^{i(\Delta_c - \Delta_p)t} \rightarrow \\ \frac{i}{2} (\Omega_p \tilde{\rho}_{32} - \Omega_c \tilde{\rho}_{13}) e^{i(\phi_p - \phi_c)} e^{i(\Delta_c - \Delta_p)t} &= (\dot{\tilde{\rho}}_{12} - \tilde{\rho}_{12}(-i(\Delta_c - \Delta_p))) e^{i(\phi_p - \phi_c)} e^{i(\Delta_c - \Delta_p)t} \rightarrow \\ \dot{\tilde{\rho}}_{12} &= \frac{i}{2} (\Omega_p \tilde{\rho}_{32} - \Omega_c \tilde{\rho}_{13}) - i\tilde{\rho}_{12}(\Delta_c - \Delta_p) \end{aligned} \quad (\text{A.22})$$

Note: this is free of all ‘fast’ time-varying exponential factors. Similarly:

$$\dot{\rho}_{13} = (\dot{\tilde{\rho}}_{13} - \tilde{\rho}_{13}(i\Delta_p)) e^{i\phi_p} e^{-i\Delta_p t} \quad (\text{A.23})$$

$$\begin{aligned} &= \frac{i}{2} (\Omega_p e^{i\phi_p} e^{-i\Delta_p t} (\rho_{33} - \rho_{11}) - \Omega_c e^{i\phi_c} e^{-i\Delta_c t} \tilde{\rho}_{12} e^{i(\phi_p - \phi_c)} e^{i(\Delta_c - \Delta_p)t}) \rightarrow \\ &(\dot{\tilde{\rho}}_{13} - \tilde{\rho}_{13}(i\Delta_p)) e^{i\phi_p} e^{-i\Delta_p t} = \frac{i}{2} (\Omega_p (\rho_{33} - \rho_{11}) - \Omega_c \tilde{\rho}_{12}) e^{i\phi_p} e^{-i\Delta_p t} \rightarrow \\ &\dot{\tilde{\rho}}_{13} = \frac{i}{2} (\Omega_p (\rho_{33} - \rho_{11}) - \Omega_c \tilde{\rho}_{12}) + i\tilde{\rho}_{13}\Delta_p \end{aligned} \quad (\text{A.24})$$

Similarly:

$$\dot{\rho}_{23} = (\dot{\tilde{\rho}}_{23} - \tilde{\rho}_{23}(i\Delta_c)) e^{i\phi_c} e^{-i\Delta_c t} \quad (\text{A.25})$$

$$\begin{aligned} &= \frac{i}{2} (\Omega_c e^{i\phi_c} e^{-i\Delta_c t} (\rho_{33} - \rho_{22}) - \Omega_p e^{i\phi_p} e^{-i\Delta_p t} \tilde{\rho}_{21} e^{-i(\phi_p - \phi_c)} e^{-i(\Delta_c - \Delta_p)t}) \rightarrow \\ &(\dot{\tilde{\rho}}_{23} - \tilde{\rho}_{23}(i\Delta_c)) e^{i\phi_c} e^{-i\Delta_c t} = \frac{i}{2} (\Omega_c (\rho_{33} - \rho_{22}) - \Omega_p \tilde{\rho}_{21}) e^{i\phi_c} e^{-i\Delta_c t} \rightarrow \\ &\dot{\tilde{\rho}}_{23} = \frac{i}{2} (\Omega_c (\rho_{33} - \rho_{22}) - \Omega_p \tilde{\rho}_{21}) + i\tilde{\rho}_{23}\Delta_c \end{aligned} \quad (\text{A.26})$$

All the other terms are just complex conjugates of the ones already given. This transformation/substitution operation got rid of all the fast terms and absorbed phase factors in the exponentials leaving us with equations we can more easily work with.

### A.3 Liouville-von Neumann Equation:

The Liouville-von Neumann equation can be derived from the Schrödinger equation, following Scully and Zubairy [13] pg. 160-161:

$$i\hbar \frac{d}{dt} |\psi\rangle = H |\psi\rangle$$

The density matrix:

$$\rho = \sum P_\psi |\psi\rangle \langle\psi|$$

We can take a derivative:

$$\dot{\rho} = \sum P_{\psi} \left( |\dot{\psi}\rangle \langle\psi| + |\psi\rangle \langle\dot{\psi}| \right)$$

Sub in from the Schrödinger Equation:

$$\begin{aligned} \dot{\rho} &= \sum P_{\psi} \left( \frac{-i}{\hbar} H |\psi\rangle \langle\psi| + |\psi\rangle \langle\psi| H \frac{i}{\hbar} \right) \\ \dot{\rho} &= \frac{-i}{\hbar} \sum P_{\psi} (H |\psi\rangle \langle\psi| - |\psi\rangle \langle\psi| H) \\ \dot{\rho} &= \frac{-i}{\hbar} [H, \rho] \end{aligned}$$

or:

$$i\hbar \frac{\delta\rho}{\delta t} = [\rho, H] \quad (\text{A.27})$$

We can also incorporate the relaxation rather naturally by an additional relaxation matrix:

$$\langle n | \Gamma | m \rangle = \gamma_n \delta_{nm}$$

The equation of motion becomes:

$$\dot{\rho} = \frac{-i}{\hbar} [H, \rho] - \frac{1}{2} \{\Gamma, \rho\}$$

## A.4 Unitary Transformation in Density Matrix Formalism

This section will discuss one of the convenient things about working with the density matrix. Rather than the cumbersome change of variables as discussed before we can accomplish the same simplifications in a cleaner way via a unitary transformation. This discussion is based in part on Daniel Steck's Quantum Optics notes[85].

Starting with Steck 5.33

$$\tilde{H} = \hat{U} \hat{H} \hat{U}^\dagger + i\hbar(\delta_t U) U^\dagger \quad (\text{A.28})$$

The operator that we want to use is a unitary operator, denoted by  $\hat{U}$ , which means it changes the overall phase but not the magnitude of our state vector,  $\hat{A}$ .

$$\hat{A} = \omega_k |k\rangle \langle k|$$

$$\hat{U} = \exp(i\omega_k t |k\rangle \langle k|)$$

Let us use a generic matrix so we can look at how this works:

$$\hat{U} = \begin{bmatrix} e^{i\alpha_1 t} & 0 & 0 \\ 0 & e^{i\alpha_2 t} & 0 \\ 0 & 0 & e^{i\alpha_3 t} \end{bmatrix} \quad (\text{A.29})$$

$$\begin{aligned} \tilde{H} = & \hbar \begin{bmatrix} e^{i\alpha_1 t} & 0 & 0 \\ 0 & e^{i\alpha_2 t} & 0 \\ 0 & 0 & e^{i\alpha_3 t} \end{bmatrix} \begin{bmatrix} \omega_1 & 0 & -\frac{\Omega_p}{2} e^{i\omega_p t} \\ 0 & \omega_2 & -\frac{\Omega_c}{2} e^{i\omega_c t} \\ -\frac{\Omega_p}{2} e^{-i\omega_p t} & -\frac{\Omega_c}{2} e^{-i\omega_c t} & \omega_3 \end{bmatrix} \begin{bmatrix} e^{-i\alpha_1 t} & 0 & 0 \\ 0 & e^{-i\alpha_2 t} & 0 \\ 0 & 0 & e^{-i\alpha_3 t} \end{bmatrix} \\ & + i\hbar \begin{bmatrix} i\alpha_1 e^{i\alpha_1 t} e^{-i\alpha_1 t} & 0 & 0 \\ 0 & i\alpha_2 e^{i\alpha_2 t} e^{-i\alpha_2 t} & 0 \\ 0 & 0 & i\alpha_3 e^{i\alpha_3 t} e^{-i\alpha_3 t} \end{bmatrix} \end{aligned}$$

$$\tilde{H} = \hbar \begin{bmatrix} \omega_1 & 0 & -\frac{\Omega_p}{2} e^{i\omega_p t} e^{-i\alpha_3 t} e^{i\alpha_1 t} \\ 0 & \omega_2 & -\frac{\Omega_c}{2} e^{i\omega_c t} e^{-i\alpha_3 t} e^{i\alpha_2 t} \\ -\frac{\Omega_p}{2} e^{-i\omega_p t} e^{-i\alpha_1 t} e^{i\alpha_3 t} & -\frac{\Omega_c}{2} e^{-i\omega_c t} e^{-i\alpha_2 t} e^{i\alpha_3 t} & \omega_3 \end{bmatrix}$$

$$+ i\hbar \begin{bmatrix} i\alpha_1 e^{i\alpha_1 t} e^{-i\alpha_1 t} & 0 & 0 \\ 0 & i\alpha_2 e^{i\alpha_2 t} e^{-i\alpha_2 t} & 0 \\ 0 & 0 & i\alpha_3 e^{i\alpha_3 t} e^{-i\alpha_3 t} \end{bmatrix}$$

$$\tilde{H} = \hbar \begin{bmatrix} \omega_1 - \alpha_1 & 0 & -\frac{\Omega_p}{2} e^{i\omega_p t} e^{-i\alpha_3 t} e^{i\alpha_1 t} \\ 0 & \omega_2 - \alpha_2 & -\frac{\Omega_c}{2} e^{i\omega_c t} e^{-i\alpha_3 t} e^{i\alpha_2 t} \\ -\frac{\Omega_p}{2} e^{-i\omega_p t} e^{-i\alpha_1 t} e^{i\alpha_3 t} & -\frac{\Omega_c}{2} e^{-i\omega_c t} e^{-i\alpha_2 t} e^{i\alpha_3 t} & \omega_3 - \alpha_3 \end{bmatrix}$$

This generic approach lets us set some conditions. For example to eliminate the oscillating terms in  $H_{13}$  and  $H_{23}$ :

$$-\alpha_3 + \alpha_1 + \omega_p = 0$$

$$\alpha_2 - \alpha_3 + \omega_c = 0$$

We have 3 variables and 2 equations so one free parameter. let us also set  $\omega_1 = \alpha_1$  to further simplify our Hamiltonian by making  $H_{11}$  zero, yielding:

$$\alpha_3 = \omega_1 + \omega_p \tag{A.30}$$

$$\alpha_2 = \alpha_3 - \omega_c = \omega_1 + \omega_p - \omega_c \tag{A.31}$$

Applying to our Hamiltonian:

$$\tilde{H} = \hbar \begin{bmatrix} \omega_1 - \alpha_1 & 0 & -\frac{\Omega_p}{2} e^{i\omega_p t} e^{-i\alpha_3 t} e^{i\alpha_1 t} \\ 0 & \omega_2 - \alpha_2 & -\frac{\Omega_c}{2} e^{i\omega_c t} e^{-i\alpha_3 t} e^{i\alpha_2 t} \\ -\frac{\Omega_p}{2} e^{-i\omega_p t} e^{-i\alpha_1 t} e^{i\alpha_3 t} & -\frac{\Omega_c}{2} e^{-i\omega_c t} e^{-i\alpha_2 t} e^{i\alpha_3 t} & \omega_3 - \alpha_3 \end{bmatrix}$$

Simplifies it to:

$$\tilde{H} = \hbar \begin{bmatrix} 0 & 0 & -\frac{\Omega_p}{2} \\ 0 & \Delta_p - \Delta_c & -\frac{\Omega_c}{2} \\ -\frac{\Omega_p}{2} & -\frac{\Omega_c}{2} & \Delta_p \end{bmatrix} \quad (\text{A.32})$$

Let us also note our generic unitary transform matrix is:

$$\hat{U} = \begin{bmatrix} e^{i\alpha_1 t} & 0 & 0 \\ 0 & e^{i\alpha_2 t} & 0 \\ 0 & 0 & e^{i\alpha_3 t} \end{bmatrix} = \begin{bmatrix} e^{i\omega_1 t} & 0 & 0 \\ 0 & e^{i(\omega_1 + \omega_p - \omega_c)t} & 0 \\ 0 & 0 & e^{i(\omega_1 + \omega_p)t} \end{bmatrix} \quad (\text{A.33})$$

## A.5 Steady State Small Probe Solution

At this point our problem has become deriving an expression for the coherence between the states linked by the probe. This function of laser powers (Rabi frequencies) and detunings should give our desired EIT resonance shape, as well as a normal resonance shape when we turn off the control laser. An analytical solution for the coherence can be found if we consider that in steady state, all of our  $\dot{\rho}$  equations will be equal to zero. Additionally, we will assume that essentially all the population stays in the probe ground state because the probe beam is weak. Starting from our equations for the coherences (equation 2.15 and adjacent ) and employing these simplifications:

Our  $\dot{\tilde{\rho}}_{12}$  equation:

$$\dot{\tilde{\rho}}_{12} = \frac{i}{2} (\Omega_p \tilde{\rho}_{32} - \Omega_c \tilde{\rho}_{13}) - i \tilde{\rho}_{12} (\Delta_c - \Delta_p) - \frac{(\Gamma_{22} + \Gamma_{11})}{2} \tilde{\rho}_{12}$$

yields:

$$i\Omega_c \tilde{\rho}_{13} = -(2i(\Delta_c - \Delta_p) + (\Gamma_{22} + \Gamma_{11})) \tilde{\rho}_{12} + i\Omega_p \tilde{\rho}_{32} \quad (\text{A.34})$$

$\dot{\tilde{\rho}}_{13}$  equation yields:

$$\dot{\tilde{\rho}}_{13} = \frac{i}{2} (\Omega_p (\rho_{33} - \rho_{11}) - \Omega_c \tilde{\rho}_{12}) + i \tilde{\rho}_{13} \Delta_p - \frac{(\Gamma_{33} + \Gamma_{11})}{2} \tilde{\rho}_{13}$$

Assuming population in  $\rho_{33}$  is negligible and  $\rho_{11} = 1$ , this becomes:

$$i\Omega_p + i\Omega_c\tilde{\rho}_{12} = (2i\Delta_p - (\Gamma_{33} + \Gamma_{11}))\tilde{\rho}_{13} \quad (\text{A.35})$$

Our  $\dot{\tilde{\rho}}_{23}$  equation:

$$\dot{\tilde{\rho}}_{23} = \frac{i}{2} (\Omega_c(\rho_{33} - \rho_{22}) - \Omega_p\tilde{\rho}_{21}) + i\tilde{\rho}_{23}\Delta_c - \frac{(\Gamma_{33} + \Gamma_{22})}{2}\tilde{\rho}_{23}$$

assuming populations in  $\rho_{33}$  and  $\rho_{22}$  are negligible, becomes:

$$\tilde{\rho}_{23} = \frac{i\Omega_p\tilde{\rho}_{21}}{2i\Delta_c - (\Gamma_{33} + \Gamma_{22})} \quad (\text{A.36})$$

Now we can substitute equation A.36 into A.34; notice however that this term will now be second order in  $\Omega_p$ , *i.e.*, very small and can be neglected, yielding the following:

$$i\Omega_c\tilde{\rho}_{13} = -(2i(\Delta_c - \Delta_p) + (\Gamma_{22} + \Gamma_{11}))\tilde{\rho}_{12}$$

Now let us reorganize this for  $\rho_{12}$ :

$$\tilde{\rho}_{12} = \frac{-i\Omega_c\tilde{\rho}_{13}}{(2i(\Delta_c - \Delta_p) + (\Gamma_{22} + \Gamma_{11}))}$$

and plug into equation A.35

$$i\Omega_p + i\Omega_c \left( \frac{-i\Omega_c\tilde{\rho}_{13}}{(2i(\Delta_c - \Delta_p) + (\Gamma_{22} + \Gamma_{11}))} \right) = (2i\Delta_p - (\Gamma_{33} + \Gamma_{11}))\tilde{\rho}_{13}$$

Solve for  $\rho_{13}$

$$\left( (2i\Delta_p - (\Gamma_{33} + \Gamma_{11})) + \frac{-\Omega_c^2}{(2i(\Delta_c - \Delta_p) + (\Gamma_{22} + \Gamma_{11}))} \right) \tilde{\rho}_{13} = i\Omega_p$$

$$\tilde{\rho}_{13} = \frac{i\Omega_p (2i(\Delta_c - \Delta_p) + (\Gamma_{22} + \Gamma_{11}))}{(2i(\Delta_c - \Delta_p) + (\Gamma_{22} + \Gamma_{11})) (2i\Delta_p - (\Gamma_{33} + \Gamma_{11})) - \Omega_c^2} \quad (\text{A.37})$$

We can make some further simplifications. Let us assume the control beam is on resonance, *i.e.*,  $\Delta_c = 0$ . Let us also assume there is no decay between the ground states; *i.e.*,  $\Gamma_{11} = \Gamma_{22} = 0$ .

$$\tilde{\rho}_{13} = \frac{2\Delta_p\Omega_p}{4\Delta_p^2 + 2i\Gamma_{33}\Delta_p - \Omega_c^2} \quad (\text{A.38})$$

Put it all together to get the susceptibility:

$$\chi = \frac{N\mu_{31}^2}{\epsilon_0\hbar} \frac{2\Delta_p\Omega_p}{4\Delta_p^2 + 2i\Gamma_{33}\Delta_p - \Omega_c^2} \quad (\text{A.39})$$

This is the simplest expression that contains the EIT behavior that we want to see.

## A.6 6-level System Unitary Transformation:

The total Hamiltonian:

$$H = \frac{\hbar}{2} \begin{bmatrix} 2\omega_1 & 0 & 0 & 0 & -\Omega_r e^{i\omega_r t} & 0 \\ 0 & 2\omega_2 & 0 & 0 & 0 & -\Omega_p e^{i\omega_p t} \\ 0 & 0 & 2\omega_3 & 0 & 0 & -\Omega_c e^{i\omega_c t} \\ 0 & 0 & 0 & 2\omega_4 & 0 & 0 \\ -\Omega_r e^{-i\omega_r t} & 0 & 0 & 0 & 2\omega_5 & 0 \\ 0 & -\Omega_p e^{-i\omega_p t} & -\Omega_c e^{-i\omega_c t} & 0 & 0 & 2\omega_6 \end{bmatrix}$$

Let us transform to get rid of oscillatory pieces. As in section A.4:

$$\tilde{H} = \hat{U} \hat{H} \hat{U}^\dagger + i\hbar(\delta_t U)U^\dagger$$

Generically:

$$\hat{U} = \begin{bmatrix} e^{i\alpha_1 t} & 0 & 0 & 0 & 0 & 0 \\ 0 & e^{i\alpha_2 t} & 0 & 0 & 0 & 0 \\ 0 & 0 & e^{i\alpha_3 t} & 0 & 0 & 0 \\ 0 & 0 & 0 & e^{i\alpha_4 t} & 0 & 0 \\ 0 & 0 & 0 & 0 & e^{i\alpha_5 t} & 0 \\ 0 & 0 & 0 & 0 & 0 & e^{i\alpha_6 t} \end{bmatrix}$$

Applying the von-Neumann equation to these ingredients, you get the following:

$$\tilde{H} = \frac{\hbar}{2} \left[ \begin{array}{ccccccc} 2\omega_1 - 2\alpha_1 & 0 & 0 & & & & \\ 0 & 2\omega_2 - 2\alpha_2 & 0 & & & & \\ 0 & 0 & 2\omega_3 - 2\alpha_3 & & & & \dots \\ 0 & 0 & 0 & & & & \\ -\Omega_r e^{-i\omega_r t} e^{-i\alpha_1 t} e^{i\alpha_5 t} & 0 & 0 & & & & \\ 0 & -\Omega_p e^{-i\omega_p t} e^{-i\alpha_2 t} e^{i\alpha_6 t} & -\Omega_c e^{-i\omega_c t} e^{-i\alpha_3 t} e^{i\alpha_6 t} & & & & \\ & 0 & -\Omega_r e^{i\omega_r t} e^{-i\alpha_5 t} e^{i\alpha_1 t} & 0 & & & \\ & 0 & 0 & -\Omega_p e^{i\omega_p t} e^{-i\alpha_6 t} e^{i\alpha_2 t} & & & \\ & 0 & 0 & -\Omega_c e^{i\omega_c t} e^{-i\alpha_6 t} e^{i\alpha_3 t} & & & \\ & 2\omega_4 - 2\alpha_4 & 0 & 0 & & & \\ & 0 & 2\omega_5 - 2\alpha_5 & 0 & & & \\ & 0 & 0 & 2\omega_6 - 2\alpha_6 & & & \end{array} \right]$$

Since we have more parameters than conditions, we have some freedom in choosing them so as to clean up the Hamiltonian and eliminate some terms. Choosing the following configuration:

$$\begin{aligned} \alpha_1 &= \omega_1 \\ \alpha_2 &= \omega_2 \\ \alpha_4 &= \omega_4 \\ \alpha_3 &= \omega_p + \omega_2 - \omega_c \\ \alpha_5 &= \omega_r + \omega_1 \\ \alpha_6 &= \omega_2 + \omega_p \end{aligned} \tag{A.40}$$

Yields the following Hamiltonian:

$$\tilde{H} = \frac{\hbar}{2} \begin{bmatrix} 0 & 0 & 0 & 0 & -\Omega_r & 0 \\ 0 & 0 & 0 & 0 & 0 & -\Omega_p \\ 0 & 0 & 2(\Delta_p - \Delta_c) & 0 & 0 & -\Omega_c \\ 0 & 0 & 0 & 0 & 0 & 0 \\ -\Omega_r & 0 & 0 & 0 & 2\Delta_r & 0 \\ 0 & -\Omega_p & -\Omega_c & 0 & 0 & 2\Delta_p \end{bmatrix} \quad (\text{A.41})$$

## Appendix B: Index Enhancement Experiment

Some of the material in this appendix chapter is discussed in chapter 2, [Refractive Index Enhancement in Atomic Systems Using EIT](#), section 2.3, but there is a lot more science from that experiment I would like to include in this thesis. It does not really fit with the the main story, so I will include it here. I do not want to leave this out because it discusses an experiment in which I did the experimental work and am pretty proud of it[19].

As discussed briefly in section 2.3, the key idea of this experiment was to engineer the refractive index by utilizing a combination of two Raman resonances, a gain resonance and an absorption resonance. Those resonances can be moved in frequency relative to each other by changing their 2-photon detunings, see figure 2.8. Since the single-photon detuning of the Raman beams is large compared to their two-photon detuning, adjusting the 2-photon detuning over a small range does not change the response of each resonance very much. This flexibility is a huge strength of this technique. This is much easier to do than try and find a system with both a gain and absorption resonance at close to the same frequency as set by the atomic structure.

### Experiment Set-Up

The experiment was performed in Rubidium 85. Figure B.1 shows the Rb hyperfine structure and laser detunings<sup>1</sup>.

Let me explain the experiment in a little more detail. One of the interesting things about this experiment, compared to our current Rb experiments, or our new Eu:YSO effort, is that it is performed in a vapor cell. The apparatus is simple comparatively; we need no vacuum system or cryostat, in fact we actually heat the vapor to increase the atomic density. Were I to be in a position to be setting up a lab, I think vapor-cell experiments are really enticing as a place to start because of these logistical advantages. See figure B.2 for a schematic of the set-up.

The heated, 1 mm long, natural abundance Rb vapor cell is housed in mu-metal magnetic shielding canister to prevent Zeeman effects. The vapor cell contains 10 Torr of nitrogen as a

---

<sup>1</sup>Note: this figure as well as the other figures in this appendix are reprinted with permission from [19] © 2015 by the American Physical Society.

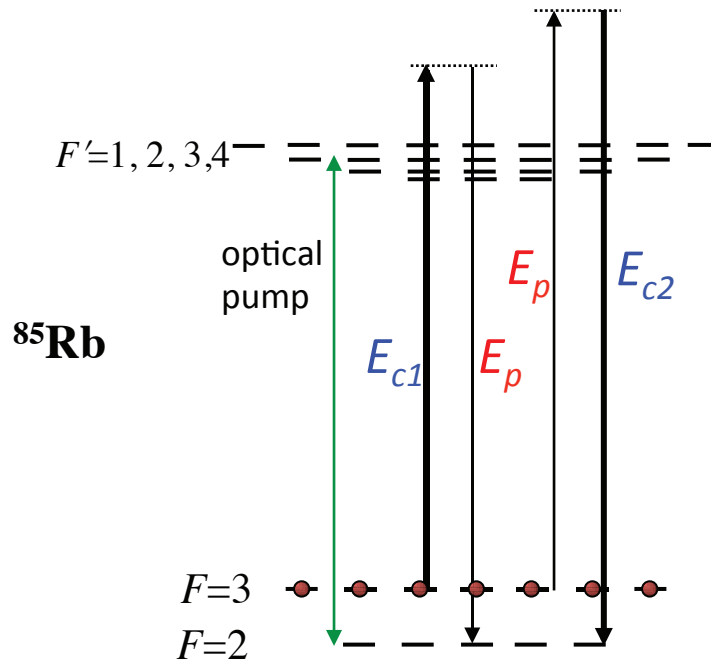


Figure B.1: Rubidium energy level structure: The D2 line in  $^{85}\text{Rb}$  was used for this index enhancement experiment. Population is pumped via strong control laser (and additional pump laser for some configurations) to  $F=3$ . Absorptive and gain Raman transitions are formed between hyperfine ground states by the application of two control lasers.  $E_{c1}$  is  $\Delta_{hf}$  below the probe,  $E_p$ , while  $E_{c2}$  is spaced  $\Delta_{hf}$  above, where  $\Delta_{hf}$  is the hyperfine ground state splitting of 3.035 GHz.

buffer gas. Control and probe lasers are derived from a single ECDL and hyperfine ground state level splittings are achieved via high frequency AOMs. Control beams are combined together and then combined on a beam cube with the probe beam. These beams pass through the vapor cell and the probe is separated via a high-quality polarizer, a Glan-Taylor. Note, because of the fact we are working with a heated gas, it is very important that the laser beams have clean spatial modes (we pass them through single-mode fibers) and are co-linear. Poorly overlapped beams will sample different Doppler-classes of atoms and the experiment will not work. Additionally, we use

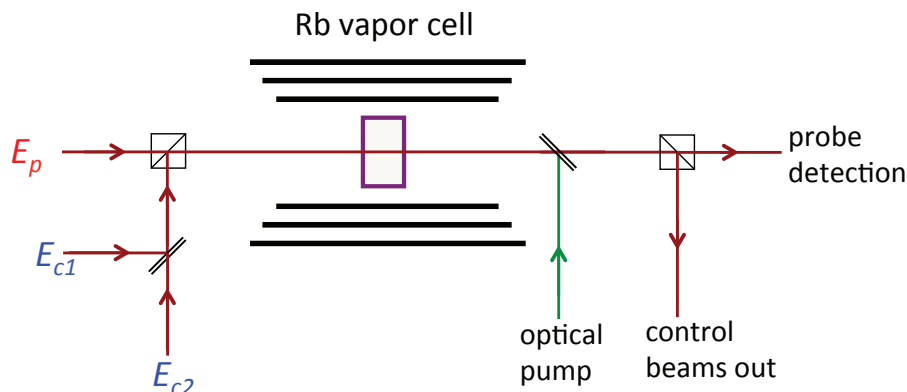


Figure B.2: Raman Index Enhancement Experiment Set-Up: Heated Rb vapor cell is housed in magnetically-shielded enclosure. Control lasers are combined together and combined with probe on a polarizing cube. Glan-taylor allows for separation of probe beam from control beams on far side of experiment region. Note: only the center of the probe is sampled, a small pinhole is placed in front of photodiode.

a pinhole on the probe beam at detection to only sample the center of the beam, to limit ourselves to more uniform intensity.

## Absorption Spectroscopy

One aspect of this experiment that worked remarkably well was the absorption spectroscopy measurements of the D2 line. In order to accurately characterize changes in refractive index, we need to know the density of the Rb vapor precisely. We can estimate it from the temperature of the cell, but a better method is to fit the absorption spectrum to a model that includes the broadened linewidths, matrix elements, and other parameters, and derive from that the density. Absorption spectroscopy was performed by manually scanning the laser (by adjusting its diode current and grating position) across the D2 line for different cell temperatures. See figure B.3 for experimental data and density fits, data summarized in table B.1.

Although we are only utilizing the  $^{85}\text{Rb}$  energy level structure for our Raman transitions, the  $^{87}\text{Rb}$  is also present as its a natural abundance vapor cell. As the cell temperature is increased,

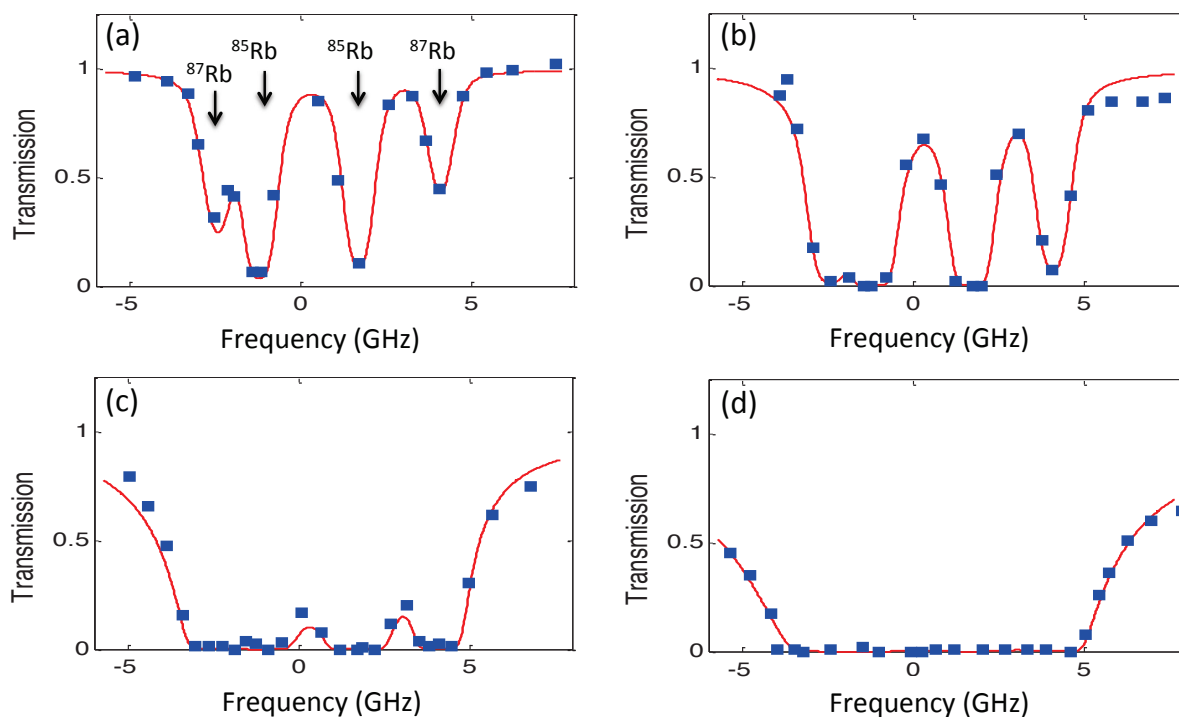


Figure B.3: Absorption spectroscopy of  $^{85}\text{Rb}$  D2 line. As the temperature is increased ( a)=96, b)=115, c)=144, d)=163°C), the vapor density increases and there is more laser absorption. Spectral features become increasingly saturated until the 4 formerly distinct features corresponding to the two pairs of ground manifolds for  $^{85}\text{Rb}$  and  $^{87}\text{Rb}$  all merge into one saturated feature. Calculation and experiment agree very well.

the density increases and the spectral features get increasingly saturated. This can be seen in the absorption spectroscopy scans. Initially you can resolve 4 features, two ground state manifolds for  $^{85}\text{Rb}$  separated by 3.035 GHz and two ground state manifolds for  $^{87}\text{Rb}$  separated by its larger hyperfine ground state splitting of 6.085 GHz. The  $^{87}\text{Rb}$  absorption appears smaller, especially at low temperature, because natural abundance Rb is about 27%  $^{87}\text{Rb}$ .

I should also mention, that we can improve performance somewhat with the application of a dedicated pump laser, as shown in figure B.1. This has the effect of making sure the vast majority of the population is in  $F=2$ . This in turn improves the Raman transition performance. At high

Temperature ( $^{\circ}\text{C}$ )	Density $N/\text{cm}^3$
96	$4.4 \times 10^{12}$
115	$1.5 \times 10^{13}$
144	$7.1 \times 10^{13}$
163	$1.8 \times 10^{14}$

Table B.1: Rb vapor cell density with temperature

control power, the control,  $E_{c1}$ , does a relatively good job depleting  $F=2$  as it is closest to being resonant of the control beams.

## Index Enhancement

Accurate knowledge of the density as discussed above is combined with the gain and absorption features manifest over the length of the vapor cell to back out the imaginary part of index of refraction. The imaginary part of the index can then be used to infer the change in the real index via Kramers-Kronig relationships, see section 2.3 and appendix D.

Experimental data showing index enhancement of  $\sim 0.4 \times 10^{-4}$  was already shown in the main body of this thesis, see figure 2.9. It is very neat to be able to move the resonances around by changing their detunings and see this reflected in the location in frequency of gain and absorption. The flexibility of this Raman scheme is pretty amazing.

## Experimental Limitations

So how much can we change the index using this technique? Although this experiment was a substantial improvement ( $\times 100$ ) over our earlier proof of principle experiment [18], there is still a lot of room to improve further. In principle, the maximum expected index modification is  $\Delta n \sim 0.4$ .

We have a couple knobs that we can turn to try and increase the index enhancement effect, namely 1) the temperature/density, and 2) the power of the Raman control lasers. If we look at the

maximum Raman gain that we observe for example, as we increase the temperature, we see the probe gain increase and then it saturates above about 160 °C. See figure B.4. There are a variety of effects that could be curtailing us at high temperature/density. Rb could be starting to form molecules. The interaction of Rb with the walls of the cell could be interfering, causing additional relaxation and degrading the atomic coherence. There could be radiation trapping. We need a more sophisticated understanding of the dynamic at high density.

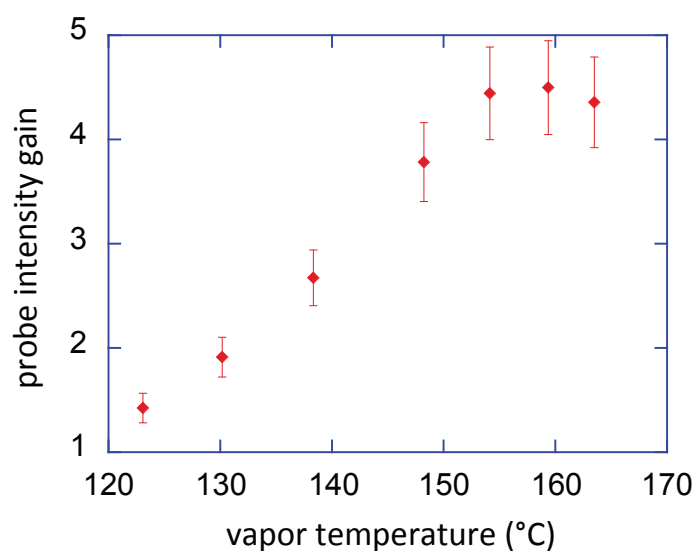


Figure B.4: Saturation of Raman gain with temperature. Raman gain increases up to  $\sim 160^\circ\text{C}$  and then saturates.

Note, we see a similar saturation behavior with the control beam power. The amount of gain increases with control laser power up to about 100 mW and then stops increasing.

An additional technical limitation is that we do not see optimal performance with both control lasers on at the same time, *i.e.*, the gain and absorption resonances are larger if we have only their respective control laser on. It seems reasonable that with a relatively large amount of control-beam light at play in the vapor cell, it may cause problems including some sort of negative cross-talk between the two resonances/Raman transitions that degrades the performance of each. Let me mention one other result related to this. The maximum gain or absorption that we observe, when

using only one control beam or the other, is about a factor of 10. See figure B.5 for experimental data. If we could manage to drive both of our Raman transitions without having them interfere with each other and get the performance that we see for the resonances independently, such gain and absorption would correspond to a real enhancement to the index of refraction with a maximum value of about  $1.5 \times 10^{-4}$ , twice to three times what we have observed.

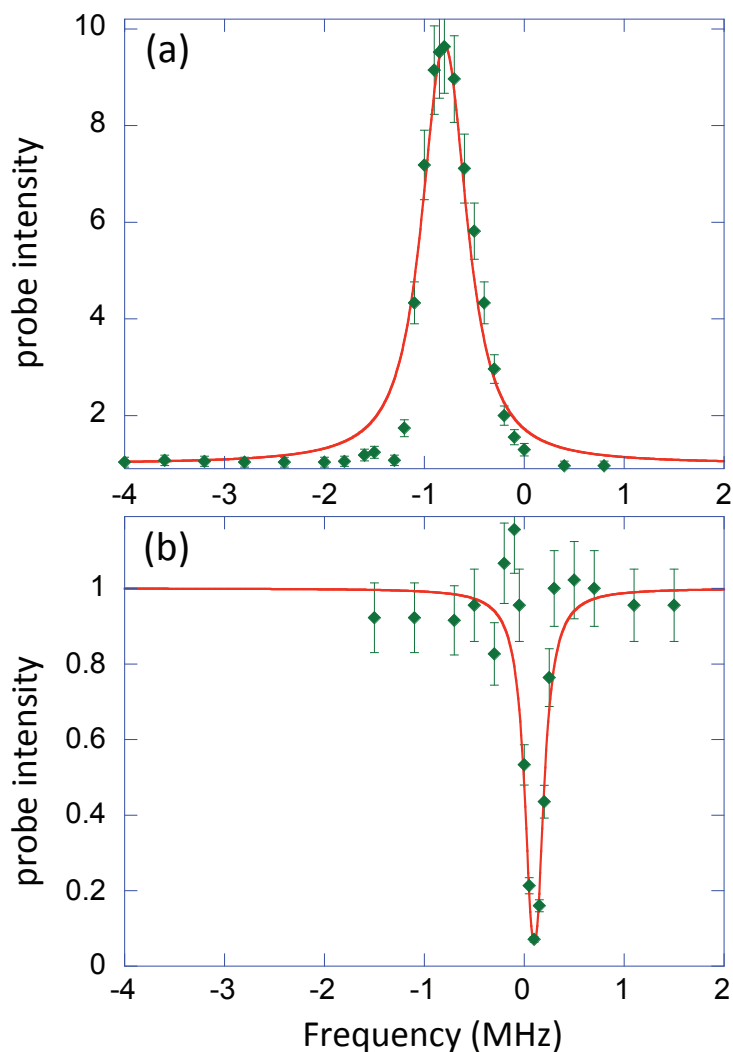


Figure B.5: Maximum observed gain and absorption: We get better gain or absorption performance when only one of the control beams is on at a time. In this mode, we have seen a gain as high as a factor of 10 a) and absorption of a factor of 13 b).

## Future Prospects for this Experiment

In the time since this experiment was performed, the laser system has been utilized with another experiment[29], and that experiment is wrapping up. Now may be the time to implement some changes and give this Raman experiment another go.

1. **Cell Material:** One of the issues that arises at high temperature/density is that the Rubidium atoms start to interact more with the walls of the vapor cell, causing relaxation and degrading the atomic coherence. One simple modification to the experiment we could make would be to swap our glass cells with a sapphire cell. Apparently such cells work better than glass at high temperature as the Rb interacts less with the sapphire walls.

Another possibility in this vein that we need to investigate is the use of an anti-relaxation coating on the inside of the cell. The cells we currently use are plain glass. There is a lot of interest in anti-relaxation coatings for use in magnetometry experiments. Straessle has a nice discussion of the different coating options in a recent paper [86]. The best coatings (the coating that allow for the most bounces off the cell walls) are alkenes, but they only work up to about 30°C. Another class of coatings, alkanes, degrade above 90°C, still much too low for our application. Ideally we would heat the cell to at least 160°C. There is one class of coatings, organosilanes, such as octadecyltrichlorosilane (OTS), that bond to the glass and are stable up to 170°C. This could be a fruitful thing to try in our experiment. Such a coating may allow us to utilize a shorter cell as well.

2. **Cell Geometry:** Another easy-to-try modification that we could make to the experiment would be to use a shorter cell. We tried a shorter cell previously but it did not seem to work as well as our longer cell. Perhaps it was an issue of the aspect ratio of the cell. Also, if we were to try cells of a different material, perhaps the short cell would work better.
3. **Single Isotope:** A really easy thing to try would be a single isotope vapor cell. Perhaps there are some detrimental processes happening between the two isotopes at high temperature/pressure that would be improved if we had a single isotope sample.

4. **Operating on the D1 line:** This would be the most sophisticated change to the set-up and would require changing the set-up from 780 nm lasers to 795 nm. This modification has already been made! In the course of recent localization experiments using the laser set-up, the Rb laser system was changed to operate on the D1 line. This already being done only adds to the incentive to give these experiments another attempt.

## Appendix C: Calculating Optical Transitions

The purpose of this appendix is to collect some information about using codes to calculate atomic structure information for Eu. It is long on procedure and is not really science, so is best put in an appendix. It will feature two methods: 1) calculations for the free ion using the Cowan code and 2) calculations for the ion in a crystal using RELIC. The actual details of using the Cowan code is a little confusing. I have collected more information in another document about how to use the Cowan code<sup>1</sup>. We will include just the results of these investigation here.

### C.1 Free Ion: Calculating the $Eu^{3+}4F$ Magnetic Dipole Spectrum with Cowan's Code

As a first step in our  $Eu^{3+}$  structure investigations, we can look at the free ion. There are programs that allow us to calculate wavelengths, transitions strengths and other information for free atoms and ions. The Cowan code is one such program and was used to calculate the wavelengths, decay rates, and other parameters of the lowest-lying magnetic dipole transitions, of which our  ${}^5D_1 - {}^7F_0$  is one. It is pretty neat once you figure out how to run the code; the only essential input information is the configuration. You put in 4F and that there are 6 electrons and it calculates all the levels and magnetic transitions.

Let me note a couple of relations for helping to interpret the output from the code. For one, we can relate the oscillator strength to the decay rate. They are different ways of expressing the strength of the transition including oscillator strength, matrix element and line strength,  $\mu^2$ .

They are related through some factors, see Cowan's book[42] equation 14.38:

$$gA = \frac{8\pi^2 e^2 \sigma^2}{mc} gf \quad (C.1)$$

$e$  and  $m$  are the charge and mass of the electron, respectively.  $\sigma$  is the wavenumber (You will need to convert to inverse meters to be dimensionally consistent). Note there is an implicit

---

<sup>1</sup>Note to Yavuzlab: see the wiki

factor of  $1/4\pi\epsilon_0$ . If we evaluate this expression, it is a way for us to convert between decay rates and oscillator strengths.

We would like to extract from the output of the Cowan code a matrix element that we could use in our simulations. We can calculate this from the decay rate or oscillator strength, Cowan equation 14.33 or 14.37, respectively. This will give you an effective matrix element in units of  $ea_0$  as if the transition were an electric dipole transition. We can convert this effective electric dipole matrix element into a magnetic dipole matrix element by multiplying by  $c$ . This is just a realization that to get the same response, being that B is weaker than E by a factor of  $c$ , the magnetic matrix element must be  $c$  stronger. This can then be expressed in terms of the Bohr magneton,  $\frac{e\hbar}{2m_e}$ .

$$\mu_{effE1} \rightarrow c\mu_{effE1} = \mu_{M1} \quad (C.2)$$

(As an aside, we should see if there are any required modifications to this for magnetic dipole transitions, as these expressions were developed toward electric transitions.)

A couple of notes about these expressions in Cowan's book: I found them confusing because they appear to be written as if  $S$  is dimensionless: *i.e.*, a factor of  $e^2a_0^2$  in the prefactor. The wavenumber appears to be treated differently though,  $\sigma$  does have units of 1/length. Let us evaluate it:

$$S = gf \frac{3h}{8\pi^2 m c a_0^2 \sigma} = 3.1 \times 10^{-7} e^2 a_0^2 \rightarrow \mu = 5.6 \times 10^{-4} ea_0 \quad (C.3)$$

Let us organize some of this information, including calculating matrix elements for all our Eu lines of interest in table C.1:

A few comments on the allowed transitions: Interestingly, our transition is not particularly strong, although stronger than the  ${}^5D_0 - {}^7F_0$  which is not computed by the Cowan code as it is E1 and M1 forbidden. It appears that there are slightly stronger red ( ${}^5D_0 \rightarrow {}^7F_1$ ) and considerably stronger yellow ( ${}^5D_1 \rightarrow {}^7F_2$ ) transitions, which I suspect are responsible for the majority of the fluorescence that we see when we put green light into the crystal. The  ${}^5D_0 \rightarrow {}^7F_0$  is probably part of that as it is stronger than one might expect an electric quadrupole transition to be. Note:

Transition		E ( $cm^{-1}$ )	$\lambda$ (nm)	$log_{10}(gf)$	gf	gA (Hz)	$\mu(\mu_B)$	$\mu_{Eff}(ea_0)$
$5D_0$	$7F_1$	16413	609	-7.056	8.79E-8	15.8	0.34	1.328E-3
$5D_1$	$7F_0$	18691	535	-7.751	1.77E-8	4.134	0.14	5.59E-4
$5D_1$	$7F_1$	18260	548	-10.353	4.44E-11	9.87E-3	0.01	2.83E-5
$5D_1$	$7F_2$	17518	571	-6.708	1.96E-7	40.1	0.5	1.919E-3
$5D_1$	$5D_0$	1847	5414	-6.376	4.21E-7	0.958	2.24	8.66E-3
$7F_2$	$7F_1$	742	13477	-6.184	6.55E-7	0.240	4.42	1.7042E-2
$7F_1$	$7F_0$	430	23236	-6.697	2.01E-7	0.0248	3.21	1.2402E-2

Table C.1: Eu transitions of interest from Cowan code

Ofelt has calculated some of these oscillator strengths for  $EuCl_3$ [46]; the agreement for the red and green lines seems too good to be true.

Something else that is interesting is that intra-manifold transitions are also magnetic dipole allowed, and in fact are predicted to be stronger than our transition of interest.  ${}^5D_1 - {}^5D_0$  is  $15\times$  stronger than  ${}^5D_1 - {}^7F_0$ . Combining this with information about nonradiative decay, we should be able to model incoherent processes pretty easily and see, for example, if population is accumulating somewhere it should not be. Were we to look at the spectral content of the fluorescence, we would get addition information to help us understand this aspect of our system.

A question crops up regarding our magnetic dipole transitions. If these magnetic transition are so weak, do we need to consider electric quadrupole transitions as well? Are they of comparable strength? One would think this could be particularly important in the crystal system that is going to mix different kinds of interactions. I tried to see if the Cowan code could help me address this question by looking for D2 transitions, but I did not find anything, and couldn't get any electric quadrupole spectrum output. It appears E2 transitions should be something like  $1000\times$  weaker than the M1 transitions, and so this should not be an issue for us.

In summary, this information from the Cowan code is useful as it gives us insight into the relative strengths of the allowed magnetic dipole transitions in Eu. We can also note some key

observations: 1) Our transition is not the strongest from the  ${}^5D_1$ . The  ${}^5D_1 - {}^7F_2$  is about  $3\times$  stronger than to the  ${}^7F_0$ . 2) There are also allowed magnetic dipole transitions between levels in a manifold:  ${}^5D_1 - {}^5D_0$ ,  ${}^7F_2 - {}^7F_1 - {}^7F_0$ . In fact the  ${}^5D_1 - {}^5D_0$  is much stronger in that it has a larger matrix element than the  ${}^5D_1 - {}^7F_0$ , but less likely because the decay rate is also proportional to the energy of the transitions squared, and the  ${}^5D_1 - {}^5D_0$  is a much lower energy transition (about  $10\times$  less).

I would also add that these other transitions and understanding this material are quite important to our experiment, as this is a significant difference between our experiment and other rare-earth doped crystal experiments with Eu, as most of them deal with the yellow transition from the  ${}^5D_0$ .

## **C.2 (not) Free Ion: influence of the crystal environment and Judd-Ofelt theory:**

Looking at the free ion is good for first order understanding, but in order to really model what's going on, we need to incorporate the influence of the crystal. This can be accomplished through Judd-Ofelt theory.

### **C.2.1 Background**

A consequence of being in the crystal is that transitions that are not allowed in the free ion become allowed and in fact may be stronger than the allowed magnetic dipole transitions[44]. These transitions are called 'forced electric dipole' transitions. Additionally, the perturbing influence of the crystal environment can affect the allowed magnetic dipole transitions, although, it seems the M1 transitions are much more weakly influenced by the crystal environment.

There is a large and established body of theoretical work that investigates intra-F-level transitions in rare-earth doped crystals and glasses. The theory is known as Judd-Ofelt theory, after the architects of the original theory(1962). I am fond of this paper[43] on the subject by Hehlen, Brik and Kramer. Walsh also has a nice chapter on the subject[47]. There are whole books written on the subject, but let me explain it a little bit here, drawing heavily on the already cited review papers and software documentation.

One of the main lessons regarding this material is that a large part of the task of calculating, for example, forced transitions in a crystal, is to have good theoretical grounding of the atomic physics problem irrespective of the crystal. What I mean is that it is difficult to solve for the wavefunctions and energies of the rare-earth ions because they are heavy and complicated. For one they are not particularly well described by LS-coupling. In LS coupling, one treats spin and orbital angular momentum separately, *i.e.*,  $S = \sum s_i$  and  $L = \sum l_i$ , and then see how those two vectors combine:  $J = L + S$ . However, the alternative, j-j coupling where one couples the spin and orbital angular momentum of each individual electron together first, *i.e.*,  $s_i + l_i = j_i$  and then combine to find the total J,  $J = \sum j_i$ , does not work very well either. This situation is known as the ‘intermediate coupling’ regime, and another way to think about it is to recognize that the spin-orbit interaction becomes comparable in strength to the electrostatic interaction for these heavy atoms. A way to visualize this energy splitting is to consider that the spin-orbit interaction splits the J levels in a given manifold, and, as we know from working in our system, that splitting is significant:  $\sim 1700\text{cm}^{-1}$  between the  ${}^5D_1$  and  ${}^5D_0$  and  $\sim 500\text{-}1000\text{cm}^{-1}$  in the ground  ${}^7F$  manifold. On the one hand this makes the problem more difficult to solve. On the other hand, it is interesting as Hehlen and his co-authors note that the spin-orbit and electrostatic interaction is the vast majority of the interaction (they quote 80-90%) in these atoms and so an approach that finds the energies due just to those interactions (the intermediate coupling approximation) is still quite useful.

In addition to being in the intermediate coupling regime, the rare-earth configurations are also complicated, and Eu is one of the most complicated. This is due simply to the fact that there are many ways to arrange  $\text{Eu}^{3+}$ 's 6 electrons (micro-states) in the 4F level in the L-S scheme; there are 3003. This in of itself is not such a problem, as we do not care about the vast majority of those configurations, as our transition does not operate on them, but there is an additional complication. This comes about from the fact that different micro-states can have the same term, *i.e.*, different arrangements of the individual electrons in the L-S scheme can have the same total L and S, and so there is an ambiguity in the LS term labeling. This ambiguity is dealt with by the introduction of another quantum number, not a fundamental quantum number but a label called the seniority

number, often indicated in parenthesis following the term. A related very interesting detail is that in the LS basis our wavefunctions are not pure either.

The lesson from this is that we have to account carefully for both the electrostatic and spin orbit interactions in the ion by itself before we will have any hope of working in the perturbative environment of the crystal. With that discussion in mind we can start to identify some of the ingredients that go into the Judd-Ofelt calculation, we will discuss mostly qualitatively. Working in the LS basis, evaluating the Coulomb interaction yields (copying from Hehlen[43]):

$$\langle 4f^N SL | \hat{H}_C | 4f^N S' L' \rangle = \delta_{SS'} \delta_{LL'} 49(-1)^L \sum_{k=0,2,4,6} \begin{pmatrix} 3 & k & 3 \\ 0 & 0 & 0 \end{pmatrix}^2 \begin{Bmatrix} 3 & 3 & k \\ 3 & 3 & L \end{Bmatrix} F(k)$$

Where this is to represent an expression for Coulomb energies in the LS basis. The important issue from this is that the electrostatic interaction yields an expression that is proportional to  $F(k)$ , which are known as Slater integrals. These contain the overlap between wavefunctions and are dependent on the ion, but the prefactor is composed of numbers, angular momentum factors, and other parameters, that can all be looked up/are tabulated. The three Slater integrals have been investigated experimentally for  $\text{Eu}^{3+}$  and their values are fairly well known. I will add here, at the risk of injecting some confusion, that the Slater integrals are affected by the host crystal (which seems reasonable), but that fortunately they seem to have very similar values for a wide variety of hosts. This is good news for us, as there is not much literature on the crystal field parameters of our YSO crystal. In tension with the Coulomb interaction, is the spin orbit interaction. As quoted by Hehlen:

$$\begin{aligned} & \langle 4f^N SL | \hat{H}_{SO} | 4f^N S' L' \rangle \\ & = \zeta(-1)^{J+L+S'} \sqrt{l(l+1)(2l+1)} \begin{Bmatrix} S & S' & 1 \\ L' & L & J \end{Bmatrix} \langle l^N SL || V^{(11)} || l^N S' L' \rangle \end{aligned}$$

Now we are looking at the contribution from the spin-orbit Hamiltonian. The pertinent point from this expression is that we again have a complicated expression including a reduced matrix

element that we can calculate, except now the relevant experimental input is the first term:  $\zeta$ , the spin-orbit coupling parameter. This number is constant for a given ion and tells us something about the strength of the spin-orbit interaction. It makes sense that there is variation in the strength of the spin-orbit interaction across the rare-earths, as they change in size. In general the interaction gets stronger with heavier ions. I will mention with regards to this parameter as well, that it is going to depend on the host, but for Eu there seems to be little variation between hosts.

At this point we are able to account for the Coulomb and spin-orbit interaction for our intra-configurational 4F transitions; now comes the Judd-Ofelt contribution. Qualitatively the idea is that the crystal field can mix opposite-parity wavefunctions (principally the  $4F^{N-1}5D$ ) into the 4F wavefunctions. This can make it so that transitions that were formerly forbidden become a little bit allowed. This is treated perturbatively and some assumptions are made, but it reduces to an expression with three terms, again from Hehlen:

$$f = \frac{8\pi^2 m_e}{3h} \frac{\nu}{(2J+1)n} \sum_{k=0,2,4,6} \Omega_{(\lambda)} |\langle l^N SLJ || U^{(\lambda)} || l^N S' L' J' \rangle|^2$$

Now an amazing thing about this is that this approach yields/depends on just three parameters. These three numbers give the forced electric dipole contributions from the crystal, the reduced matrix elements and other factors quantities, that can be calculated in the context of Judd-Ofelt theory.

Now this discussion only gives us a flavor; this would be quite complicated to implement from first principles. For one we would have to come up with the wavefunctions, in addition to the actual Judd-Ofelt implementation. That is why it is awesome that others have done it for us and provided the program for others to use. There is a software package available from Los Alamos, developed by Hehlen and colleagues, called (Rare Earth Level Intensity Calculation) RELIC that implements this theory. RELIC lets us pursue a variety of rare-earth doped crystal calculations.

Thankfully the documentation/use of the program is pretty straight-forward compared to the Cowan code.

## C.2.2 What can we learn from RELIC?

We should be able to use the RELIC software to calculate the forced electric and magnetic dipole strengths and decay rates for our transition. The Judd-Ofelt parameters for YSO are quoted in the literature by Li[38] for Er:YSO and by Xue[87] for Eu:YSO, although unfortunately the numbers differ a fair amount, so it is hard to know if they should be trusted.

The first thing I did was try using the F(2), F(4), F(6) and spin-orbit parameter  $\zeta$  from the documentation for  $\text{Eu}^{3+}$  with the the Judd-Ofelt parameters from Xue with a constant refractive index of 1.79, as this is the approximate index of YSO. We get some interesting results. Let us compare the RELIC results for in the crystal, with the free-ion results from the Cowan code.

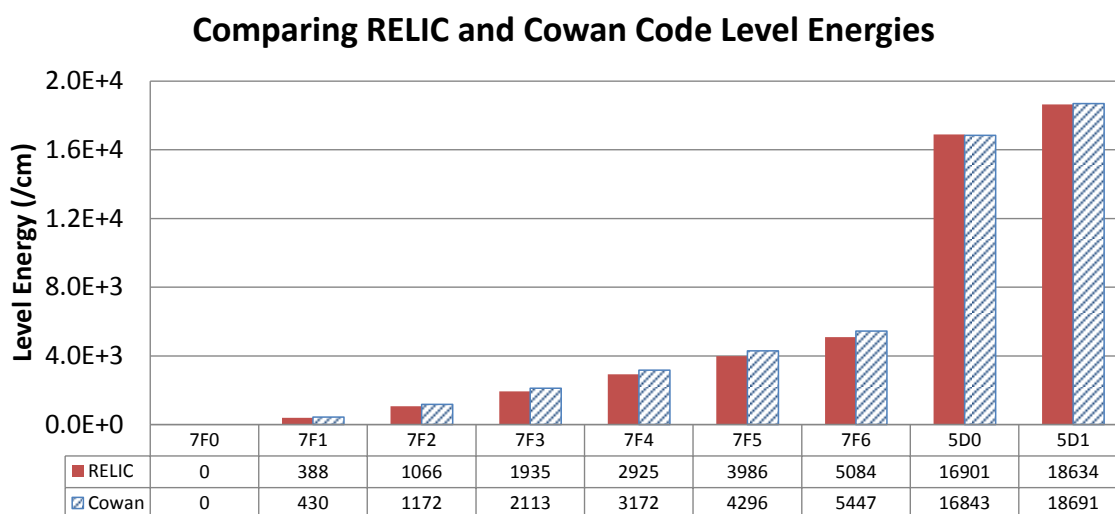


Figure C.1: RELIC vs Cowan code Energy Levels

The energy levels are very similar for the RELIC and Cowan code calculation, differing at most by only a few percent. See figure C.1.

However, it gets interesting when we look at the transition oscillator strengths, they are pretty wildly different. See figure C.2. The intra-manifold transitions seem to be a lot stronger in the Cowan code calculation compared to the RELIC calculation for whatever reason. The transitions

### Comparing RELIC and Cowan Code for M1 Transitions

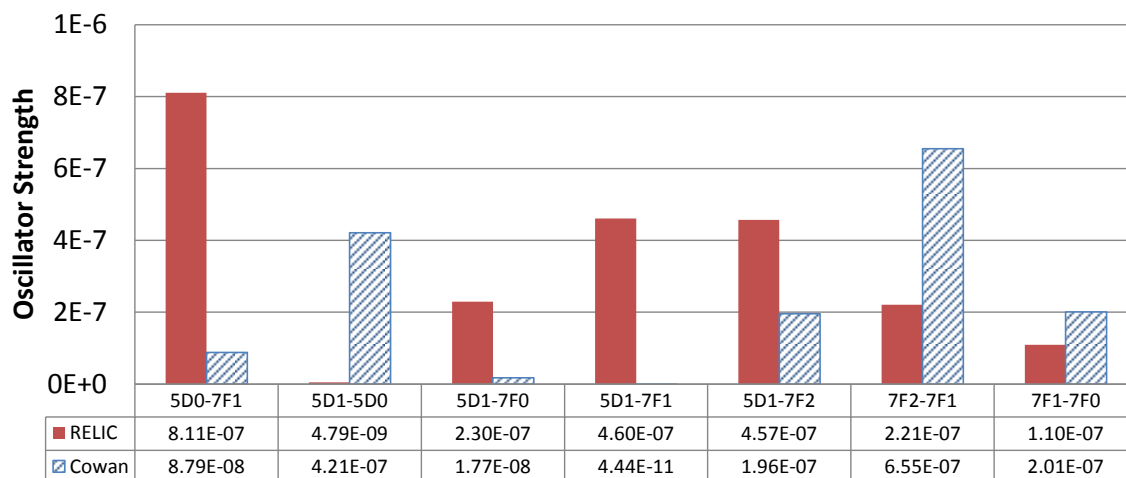


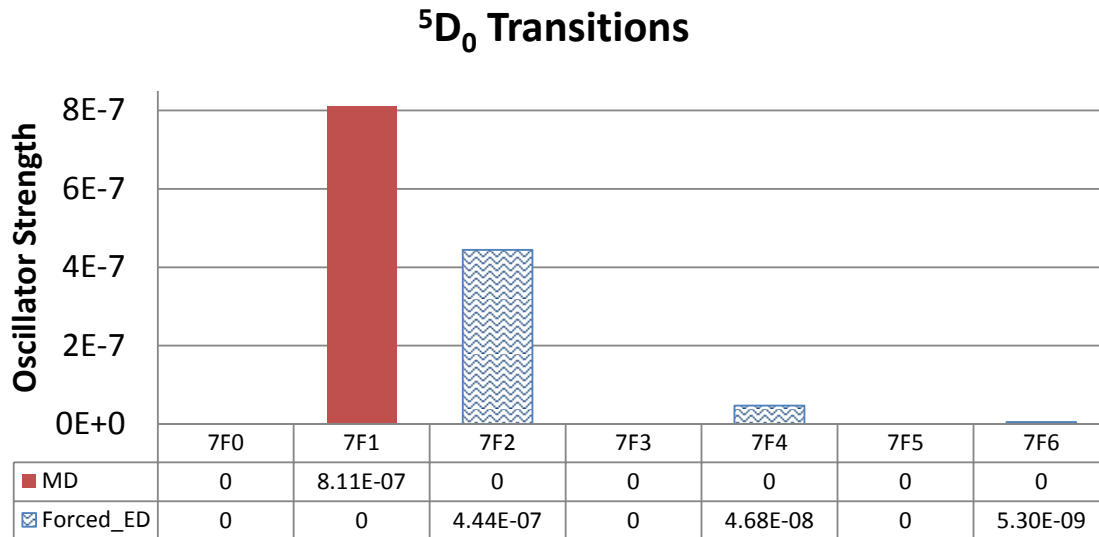
Figure C.2: RELIC vs Cowan Code Oscillator Strengths

to  ${}^7F_1$  seem much stronger in the RELIC calculation. I am not sure what conclusions to draw from this comparison. The most consequential issue is that the RELIC calculation for our transition predicts the oscillator strength to be  $\sim 10\times$  stronger than predicted by the Cowan code; hopefully the RELIC number is correct.

Judd-Ofelt parameters do not matter for this calculation very much as the magnetic dipole transitions are not perturbed very much by the crystal. This was confirmed in RELIC by setting the Judd-Ofelt parameters to zero and looking at the change to the magnetic dipole transitions; there was not much change, although the the forced electric dipole transitions were turned off as we would expect from Judd-Ofelt theory. This does suggest that there is a pretty big difference between the oscillator strengths calculated with RELIC and the Cowan code for our transition that is not attributable to the crystal. It is also possible that there is some factor such as the degeneracy that is treated differently in the Cowan code and RELIC that may be involved.

Let us examine transitions from  ${}^5D_1$  and  ${}^5D_0$  (See figures C.3 and C.4.) and see what RELIC can tell us about the forced electric dipole contributions.

This has a number of interesting features. For one, the M1 transition to  ${}^7F_1$  is the only allowed magnetic transition. Also, there are forced E1 transitions, but only to even J. This is as expected

Figure C.3:  ${}^5D_0$  Lines

according to selection rules. For forced electric dipole transition rules, see Tanner[44], If  $J=0$  or  $J'=0$ , then  $|\Delta J| = 2, 4, 6$ . This is interesting in our context as  ${}^5D_0 \rightarrow {}^7F_0, {}^7F_1$  and  ${}^5D_1 \rightarrow {}^7F_0, {}^7F_1$  cannot be forced electric dipole transitions. This clarifies our situation somewhat as the forced electric dipole transitions are going to be more dependent on the host and this removes that issue for us as there is no forced E1 contribution to our transition. Probably the most interesting are the transitions from  ${}^5D_1$ . See figure C.4.

We see that there are four allowed M1 transitions from the  ${}^5D_1$  and that they are stronger for the most part than the forced E1 transitions. As we expect and similar to Cowan, our M1 transition is not the strongest from  ${}^5D_1$ ; the  ${}^5D_1 \rightarrow {}^7F_1$  is twice as strong. The  ${}^5D_1 \rightarrow {}^5D_0$  transition is much suppressed as calculated by RELIC compared to Cowan. Let us take a second and back out what our matrix element is according to the oscillator strength from RELIC:

$$S = gf \frac{3h}{8\pi^2 m c a_0^2 \sigma} = \frac{gf}{3.0376E - 6\sigma} = 4 \times 10^{-6} e^2 a_0^2 \rightarrow \mu = 2 \times 10^{-3} e a_0 \quad (\text{C.4})$$

Our effective matrix element is approximately  $2 \times 10^{-3} e a_0$  according to RELIC, substantially ( $\sim 3.5\times$ ) larger than our Cowan code prediction. Next let us look at all the intra-manifold transitions, see figure C.5.

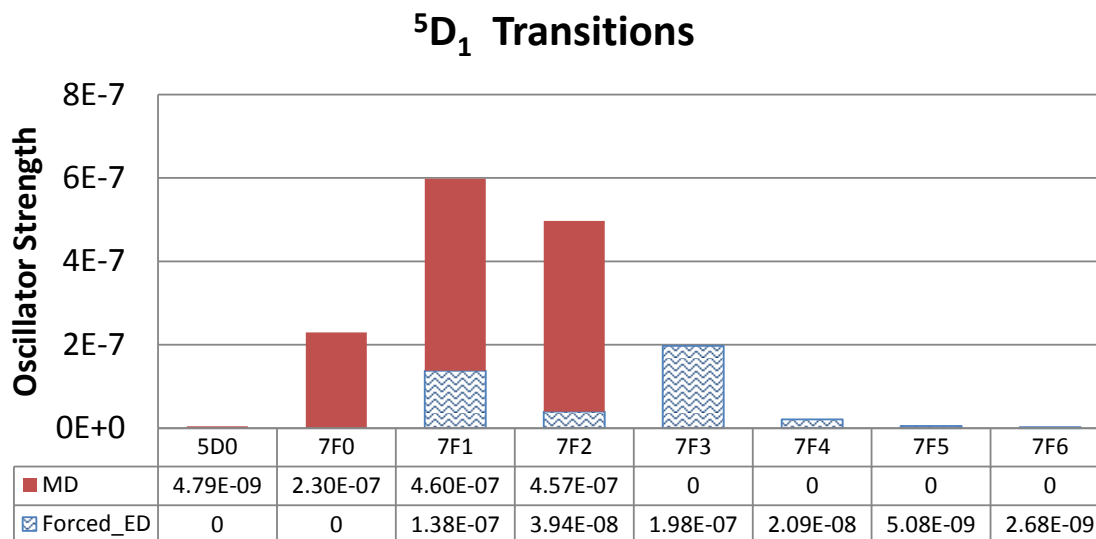


Figure C.4:  $^5D_1$  Lines: Note: our transition is purely a magnetic dipole transition.

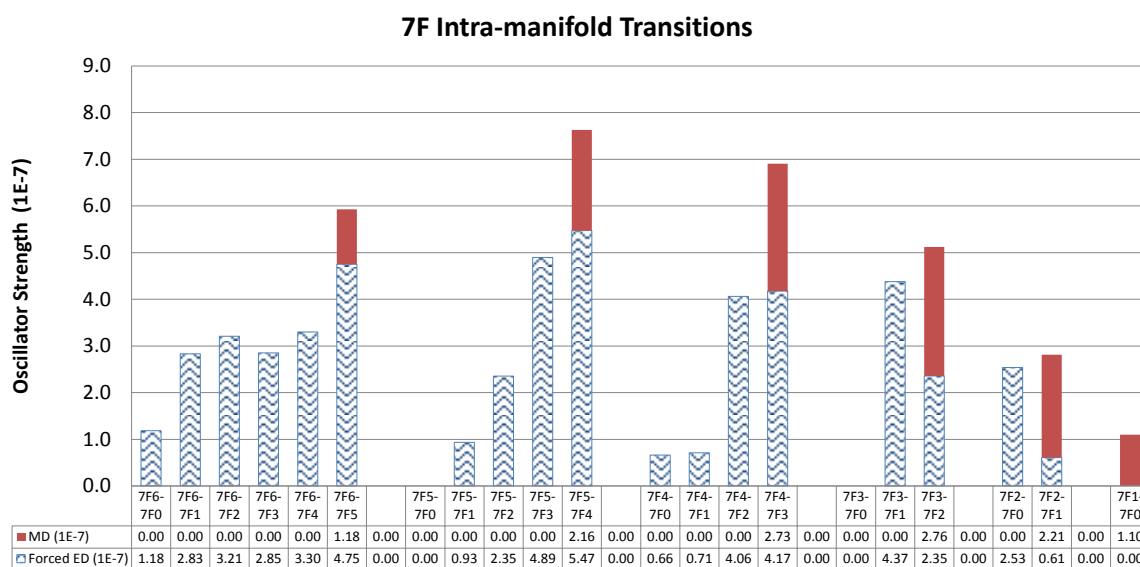


Figure C.5:  $^7F$  Transitions

Note: in this figure, in order to make it a little more readable, all the oscillator strengths are divided by a factor of  $10^{-7}$ . Among these intra-manifold transitions, the forced E1 contribution is both significant (larger than the M1 part), and also present between states with very different J. Interestingly, as we would expect according to selection rules, transitions between J=0 and J=odd

are not present. Also the strengths of transitions to terms with small  $J$ , are suppressed compared to transitions between states of larger  $J$ .

Another interesting thing to look at are the transition rates; see figure C.6. These figures are not super exciting as they are very similar to what we have already discussed. The rates are closely related to the oscillator strengths, but it is interesting to see the influence of the factor of energy squared,  $\sigma^2$ , and how it suppresses the rates for transitions that are low-energy. We can compute these out from the oscillator strengths. See equation C.1.

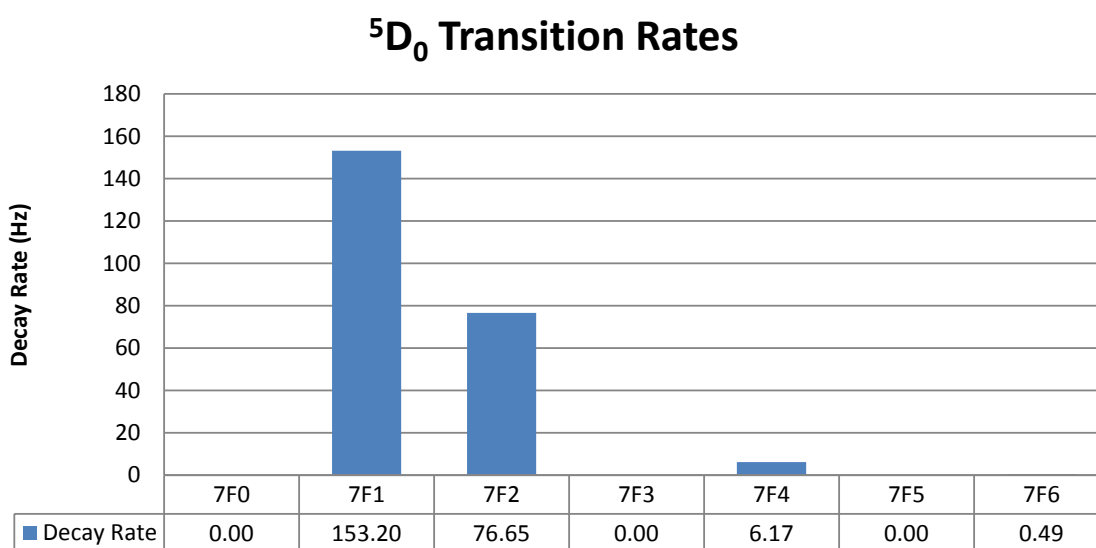


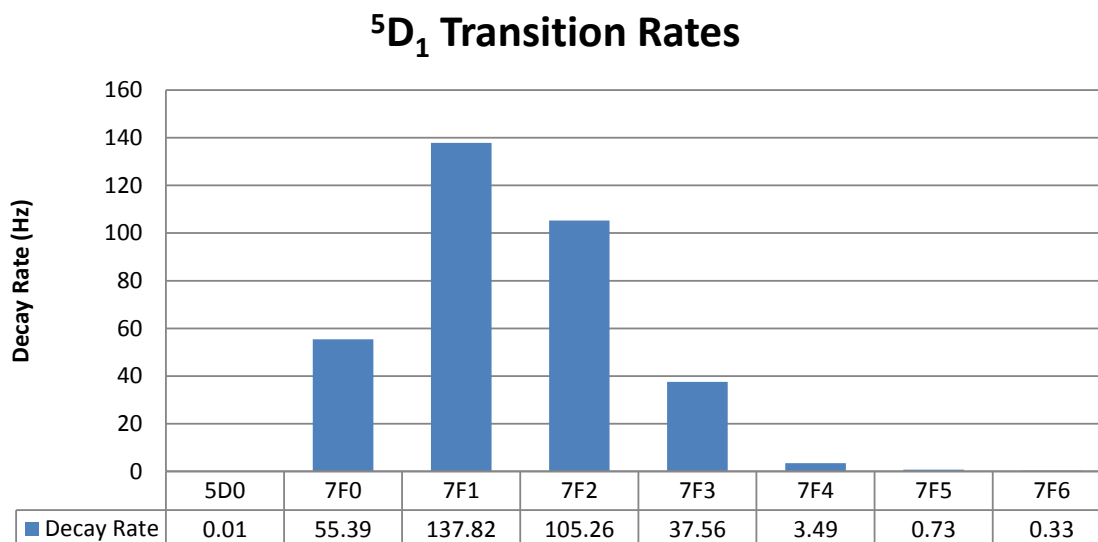
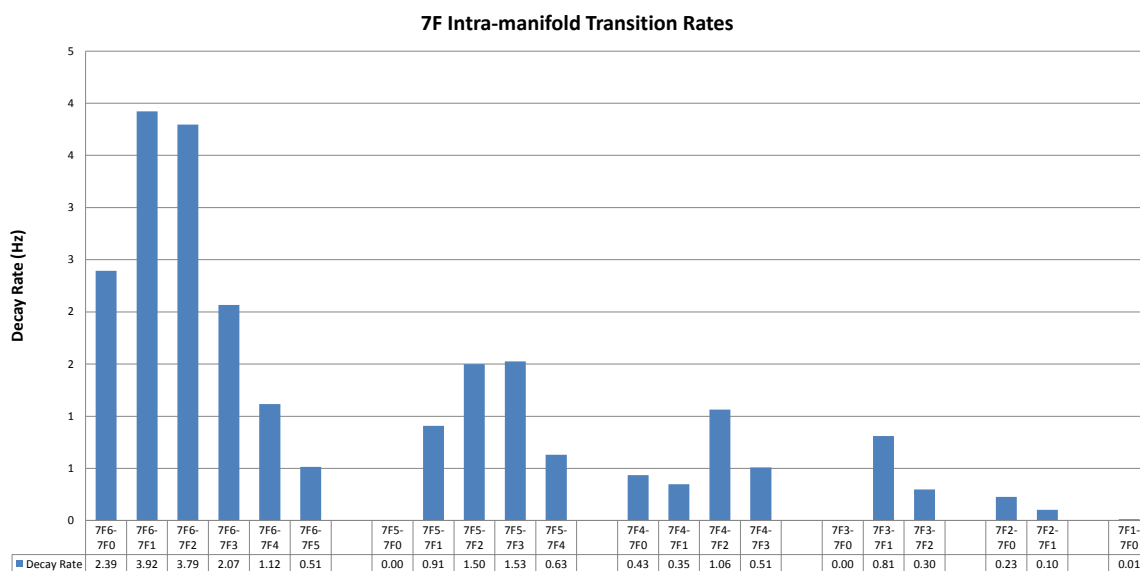
Figure C.6:  $^5D_0$  Transition Rates

The rates are very small, but this is part of the appeal of these interactions and what got the attention of researchers a long time ago: A narrow spectral line in a solid.

Lastly, let us inspect the transition rates between the  $^7F$  levels. See figure C.8.

This is interesting as it is even more dramatic how decays between the lowest levels are suppressed. Decays from say  $^7F_6$  to  $^7F_4$  are more likely than those between lower states. It is also interesting in that these are much less likely optically than the transitions between  $^5D$  and  $^7F$ .

There are a number of other issues we looked at with RELIC. We compared our results using different Judd-Ofelt parameters from both Xue[87] and Li[38]. There was not a dramatic difference, a 10-15% change in oscillator strengths at most. Also, we incorporated a Sellmeier model

Figure C.7:  ${}^5D_1$  Transition RatesFigure C.8: Intra-manifold  ${}^7F$  Transition Rates

for the refractive index of YSO, based on the work of Beach and colleagues for NdYSO[88]. Carefully incorporating this changed the oscillator strengths very little for our transitions, by less than a percent or so in most cases. The only outlier was  $\sim 5\%$  change in the oscillator strength of the  ${}^7F_6 - {}^7F_1$  transition; perhaps this is a ‘hypersensitive’ transition. An aside: One interesting thing

about  $\text{Eu}^{3+}$  is that it has so-called hypersensitive transitions. These are forced electric dipole transitions that are very sensitive to the crystal environment. They are not very well understood and not explained within Judd-Ofelt theory. Interestingly, a few of the low-lying transitions in Eu are identified as hypersensitive[89], including the  ${}^7F_1 - {}^5D_1$ ,  ${}^7F_0 - {}^5D_2$  and  ${}^5D_0 - {}^7F_2$  transitions. We did not, however, observe any large changes on any of these transitions in RELIC when changing the refractive index model or Judd-Ofelt parameters.

One other additional objective that would be good to pursue in RELIC would be to try fitting the Judd-Ofelt numbers to quoted transitions. The software is set up in part to do this, and it would be great to verify/compare the results of such a fitting procedure to existing numbers in the literature[38, 87]. That would be a result in itself; however, at this point, we do not have experimental numbers for the oscillator strengths or sufficient data to move forward with this.

## Appendix D: Kramers-Kronig Comments

The following will be a short section on Kramer-Kronig relationships. This is a nice mathematical procedure that lets you divine the real part of the electric susceptibility if you have the imaginary part or vice versa. Interestingly, Kramers-Kronig is a consequence of causality. This explanation comes from some notes by Scott Sanders at UW, supplemented by notes from UCF[90, 91].

The core of the idea is that you can't have instantaneous polarization response. As a result, the polarization response depends on frequency, which means that the electric susceptibility is a frequency-dependant quantity,  $\chi(\omega)$ . You can derive that frequency-dependant susceptibility by looking at the Fourier transform of the temporal impulse response  $\chi(\omega) = 2\pi\mathcal{F}(\chi(t))$ .

Here is the argument: If you have a temporal signal that turns-on, that signal is unaffected by multiplying it by a step function. *i.e.*,

$$\chi(t) = \chi(t)\theta(t)$$

Now this means that their Fourier transforms must also be the same:

$$\mathcal{F}[\chi(t)] = \mathcal{F}[\chi(t)\theta(t)]$$

As we know the Fourier transform of a product is the same as the convolution of the Fourier transforms of each signal being multiplied.

$$\mathcal{F}[\chi(t)] = \mathcal{F}[\chi(t)\theta(t)] = \mathcal{F}[\chi(t)] * \mathcal{F}[\theta(t)]$$

We can look up the Fourier transform for the step function and for the susceptibility.

$$\mathcal{F}[\chi(t)] = \int \chi(t)e^{i\omega t} dt$$

$$\mathcal{F}[\theta(t)] = \frac{1}{2}\delta(\omega) + \frac{i}{2\pi\omega}$$

Then we can perform the convolution between these two Fourier transforms:

$$\mathcal{F}[\chi(t)] * \mathcal{F}[\theta(t)] = \int \int \chi(t) e^{i\omega' t} dt \left( \frac{1}{2} \delta(\omega - \omega') + \frac{i}{2\pi(\omega - \omega')} \right) d\omega'$$

Now the delta function under integration just selects  $\omega$ , which allows us to break the expression into real and imaginary parts:

$$= \frac{1}{2} \int \chi(t) e^{i\omega t} dt + \int \frac{i}{2\pi(\omega - \omega')} \int \chi(t) e^{i\omega' t} dt d\omega'$$

$$\chi(\omega) = \frac{1}{2} \chi(\omega) + \frac{i}{2\pi} \int \frac{\chi(\omega')}{\omega - \omega'} d\omega'$$

Simplifying:

$$\chi(\omega) = \frac{i}{\pi} \int \frac{\chi(\omega')}{\omega - \omega'} d\omega'$$

Next, let us recognize we are free to separate the susceptibility into real and imaginary parts:

$$\chi(\omega) = \chi'(\omega) + i\chi''(\omega) = \frac{i}{\pi} \int \frac{\chi'(\omega')}{\omega - \omega'} d\omega' + \frac{i}{\pi} \int \frac{i\chi''(\omega')}{\omega - \omega'} d\omega'$$

And collecting pieces gives relationships between real and imaginary parts of the susceptibility:

$$\chi'(\omega) = -\frac{1}{\pi} \int \frac{\chi''(\omega')}{\omega - \omega'} d\omega'$$

$$\chi''(\omega) = \frac{1}{\pi} \int \frac{\chi'(\omega')}{\omega - \omega'} d\omega'$$

Now it is sort of difficult to visualize if we have negative frequencies in our expressions, so let us see if we can modify this expression to eliminate them. We can make use of a reality condition: the fact that for a real  $\chi(t)$ ,  $\chi'(\omega)$  is even and  $\chi''(\omega)$  is odd. This can be seen upon examination of the Fourier transform:  $\mathcal{F}(x(t)) = \int_{-\infty}^{\infty} e^{-i\omega t} dt = \int_{-\infty}^{\infty} x(t)(\cos(\omega t) - i\sin(\omega t)) dt$ .

Note: this does not say anything about the parity of the dispersion resonances but about the time signals; *i.e.*, it does not mean that an odd real susceptibility implies an even imaginary susceptibility, the parity or lack of parity of the resonance does not limit our ability to apply this

machinery to the problem. However, as a result of this reality condition, we can rearrange these expressions to not be integrating over negative frequencies:

$$\chi'(\omega) = -\frac{1}{\pi} \int_{-\infty}^{\infty} \frac{\chi''(\omega')}{\omega - \omega'} \frac{\omega + \omega'}{\omega + \omega'} d\omega' = \frac{2}{\pi} \int_0^{\infty} \frac{\omega' \chi''(\omega')}{\omega'^2 - \omega^2} d\omega' \quad (\text{D.1})$$

Similarly:

$$\chi''(\omega) = \frac{2\omega}{\pi} \int_0^{\infty} \frac{\chi'(\omega')}{\omega'^2 - \omega^2} d\omega' \quad (\text{D.2})$$

These two expressions let us convert between real and imaginary susceptibilities. So if we know what the absorption/gain looks like as a function of frequency, we can back out the real susceptibility and related index of refraction as well.

## Appendix E: Lockboxes for Eu:YSO Experiment

Probably part of most every AMO student's fate is to at some point build a 'lockbox' or two. Although they're a mess of wires and components crammed into an aluminum box, they perform a precision task, keeping your laser in line, sometimes to a degree that is really amazing considering their haphazard construction. They are prone to reliability issues and noise and especially strange noise. Often they are replaced by commercial products that would be better on most every metric except cost, although sometimes something just is not the same, and one puts the humble home-built lockbox back into service. Eventually they find their resting place in pile of their brethren and relatives until, if poorly labeled or no longer protected by their maker, they are scavenged for parts.

A lockbox is feedback circuit for a laser locking set-up. It is the electronics (or part of the electronics) whether you are doing saturated-absorption, Hänsch-Couillaud(HC) or Pound-Drever-Hall(PDH). The circuits discussed here are for HC and PDH locking as that's what we needed for our experiment. We require a circuit for the PDH lock to our ULE glass reference cavity and a circuit for HC locking, which is used to lock our SHG cavity to the laser. In principle the same circuit could serve for both applications.

These circuit designs are not really anything new, but more of a remix of circuit designs floating around the Yavuz and Saffman AMO Labs at UW Madison. I had circuitboards made by a company called Advanced Circuits<sup>1</sup>, as I figured this would help with circuit performance and it was also a procedure that I wanted to know how to do. The designs they are based on can be found in Tyler Green's thesis[66] and on the Hexagon Wiki<sup>2</sup>. I built two versions of the circuit of which this appendix will discuss the latter.

There are 4 main sections of the circuit: 1) a ramp generation section, 2) a photodiode/error-signal input section, 3) a slow feedback section that goes to a piezo (SHG cavity mirror or laser

---

<sup>1</sup>Note: they have a great, really affordable deal for students. <http://www.4pcb.com/pcb-student-discount.html>

<sup>2</sup>See: lock-box.pdf available on the Hexagon Wiki

grating), and 4) a fast feedback(FFB) section that goes to the laser current. (Actually the FFB is physically a separate circuit, but I will discuss it here as well.)

## E.1 Ramp

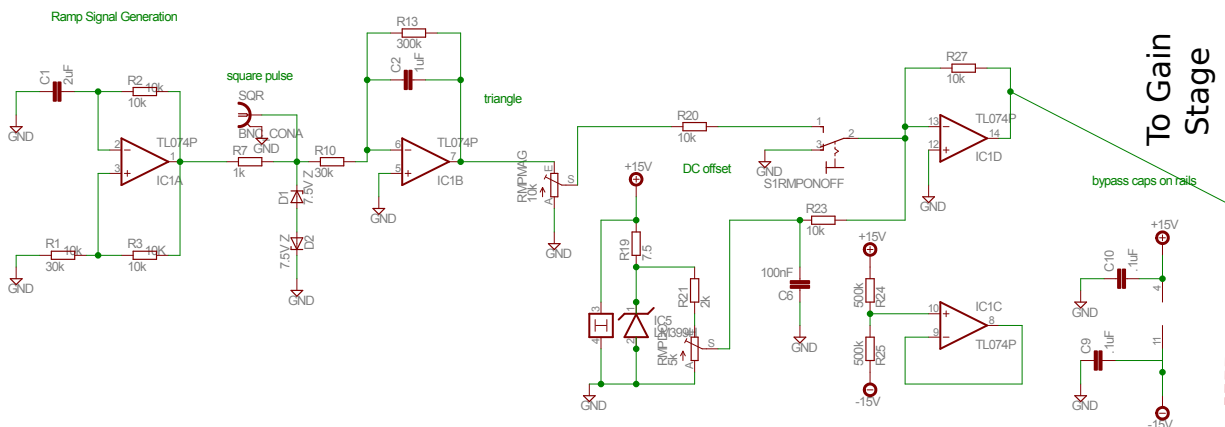


Figure E.1: Ramp Section

Our lockboxes usually have an external ramp at a very low frequency, around 10 Hz. This is so that you can ramp the piezo position and see your saturated absorption/SHG cavity/reference cavity transmission peaks to facilitate adjusting gains/offsets/etc., and ultimately locking the cavity. Since the ramp frequency does not need to change, and it is relatively easy to make a triangle wave, I thought I would incorporate the ramp into the lockbox circuit, in order to eliminate another external connection and required piece of equipment. One motivation was that some cheap external function generators do not work especially well or have DC-drift or some other problem. The ramp signal is generated by 2 op-amp stages. The first is a relaxation oscillator which creates a square wave. This square wave is clipped with two shunt diodes to flatten the output. Note: this square wave also has a pick-off, as this is a convenient trigger for the oscilloscope. Next the square wave is integrated to create a triangle wave. There is a potentiometer(pot) that controls the size of the square wave. Next a LM399-based positive DC voltage reference is added to the triangle wave. The reference is positive because the piezo driver should only be supplied with positive voltage. This DC reference

is controlled by a pot as well. The DC offset control and ramp size control gives you the two knobs you need to zero in on a cavity peak and facilitate finding a good piezo voltage at which to turn on the lock. Note, when the lock is switched on, the ramp is grounded (S1RMPONOFF), but the DC contribution is still added to the feedback voltage.

There are more sophisticated ways to generate a triangle wave that would probably give a more linear/perhaps more stable result, but this seemed to work fine. Also, since the voltage range you are scanning over is small, the nonlinearity of the ramp is not much of a problem. Note: there is one unused op-amp in the package. It is held at about zero input voltage and wired with feedback so that it does not charge up, rail, or cause any issues.

## E.2 Photodiode Input Section

This input section is very similar to the differential input section found in the Saffman group's lockbox circuit. Initially I experimented with using a purpose-built low-noise differential amplifier chip for our input stage. However I found that we needed a little more flexibility in the circuit. That chip did not allow us to easily adjust the DC offset or relative size of the two inputs, so I changed to this configuration.

The first stage is an op-amp set up as a differential amplifier. A potentiometer is in the feedback path to adjust the size of one of the inputs relative to the other; *i.e.*, to balance the signal size from the two photodiodes (PD) for HC locking. For PDH locking, you only use one of the PD inputs and ground the other with a BNC terminator. You can switch the polarity of the error signal in PDH by switching which PD input you use.

One outstanding issue is that the circuit has impedance matching 50 ohm resistors on the photodiode inputs. In practice, I found that the circuit worked without including these resistors, and if they're included, they will shrink the input signal significantly. For now they are left out of the constructed lockbox, hopefully this impedance mismatch will not pose any issues; if this becomes a problem, we can modify accordingly.

Immediately after the input stage is a switched pick-off for the fast feedback branch. The first version of the circuit incorporated an active FFB circuit, á la Tyler Green's circuit[66], but this

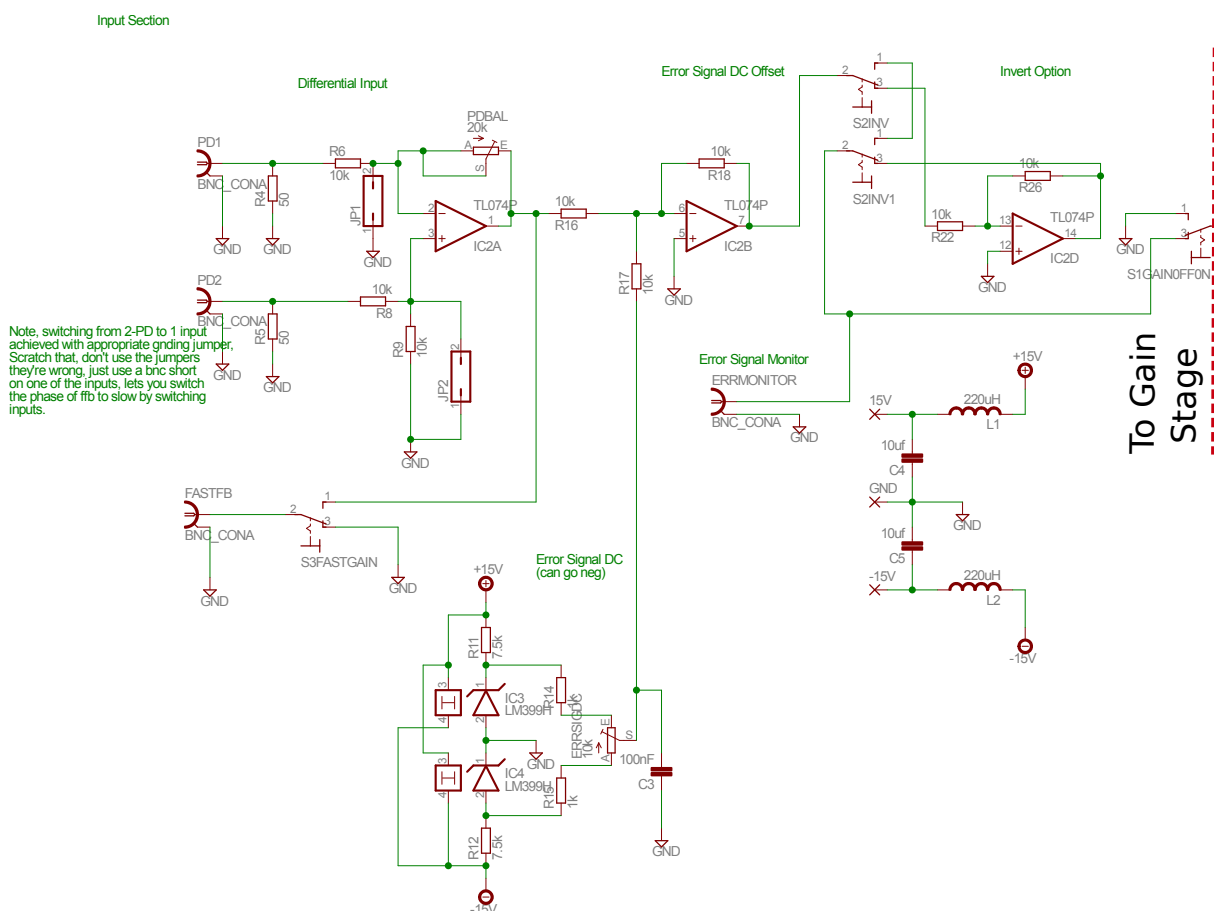


Figure E.2: Photodiode Input Section

was dropped in version 2 in favor of a simpler external passive circuit. The FFB is discussed in section E.4 of this appendix. We should not need extremely high locking bandwidth, as we are not locking to a cavity with as high finesse as the cavity Green was working with. In terms of the fast feedback branch, all that the circuit does is subtract the two photodiode inputs when used for HC locking. For PDH, it just passes the signal through, although you can switch the FFB polarity independently from the slow feedback by switching the PD inputs. Also, passing the FFB signal through the lockbox should act as a buffer and may have impedance advantages.

The other branch is the slow (piezo) feedback and is run through an optional inverting stage controlled by switch 2. After the differential section, a DC voltage reference similar to the one used

in the ramp section is added, although this reference can be negative. The DC offset pot and the balancing pot allow us to clean up the error signal, ideally resulting in a signal that is symmetrical and centered around zero. The slow feedback branch is grounded by switch 1 when the ramp is on (S1GAINOFFON).

Note: there are a few accessories visible in this diagram as well. There are filtering capacitors and inductors on the supply rails; this is a tie-over from Saffman group's circuit. Although as of right now, 100  $\mu\text{H}$  inductors are in the circuit. I wasn't sure how much current the circuit was going to draw, so I used a smaller inductors that could handle more current. As of right now, the circuit draws at most about 300-400 mA right at turn-on; this is the LM399 reference diode heaters heating up. There are also filtering capacitors visible on the op-amp package rails.

### E.3 Slow Feedback

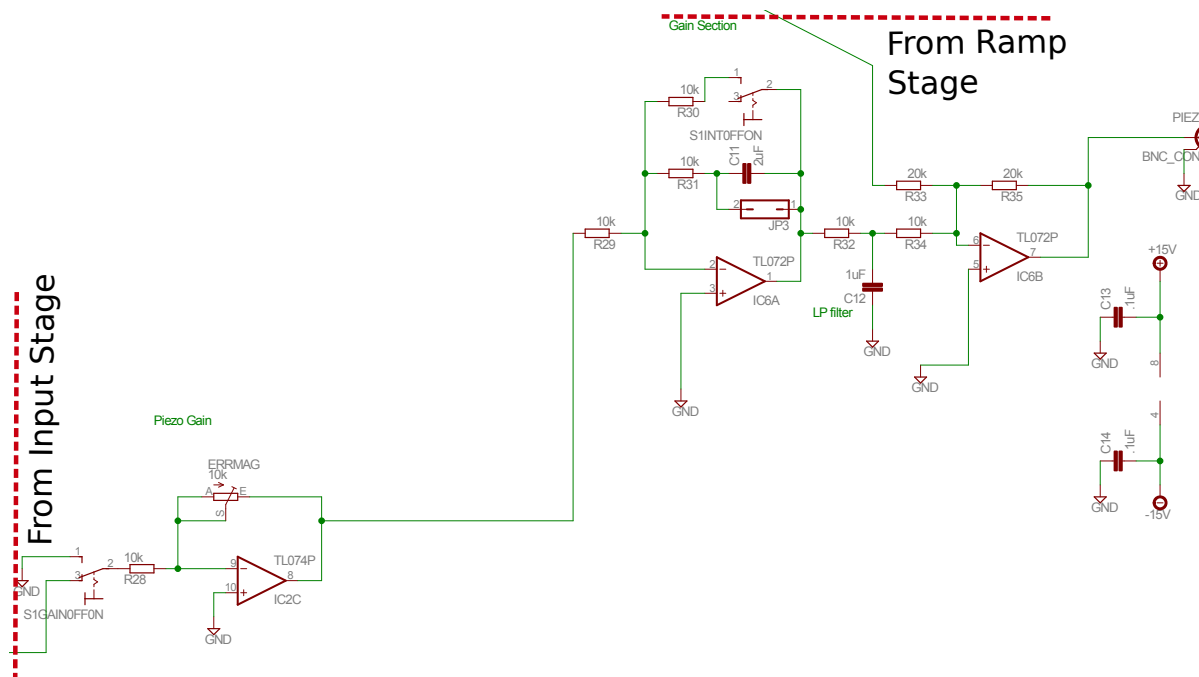


Figure E.3: Slow (Piezo Voltage) Feedback Section

The input section and the ramp section both feed into the gain stage. After the on-off switch, the slow feedback branch is sent to a gain stage that controls the size of the error signal.

The slow (piezo) feedback section is the heart of the lockbox. The error signal is run into an integrator stage (IC3A). In the actual implementation we used an OP200 op amp, as it has better offset voltage characteristics and smaller leakage currents which is better for an integrator stage. Also, when the error signal is off and the ramp on, the integrator is bypassed through a 10k resistor. This keeps the stage from railing when not feeding back the error signal. Switch 1 is a 3-pole switch and controls the integrator (S1INTOFFON) turn-off as well ramp on-off(S1RMPONOFF) and feedback on-off(S1GAINOFFON).

The integrator stage has very high DC gain as we want that for the piezo feedback. This is followed by a passive filter to further suppress gain at low, but not DC, frequencies(*i.e.*, the piezo resonance frequency). Adjusting the capacitor C12 controls this roll-off. Also, adjusting resistor R30 and capacitor C11 will modify the integrator feedback performance. These parameters were tuned to give the best performance. Most importantly, increasing C12 seemed to help avoid the piezo resonating. After the integrator stage is a stage that adds the feedback signal to the DC contribution of the ramp signal. This sum goes to the cavity piezo driver. Figure E.4 shows the expected piezo stage (last two amplifier stages) performance generated with the circuit simulation package Multisim.

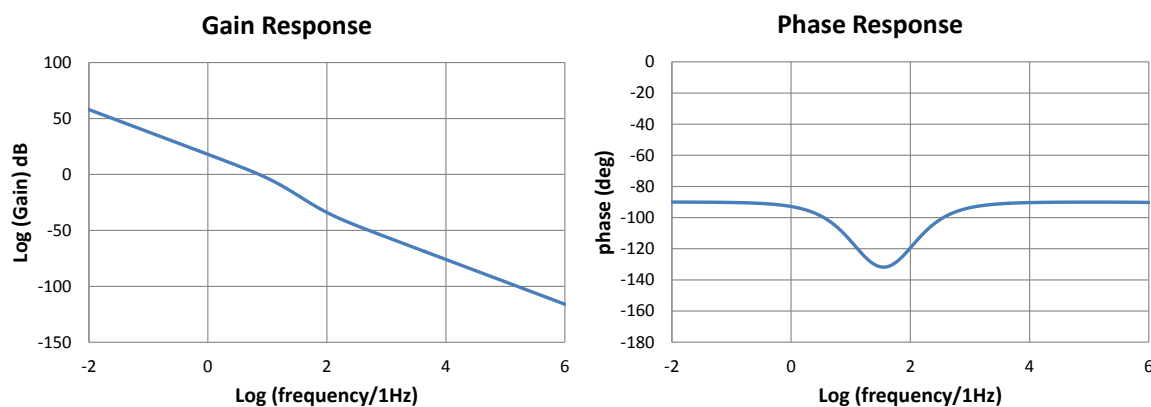


Figure E.4: Slow Feedback Simulated Performance

As you can see, the roll-off is at very low frequency. Despite the gain being about -30dB at 100Hz, we still see piezo oscillations on top of the transmitted cavity signal if we turn up the gain

a bit; it is easy to make the piezo resonate. The phase margin is about 45 degrees at very low frequency and is better everywhere else.

## E.4 Fast Feedback

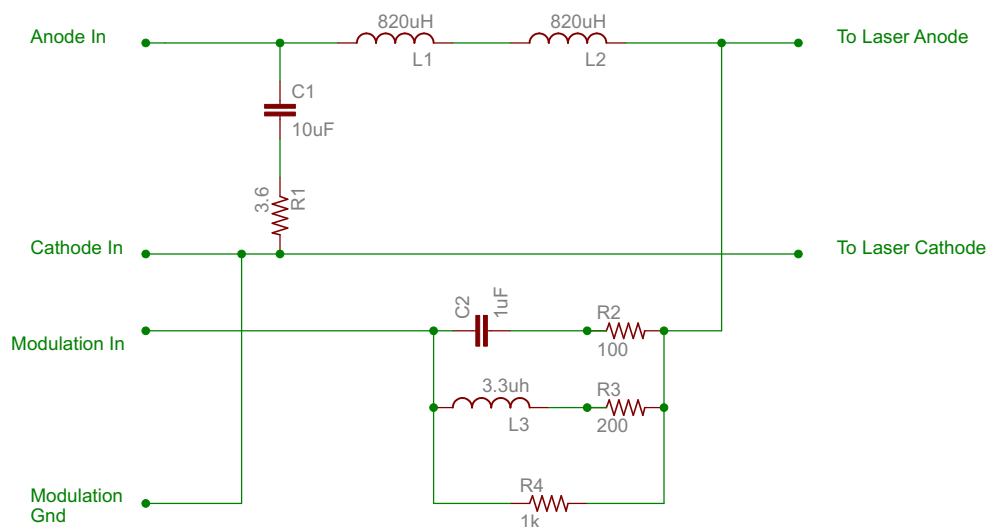


Figure E.5: Fast (Laser Current) Feedback Section

Originally I had an active fast feedback branch on the lockbox circuitboard. Before we had the ULE reference cavity, we locked the laser to the SHG cavity, and so this was a desired feature. Even though the SHG cavity is a poor reference cavity, it fluctuates relatively slowly compared to the fast feedback time-scale, so locking the laser to it suppresses fast laser fluctuations. Incorporating FFB definitely enhanced feedback performance, and could be seen by turning it off and on while trying to maintain slow feedback. After we locked the laser to the reference cavity, we no longer needed a FFB branch in the SHG circuit, so this is not currently used.

The passive fast feedback circuit is pretty simple. It sits in-line between the laser driver and the laser and has an input for the fast feedback (modulation). There is a very low impedance filter on the diode driver output, 3.6  $\Omega$  to ground, as the driver expects a low impedance, a forward biased laser diode. There is low-pass voltage filtering by capacitance to ground and inline inductors to

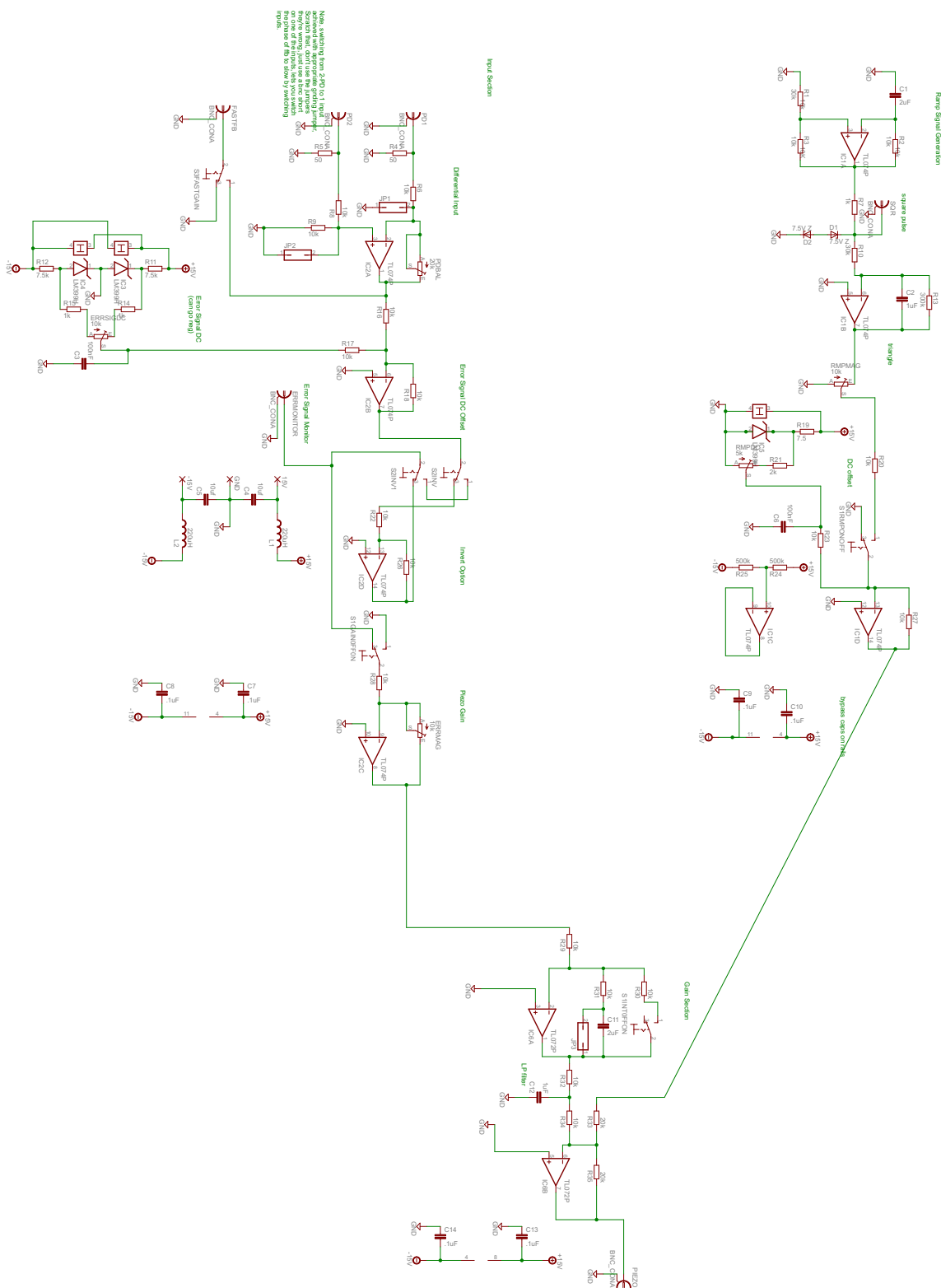
suppress current noise. The actual feedback portion consists of a bandpass filter formed by parallel capacitor and inductor branches.

## **E.5 Circuit Revisions/Issues**

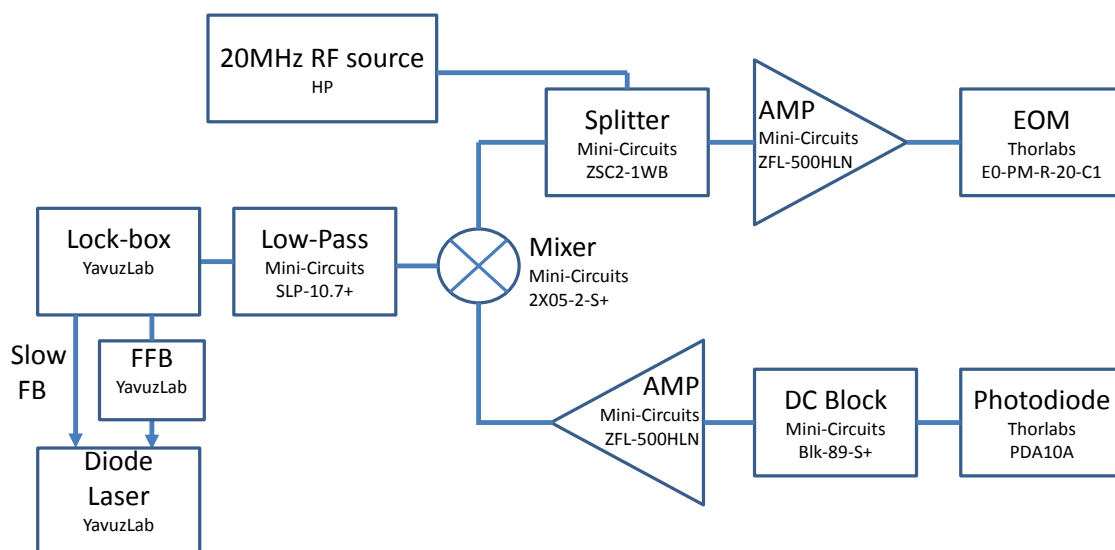
Like any circuit project, version 1 contained some problems that were fixed in version 2 and version 2 still has a few issues that should be fixed if we are to produce more of these or similar circuits.

1. R20 needs to be between S1RMPONOFF and IC1D rather than before the switch.
2. Jumpers on the input stage that I thought would be clever are really unnecessary/wrong, a BNC short at the input fixes the issue.
3. The piezo feedback switch should be put after the gain section so we can observe changes in the feedback signal magnitude.
4. The error signal DC offset pot direction changes with invert switch; this is not ideal.

## **E.6 Full Circuit Diagram**



## E.7 PDH Circuit Diagram



## Appendix F: Broadening Suppression Idea

This topic is not central to our Eu:YSO experiments, but is not unrelated either. The idea is developed in the following paper[77], and this appendix will serve as a sort of advertisement for it. The paper frames the problem around Doppler broadening, but it may also be applicable to other kinds of broadening, such as the inhomogeneous broadening of spectral lines that we observe in our Eu doped YSO crystal. It would be an interesting experiment in of itself to see if we could observe this effect in a crystal system. Suppressing inhomogeneous broadening and as a result boosting the effective density of a crystal system could have applications in building new kinds of lasers, for example. Below is a picture of the level scheme for the idea:

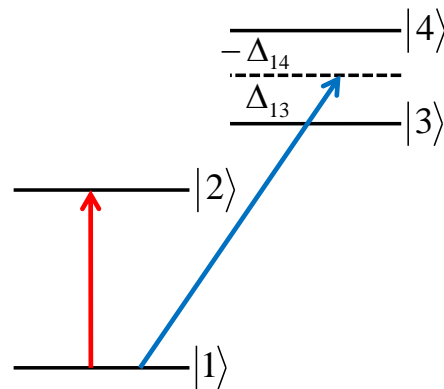


Figure F.1: Broadening Suppression Level Scheme

Qualitatively, the idea is that to suppress the inhomogeneous broadening on a transition between levels  $|1\rangle$  and  $|2\rangle$ , you apply an additional strong laser,  $E_s$ , between the ground state and an excited state pair,  $|3\rangle$  and  $|4\rangle$ . The laser is tuned to sit equidistant between the two excited states. If an atom is at the center of the inhomogeneous broadening distribution, the applied Stark shifts cancel. If the atom is shifted,  $E_p$  is no longer resonant and is not at the center of the inhomogeneous broadening. In that case,  $E_s$  will also be detuned, no longer lying exactly between states  $|3\rangle$  and  $|4\rangle$ . As a result, the Stark shifts no longer cancel and that net Stark shift can put  $E_p$  back into resonance. See [77] for more details.

## PUBLICATIONS

This is a very brief section that lists the author's publications while a graduate student at UW Madison, as some are not featured in this thesis.

1. N. Brewer, **Z.J. Simmons**, D.D. Yavuz. "Optical magnetic-dipole transition experiments in Eu:YSO..." (coming soon)

*There will be upcoming publications on our Eu:YSO experiments, hopefully in the near future. Many of the issues explored in this thesis will inform and substantively contribute to this future work.*

2. J.A. Miles, D. Das, **Z.J. Simmons**, D.D. Yavuz. "Localization of atomic excitation beyond the diffraction limit using electromagnetically induced transparency" (in publication)

*This is a further development of the localization project in publications: 7 and 4. Jared greatly improved the experiment and wrote his thesis on it. I made only a small contributor to this effort.*

3. D.D. Yavuz, N.R. Brewer, J.A. Miles, **Z.J. Simmons**. "Suppression of inhomogeneous broadening using the ac Stark shift" *Phys. Rev. A* **88** 063836 (2013).

*This was an idea that Deniz was pursuing and we helped with simulations. This could have applicability to our doped crystal experiments as a way to boost atomic density. It is mentioned in chapter 8 and appendix F.*

4. J.A. Miles, **Z.J. Simmons**, D.D. Yavuz. "Subwavelength localization of atomic excitation using electromagnetically induced transparency" *Phys. Rev. X* (2013).

*This was a major upgrade of our localization experiment, building on publication 7 and going below the diffraction limit. Jared Miles led the experiment and I mostly helped with simulation work, for example using density matrix simulations to try and reproduce the experimental results we were seeing in the lab.*

5. D.D. Yavuz, **Z.J. Simmons**. "Optical imaging with nanoscale resolution using optical nonlinearities and spatiotemporal modulation" *Phys. Rev. A* **86** 013817 (2013).

*This is a little bit different than our other work. Deniz was working on this idea and I helped as I have an interest in superresolution microscopy and have spent some time studying it. This was a great chance to apply and develop some of those superresolution ideas.*

6. **Z.J. Simmons**, N.A. Proite, J. Miles, D.E. Sikes and D.D. Yavuz. “Refractive index enhancement with vanishing absorption in short, high-density vapor cells” *Phys. Rev. A* **85** 053810 (2012).

*This was an experiment I lead on index enhancement using Raman transitions in atomic vapor. This work built on and improved what Proite[18] and others had already done. This material is discussed in chapter 2 and explored in more detail in appendix B.*

7. N.A. Proite, **Z.J. Simmons** and D.D. Yavuz. “Observation of atom localization using Electromagnetically Induced Transparency” *Phys. Rev. A* **83** 041803(R) (2011).

*This was the project I started on with YavuzLab, working with Nick Proite. He wrote his thesis on this subject and there have been a number of improvements and publications in our lab that have built upon this experiment.*

## REFERENCES

- [1] V. Veselago, “The electrodynamics of substances with simultaneously negative values of  $\epsilon$  and  $\mu$ ,” *Soviet Physics Uspekhi*, vol. 10, no. 4, pp. 509–514, 1968.
- [2] P. Milonni, *Fast Light, Slow Light and Left-Handed Light*. Series in Optics and Optoelectronics, CRC Press, 2004.
- [3] R. W. Ziolkowski and E. Heyman, “Wave propagation in media having negative permittivity and permeability,” *Physical Review E*, vol. 64, p. 056625, Oct. 2001.
- [4] J. Pendry, “Negative refraction makes a perfect lens,” *Physical review letters*, vol. 85, pp. 3966–9, Oct. 2000.
- [5] C. M. Soukoulis and M. Wegener, “Past achievements and future challenges in the development of three-dimensional photonic metamaterials,” *Nature Photonics*, vol. 5, pp. 523–530, July 2011.
- [6] S. Xiao and V. M. Shalaev, “Tunable and Active Optical Negative Index Metamaterials,” in *PLASMONICS AND PLASMONIC METAMATERIALS - Analysis and Applications* (G. Shvets and I. Tsukerman, eds.), ch. 9, pp. 255–284, World Scientific Publishing Company, 2012.
- [7] D. E. Sikes and D. D. Yavuz, “Negative refraction with low absorption using Raman transitions with magnetoelectric coupling,” *Physical Review A - Atomic, Molecular, and Optical Physics*, vol. 82, no. 1, pp. 2–5, 2010.
- [8] D. E. Sikes and D. D. Yavuz, “Negative refraction using Raman transitions and chirality,” *Physical Review A - Atomic, Molecular, and Optical Physics*, vol. 84, no. 5, pp. 1–15, 2011.
- [9] H. Xiao and K. E. Oughstun, “Failure of the group-velocity description for ultrawideband pulse propagation in a causally dispersive, absorptive dielectric,” *Journal of the Optical Society of America B*, vol. 16, no. 10, p. 1773, 1999.
- [10] S. Harris, “Electromagnetically Induced Transparency,” *Physics Today*, vol. 50, no. 7, pp. 36–42, 1997.

- [11] M. Fleischhauer and J. P. Marangos, “Electromagnetically induced transparency : Optics in coherent media,” *Review of Modern Physics*, vol. 77, no. April, pp. 633–673, 2005.
- [12] W. Erickson, *Electromagnetically Induced Transparency*. Undergraduate thesis, Reed, 2012.
- [13] M. Scully and S. Zubairy, *Quantum Optics*. Cambridge University Press, 1997.
- [14] M. O. Scully, “Enhancement of the Index of Refraction via Quantum Coherence,” *Physical Review*, vol. 67, no. 14, pp. 1855–1858, 1991.
- [15] M. O. Scully and M. Fleischhauer, “High-Sensitivity Magnetometer Based on Index-Enhanced Media,” *Physical Review Letters*, vol. 69, no. 9, pp. 1360–1363, 1992.
- [16] M. Fleischhauer, C. H. Keitel, M. O. Scully, C. Su, B. T. Ulrich, and S.-Y. Zhu, “Resonantly enhanced refractive index without absorption via atomic coherence,” *Physical Review A*, vol. 46, no. 3, pp. 1468–1487, 1992.
- [17] D. D. Yavuz, “Refractive index enhancement in a far-off resonant atomic system,” *Physical Review Letters*, vol. 95, no. 22, pp. 1–4, 2005.
- [18] N. Proite, B. Unks, J. Green, and D. Yavuz, “Refractive Index Enhancement with Vanishing Absorption in an Atomic Vapor,” *Physical Review Letters*, vol. 101, p. 147401, Sept. 2008.
- [19] Z. J. Simmons, N. a. Proite, J. Miles, D. E. Sikes, and D. D. Yavuz, “Refractive index enhancement with vanishing absorption in short, high-density vapor cells,” *Physical Review A - Atomic, Molecular, and Optical Physics*, vol. 85, no. 5, pp. 1–11, 2012.
- [20] N. A. Proite, B. E. Unks, J. T. Green, and D. D. Yavuz, “Observation of Raman self-focusing in an alkali-metal vapor cell,” *Physical Review A - Atomic, Molecular, and Optical Physics*, vol. 77, no. 2, pp. 1–4, 2008.
- [21] D. E. Sikes, *Theoretical Schemes for Negative Refraction and Enhanced Refractive Index in Atomic Systems*. PhD thesis, UW Madison, 2012.
- [22] J. Kästel, M. Fleischhauer, S. Yelin, and R. Walsworth, “Tunable Negative Refraction without Absorption via Electromagnetically Induced Chirality,” *Physical Review Letters*, vol. 99, p. 073602, Aug. 2007.
- [23] J. Kästel, M. Fleischhauer, S. F. Yelin, and R. L. Walsworth, “Low-loss negative refraction by laser-induced magnetoelectric cross coupling,” *Physical Review A - Atomic, Molecular, and Optical Physics*, vol. 79, no. 6, pp. 1–13, 2009.
- [24] J. J. McClelland and J. L. Hanssen, “Laser cooling without repumping: A magneto-optical trap for erbium atoms,” *Physical Review Letters*, vol. 96, no. 14, pp. 1–4, 2006.
- [25] M. Lu, S. H. Youn, and B. L. Lev, “Trapping ultracold dysprosium: A highly magnetic gas for dipolar physics,” *Physical Review Letters*, vol. 104, no. 6, pp. 1–4, 2010.

- [26] J. Miao, J. Hostetter, G. Stratis, and M. Saffman, “Magneto-optical trapping of holmium atoms,” *Physical Review A*, vol. 89, no. 4, p. 041401, 2014.
- [27] B. Lauritzen, N. Timoney, N. Gisin, M. Afzelius, H. de Riedmatten, Y. Sun, R. M. Macfarlane, and R. L. Cone, “Spectroscopic investigations of  $Eu^{3+} : Y_2SiO_5$  for quantum memory applications,” *Physical Review B*, vol. 85, p. 115111, Mar. 2012.
- [28] N. A. Proite, Z. J. Simmons, and D. D. Yavuz, “Observation of atomic localization using Electromagnetically Induced Transparency,” *Physical Review A*, vol. 83, no. 4, p. 4, 2010.
- [29] J. A. Miles, Z. J. Simmons, and D. D. Yavuz, “Subwavelength localization of atomic excitation using electromagnetically induced transparency,” *Physical Review X*, vol. 3, no. 3, pp. 1–8, 2014.
- [30] A. Freeman and R. Watson, “Theoretical Investigation of Some Magnetic and Spectroscopic Properties of Rare-Earth Ions,” *Physical Review*, vol. 127, no. 6, pp. 2058–2075, 1962.
- [31] J. Van Vleck, “The Puzzle of Rare-earth Spectra in Solids.,” *Journal of Physical Chemistry*, 1937.
- [32] J. Longdell, a. Alexander, and M. Sellars, “Characterization of the hyperfine interaction in europium-doped yttrium orthosilicate and europium chloride hexahydrate,” *Physical Review B*, vol. 74, p. 195101, Nov. 2006.
- [33] A. Kaplianskii and R. Macfarlane, *Spectroscopy of solids containing rare earth ions*. Modern problems in condensed matter sciences, North-Holland, 1987.
- [34] G. Buisson and C. Michel, “Serie Isomorphe D’orthosilicates ( $T_2SiO_5$ ) Et D’orthogermanates ( $T_2GeO_5$ ) De Terres Rares,” *Mat. Res . Bull.*, vol. 3, pp. 193–197, 1968.
- [35] B. Maksimov, V. Ilyukhin, Y. A. Kharitonov, and N. V. Belov, “Crystal Structure of Yttrium Orthosilicate  $Y_2O_3SiO_2 = Y_2SiO_5$ . Dual Function of Yttrium,” *Soviet Physics - Crystallography*, vol. 15, no. 5, pp. 926–933, 1970.
- [36] A. Becerro and A. Escudero, “Revision of the crystallographic data of polymorphic  $Y_2Si_2O_7$  and  $Y_2SiO_5$  compounds,” *Phase Transitions*, vol. 77, pp. 1093–1102, Dec. 2004.
- [37] C. Cannas, M. Mainas, A. Musinu, G. Piccaluga, S. Enzo, M. Bazzoni, A. Speghini, and M. Bettinelli, “Structural investigations and luminescence properties of nanocrystalline europium-doped yttrium silicates prepared by a sol gel technique,” *Optical Materials*, vol. 29, pp. 585–592, 2007.
- [38] C. Li, C. Wyon, and R. Moncorge, “Spectroscopic Properties and Fluorescence Dynamics of  $Er^{3+}$  and  $Yb^{3+}$  in  $Y_2SiO_5$ ,” *IEEE Journal of Quantum Electronics*, vol. 28, no. 4, pp. 1209–1221, 1992.

- [39] X. A. Shen and R. Kachru, “ ${}^7F_0 - {}^5D_1$  Transition in  $Eu^{3+} : Y_2SiO_5$ ,” *J. Opt. Soc. Am. B*, vol. 11, no. 4, pp. 591–596, 1994.
- [40] R. Robinett, *Quantum Mechanics : Classical Results, Modern Systems, and Visualized Examples: Classical Results, Modern Systems, and Visualized Examples*. OUP Oxford, 2006.
- [41] F. Könz, Y. Sun, C. Thiel, R. Cone, R. Equall, R. Hutcheson, and R. Macfarlane, “Temperature and concentration dependence of optical dephasing, spectral-hole lifetime, and anisotropic absorption in  $Eu^{3+} : Y_2SiO_5$ ,” *Physical Review B*, vol. 68, p. 085109, Aug. 2003.
- [42] R. Cowan, *The Theory of Atomic Structure and Spectra*. Los Alamos Series in Basic and Applied Sciences Series, University of California Press, 1981.
- [43] M. P. Hehlen, M. G. Brik, and K. W. Krämer, “50th anniversary of the JuddOfelt theory: An experimentalist’s view of the formalism and its application,” *Journal of Luminescence*, vol. 136, pp. 221–239, Apr. 2013.
- [44] P. A. Tanner, “Some misconceptions concerning the electronic spectra of tri-positive europium and cerium,” *Chemical Society reviews*, vol. 42, pp. 5090–101, June 2013.
- [45] B. Judd, “Optical absorption intensities of rare-earth ions,” *Physical Review*, vol. 197, no. 3, 1962.
- [46] G. S. Ofelt, “Intensities of crystal spectra of rare-earth ions,” *The Journal of Chemical Physics*, vol. 37, no. 1962, pp. 511–520, 1962.
- [47] B. M. Walsh, “Judd-ofelt theory: principles and practices brian m. walsh,” *Advances in Spectroscopy for Lasers and Sensing*, pp. 403–433, 2006.
- [48] M. J. Weber, “Radiative and multiphonon relaxation of rare-earth ions in  $Y_2O_3$ ,” *Physical Review*, vol. 171, no. 1966, pp. 283–291, 1968.
- [49] L. Petersen, *High-resolution spectroscopy of praseodymium ions in a solid matrix : towards single-ion detection sensitivity*. PhD thesis, ETH Zurich, 2011.
- [50] R. Yano, M. Mitsunaga, and N. Uesugi, “Ultralong optical dephasing time in Eu ARoom,” *Optics Letters*, vol. 16, no. 23, pp. 1884–1886, 1991.
- [51] R. Yano, M. Mitsunaga, and N. Uesugi, “Nonlinear laser spectroscopy of  $Eu^{3+} : Y_2SiO_5$  and its application to time-domain optical memory,” *J. Opt. Soc. Am. B*, vol. 9, no. 6, pp. 992–997, 1992.
- [52] F. Graf, A. Renn, G. Zumofen, and U. Wild, “Photon-echo attenuation by dynamical processes in rare-earth-ion-doped crystals,” *Physical Review B*, vol. 58, no. 9, pp. 5462–5478, 1998.

- [53] M. J. Weber and R. F. Schaufele, "Radiative and Nonradiative Transitions in the Fluorescence Decay of  $Eu^{3+}$  in  $SrTiO_3$ ," *The Journal of Chemical Physics*, vol. 43, no. 5, p. 1702, 1965.
- [54] M. J. Weber, "Multiphonon Relaxation of Rare-Earth Ions in Yttrium Orthoaluminate," *Physical Review B*, vol. 8, no. 1, pp. 54–64, 1973.
- [55] G. Liu and B. Jacquier, *Spectroscopic Properties of Rare Earths in Optical Materials*. Springer Series in Materials Science, Springer Berlin Heidelberg, 2006.
- [56] J. M. F. van Dijk, "On the nonradiative and radiative decay rates and a modified exponential energy gap law for 4f4f transitions in rare-earth ions," *The Journal of Chemical Physics*, vol. 78, no. 9, p. 5317, 1983.
- [57] D. S. Ray and M. Chowdhury, "Radiationless transitions in trivalent lanthanide ions embedded in solids," *Proc. Indian Acad. Sci.*, vol. 93, no. 6, pp. 905–916, 1984.
- [58] Z. Sun, M. Li, and Y. Zhou, "Thermal properties of single-phase  $Y_2SiO_5$ ," *Journal of the European Ceramic Society*, vol. 29, pp. 551–557, 2009.
- [59] R. Orbach, "Spin-Lattice Relaxation in Rare-Earth Salts," *Proceedings of the Royal Society of London. Series A, Mathematical and Physical Sciences*, vol. 264, no. 1319, pp. 458–484, 1961.
- [60] W. R. Babbitt, A. Lezama, and T. W. Mossberg, "Optical dephasing, hyperfine structure, and hyperfine relaxation associated with the 580.8-nm  ${}^7F_0 - {}^5D_0$  transition of europium in  $Eu^{3+} : Y_2O_3$ ," *Physical Review B*, vol. 39, no. 4, pp. 1987–1992, 1989.
- [61] C. J. Hawthorn, K. P. Weber, and R. E. Scholten, "Littrow configuration tunable external cavity diode laser with fixed direction output beam," *Review of Scientific Instruments*, vol. 72, no. 12, p. 4477, 2001.
- [62] A. S. Arnold, J. S. Wilson, and M. G. Boshier, "A simple extended-cavity diode laser," *Review of Scientific Instruments*, vol. 69, no. 3, p. 1236, 1998.
- [63] D. A. Smith and I. G. Hughes, "The role of hyperfine pumping in multilevel systems exhibiting saturated absorption," *American Journal of Physics*, vol. 72, no. 5, p. 631, 2004.
- [64] Q. F. Chen, A. Troshyn, I. Ernsting, S. Kayser, S. Vasilyev, A. Nevsky, and S. Schiller, "Spectrally narrow, long-term stable optical frequency reference based on a  $Eu^{3+} : Y_2SiO_5$  crystal at cryogenic temperature," *Physical Review Letters*, vol. 107, no. 22, pp. 1–4, 2011.
- [65] E. D. Black, "An introduction to Pound-Drever-Hall laser frequency stabilization," *American Journal of Physics*, vol. 69, no. 1, p. 79, 2001.
- [66] J. T. H. Green, *Optical Cavity-Based Continuous-Wave Raman Generation*. PhD thesis, UW Madison, 2010.

- [67] J. J. Weber, *Continuous-Wave Light Modulation Using Stimulated Raman Scattering*. PhD thesis, UW Madison, 2014.
- [68] R. W. P. Drever, J. L. Hall, F. V. Kowalski, J. Hough, G. M. Ford, a. J. Munley, and H. Ward, “Laser phase and frequency stabilization using an optical resonator,” *Applied Physics B Photonics and Laser Chemistry*, vol. 31, no. 2, pp. 97–105, 1983.
- [69] Corning, “ULE Corning Code 7972 Ultra Low Expansion Glass.” available here: <https://www.corning.com/media/worldwide/csm/documents/D20FD2EA-7264-43DD-B544-E1CA042B486A.pdf>.
- [70] T. W. Hansch and B. Couillaud, “Laser Frequency Stabilization by Polarization Spectroscopy of a Reflecting Reference Cavity,” *Optics Communications*, vol. 35, no. 3, pp. 3–6, 1980.
- [71] M. Vainio, J. E. Bernard, and L. Marmet, “Cavity-enhanced optical frequency doubler based on transmission-mode HänschCouillaud locking,” *Applied Physics B*, vol. 104, pp. 897–908, Feb. 2011.
- [72] M. Sieghart, *A frequency stabilized diode laser system Diploma thesis*. PhD thesis, University of Bonn, 2011.
- [73] I. Ricciardi, M. De Rosa, A. Rocco, P. Ferraro, and P. De Natale, “Cavity-enhanced generation of 6 W cw second-harmonic power at 532 nm in periodically-poled  $MgO : LiTaO_3$ ,” *Optics express*, vol. 18, no. 11, pp. 10985–10994, 2010.
- [74] M. Nilsson, L. Rippe, S. Kröll, R. Klieber, and D. Suter, “Hole-burning techniques for isolation and study of individual hyperfine transitions in inhomogeneously broadened solids demonstrated in  $Pr^{3+} : Y_2SiO_5$ ,” *Physical Review B - Condensed Matter and Materials Physics*, vol. 70, pp. 1–11, 2004.
- [75] M. P. Wood and J. E. Lawler, “Aberration-corrected echelle spectrometer for measuring ultraviolet branching fractions of iron-group ions.,” *Applied optics*, vol. 51, no. 35, pp. 8407–12, 2012.
- [76] D. Price, “Empirical Lineshape for Computer Fitting of Spectral Data,” *Australian Journal of Physics*, vol. 34, pp. 51–56, 1981.
- [77] D. D. Yavuz, N. R. Brewer, J. a. Miles, and Z. J. Simmons, “Suppression of inhomogeneous broadening using the ac Stark shift,” *Physical Review A*, vol. 88, p. 063836, Dec. 2013.
- [78] A. Siegman, *Lasers*. University Science Books, 1986.
- [79] M. Kasperczyk, S. Person, D. Ananias, L. D. Carlos, and L. Novotny, “Excitation of Magnetic Dipole Transitions at Optical Frequencies,” *Physical Review Letters*, vol. 114, no. 16, 2015.

- [80] Q. Liang, H. Wang, and Z. Jiang, “Investigation on electromagnetically induced transparency and slowdown of group velocity in an  $Eu^{3+} : Y_2SiO_5$  crystal,” *Frontiers of Optoelectronics in China*, vol. 1, no. 3-4, pp. 318–322, 2008.
- [81] S. Materials, “Laser Materials Y2SiO5.” available here: <http://www.scientificmaterials.com/downloads/YSO.pdf>.
- [82] R. Equall, Y. Sun, R. Cone, and R. Macfarlane, “Ultraslow optical dephasing in  $Eu^{3+} : Y_2SiO_5$ ,” *Physical Review Letters*, vol. 72, no. 14, pp. 2179–2182, 1994.
- [83] R. L. Ahlefeldt, M. Zhong, J. G. Bartholomew, and M. J. Sellars, “Minimizing Zeeman sensitivity on optical and hyperfine transitions in  $EuCl_3 \cdot 6H_2O$  to extend coherence times,” *Journal of Luminescence*, vol. 143, pp. 193–200, 2013.
- [84] D. D. Yavuz and N. R. Brewer, “Left-handed electromagnetic waves in materials with induced polarization and magnetization,” *Physical Review A*, vol. 90, no. 6, p. 063807, 2014.
- [85] D. A. Steck, *Quantum and Atom Optics*. 2007.
- [86] R. Straessle, M. Pellaton, C. Affolderbach, Y. Pétremand, D. Briand, G. Mileti, and N. F. De Rooij, “Microfabricated alkali vapor cell with anti-relaxation wall coating,” *Applied Physics Letters*, vol. 105, no. 4, 2014.
- [87] S. Xue, Y. Zhan, M. Yu, and C. Wang, “Optical Properties of  $Eu^{3+} : Y_2SiO_5$  crystal,” in *Solid-State and Integrated Circuit Technology, 2006. ICSICT '06. 8th International Conference on*, pp. 3–5, 2006.
- [88] R. Beach, M. Shinn, L. Davis, R. Solarz, and W. Krupke, “Optical absorption and stimulated emission of neodymium in yttrium orthosilicate,” *IEEE Journal of Quantum Electronics*, vol. 26, no. 8, pp. 1405–1412, 1990.
- [89] C. Gorller-Walrand and K. Binnemans, “Spectral intensities of the f-f transitions searchable,” in *Handbook on the Physics and Chemistry of Rare Earths* (K. Gschneidne Jr. and L. Eyring, eds.), vol. 25, p. 101, North-Holland, Amsterdam, 1998.
- [90] S. Sanders, “kramers kronig lecture notes UCF.” available here: [https://homepages.cae.wisc.edu/~ssanders/me\\_770/supplemental\\_material/kramers-kronig/kramers\\_kronig\\_lecture\\_notes\\_UCF.pdf](https://homepages.cae.wisc.edu/~ssanders/me_770/supplemental_material/kramers-kronig/kramers_kronig_lecture_notes_UCF.pdf).
- [91] CREOL, “Kramers-Kronig Relations.” available here: <https://sharepoint.creol.ucf.edu/Kik/ose5312/Slides/OSE5312%20slides%20class%2004%20-%20Kramers-Kronig%20relations.pdf>.